

Chemical and physical
properties of molecular
nanostructures on surfaces
investigated by means of
scanning probe microscopy

a Ph.D. thesis

by

Benjamin Jose Mallada Faes



Doctoral program of Nanomaterial Chemistry

Department of Physical Chemistry

Faculty of Science | Palacký University

Olomouc

2023

Title: Chemical and physical properties of molecular nanostructures
on surfaces investigated by means of scanning probe microscopy

Author: Mgr. Benjamin Jose Mallada Faes

Advisor: Doc. Ing. Pavel Jelínek, Ph.D.

Co-Advisor: Mgr. Bruno de la Torre, Ph.D.

Study programme: Chemistry - Physical Chemistry - Nanomaterial Chemistry

Form of study: Full time

Institution: Department of Chemistry, Faculty of Science,
Palacký University Olomouc

Year: 2023

Pages: 168

I hereby declare that this thesis is the result of my own work and all sources used are named in the list of references, in accordance with the Methodological Instructions on Ethical Principles in the Preparation of University Theses.

Abstract

In this thesis it is explored the application of the high-resolution imaging capabilities of scanning probe microscopy (SPM) techniques to investigate and understand the details of on-surface synthesis of molecular structures on surfaces and the real-space visualization of charge distributions at the atomic scale. The first part focuses on the on-surface synthesis of porphyrin-based polymers, the introduction of defects into anthracene-based polymeric wires, and the synthesis of single molecules containing non-benzenoid regions with 4-8 membered rings. Through a combination of experimental studies and theoretical simulations, we elucidate the mechanisms and dynamics underlying these processes with atomic precision. In the second part, it is introduced the characterization and visualization in the real-space of charge distributions in single atoms. By employing SPM techniques and tailored functionalized tips, it is directly visualized the unique charge distribution of single B and N substitutional dopants in graphene, the observation of the anisotropic charge distribution know as σ -hole in a single bromine atom and finally the characterization of the anisotropic charge distribution know as π -hole in an halogenated anthracene-based polyaromatic hydrocarbon.

Keywords: SPM, STM, nc-AFM, KPFM, on-surface synthesis, anisotropic charge distribution, non-covalent interactions, σ -hole, π -hole.

Acknowledgements

First, I want to thank my supervisor, Prof. Pavel Jelínek, for providing the means to develop my doctoral studies. Under his guidance, I have learned the importance of meticulous attention to detail in any phenomena and the subtle intertwining of experiments and theory. To my experimental supervisor, Dr. Bruno de la Torre, I also extend my gratitude for teaching me all his skills in SPM. With him, I have learned that endurance in performing experiments is sometimes the only option to observe a phenomenon and to always collect data, regardless of its appearance, whether it is ugly or noisy. This appreciation is also extended to Dr. Martin Svec, who introduced me to the experimental field of STM when we only had a room temperature STM available. I also want to thank all my colleagues and friends in the Nanosurf Lab for their support. While I won't enumerate them here, as it has been done elsewhere, I want to emphasize those who provided (or shared with me) a clean surface. Each of them, to a lesser or greater degree, has created great experiences that I will always remember. Lastly, a special thanks goes out to Daniela for sharing these years with me.

Sin embargo, en ultima instancia, este trabajo se lo dedico a mi madre. Gracias por apoyar (y en ocasiones compartir) la miriada de intereses, conexos e inconexos, que me han llevado por este camino.

Contents

Acknowledgments	iv
List of publications	vii
Introduction	xi
1 Scanning Probe Microscopy	1
1.1 Scanning Tunneling Microscopy	1
1.1.1 The tunneling current	2
1.1.2 The STM feedback loop	6
1.2 Non-contact atomic force microscopy	8
1.3 Kelvin Probe Force Microscopy	13
1.3.1 Introduction	13
1.3.2 Experimental KPFM	17
2 Experimental setup and methods	23
2.1 UHV chamber and low-temperature STM/AFM	23
2.2 Sample and tip preparations	24
3 On-surface synthesis of molecular nanostructures	30
3.1 Strain-driven synthesis of non-benzenoid compounds from helical precursors	33

3.1.1	Introduction	33
3.1.2	Author's contribution to the published work	38
3.2	Magnetic anisotropy of one-dimensional porphyrin coordination polymers	48
3.2.1	Introduction	48
3.2.2	Author's contribution to the published work	52
3.3	Characterization of defects in 1D-anthracene conjugated polymers	62
3.3.1	Introduction	62
3.3.2	Author's contribution to the published work	68
4	Charge distribution visualization with KPFM	79
4.1	Charge Distribution of single boron and nitrogen dopants in graphene	82
4.1.1	Introduction	82
4.1.2	Author's contribution to the published work	87
4.2	Direct imaging of σ -hole	96
4.2.1	Author's contribution to the published work	103
4.3	Direct imaging of π -hole	110
4.3.1	Author's contribution to the published work	115
5	Conclusions and outlook	132
	Bibliography	135
	List of figures	149
	List of abbreviations	150

List of publications

- [1] A. Jimenez-Martin, F. Villalobos, **B. Mallada**, S. Edalatmanesh, A. Matěj, J. M. Cuerva, P. Jelinek, A. G. Campaña, and B. de la Torre, “On-surface synthesis of non-benzenoid conjugated polymers by selective atomic rearrangement of ethynylarenes”, *Chemical Science* 14, 1403–1412 (2023).
- [2] **B. Mallada**, Q. Chen, T. Chutora, A. Sanchez-Grande, B. Cirera, J. Santos, N. Martin, D. Ecija, P. Jelinek, and B. de la Torre, “Resolving atomic-scale defects in conjugated polymers on-surfaces”, *Chemistry—A European Journal* 28, e202200944 (2022).
- [3] J. I. Mendieta-Moreno, **B. Mallada**, B. de la Torre, T. Cadart, M. Kotora, and P. Jelinek, “Unusual scaffold rearrangement in polyaromatic hydrocarbons driven by concerted action of single gold atoms on a gold surface”, *Angewandte Chemie International Edition* 61, e202208010 (2022).
- [4] K. Biswas, J. I. Urgel, K. Xu, J. Ma, A. Sanchez-Grande, P. Mutombo, A. Gallardo, K. Lauwaet, **B. Mallada**, B. de la Torre, et al., “On-surface synthesis of a dicationic diaza hexabenzocoronene derivative on the au (111) surface”, *Angewandte Chemie International Edition* 60, 25551–25556 (2021).
- [5] **B. Mallada**, P. Blonski, R. Langer, P. Jelinek, M. Otyepka, and B. de la Torre, “On-surface synthesis of one-dimensional coordination polymers with tailored magnetic anisotropy”, *ACS Applied Materials & Interfaces* 13, 32393–32401 (2021).
- [6] **B. Mallada** *, A. Gallardo*, M. Lamanec*, B. De La Torre, V. Spirko, P. Hobza, and P. Jelinek, “Real-space imaging of anisotropic charge of σ -hole by means of kelvin probe force microscopy”, *Science* 374, 863–867 (2021).
- [7] **B. Mallada** *, B. de la Torre*, J. I. Mendieta-Moreno, D. Nachtigallova, A. Matěj, M. Matoušek, P. Mutombo, J. Brabec, L. Veis, T. Cadart, et al., “On-surface strain-driven synthesis

of nonalternant non-benzenoid aromatic compounds containing four-to eight membered rings”, *Journal of the American Chemical Society* 143, 14694–14702 (2021).

[8] B. Cirera, A. Sanchez-Grande, B. de la Torre, J. Santos, S. Edalatmanesh, E. Rodriguez Sanchez, K. Lauwaet, **B. Mallada**, R. Zbořil, R. Miranda, et al., “Tailoring topological order and π -conjugation to engineer quasi-metallic polymers”, *Nature nanotechnology* 15, 437–443 (2020).

[9] **B. Mallada**, S. Edalatmanesh, P. Lazar, J. Redondo, A. Gallardo, R. Zbořil, P. Jelínek, M. Švec, and B. de la Torre, “Atomic-scale charge distribution mapping of single substitutional p-and n-type dopants in graphene”, *ACS Sustainable Chemistry & Engineering* 8, 3437– 3444 (2020).

[10] B. de la Torre, A. Matěj, A. Sanchez-Grande, B. Cirera, **B. Mallada**, E. Rodriguez Sanchez, J. Santos, J. I. Mendieta-Moreno, S. Edalatmanesh, K. Lauwaet, et al., “Tailoring π -conjugation and vibrational modes to steer on-surface synthesis of pentalene-bridged ladder polymers”, *Nature Communications* 11, 4567 (2020).

[11] J. Redondo, P. Lazar, P. Prochazka, S. Průša, **B. Mallada**, A. Cahlík, J. Lachnitt, J. Berger, B. Šmíd, L. Kormoš, et al., “Identification of two-dimensional feo2 termination of bulk hematite α -fe2o3 (0001) surface”, *The Journal of Physical Chemistry C* 123, 14312–14318 (2019).

In preparation

[12] M. Grabarics*, **B. Mallada***, A. Jiménez-Martín, P. Jelinek, B. de la Torre, and S. Rauschenbach, “Atomic-scale imaging of individual cyclic oligosaccharides with non contact atomic force microscopy”, In preparation (2023).

[13] A. Jiménez-Martín, **B. Mallada**, et al., “Building up atomically-precise topological heterostructures in one-dimensional conjugated polymers”, In preparation (2023).

[14] **B. Mallada***, M. Ondracek*, M. Lamanec, A. Gallardo, A. Jimenez-Martin, B. de la Torre, P. Hobza, and P. Jelinek, “Visualization of π -hole in molecules by means of kelvin probe force microscopy”, ChemRxiv preprint <https://doi.org/10.26434/chemrxiv-2023-gw0xn> - Submitted (2023).

[15] J. Redondo, J. Michalicka, G. Franceschi, B. Šmíd, N. Kumar, O. Man, M. Blatnik, D. Wrana, F. Kraushofer, **B. Mallada**, et al., “Hematite α -Fe₂O₃ (0001) in top and side view: resolving long-standing controversies about its surface structure”, arXiv preprint arXiv:2303.06023 - Submitted (2023).

[16] F. Villalobos Romero*, **B. Mallada***, et al., “Atomic-scale imaging of individual cyclic oligosaccharides with non-contact atomic force microscopy”, In preparation (2023).

I live not in myself, but I become
Portions of that around me; and to me
High mountains are a feeling.

Childe Harold's Pilgrimage III, 72

Lord Byron

Introduction

Basic science plays a crucial role in driving breakthroughs and establishing the necessary knowledge for future applications with effects on society. Through the accumulation of knowledge, various fields are influenced, leading to the emergence of new applications that can shape our world for years, if not decades, to come. This relationship between scientific discovery and development forms a continuous feedback loop, where even the simplest observations and hypotheses on atomic-scale phenomena can pave the way for groundbreaking techniques and tools. One notable example is the family of scanning probe microscopy techniques, which enable atomically precise imaging and manipulation of individual atoms and molecules. In this thesis, I present a comprehensive exploration of systems characterized at the atomic scale, employing scanning probe microscopy techniques. From the study of long polymeric wires spanning hundreds of nanometers to the resolution of features at the single-atom level, these investigations contribute to our understanding of matter at its most fundamental level.

The Chapter 1 and Chapter 2 introduce the foundations of the experimental scanning probe microscopy (SPM) techniques used through this work, with a special focus on scanning microscopy (STMM), frequency modulated atomic force microscopy (FM-AFM), and Kelvin probe force microscopy (KPFM). The results presented in this thesis are organized in Chapters 3 and 4, encompassing a selection of six published results in the fields of

on-surface synthesis and charge distribution imaging with submolecular resolution. The Chapter 3 is divided into three sections, each corresponding to published results in the field of on-surface synthesis. In Section 3.1, strain-driven chemical reactions on a metallic surface are introduced to obtain non-benzenoid compounds with up to eight-membered rings. The starting precursor is a chiral helical molecule under internal stress due to the geometrical constraints imposed by the surface. This strain in the molecule drives the kinetics of the possible reaction courses and enables the formation of thermodynamically not favourable species on the surface. In the Section 3.2 is presented the on-surface synthesis of an iron porphyrin-based coordination polymer using an Ullman-like mechanism. In the first step of the synthesis, the polymer is linked by phenyl groups that keep each linker tilted and out-of-plane. In the second annealing step, the monomers cyclohydrogenate into a planar polymer. In each of these steps, the magnetic anisotropy of the monomers is modified by the intramolecular rearrangements of the linkers. These changes in the morphology and the magnetic properties are studied by means of AFM and scanning tunneling spectroscopy (STS). The Section 3.3 of Chapter 3, opens the study of the incorporation of defects into anthracene-based polymers. These defects, consisting mostly of cyclohydrogenations into five and six-membered rings between the monomers, dramatically change the molecules' local magnetic properties. In particular, it is compared the case of a 6-5 defect and a 6-6-5 defect and how the incorporation of 6-6-5 introduces one single net spin into the monomer.

In Chapter 4 is discussed the visualization of charge distributions in single molecules and atoms by means of Kelvin probe force microscopy. In the Section 4.1, it is commented the real space imaging of the charges of a single boron and nitrogen atoms in substitutional positions in graphene, displays approximately the same amount of charge with opposite signs. This charge is characterized spatially in both the plane (i.e. graphene lattice) and out of the plane (out of the graphene lattice). In the Section 4.2 the addressed topic

is the visualization of the charge distribution of a σ -hole in a brominated tetraphenyl molecule. This phenomenon, predicted to appear in systems containing halogen atoms, is experimentally characterized with subatomic resolution using KPFM with different tip functionalizations and complemented with a theoretical framework that provides the simulation of experimental images. Finally, in Section 4.3 is introduced the measurement of the spatial charge distribution of a π -hole, a positive anisotropic charge distribution within halogenated polyaromatic hydrocarbons measured in a single molecule of Dichlorooctafluoroanthracene.

We cannot make any factual statement about a given natural object (or physical system) without 'getting in touch' with it. This 'touch' is a real physical interaction. Even if it consists only in our 'looking at the object' the latter must be hit by light-rays and reflect them into the eye, or into some instrument of observation.

— Mind and Matter, Chapter 3 "The Principle of Objectivation"

Erwin Schrodinger

Chapter 1

Scanning Probe Microscopy

1.1 Scanning Tunneling Microscopy

Scanning Tunneling Microscopy (STM) was first discovered in the early 1980s by Gerd Binnig and Heinrich Rohrer (Nobel Prize, 1986) at IBM Zurich Research Laboratory in Switzerland[1]. The physical principle behind STM is the quantum tunnelling of electrons, which is a quantum mechanical effect that occurs when electrons have a non-zero probability of passing through a potential barrier that could not pass through. For the STM, the potential barrier is the vacuum between the metallic tip and the sample surface. The experimental realization of this principle is done by applying a bias voltage V to the sample and bringing the tip close to the surface. In this regime, electrons can tunnel through the vacuum and generate a detectable current in the order of the $I \approx 1 \text{ nA}$ (10^{-9} A) from the sample to the tip.

The tunnelling current exhibits an exponential behaviour as a function of the tip-sample distance, with the current rapidly decreasing as the tip is moved further away from the surface. This exponential behaviour is due to the exponential decay of the wavefunction Ψ of the tunnelling electrons, which determines the probability of finding the electrons on

the other side of the potential barrier. The solution of the Schrodinger equation inside of the region defined by the barrier (see Fig. 1.1) yields a solution of the form:

$$\Psi(z) = \Psi(0)e^{-kz} \quad (1.1)$$

Where $\Psi(0)$ is a constant depending on the boundary conditions and the decay constant k depending on the effective work function Φ inside the barrier:

$$k = \sqrt{\frac{2m\Phi}{\hbar^2}} \quad (1.2)$$

The atomic resolution of the STM is ultimately achieved thanks to this exponential character of the wavefunction Ψ of the electrons inside the barrier, as the majority of the current of electrons will flow just through the closest atoms of the tip and sample and decay fast elsewhere. This provides STM with a great lateral and vertical resolution, as objects changing in height by 100 pm will change the tunnelling current by an order of magnitude.

Finally, the exponential behaviour of the tunnelling current provides a highly sensitive probe of the local density of states on the surface. By utilizing a feedback mechanism to maintain a constant tunnelling current while conducting a raster scan in the XY plane, the position of the tip can be adjusted in real-time to reflect changes in the local density of states.

1.1.1 The tunneling current

As it has been show before, the wave function of the tunneling of electrons through a potential barrier depends exponentially with the spatial size of the barrier. This behavior can be summarized in the definition of a transmission coefficient T that will account the

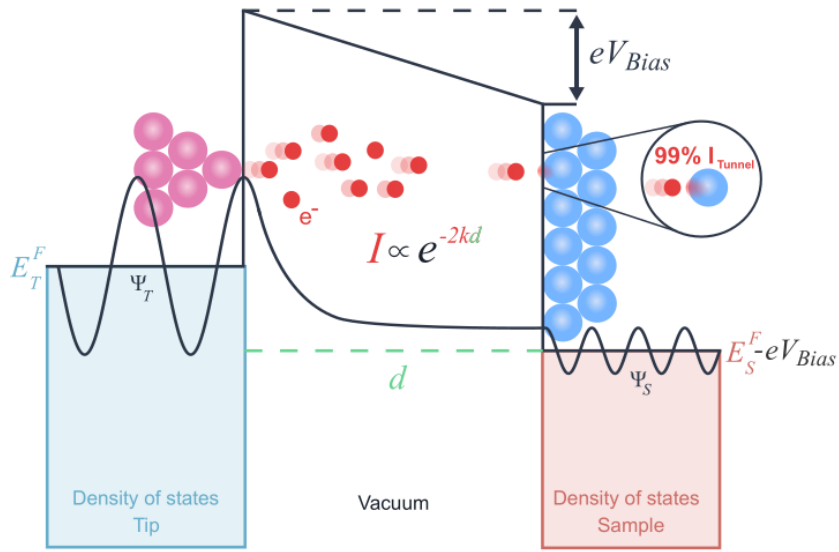


Figure 1.1: Energy level diagram of the tip-sample system with a representation of the evolution of the wavefunction of an electron (black line) across the barrier. In the experimental setup used in this work, a bias voltage V_{Bias} is applied to the sample, while the tip is grounded. The following sign convention is used: $V_{Bias} > 0$ explores the empty states of the sample, with electrons flowing from the tip to the sample, while $V_{Bias} < 0$ probes the occupied states of the sample, where electrons tunnel from the sample to the tip.

probability of finding the electron in the beginning ($z = 0$) or in the end of the tunneling barrier ($z = d$).

$$T = \frac{\psi(d)^2}{\psi(0)^2} \propto e^{-2kd} \quad (1.3)$$

The first attempt to formulate a general expression for the tunnelling current emerged in the decades spanning from 1950 to 1960, pioneered by Bardeen in the study of superconductors [2] and early transistors [3]. Based on his works, Tersoff and Hamman[4, 5] derived an approximation to the tunnelling current (see Eq. (1.4)) directly proportional to the density of states ρ of the tip and sample,

$$I = \frac{4\pi e}{\hbar} \int_0^{eV_{\text{Bias}}} \rho_{\text{tip}}(\epsilon - eV_{\text{Bias}}) \rho_{\text{sample}}(\epsilon) |T(\epsilon, V, d)|^2 d\epsilon \quad (1.4)$$

Here, $|T(\epsilon, V, d)|$ represents the transmission factor of the current from the tip states to the sample states, d denotes the tip-sample distance, V_{Bias} stands for the bias voltage, and ϵ represents the energy relative to the Fermi level of the sample.

At absolute zero temperature, the electronic states situated beneath the Fermi levels of both the tip and the sample are filled and in the absence of a bias voltage their levels are aligned if the tip and sample are close enough. However, by applying a bias voltage (V) between the tip and the sample, it is possible to induce a displacement of their respective Fermi levels relative to each other ($\Delta E_F = V$). As a result, electrons from the occupied states in the tip have the ability to tunnel through the vacuum to the unoccupied states in the sample, or vice versa, depending on the polarity of the bias (see Fig. 1.1). This important feature, shown in Eq. (1.4) and Fig. 1.1, illustrates one of the most fundamental experimental features of the STM, that is, the relationship between the tunnelling current and the density of states and therefore the measurement of the electronic properties of the sample.

In this basic description of the tunnelling current, two assumptions are commonly

made. First, the electrons contributing the most to the current (i.e., those with higher transmission T) are those with energies ϵ closer to eV_{Bias} . Secondly, for small values of the applied bias voltage V , the density of states of the tip $\rho_{\text{sample}}(\epsilon)$ and $T(\epsilon)$ can be approximated as constant. Consequently, by differentiating Equation 1.4 it is possible to obtain an expression that related current and density of states:

$$\left| \frac{dI}{dV} \right|_{eV_{\text{Bias}}} \approx \frac{4\pi e^2}{\hbar} \rho_{\text{tip}}(0) \rho_{\text{sample}}(eV_{\text{Bias}}) |T(eV_{\text{Bias}}, V, d)| \quad (1.5)$$

That can be simplified as,

$$\frac{dI}{dV} \approx \rho_{\text{sample}}(eV) \quad (1.6)$$

Therefore, as indicated by Equation 1.6, the measured current in scanning STM provides a signal that is proportional to the local density of states (LDOS). This characteristic enables the sensitivity of STM to various quantities dependent on state occupation and energy levels. For instance, the technique can be employed to investigate magnetic properties by measuring the occupation of additional electrons, which modifies the available states in molecules [6]. STM is also capable of imaging in real space molecular orbitals (i.e. HOMO, LUMO), probing electron-phonon interaction in inelastic processes, detecting the presence of topological states, determining the bandgap of materials, and much more [7].

The experimental realization of measuring a signal proportional to the LDOS typically involves numerical derivation of the STM current. However, to achieve a less noisy and more accurate measurement, a lock-in setup is commonly employed. In this setup, a small AC voltage called the modulation voltage V_{mod} , with a frequency of f_{mod} , is added to the bias voltage V applied to the sample. This modulation voltage causes the current to vary in response to the temporal changes in the bias voltage. The signal obtained from the lock-in technique is proportional to the derivative of the tunnelling current [7].

1.1.2 The STM feedback loop

The conventional design of an STM incorporates a piezoelectric scanner element, typically a piezoelectric tube made of lead zirconate titanate (PZT). This piezoelectric tube consists of four metallic surface electrodes that control the movement in the $\pm X$ and $\pm Y$ directions, while an additional electrode along the Z axis regulates the extension and retraction of the tip. By applying a voltage to one of the external electrodes, the tip can be precisely moved in incremental steps along the desired direction, enabling accurate and controlled positioning of the tip relative to the sample

STM can operate in two main modes: constant current and constant height. In the constant current mode, a feedback loop continuously monitors the tunneling current measured at the tip and compares it with a pre-defined current setpoint (Fig. 1.2). The difference between the experimental current and the setpoint is the error signal $e(t)$. This signal is used as the controlling element of the feedback loop in the Digital Signal Processor (DSP). Inside the DSP, a Proportional-Integral controller takes $e(t)$ as an input and calculates the integral and derivative terms that will produce an output signal Δz , also known as topography. Then, Δz is converted from a digital signal into an analog signal in the digital-analog converter (DAC). However, the output of the DAC is a signal in the order of ± 10 V, not sufficient to drive the piezoelectric tube in the typical range of distances needed for the control of the STM. Therefore, after the DAC stage Δz is used as input of a High-Voltage Amplifier and typically multiplied by an order of magnitude (e.g. ± 100 -300 V). Finally, the Δz signal is applied to the Z electrode of the piezoelectric tube to precisely move it by the required distance, thereby reaching the setpoint of the current and closing the feedback loop. This operational mode is commonly referred to as *topography* mode, as it tracks the variations in the position of the piezo in the Z direction while the tip scans the XY plane. It is important to note that the topography channel does not provide an accurate representation of the actual *height* or *shape* of arbitrary objects (e.g., single molecules, molecular

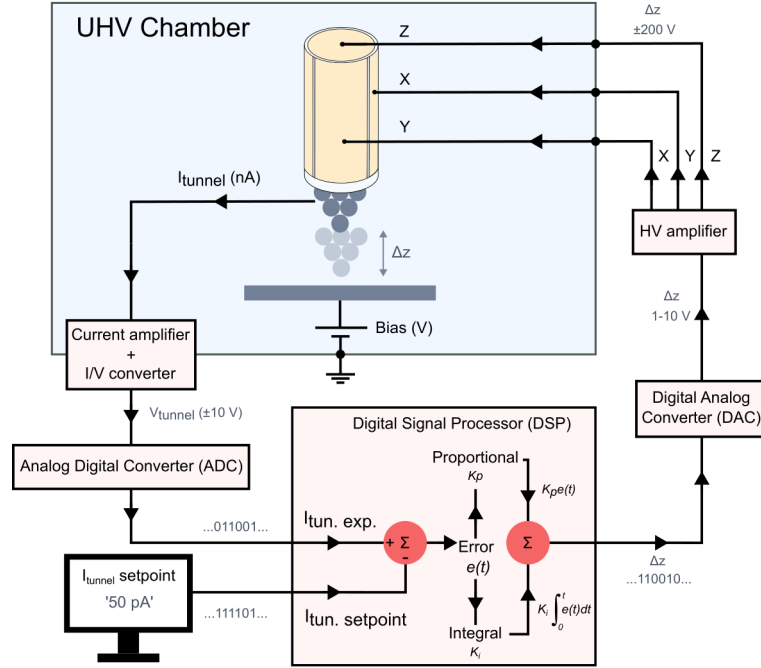


Figure 1.2: Scheme of the feedback loop diagram for the STM signal.

assemblies, etc.). This is because the tunnelling current, which the topography image is based on, is proportional to the local density of states (LDOS) of both the tip and the probed object. Therefore, the resulting topography image heavily depends on the applied bias voltage.

In constant height mode, the feedback loop remains open, and the measured signal is the tunnelling current while scanning in the XY plane. The resulting image captures topographic information, where variations in the tunnelling current correspond to smaller or larger topographic features on the surface. In this mode of operation, scanning at higher speeds is possible as the bandwidth for the current signal is determined by one of the preamplifiers, rather than being limited by the signal processing in the DSP and DAC stages. However, it is important to note that operating in constant height mode carries a risk to the sample's integrity, as the lack of a feedback mechanism increases the potential for collision with the sample.

1.2 Non-contact atomic force microscopy

The STM showed early since its creation[8] (1982) the limitations of depending on conductive tips and samples. In materials as insulators (e.g. KBr, NaCl,...), the required bias to access the empty/filled states is typically higher than the work function in metals. The STM imaging on some metallic surfaces also suggested the action of forces between the tip and the sample observed as distortions in the apparent STM atomic corrugation[9].

The measurement of the interactions between tip and sample is the object of atomic force microscopy (AFM)[10]. The tip is attached to a cantilever that can be modeled as a simple harmonic oscillator with a resonance frequency f_0 , stiffness or spring constant k , and quality factor Q . When the tip interacts with the sample, the resulting changes in the amplitude A and frequency f of the cantilever oscillation are recorded as an experimental signal proportional to the interaction between tip and sample.

The work presented in this thesis is measured in an AFM mode called non-contact AFM (nc-AFM). In this mode of operation, the tip is vibrated with an external actuator and approached to a surface without reaching contact, that is, to a distance where no permanent deformations of tip and sample happen [11]. The tip and surface are separated by a small distance typically ranging from a few angstroms to one nanometer where the probe is sensitive to the short-range interactions (electrostatics, Pauli repulsion, magnetic, chemical bonding) and the long-range interactions (van der Waals). In this regime of distances, a feedback loop tracks the variation of the amplitude A or the frequency f of the oscillation with respect to a defined setpoint due to the interactions between the tip and the sample. There are two modes for the control and monitoring of the signals, amplitude modulation (AM) and frequency modulation (FM).

The amplitude-modulation (AM-AFM) mode corresponds with an oscillator vibrating the tip with a fixed amplitude A_{drive} and frequency f_{drive} . The attractive/repulsive interac-

tions between tip and sample produce changes in the resonant frequency f_0 of the cantilever with a subsequent decrease/increase of the amplitude of oscillation that is recorded as the experimental signal. However, this mode of operation has some limitations when measuring at the atomic scale. In UHV environments, the mechanical properties of the cantilever are altered, increasing the quality factor Q of the cantilever due to the absence of air[12]. A higher Q factor indicates a system with lower damping, which means it can sustain oscillations for a longer time and has a narrower bandwidth. Conversely, a lower Q factor indicates a system with higher damping, which means it loses energy more quickly and has a broader bandwidth. Although the signal-to-noise ratio of the measured amplitude increases with Q , it also reduces the available bandwidth of operation[12]. For the AM-AFM mode, the characteristic time of change in amplitude is,

$$\tau \approx \frac{2Q}{f_0} \quad (1.7)$$

A consequence of this relation is that the recovery time for the amplitude using stiff sensors in UHV as the qPlus sensor in AM-AFM mode ($Q = 20.000$, $f = 30$ kHz) is roughly in the order of 1 Hz, making it too slow for the typical acquisition times (1 s/line).

The second case of operation is called frequency modulation (FM-AFM). This mode of operation was introduced in 1991 by Albrecht *et al.*[12] to reduce the noise and increase the sensitivity concerning the early AM operation of AFM[10, 13]. As introduced previously, in UHV conditions the mechanical properties of the cantilevers change with a tendency to become stiffer and have higher Q factors (i.e. fewer energy losses per cycle of oscillation) making AM-AFM too slow for operating in UHV. Using thermodynamic considerations[11], it was soon observed that the minimal thermal noise of the deflection in terms of the frequency obeys the expression,

$$\delta f \propto \sqrt{\frac{T}{k f_0 Q}} \quad (1.8)$$

with T the temperature of the system, k the spring constant of the cantilever, and Q . From this expression, it can be observed that using sensors with great stiffness and high-quality factors reduces greatly the deflection noise and therefore increases the accessible resolution to the AFM.

In frequency modulation, the cantilever is constantly driven to its natural frequency f_0 while keeping the amplitude A constant and the phase of the signal as $\phi = \pi/2$ (i.e. resonant condition of a driven harmonic oscillator). The changes of the frequency (see Fig. 1.3) with respect to the natural resonance due to the presence of forces is the *frequency shift* or Δf . The presence of non-conservative forces changes also the amplitude of the oscillation and the energy needed to drive again the sensor to a constant amplitude will be the excitation or dissipation channel. Experimentally, the amplitude, phase, dissipation, and frequency shift contain all the information on the interaction of the tip with the sample, and in particular, it is possible to deduce a relationship between the frequency of oscillation and the averaged forces present between the tip and sample in a full oscillation,

$$\Delta f = f - f_0 - \frac{f_0}{k_0 A^2} \left\langle F_{ts}(t) A \cos(2\pi f_0 t) \right\rangle \quad (1.9)$$

where the averaged force in a cycle of oscillation F_{ts} can be defined in terms of an effective spring constant $k_{ts} = \partial F_{ts} / \partial z$ acting between the tip and sample when a small amplitude approximation is applied to Eq. (1.9),

$$\Delta f = -\frac{f_0}{2k_0} \frac{\partial F_{ts}}{\partial z} \quad (1.10)$$

While the aforementioned expression holds true for small amplitudes, in practice, the deconvolution of the force from the experimental Δf with arbitrary amplitudes requires integrating numerically 1.10, either with the approach developed in the group of Giessibl, also known as matrix method [14] or the Sader-Jarvis method[15].

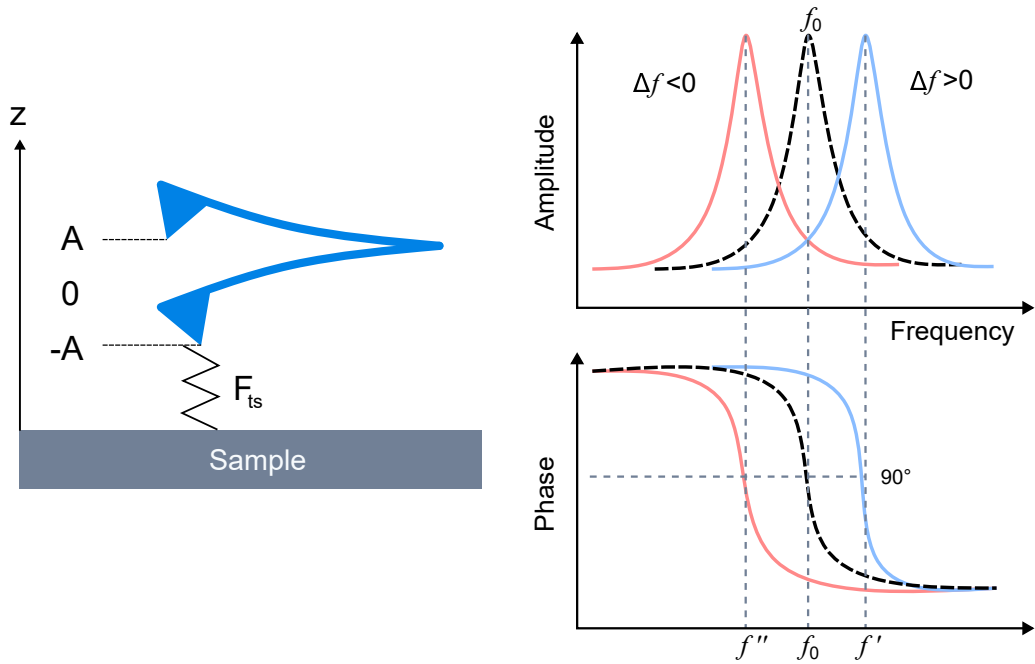


Figure 1.3: Oscillation of the AFM tip from A to $-A$. The interaction with the tip can be seen as an effective force F_{ts} changing the natural frequency f_0 by an amount Δf called the frequency shift. For an attractive interaction $\Delta f < 0$ and for a repulsive is $\Delta f > 0$.

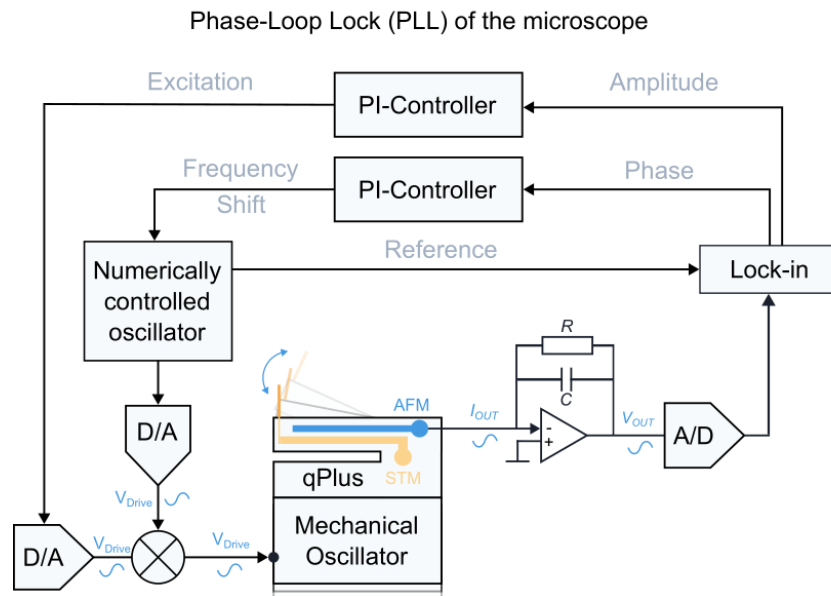


Figure 1.4: The FM-AFM feedback loop.

FM-AFM signals are controlled and manipulated using two feedback loops, one for frequency and the other for amplitude. The first step in the feedback system (see Fig. 1.4) is to drive the cantilever to its resonance frequency using an externally driven piezoelectric actuator. The piezoelectric element causes the cantilever to oscillate with a given amplitude A and natural frequency f_0 . As the cantilever approaches the sample, forces between the tip and surface cause deflection from its original position, frequency, and amplitude. In this thesis, qPlus sensors are used, where deflection of the sensor creates charges in the piezoelectric body of the sensor. Electrodes on the qPlus body collect these charges Fig. 1.4, which are then routed to a trans-impedance circuit that converts the oscillating current of the deflection into an AC voltage. This analog signal is transformed into a digital signal in an A/D converter and routed into a phase-locked loop (PLL).

The first stage of the PLL is the lock-in, where the incoming experimental deflection voltage is demodulated using a controlled oscillating signal to extract information about the forces contained in the phase and amplitude. Two signals are obtained from this stage, one proportional to the phase and the other proportional to the amplitude. The phase signal is compared with a predefined phase setpoint in a PI loop controller. The output of this operation is a digital signal that will drive a controlled oscillator (NCO) with a phase difference of $\phi = \frac{\pi}{2}$. The amplitude signal is compared to a predefined setpoint in a separate PI controller, producing a signal known as excitation. The excitation is proportional to the energy dissipated by the sensor in the presence of dissipative events such as bond creation-destruction, friction, charge/discharging events, etc. In the last stage, the loop is completed, and the phase and amplitude signals are converted into analogue signals and subsequently mixed into a voltage used to drive the mechanical oscillator.

1.3 Kelvin Probe Force Microscopy

In this section is introduced a variation of nc-AFM, more sensitive to the electrostatic character of the molecules and surfaces, called Kelvin Probe Force Microscopy. This technique was used frequently during my doctoral studies and constitutes the core for understanding Chapter 4.

1.3.1 Introduction

In 1898, Kelvin performed a simple experiment involving a capacitor made of two parallel plates made of zinc and copper [16]. When the plates were electrically connected (see Fig. 1.5-a), the gold leaves of the connected electroscope would deflect, indicating an accumulation of charge. This scenario corresponds to the zinc plate becoming positively charged with respect to the copper plate, with electrons flowing from the metal with the higher Fermi level (zinc) to the one with the lower Fermi level (copper) through the electrical connection until a thermodynamic equilibrium is reached. The built-in electrostatic potential between the plates was then equal to the difference between the work functions of both metallic plates. By adjusting the distance between the plates (and therefore the capacitance), or by applying an external electric field, it was possible to measure the amount of charge required to establish the potential difference between the plates, also known as the contact potential difference (CPD).

This principle for quantification of the charges can be also applied in an AFM setup in UHV [17–19]. The AFM can be modeled as one plate of a capacitor (see Fig. 1.5), while the other parallel plate consists of the sample, which can include surfaces, heteroatoms, single molecules, and polymers, each with different work functions, separated by a distance of z . When both materials are electrically connected, the flow of electrons from the plate with the higher Fermi level to the plate with the lower Fermi level creates a surface charge

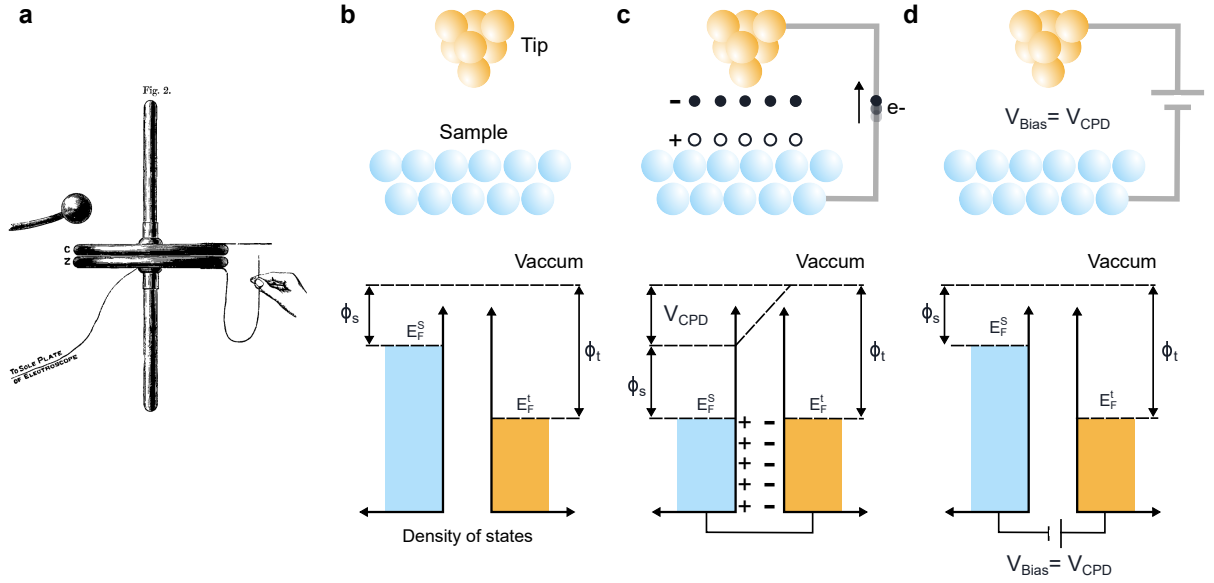


Figure 1.5: The capacitor model of KPFM.

redistribution in both materials with opposite signs. The electrostatic field built between the charged plates has a potential energy that is equal to,

$$U_{electrostatic} = \frac{1}{2}C(z)(\Phi_{tip} - \Phi_{sample})^2 = \frac{1}{2}C(z)\Delta\Phi^2 \quad (1.11)$$

Where the capacitance of the parallel plates, denoted by $C(z)$, is dependent on the work functions of the tip and sample, Φ_{tip} and Φ_{sample} . To determine the contact potential difference ($\Delta\Phi$), an external electrical field is applied in an nc-AFM setup by varying the bias voltage between the tip and sample. The frequency shift Δf is measured as a function of bias voltage, with Δf being proportional to the forces between the tip and sample. By analyzing the parabolic behavior of Δf as a function of voltage, it is possible to identify the voltage that corresponds to the nullification of the electrostatic interaction, which is known as the contact potential difference voltage (V_{CPD}).

$$\Delta f = \frac{1}{2} \frac{\partial C(z)}{\partial z} (V - V_{CPD})^2 \quad (1.12)$$

In the regime of far distances, V_{CPD} depends only on the z distance and the difference in work functions of tip and sample, providing only a global picture of the electrostatics of the system.

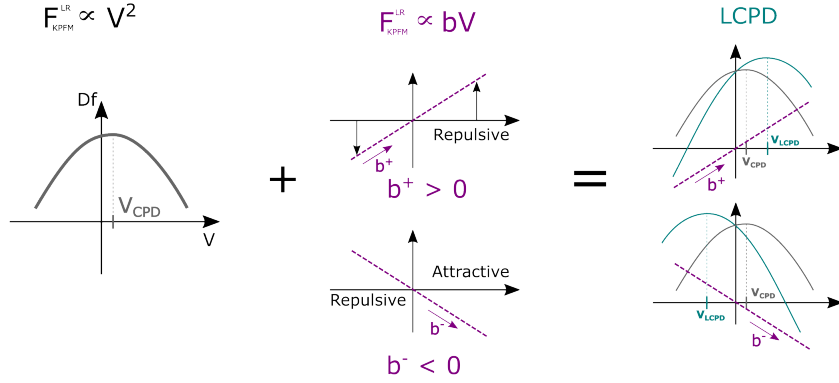


Figure 1.6: The long and short-range contributions to the LCPD signal. The addition of a linear term with the applied bias rationalizes the shift of the parabolas towards more positive/negative V if the probed charge is negative/positive.

However, as commented in Section 1.2 and Section 1.1, the atomic resolution is only achieved in regimes of relatively close distances (below 1 nm) where local variations of height/electronic properties can be resolved laterally. The local variations of V_{CPD} in this close-distance regime are known as local contact potential differences (LCPD). The complete picture of the KPFM signal in the atomic scales and its ability to map the electrostatics forces has been described elsewhere[20] and further details on the description, implementation, and application can be found in the thesis of Aurelio Gallardo [21]. Some of the main results can be then summarized as follows:

1. The KPFM signal can be modeled as the composition of a large-range $F_{KPFM}^{LR}(V, z)$ and a short-range component $F_{KPFM}^{SR}(V, \vec{r})$,

$$F_{KPFM} = F_{KPFM}^{LR}(V, z) + F_{KPFM}^{SR}(V, \vec{r})$$

2. $F_{KPFM}^{LR}(V, z)$ produces the parabolic behavior described in Eq. (1.12).
3. $F_{KPFM}^{SR}(V, \vec{r})$ follows Coulomb's law and depends on the intrinsic net charges of tip and sample and the induced dipoles by the bias voltage.
4. The effect of $F_{KPFM}^{SR}(V, \vec{r})$ on $F_{KPFM}^{LR}(V, z)$ is a lineal shift of the KPFM parabola. This shift is responsible for the resolution between positive and negative regions of the sample and is equal to the V_{LCPD} (see Fig. 1.6).
5. Positive/negative charges in the sample have a lower/higher V_{LCPD} .
6. The experimental images are a composition of an image originating from the charges of the tip and an image originating in the charges of the sample.
7. Maximizing the polarizability of the tip (i.e. using different functionalizations) increases the contribution of the charges of the sample in the experimental image.

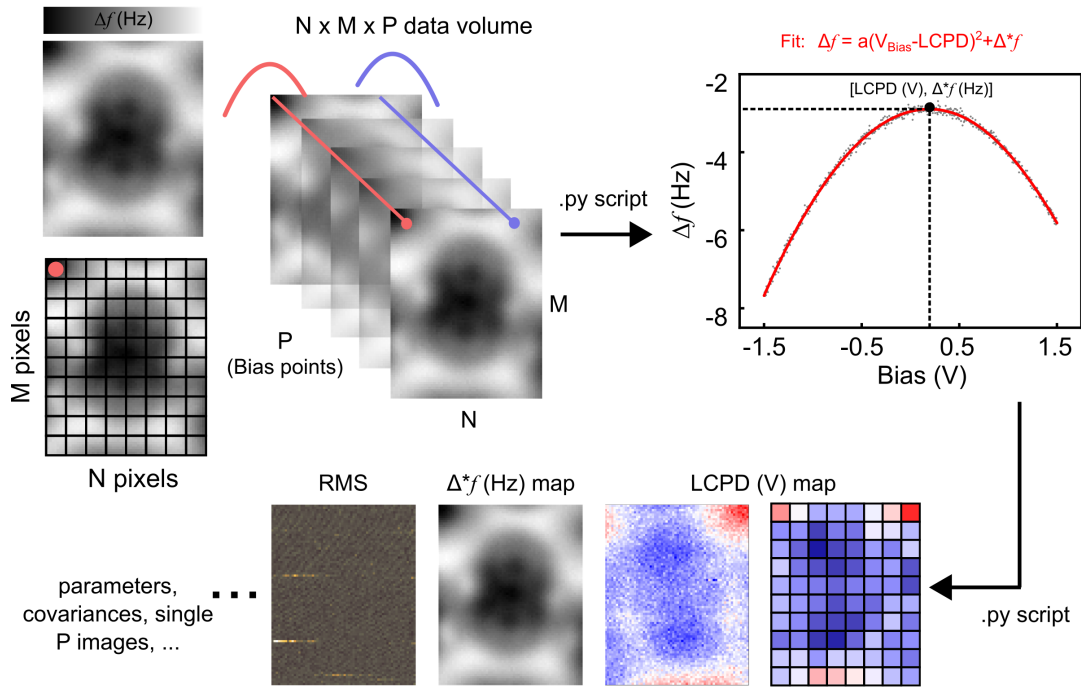


Figure 1.7: The experimental acquisition of KPFM data begins by defining an experiment grid in the XY plane (sample plane) or XZ plane (out-of-plane). The grid consists of $N \times M$ points. Using a user-defined command sequence, the AFM tip is moved to each defined point and acquires a $\Delta f(V_{Bias})$ spectroscopy with P bias voltage points. All the spectroscopies are then read, ordered, analyzed, and fitted to a parabolic model using a Python script. The parameters obtained from the fit are represented as pixel values in a grid of size $N \times M$.

1.3.2 Experimental KPFM

The experimental measurement of the local contact potential difference (LCPD) of single molecules and atoms in this thesis, was carried out using the method described in Figure 1.7. In Kelvin probe force microscopy (KPFM), the primary measurement is the bias spectroscopy recording the change in (Δf) as a function of the bias voltage (V). By sweeping the electrostatic potential V from small to large values, one can observe the nullification of electrostatic forces between the sample and the tip, resulting in the appearance of minima or maxima in Δf . As mentioned earlier, the external V value that minimizes the electrostatic forces corresponds to the LCPD of the system.

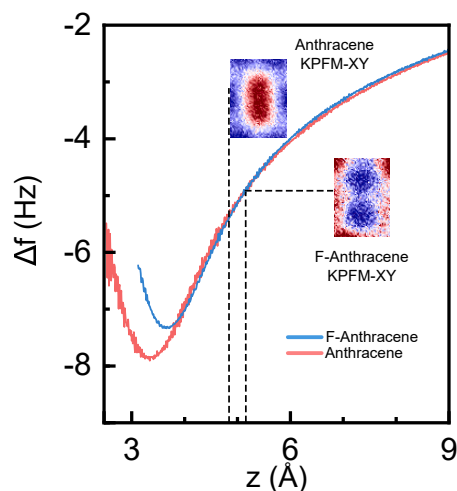


Figure 1.8: **a** Diagram of the region where the KPFM signal is most sensitive to the influence of the electrostatics. **b** Experimental example of force spectroscopies performed with a CO-tip on anthracene and a 9,10- Dichlorooctafluoroanthracene anthracene (see 4.3). The LCPD maps were performed for tip-sample distances (dotted lines) compatible with an enhancement of the electrostatic contribution.

The experimental process can be described as follows. After imaging the system of interest (e.g., a molecule) with STM or AFM, the z -feedback loop is disabled and the tip is kept at a constant height. At this point, the tip is manually approached or retracted until a suitable distance is achieved, which allows for the observation of non-distorted parabolas. If the tip is too close, the functionalized apex may bend due to the overlap of wavefunctions of the sample and tip. Conversely, if the tip is too far away, the measured value is not a local contact potential difference (LCPD), but rather a contact potential difference (CPD) without local resolution of the electrostatics. Typically, the appropriate distance range corresponds to 100-300 pm between the minima of the tip-sample interaction and the onset of purely van der Waals distances dominated regime, as depicted in Fig. 1.8. At this distance scale, the dominant interactions are the non-local dispersive forces and local electrostatics. To probe the LCPD locally, the next step is to define a grid, as shown in Fig. 1.7. Typically, a user-defined grid of points is used in the area of interest, which can be in the same plane as the surface (XY plane) or perpendicular to it (XZ plane). If the

former is the case, the software Nanonis offers a file structure called .3ds that can store the bias spectroscopies obtained at each point in XY as a binary file. These spectroscopies can record multiple channels, including frequency shift, bias, current, phase, amplitude, and excitation.

To perform the KPFM probing in the XZ or Z direction in the second case, we rely on custom Labview commands that provide direct access to the signals of the microscopy. To facilitate this type of measurement, I created a Python script that generates a sequence of commands based on user inputs: the desired number of pixels in the KPFM grid (N , M), and the width X and height Z of the grid. This script generates a .txt file that enables the tip to move a distance of X/N for N steps, perform bias spectroscopy measurements, and store the data in a .dat file. The tip then moves another distance of X/N and repeats the measurement process until it reaches a total distance of X . Next, the tip is retracted for a distance of Z/M and the process is repeated in the X direction until all N , M points of the grid are measured

The experimental data is then processed with a Python script that reads and stores the information of each point of the grid in arrays of size $N \times M \times P$ (see Fig. 1.7). Additional operations can also be applied at this stage, such as applying Gaussian filters to each curve, resizing the arrays, or creating maps of each stored channel. The next step involves fitting each of the $N \times M$ parabolas of $\Delta f(V_{Bias})$ using the least squares method and the following model:

$$\Delta f(V_{Bias}) = a(V_{Bias} - LCPD)^2 + c \quad (1.13)$$

where the bias voltage that minimizes $\Delta f(V_{Bias})$ is referred to as the $LCPD$. The parameter a is associated with the macroscopic properties of the capacitor (refer to Equation 1.12), while c collects the experimental offset of $\Delta f(V_{Bias})$ and corresponds to the value $\Delta f(LCPD)$ that minimizes the electrostatic forces. As shown in Figure 1.7, each param-

eter is stored as a pixel value in an $N \times M$ grid and visualized as images, also known as *maps*

Considering the quality assessment of the KPFM maps and its impact on experimental design holds significant importance as KPFM mapping is a time-expensive process, where each kelvin parabola requires 3-5 seconds of acquisition time and a pixel map with a resolution of 64×64 can take up to 5 hours of acquisition time. Increasing the number of pixels or the acquisition time can improve the quality of the parabolas, however, the refilling process of LHe and LN_2 that occurs every three days involves retracting the STM tip from the sample for a distance of 100 nm. The subsequent approach and repositioning of the tip on the same object (e.g. a molecule), introduces an effect called *creep* (i.e. the inertia of moving the z-piezo back and forth) and "drift" (random tip movement due to thermalization of the system), which constrain the available time where the tip will be accurately placed on the grid.

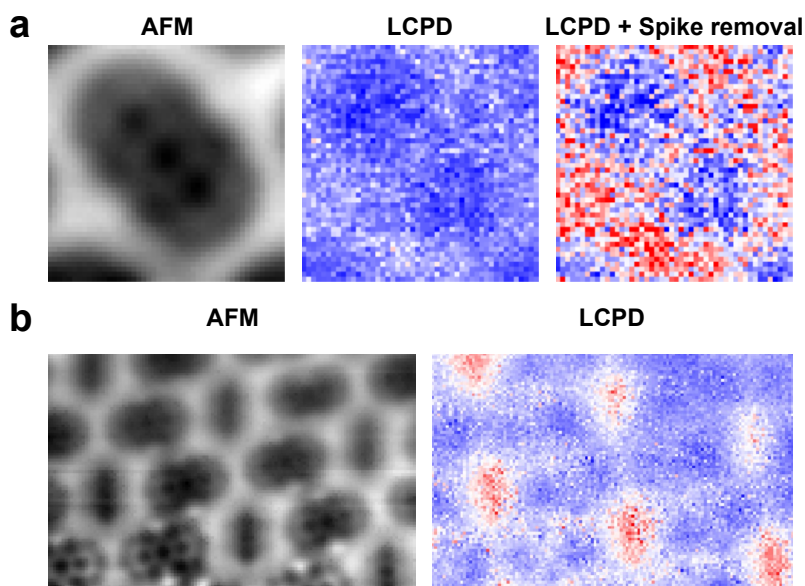


Figure 1.9: **a** Poor quality spectroscopies (i.e. noisy or absent parabolic behavior) are represented in this LCPD map of 9,10- Dichlorooctafluoroanthracene with a CO-tip (see 4.3) as spikes in the signal due to a poor fit. Depending on their number, it is possible to substitute them manually with an average value of the neighbors, deleting the pixel, applying a threshold condition for the array, or applying Gaussian filters. The solution is not specific and might involve optimizing the PLL to change the tip. **b** The change of the tip-sample distance due to *creep* is visualized in AFM and in the LCPD map of a mixed island of anthracene and 9,10- Dichlorooctafluoroanthracene (see Section 4.3). The effect can be observed mostly in AFM as a change of the resolution, from high resolution (bottom) to loss of submolecular resolution (top). The solution for compensating the *creep* often requires the stabilization of the tip's position for 12 and 24 hours.

Low-quality parabolas can appear as transients or spikes in the LCPD maps (Fig. 1.9-a) and changes in contrast (Fig. 1.9-b) may signal a loss of the functionalized tip's apex or "creep," which can be visualized directly on AFM or LCPD maps. However, the most significant contributions to LCPD resolution usually come from the tip functionalization and the tip-sample distance. In the case of tip functionalization, the polarizability of the molecule or atom at the tip's apex can dramatically enhance the measured electrostatics (e.g., Xe atoms) or obscure the electrostatics of the system due to the complex quadrupolar character of the tip (e.g., CO tips). In the case of tip-sample distance, as previously discussed (see Fig. 1.10), this distance plays a crucial role in parabola quality. Parabola

quality can be assessed by calculating the average root mean square error (RMSE) of the fit residuals, which is a good estimator of the standard deviation σ of the LCPD values and provides an indication of the goodness of the fit (see Fig. 1.10). At very close distances, the tip's apex not only experiences electrostatic interactions but also Pauli repulsion from overlapping atoms, which can distort the parabolas. Therefore, the usual high-resolution AFM operating distances are not optimal for KPFM measurements, as RMSE maps begin to show artifacts that track the shape of the molecule due to parabola distortion.

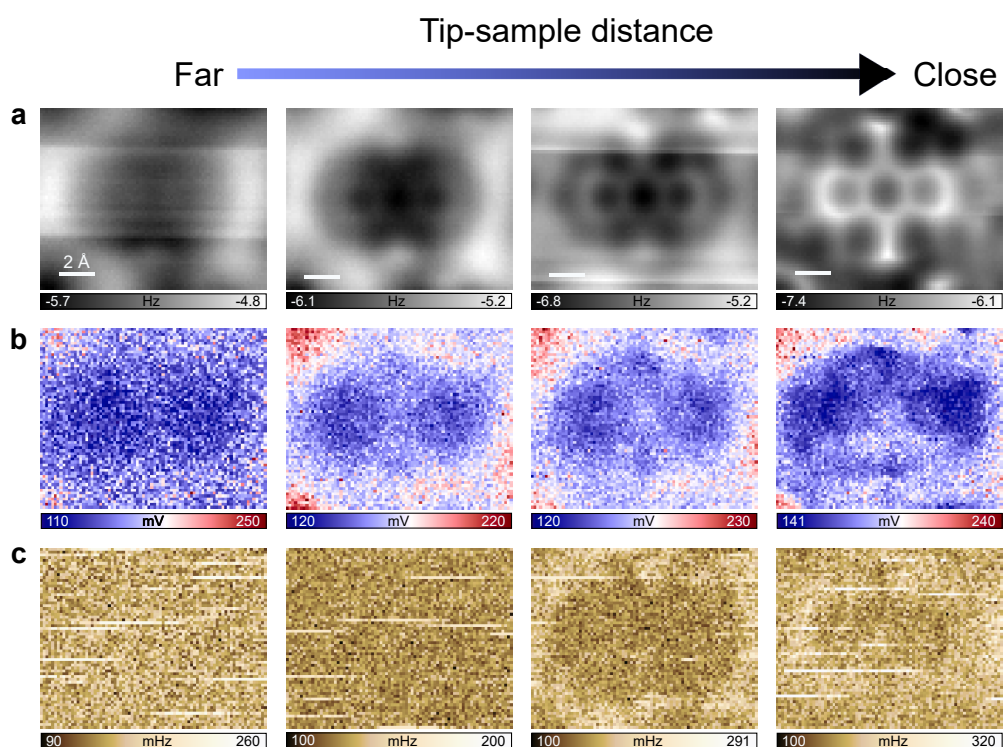


Figure 1.10: The resolution of f^* with a CO tip of a single 9,10- Dichlorooctafluoroanthracene molecule increases with smaller tip-sample distances (a) while the LCPD maps develop a clear contrast in further distances (b) where the RMSE is minimal and does not introduce artifacts in the parabolas. Each image was acquired with distance steps of $\Delta z \approx 30$ pm.

Chapter 2

Experimental setup and methods

2.1 UHV chamber and low-temperature STM/AFM

The field of surface science has always been closely tied to the interactions between surfaces and adsorbates. Adsorbates significantly alter the chemical and physical properties of surfaces, including intrinsic characteristics like catalytic activity, selective molecular binding, and electrical conductivity [22]. As mentioned in the previous section (Section 1.1), SPM techniques such as STM and nc-AFM are highly sensitive to local properties at length scales of 1 Å and can be greatly impacted by the presence of adsorbates in the form of gases, including nitrogen, carbon monoxide, and water vapor, that interact with the surface molecules or atoms. To obtain optimal results in STM or nc-AFM experiments, the sample must be free of contaminants for a period that exceeds the duration of the visualization or manipulation process (typically ranging from milliseconds to hours). This requirement, along with the use of cryogenic temperatures, implies the use of ultra-high vacuum conditions in the chamber with a typical base pressure of 10^{-10} mbar.

The SPM system used in this thesis is a custom-built Createc STM/nc-AFM machine operating in UHV at 4.4 K. It comprises three chambers: the load-lock, preparation, and

STM chambers. The load lock serves as a storage area for samples, which are transferred from atmospheric conditions to high vacuum conditions. This chamber is pumped by a turbomolecular pump and a scroll pump to maintain vacuum conditions of 10^{-8} mbar and is separated from the preparation chamber by a gate valve. The next two chambers, preparation, and SPM are pumped by getter pumps and titanium sublimation pumps to reach a base pressure of 10^{-11} mbar. The preparation chamber is equipped with a manipulator for cleaning samples, growing 2D materials, depositing molecules, inducing thermal chemical reactions, transferring samples to the SPM chamber, and monitoring sensors. It features multiple flanges for attaching external evaporators, such as Knudsen cells for molecules and metalloids, chemical vapor deposition devices, and electrospray ionization sources for non-thermal deposition of delicate, large molecules from a liquid solution outside the UHV chamber.

The SPM chamber is attached to a bath cryostat containing two concentric cylinders of LN_2 and LHe and houses the SPM block at cryogenic temperatures. The cryostats contain a volume of 14 L of LN_2 and 5.5 L of LHe with a refilling cycle of 72 hours. The SPM block contains the SPM head, suspended by springs and surrounded by concentric radiation shields at LN_2 and LHe temperatures. The SPM head includes the sample holder, accessible through a shutter door, the scanning probe (e.g. qPlus sensor), the scanning piezoelectric tube, the piezoelectric stack for coarse approach, and the table of pins for extracting the STM/AFM signals from UHV to the external electronics.

2.2 Sample and tip preparations

Sample preparation

In the past section, it has been introduced the UHV requirements for keeping surfaces clean. However, the most common state for a sample introduced into UHV conditions from the

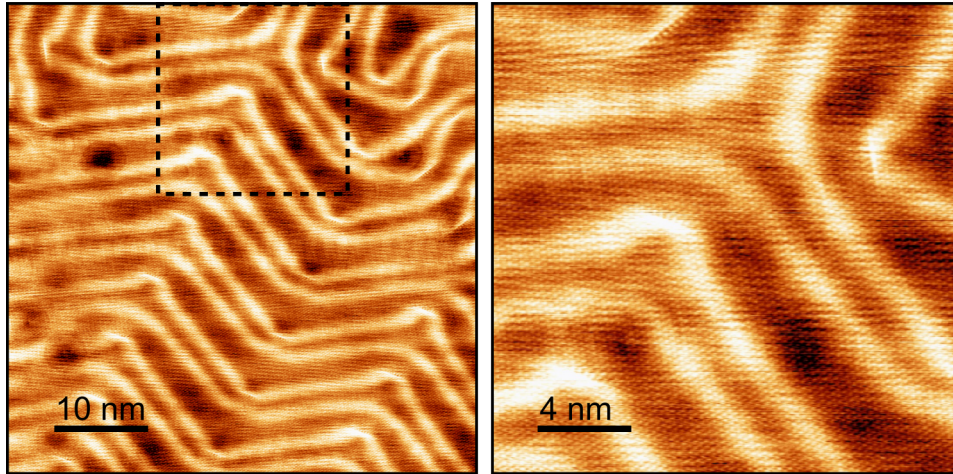


Figure 2.1: STM topography (3 mV, 30 nA) of an Au(111) clean surface. The *herringbone* (zoom-in) is atomically resolved and the presence of kinks and defects on the surface can be visualized.

air is to be covered by gas (e.g. H_2O) and solid (e.g. dust, grease,...) adsorbates. In this thesis, the used samples are mostly noble metals such as Au(111) and Ag(111). These types of samples have a standard cleaning procedure for the preparation of clean, well-defined surfaces, divided into two stages: removal of material and reconstruction of the surface. The first stage is known as *sputtering* and it involves the bombardment of the surface with ionized atoms of noble gases (e.g. Argon, Neon, Xenon,...). During this process, the preparation chamber is filled with argon gas using a leak valve. Once the argon pressure in the chamber reaches $P \approx 10^{-5}$ the sample is aligned with the sputter gun that is then activated with an electric potential of 1 kV to ionize the gas for 15 minutes. During this process, several tens to hundreds of nanometers of material are removed from the surface by the collisions of the ions with the surface. The impact of ions with the sample generates currents of $I \approx 10 \mu A$ that can be monitored with a multimeter plugged into the electrical feedthrough pins connecting the sample with the outside. After this stage, the sample is clean but the destructive nature of the ion bombardment creates a non-flat landscape on the atomic scale with a typical corrugation of several dozens of nanometers. The second

stage of preparation involves providing thermal energy to the sample to favor the mobility of the metallic atoms in the sample. Heating the sample with temperatures of around half of its melting point (e.g. for gold around 450 °C), provides enough kinetic energy for the metallic atoms to move and promote the creation of a new flat, homogeneous surface. Experimentally this is realized using a resistive heating element in contact with the sample. This resistive element is heated up by connecting it to a power supply in a ramp of two values: a flash heating of 3 minutes with (30 V, 1 A) and then a second stage of 7 minutes with (20 V, 0.4 A). During this process, the temperature of the sample is monitored in parallel with an optical IR pyrometer.

In general, once the sample is cooled down to room temperature it can be transferred to the microscope or used in further preparations. The most common preparation in this thesis is the sublimation of molecules onto metallic surfaces. To achieve this, a Knudsen or effusion cell is commonly used. In this cell, the molecule in powder form is stored and heated until it undergoes sublimation under UHV conditions. The usually low partial pressure of the molecules creates an atmosphere in UHV that promotes the adsorption of molecules to the metallic sample. Once adsorbed, the system can be characterized with SPM techniques (e.g. for example the visualization of the σ -hole in Section 4.2) or induce further chemical reactions using heat and the catalytic properties of the metallic surface (more details in Chapter 3)

Tip preparation and high resolution nc-AFM

The atomic resolution of surfaces[25, 26] was achieved relatively soon with respect to the creation of the STM (1983) and AFM (1995) [1, 8, 10] with metallic or silicon tips. These tips are relatively stiff and reactive, and in the typical range of distances of the STM, their interaction with molecules is strong enough to move or make the molecule jump to the tip upon approach. The submolecular resolution (see Section 1.2) was only achieved with

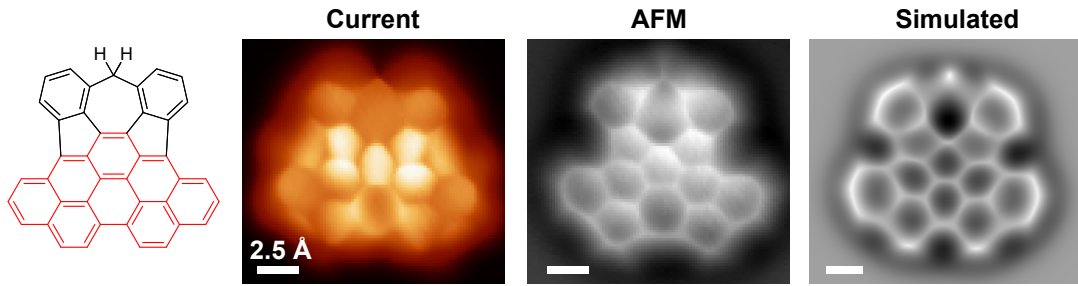


Figure 2.2: The use of functionalized tips provides submolecular resolution in nc-AFM and in STM. In this example is shown the molecule *Moth*[23] measured with a CO-tip in constant height mode ($V_{Bias} = 3$ mV). The full characterization of the properties of the molecule can be achieved by comparing the signals of current, nc-AFM, and the simulated images with the PP[24].

the controlled functionalization of the STM tip’s apex with an inert single *CO* molecule in 2009 [27]. Since then, several mechanisms for functionalizing tips (such as bias voltage ramps, close STM scanning, controlled manual tip approach) with different atoms (N₂O[28], Xe[29], etc.) have been reported, enabling submolecular high-resolution imaging (see 2.2). The origin of the high resolution in STM and AFM can be understood in terms of a simple picture where the probe (the inert atom) and the sample (the molecule) are close enough that their electrons start to experience Pauli repulsion, causing lateral bending of the probe apex. The lateral bending of the probe near a bond, where the electronic density is highly localized, emerges from sensing a saddle point in the energy landscape of the surface and molecule. This saddle point produces a sudden change in the experimental Δf signal that is observed in the recorded image as a sharp feature that can be correlated with the covalent bonds of the molecular backbone [30]. This behaviour can be captured in simulations, in particular in the probe particle (PP) model developed in 2014 by Hapala et al. [24] in our group, capable of producing simulated AFM and STM images and recently extended to simulate KPFM images[20]. In this thesis, all the simulated AFM, STM and KPFM images are simulated with the PP framework extensively explained elsewhere[24, 30–32].

All experimental data presented in this thesis were acquired with metallic, CO and

Xe functionalized tips. For achieving metallic tips, the common routine is the repeated indentation of the tip on a metallic substrate at depths ranging from 500 pm to several nanometers and applying bias voltage pulses corresponding to the work function energy scale of metals, typically around 5 eV. The tip preparation is decided upon analysis of the initial state of the tip in the STM topography images, dI/dV spectroscopies, or the frequency shift value of the oscillation control of the AFM. For example, an asymmetric apex introduces asymmetries in otherwise rounded objects, such as CO molecules, a multiple apex termination creates 'ghost' copies in the images, non-conductive tips exhibit unstable tunneling currents and are unable to measure the surface state in metals.

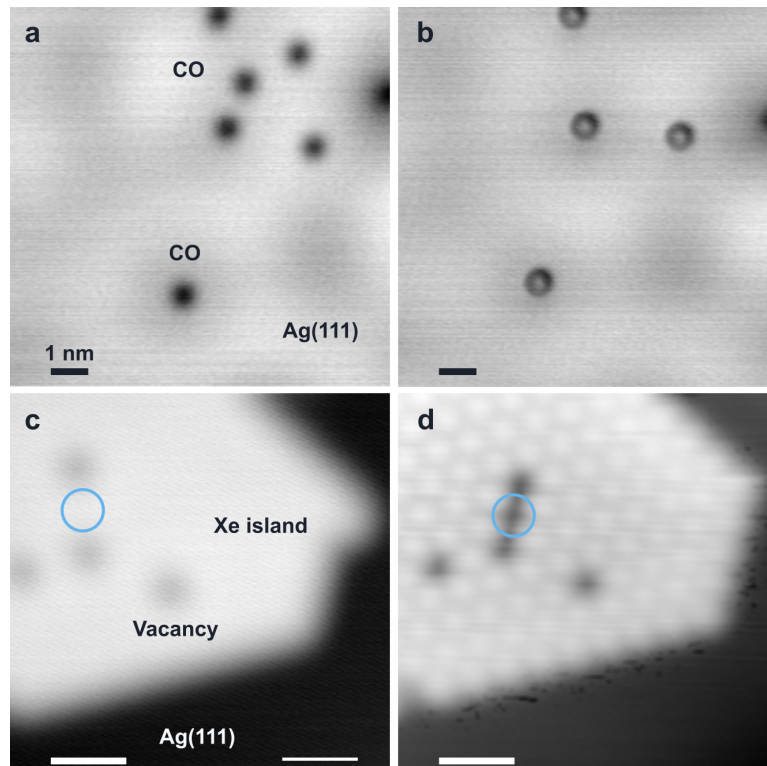


Figure 2.3: Controlled tip functionalizations with single CO (a-b) molecules and Xenon atoms (c-d) on Ag(111). Topography STM images (10 mV, 10 pA).

The first step for the tip functionalization is the adsorption of the desired atoms or gases onto the surface. This is commonly achieved by admitting a typical pressure of

$2 \cdot 10^{-8}$ mbar into the UHV chamber and opening the shutter of the STM head for around 8-10 seconds. The functionalization with a CO molecule is described in Fig. 2.3a-b. In the first step, the tip is positioned over one single CO molecule, and the STM feedback loop is opened with a reference setpoint of (20 mV, 20 pA). Next, the tip is manually approached to the surface until a sudden drop in tunneling current is detected. After picking the CO molecule, the STM feedback is closed again and the sample is re-scanned for observing the characteristic contrast inversion of CO molecules observed using a CO-functionalized tip. [33]. Another alternative method for detecting the presence of CO adsorbed on the tip apex is by observing the frustrated rotational and translational modes in the second derivative of tunneling spectroscopy. [34, 35]. The functionalization with Xe is similar to the previous case, with the difference that Xe needs to be deposited with the getter pumps turned off to prevent gas ionization, using only turbomolecular pumps, and also that organizes in hexagonal lattices on Ag(111), while the adsorption of CO is usually a random event without preferential sites. The functionalization process is similar, but the Xe tip requires usually a higher bias voltage of 10-50 mV upon approaching the tip 300-400 pm to detect a drop in the tunneling current. To confirm tip functionalization, the resolution in topography imaging should be improved, allowing for easy observation of Xe islands forming a hexagonal lattice of atoms. Additionally, a change in the absolute position of the piezoelectric tube, typically extended by approximately 150 pm, can provide further confirmation.

Chapter 3

On-surface synthesis of molecular nanostructures

On-surface synthesis has recently emerged as a promising bottom-up approach for creating complex and atomically precise molecular nanostructures. Unlike traditional solution-based methods, OSS involves chemical reactions on a solid surface, offering several advantages over conventional wet chemistry. A heterogeneous catalytic medium (i.e., metal surface and the vacuum) introduces a novel chemical environment with geometrical boundaries and molecule-surface interactions. Geometrical constrictions in this environment favour highly desired properties, such as the direct self-assembly of molecules guided by surface chemistry and the interaction between molecules. As a result, ordered and regular structures can form thanks to the geometrical confinement to a 2D surface and the role of molecule-surface interactions. Together, these effects can modify the energy barriers of reaction pathways that would otherwise be highly inefficient or impossible to achieve using solution-based chemistry. Moreover, surface confinement enables the use of highly surface-specific characterization techniques, such as SPM. These techniques allow for direct observation and characterization of single products at various stages of the chemical

reactions, enabling the tracking of reaction mechanisms at the atomic level.

The field of on-surface synthesis has made significant advances in achieving precise control over the composition of materials at the atomic scale. For instance, the synthesis of conjugated organic polymers and graphene nanoribbons has successfully produced structures with lengths on the order of several hundreds of nanometers, confined to specific directions defined by the surface without the formation of byproducts or limitations of solubility. Various systems have been explored, including the synthesis of macrocycles[36–38], triangulenes[39–42], the biphenylene carbon allotrope[43], the design of narrow band gap polymers[44, 45], the realization of Clar’s goblet[46] or the recent observations of topological end states of graphene nanoribbons by induced STM fluorescence[47].

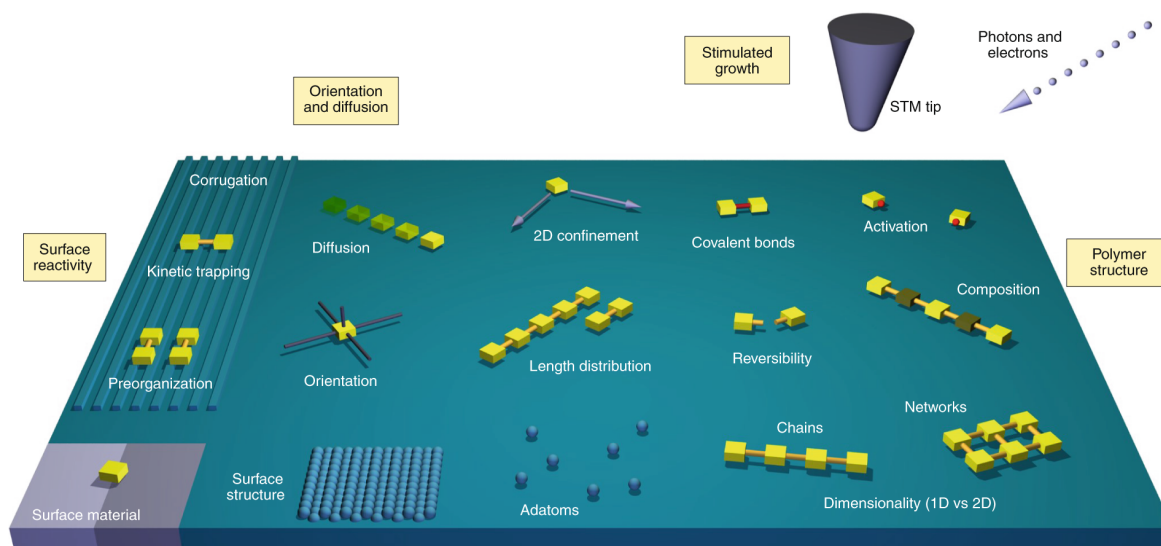


Figure 3.1: Schematic representing the general properties of on-surface synthesis. Adapted with permission from [48]. Copyright 2020 Springer Nature.

In on-surface synthesis (OSS), various reaction mechanisms are commonly used, such as the Ullmann coupling mechanism. This mechanism involves the formation of a C-C bond mediated by the rupture of the carbon-halogen bond forming radicals in the presence of a metal catalyst, typically copper, gold, or silver. Although Ullmann coupling is the most widely used mechanism for polymer synthesis and is utilized in two of the results

presented in this chapter [49, 50], other mechanisms are also available, including the Glaser coupling, Diels-Alder reactions, and ring annulations by cyclohydrogenations. The latter mechanism involves the loss of one or two hydrogen atoms and the subsequent cyclization of the radicalized groups into new rings. This mechanism plays a crucial role in the rearrangement of molecular backbones in polymers [49, 50] and in driving a 3D strained helical product into a planar object with several non-benzenoid regions [51].

In addition to these mechanisms, the internal rearrangement of individual functional groups or monomers within single molecules and polymers also significantly influences the chemistry of OSS. The complex interplay of molecular vibrations, strain in the molecular scaffold, and geometrical boundaries induced by the surface create an ideal environment for highly specific and efficient reactions to occur. Therefore, on-surface synthesis is a powerful method that exploits the reactivity of surfaces to control the location, orientation, and bonding configuration of synthesized products.

In this chapter, I present an overview of three selected results in the field of OSS that demonstrate the formation of well-defined structures with tunable properties due to the reactivity and geometrical constraints imposed by the surface. The first result focuses on the utilization of a strained helical compound and the interplay of this strain with the surface to synthesize a polycyclic aromatic hydrocarbon (PAH) compound with non-benzenoid regions, including 4-5-6-7-8 membered rings. The second result shows how the selection of a porphyrin precursor containing a coordinated Fe atom and its subsequent reaction on the surface. This reaction leads to the formation of conjugated polymers with tailored magnetic properties, which depend on the degree of planarization of the polymer. Lastly, I present a study of a unique case of defects in anthracene polymers incorporating magnetic behaviour, which is part of a larger project where highly aromatic polymers, connected by ethynylene bridges, were synthesized from anthracene, pentacene, and bisanthene monomers.

3.1 Strain-driven synthesis of non-benzenoid compounds from helical precursors

3.1.1 Introduction

The stability of a chemical compound is often determined by the relative positions of functional groups on the molecular scaffold. Steric hindrance repulsion between different parts of the molecule may arise from the presence of different orbital hybridizations or chemical species. This repulsion effect leads to an intrinsic strain in the molecular scaffold. The imposition of extra geometrical constraints on the spatial configuration of bonds and atoms is one way to regulate this strain. Employing well-defined surfaces is another way to influence how the molecule configures in space. When molecules adsorb on surfaces, a molecular rearrangement can occur due to the appearance of attractive dispersive forces that act on the molecular scaffold to accommodate the new spatial boundaries. The rearrangement of the molecular scaffold can have dramatic consequences, such as locking the chirality of a molecule upon adsorption [52, 53] or determining its possible conversion into other products [54, 55].

The role of strain in the stability of the molecular scaffold provides novel chemical routes for synthesizing products with unusual electronic properties, such as molecules with non-benzenoid regions. These regions can dramatically alter the optical and electronic properties of the molecules, as illustrated by the well-known examples of naphthalene, which is a white powder, and azulene, which exhibits a deep blue colour. Other properties determined by the presence of non-benzenoid regions include symmetry breaking between bonding and antibonding orbital energies, net localized charges, ambipolar character, tailored local/global aromaticity, and the introduction of intrinsic magnetic properties without the participation of metallic atoms. However, the wet chemistry synthesis of compounds

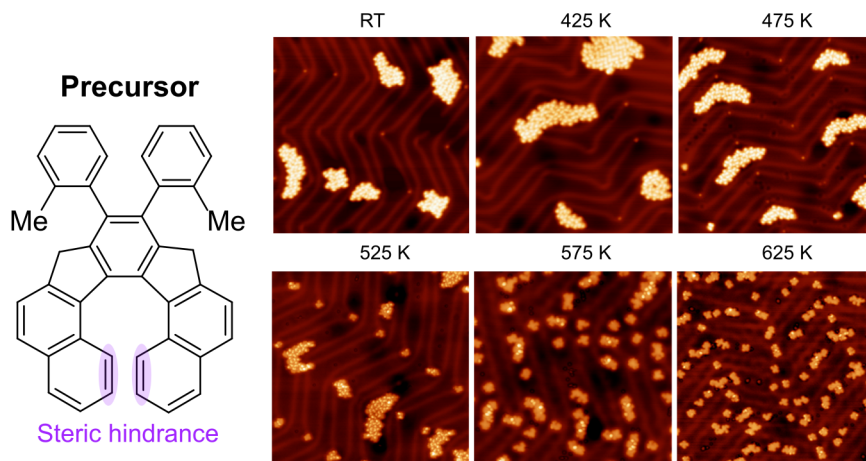


Figure 3.2: Sequence of topography STM images of the precursor deposited on Au(111) and the subsequent reactions at different temperatures (Imaging parameters $V_{Bias} = 100$ mV, 10 pA). The production of planar products is maximized at around 600 K.

containing non-benzenoid regions is often impeded by the high reactivity of these molecules and the solvent's impact on the non-benzenoid moieties. Therefore, alternative approaches such as OSS are needed to overcome these challenges. This section introduces a case study of a helical, strained molecule that undergoes a skeletal rearrangement upon thermal activation on an Au(111) surface in UHV, resulting in the production of planar products containing non-benzenoid regions. The starting material is a member of the [7]helical indeno[1,2-b]fluorene family, known as the precursor, which was synthesized by Prof. Martin Kotora's group (details of the synthesis can be found in [51]). The precursor was sublimated in UHV by heating it up to 450 K inside a Knudsen cell and exposing a clean sample of Au(111) to the sublimated molecule. After adsorption, the molecule was characterized (see Fig. 3.2) using STM and nc-AFM at 4.2 K. The thermal activation of the precursor was achieved by heating the sample up to 625 K, which maximizes the production of single planar products. High-resolution nc-AFM was used to identify all products on the surface, including non-planar or ill-defined molecules that were also characterized (Fig. 3.3) to assess the production of the dominant planar objects. However, these molecules were not explored in detail as they exhibit broken parts or require fusion with fragments to rationalize their

production.

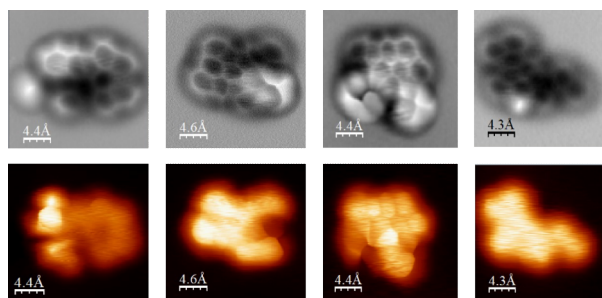


Figure 3.3: Constant height nc-AFM (top row) and current (bottom row) images with CO-tip of a selection of oligomers with broken or 3D features.

The planar structures, which are defined as objects in which all carbon atoms in the backbone are coplanar, were distinguished from other structures in the STM topography images by the absence of bright spots. The chemical structures of these planar objects were determined using high-resolution constant height nc-AFM with a CO-functionalized tip. The family of planar products can be categorized into five molecules, labelled P1 to P5, with a statistical relative incidence of P1:P2:P3:P4:P5 of 32:25:22:15:6.

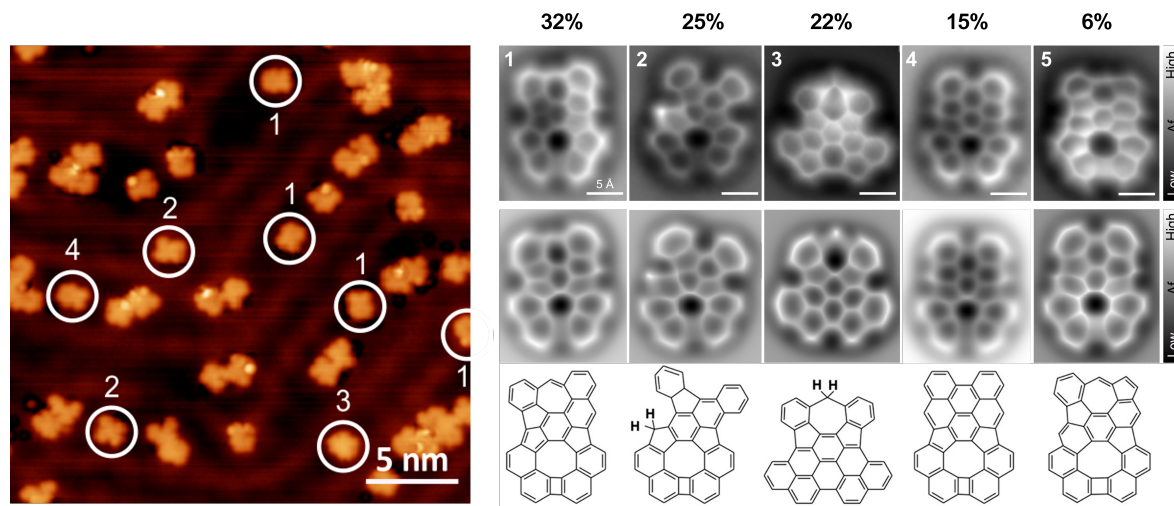


Figure 3.4: The collection of planar objects on the Au(111) surface. In the left panel, an STM topography image ($V_{Bias} = 100$ mV, 10 pA). In the right panel, the experimental constant height nc-AFM with CO-tip (top row), simulated PP nc-AFM (middle row) and structural models (bottom row).

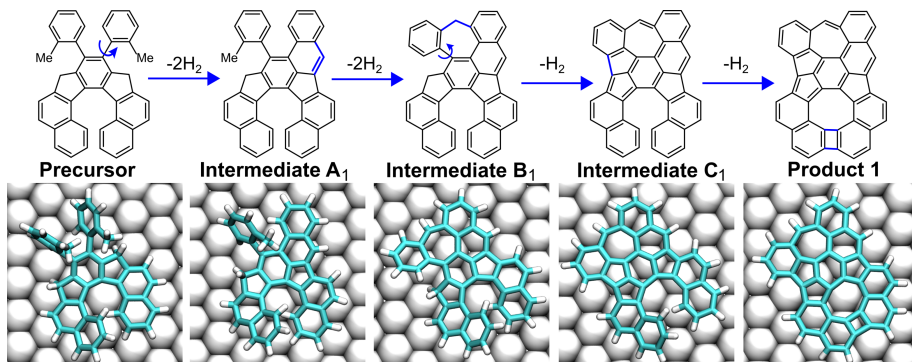


Figure 3.5: The sequence of rotations, dehydrogenations and annulations leading to **All-in** (top row). In the bottom row, snapshots of the MD calculations corresponding to each stage.

Out of the products studied, P1 (also known as **All-in**) is particularly relevant to this discussion due to its non-benzenoid 4-5-6-7-8 membered rings. P1 can be directly compared with its **symmetric** counterpart, P4. The third product, **Moth**, involves an intriguing mechanism that requires the concerted motion of two gold adatoms on the surface to cleave different carbon bonds, but is out of the scope of this section[23].

According to our DFT calculations, the symmetric product P4 should be 2.2 eV more thermodynamically stable than the all-in product. However, this does not align with the proportions of each product found on the surface, where **All-in** makes up 32% of the population while P4 only comprises 15%. This discrepancy suggests that the reaction may be kinetically driven rather than thermodynamically driven. To better understand the chemical pathway from the precursor to **All-in**, we used molecular dynamics simulations with hybrid QM/MM methods[56]. These simulations allow us to track the temporal evolution of relevant spatial coordinates, such as the position of a methyl group, which can serve as reaction coordinates and provide insight into the chemical pathway. The higher yield of the **All-in** product compared to the symmetric case can be attributed to the minimization of free energy, which is dependent on the traveling distances of the methyl group that is furthest away from the helical part. The planarization of this methyl

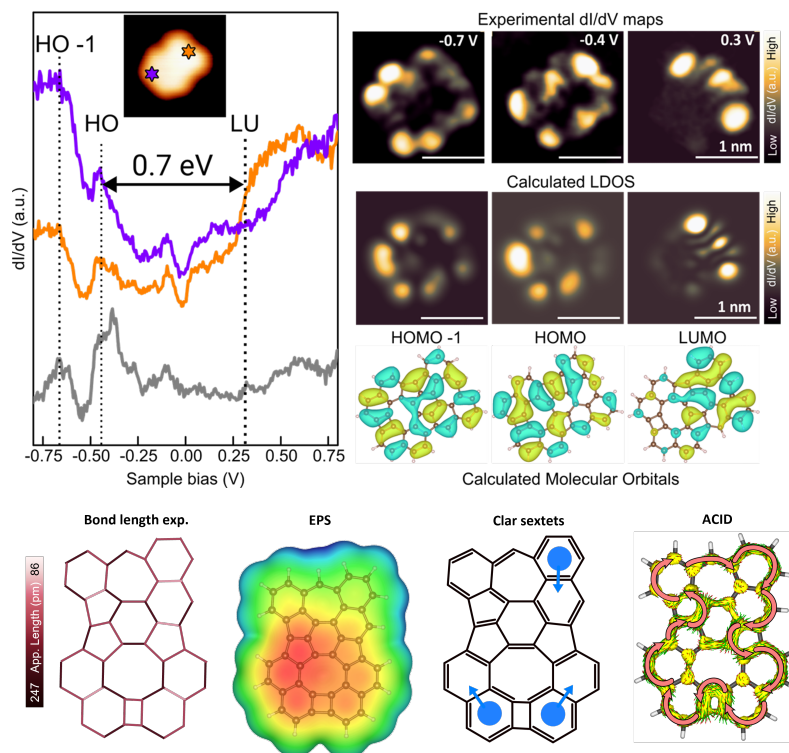


Figure 3.6: Experimental STS measurements and experimental and calculated STS maps visualizing the HOMO-LUMO of **All-in** (top row). Experimental bond-length analysis (shorter bonds/double bonds, longer bonds/single bonds), calculated electrostatic potential surface, aromaticity in terms of Clar's sextets and the anisotropic current-induced density, with clock-wise direction (globally aromatic).

into a hexagonal ring increases the dispersive forces and determines subsequent steps in the chemical pathway (Fig. 3.5). The other free methyl undergoes annulation into a heptagonal ring to form the **All-in** product with a shorter traveling distance compared to closing into a hexagonal ring in the perpendicular direction, which results in the symmetric case. By tracking the temporal variation of the spatial coordinates with molecular dynamics simulations, we can rationalize the differences in the population of the products on the surface.

The **All-in** product underwent a complete experimental and theoretical characterization, including an examination of its electronic properties and aromaticity, as illustrated in

Fig. 3.6. The STS measurements and maps revealed a molecular band-gap of 0.7 eV, with a pronounced closed-shell character and electron localization in the azulene moiety (i.e., the 5-7 rings), as evidenced by the LUMO experimental map. However, the charge localization in the azulene moiety interacted with the CO-tip quadrupole, leading to apparent bond length distortions in nc-AFM and hindering the full characterization of each bond's single or double character. To ascertain the global aromaticity of **All-in**, we employed a combination of theoretical techniques (NICS, HOMA, IMS, ACID DMRG calculations[57]) and experimental bond lengths. The results showed that All-in's global aromaticity stems from a strong main aromatic ACID current involving all the π -electrons while avoiding antiaromatic regions such as the 8-membered ring.

3.1.2 Author's contribution to the published work

In this work, I prepared and conducted the surface reactions, performed the experimental acquisition of STM and nc-AFM, the statistical and bond length analysis, discussed both experimental and simulated findings, began drafting the manuscript, prepared the figures, and participated in the discussions with my collaborators.

On-Surface Strain-Driven Synthesis of Nonalternant Non-Benzenoid Aromatic Compounds Containing Four- to Eight-Membered Rings

Benjamin Mallada,[†] Bruno de la Torre,^{*,†} Jesús I. Mendieta-Moreno, Dana Nachtigallová,^{*} Adam Matěj, Mikulas Matoušek, Pingo Mutombo, Jiri Brabec, Libor Veis,^{*} Timothée Cadart, Martin Kotora,^{*} and Pavel Jelínek^{*}



Cite This: *J. Am. Chem. Soc.* 2021, 143, 14694–14702



Read Online

ACCESS |



Metrics & More

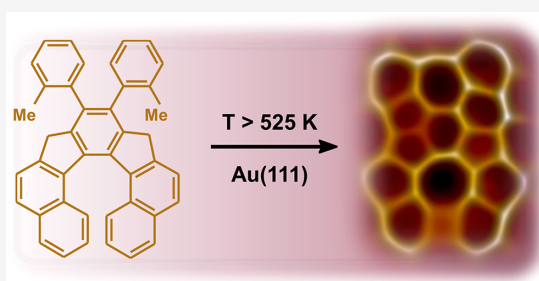


Article Recommendations



Supporting Information

ABSTRACT: The synthesis of polycyclic aromatic hydrocarbons containing various non-benzenoid rings remains a big challenge facing contemporary organic chemistry despite a considerable effort made over the last decades. Herein, we present a novel route, employing on-surface chemistry, to synthesize nonalternant polycyclic aromatic hydrocarbons containing up to four distinct kinds of non-benzenoid rings. We show that the surface-induced mechanical constraints imposed on strained helical reactants play a decisive role leading to the formation of products, energetically unfavorable in solution, with a peculiar ring current stabilizing the aromatic character of the π -conjugated system. Determination of the chemical and electronic structures of the most frequent product reveals its closed-shell character and low band gap. The present study renders a new route for the synthesis of novel nonalternant polycyclic aromatic hydrocarbons or other hydrocarbons driven by internal stress imposed by the surface not available by traditional approaches of organic chemistry in solution.



INTRODUCTION

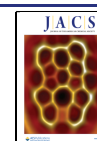
The aim of organic chemistry is to search for novel reaction mechanisms and molecular compounds featuring interesting structural and material properties. Polycyclic aromatic hydrocarbons (PAHs) represent probably the most abundant and nowadays frequently studied organic molecule family. They have enormous industrial and environmental implications to everyday life, and, at the same time, they are assumed to play an essential role in the origin of Life.¹ PAHs are composed of multiple carbon rings containing carbon and hydrogen atoms. The sp^2 -hybridization of C atoms and, consequently, a partial delocalization of π -electrons are responsible for the (anti)-aromatic character of the rings. PAHs contain mostly benzene (aromatic) rings. However, other non-benzenoid rings, such as four-, five-, seven-, eight-, or even higher-membered rings, can be present in PAH structures, causing an internal charge transfer, giving rise to exciting material properties for opto- and nanoelectronics.^{2–4} However, these properties are commensurate with their nontrivial electronic character, such as broken aromaticity or the introduction of a radical character, both limiting their stability and making their syntheses difficult. As a result, only a very limited number of PAHs containing multiple non-benzenoid rings have been synthesized using traditional organic chemistry.^{5,6}

Recently introduced on-surface chemistry provides an interesting alternative for the syntheses of new chemical

compounds inaccessible by traditional organic chemistry methods.^{7,8} At the same time, it allows sample characterization of reaction products and detailed tracking of the reaction pathway by surface science techniques such as scanning probe microscopy.^{5,2} For example, unique and structurally diverse nanographene molecules have been synthesized on metal surfaces. Interestingly, these systems contain nonhexagonal regions composed of five- and seven-membered rings forming, for example, the azulene regions, rather than homogeneous hexagonal nanographene structures. Similarly, the on-surface syntheses have allowed producing curved nanographenes with regularly fused heptagons and pentagons,⁹ helical nanographenes with azulene units,¹⁰ non-benzenoid nanographenes,¹¹ or polyazulene nanoribbons.¹² Although such rearrangements have also been occasionally observed in solution chemistry during the Scholl reaction,^{13,14} the requirement for a strongly acidic catalyst ultimately makes it unintended.

Received: June 15, 2021

Published: August 11, 2021



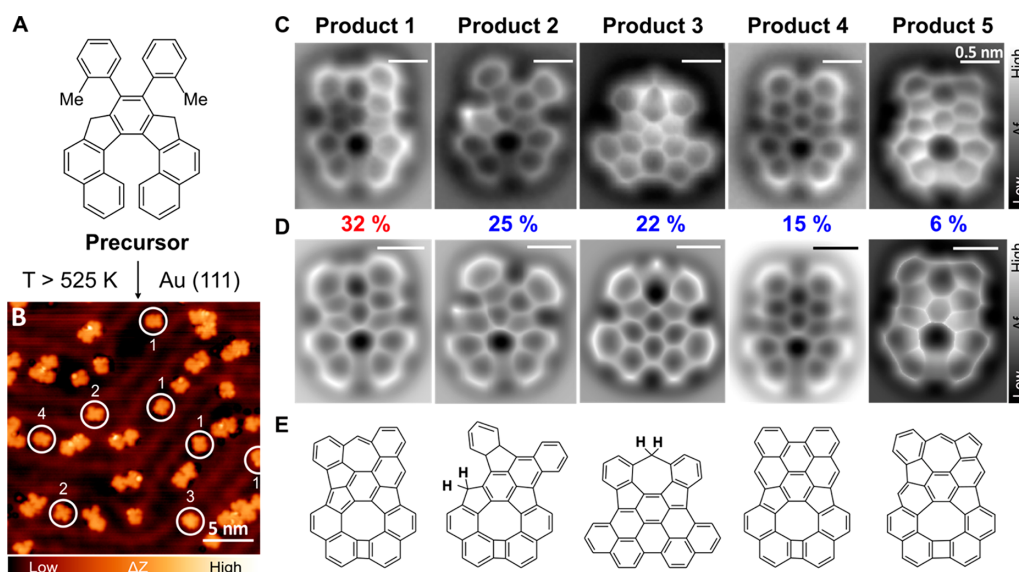


Figure 1. On-surface synthesis of non-benzenoid molecules including four–eight-membered rings. (A) Chemical structure of the precursor molecule, which deposited on the Au(111) surface under UHV conditions, undergoes chemical transformation upon thermal annealing at >525 K. (B) Representative constant-current STM image of the sample after annealing up to 575 K shows the presence of various planar and nonplanar molecular products. (C) High-resolution AFM images acquired with a CO-tip of five planar products found on the surface after annealing. (D) Simulated nc-AFM images with a CO-tip for five planar products using an optimized molecular structure obtained from total energy DFT calculations. (E) Chemical structure of the products.

The stability of molecules is often determined by a strain in their molecular framework caused by steric repulsions, usually being the primary cause of their molecular structure rearrangements (and other desirable or undesirable processes) to a variety of products. However, such rearrangements are often difficult to induce. The adsorption of the strained molecules on metal surfaces can make such processes much easier and induce hitherto otherwise unlikely reaction pathways.^{15,16} The feasibility of such processes results, no doubt, from multiple overlaps between the orbitals of the adsorbed molecule and the metal surface.^{7,8} For instance, one of such well-documented processes in nanographene molecules is the Stone–Wales rearrangement.^{17,18}

One of the potentially exciting pathways for the preparation of nanographene molecules that possess nonhexagonal regions is the surface transformation of compounds having rigid and strained 3D architectures. In this respect, helicenes and other types of helical molecules represent attractive candidates for studying strain-induced reactions on metal surfaces with their eventual planarization being the ultimate target. The planarization is usually accompanied by bond reorganizations (skeletal rearrangements) in their molecular scaffold to accommodate the final planar molecular arrangement optimizing dispersive interaction with the underlying substrate. Thus, the interaction between the molecule's framework and the metal surface often induces otherwise tricky or even not accessible processes to occur either in solution or in the gas phase. The conversion of a [7]helicene to a planar coranulene derivative on a Ag(111) surface¹⁹ or the transformation of helical compounds with azuleno moieties to planar species with fulvaleno segments on a Cu(001) surface²⁰ demonstrates such surface-induced reactions. Although several reports on the deposition of helical compounds on metal surfaces have been

published,^{21–23} their further transformations have not been studied yet in detail and, thus, the above-mentioned studies^{16,19} represent unique reports on the planarization of helical compounds in this potentially attractive but hitherto unexplored area.

RESULTS AND DISCUSSION

Atomic-Scale Characterization of on-Surface Reaction Products. Recently we have developed a new approach to synthesize a series of structurally rigid [7]helical indenofluorenes (7-IFs),²⁴ systems with curved architecture, which are potentially attractive substrates for different structural modifications, e.g., strain-induced rearrangement, cyclodehydrogenation, and planarization. For this purpose, we have synthesized an indenofluorene-based system (see Figure 1A and SI) and explored the possibilities of its transformation via cyclodehydrogenation to form unusual planar aromatic species.

We deposited the precursor via thermal sublimation at 450 K from a Knudsen cell onto a Au(111) surface held at room temperature under UHV (ultra-high-vacuum) conditions. The freshly prepared sample was inspected by cryogenic STM/nc-AFM (scanning tunneling microscopy/noncontact atomic force microscopy) at 4.2 K. Figure S1 displays a representative set of STM images showing the evaluation of molecules on the surface upon gradual annealing ranging from 425 to 625 K. At 425 K, the precursors remain stable and arrange in two-dimensional islands with no apparent long-range order. Subsequent thermal annealing of the molecule-decorated Au surface to $T \approx 525$ K for 30 min gives rise to the thermally induced chemical transformation of the precursor into significantly different molecular products.

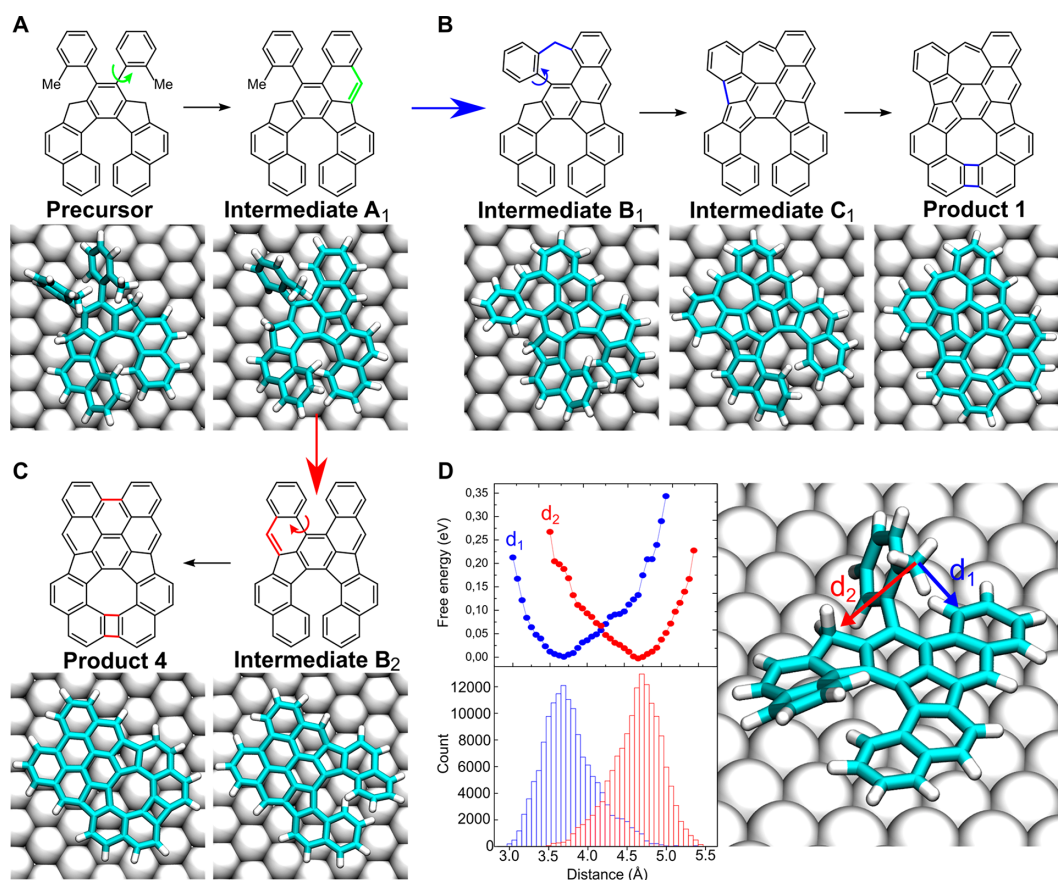


Figure 2. Course of the chemical reaction from precursor toward P1 and P4 products. (A) Chemical transformation of the precursor to intermediate A₁. Subsequent steps of the chemical transformation toward (B) the products P1 and (C) P4. (D) Histogram showing the time distribution of d₁ and d₂ distances along the reaction coordinates for the reaction steps A₁ → B₁ and A₁ → B₂, respectively, calculated by the QM/MM method at 600 K and corresponding free energy F profile derived from the probability p , where $p = \hat{\epsilon}(-\Delta F/k_B T)$ with the probability p calculated for each interval of the histogram as $p = (\text{counts of interval})/(\text{total counts})$. A more feasible reaction toward d₁ explains the reaction mechanism enabling the formation of energetically less stable product P1 instead of P4.

Figure 1B shows a characteristic STM image of the surface after the annealing procedure at $T \approx 575$ K, revealing the precursor's chemical transformation, including its planarization. Planar structures of the products are unambiguously distinguishable in STM images by lack of bright spots in their images. Here, planar refers to those molecules in which all carbon atoms in the backbone are coplanar, as depicted by nc-AFM images. Four observed planar objects detected in the STM image are labeled 1, 2, 3, and 4. Their chemical structures were determined using high-resolution nc-AFM measurements with a CO-functionalized tip.^{25,26} Figure 1C shows constant-height nc-AFM images of all the planar products P1, P2, P3, P4, and P5 observed after annealing the sample at $T \geq 525$ K. Total energy density functional theory (DFT) simulations²⁷ of possible products formed on the Au(111) surface predict their planarity and positioning at ~ 3.3 Å above the surface (Figure S2), resulting from the attractive dispersion interactions between P(1–4) molecules and the surface. Very good agreement between experimental and simulated²⁸ high-resolution nc-AFM images (compare Figure 1C and D) allows us to unambiguously assign the structure of the planar

products, which contain four- to eight-membered rings (see Figure 1E). Further annealing at an elevated temperature up to 625 K does not alter the occurrence of the planar structures but enhances the frequency of oligomers and other unidentifiable objects, as shown in Figure S1. At 575 K, the planar structures represent $\sim 30\%$ of the total molecular structures, while most products comprise other minority nonplanar monomers and fused oligomers (Figure 1B). Statistical analyses performed on several samples annealed up to 575 K including around 223 planar products exhibit the relative incidences of products P1:P2:P3:P4:P5 as 32:25:22:15:6. The most populated, P1, has the most exotic chemical structure, consisting of four- to eight-membered rings and, thus, will be the main focus of our investigations reported in the rest of this article.

Figure S2 displays fully optimized structures of P1–P5 products on the Au(111) surface performed at the DFT level. From the chemical structure of the precursor and the products, we proposed a tentative course of reaction steps (see Figure S3 and related discussion). P2 and P3 chemical structures have one carbon atom less than the precursor, suggesting a

demethylation process upon their formation.²⁹ On the other hand, P1 and P4 products conserve the number of carbon atoms during the reaction course. Thus, the product formations proceed via subsequent dehydrogenation processes, removing the same number of hydrogens in all three cases. The same chemical content of P1 and P4 allows for a direct estimate of their relative stabilities, comparing their total energies. Interestingly, the total energy DFT calculations predict larger thermodynamical stabilities of P4 (by 2.2 eV) than P1 (see Figure 1C), in stark contrast with their relative abundances observed in the experiment. This points out that the reaction mechanism is determined rather by kinetic processes instead of thermodynamics of the final products. Thus, possible reaction pathways toward P1 and P4 formations will be analyzed below.

Figure S3 displays a tentative reaction pathway toward P1–P5 products with an underlying discussion. The reaction course toward P2 and P3 must involve C–C bond cleavage processes that are rare or even unprecedented (the formation of P3). Moreover, the participation of gold atoms in the C–C bond cleavage step may play an important role. Due to the complexity of this process, we will discuss this reaction mechanism elsewhere.

Deposition of the highly nonplanar helical precursor on the surface (see Figure S2) causes internal stress imposed on the molecule resulting from the competition between attractive dispersion interactions and steric repulsions between nonplanar phenyl groups and/or the helical part of the precursor and the underlying metallic substrate. DFT simulations predict that such competition leads to an asymmetric arrangement of phenyl groups with methyl groups pointing out of the surface (Figure S2). This asymmetric arrangement is determined by the chirality of the molecule's helical part (see Figure 2A). Importantly, the surface-induced geometrical constraint determines the course of reactions, as will be demonstrated below.

It is worth noting that preliminary results of annealing the precursor on Ag(111) up to 575 K reveal the reaction course is quite different. The annealing of the precursor on Ag(111) at 575 K led to an exclusive appearance of quite distinct molecular products from the planar products P1–P5 obtained on the Au(111) surface. Figure S4 displays a set of high-resolution nc-AFM/STM images of some of those products, revealing highly nonplanar characters for which it is not possible to derive a simple transformation from the precursor at first glance.

Analysis of the Reaction Pathway. Possible reaction pathways from the precursor toward P1 and P4 products are displayed in Figure S3 and summarized in Figure 2A. Note that the precursor may adopt different rotamer configurations indicated by orientation of *o*-tolyl groups. Since the reaction is thermally driven by annealing at elevated temperatures >525 K, it is reasonable to assume that at these temperatures both *o*-tolyl groups in the precursor will be able to move between different rotamer configurations. However, the presence of the surface will impose a constraint on the rotamers. We calculated the free energy of each rotamer on the surface (see Figure S5). We found that rotamer 1 has the lowest free energy on the surface. Consequently, it will be the most populated, playing the dominant role in the reaction course. Therefore, in the following analysis of the reaction pathway, we consider this rotamer as the starting point.

The reaction schemes include dehydrogenation accompanied by annulation or cyclization processes divided into four consecutive steps. Two possible reaction channels starting from the precursor are considered in the first step: (i) construction of a six-membered ring via annulation of a methyl group with the central carbon of the fluorene unit accompanied by dehydrogenation processes, leading to intermediate A1, shown in Figures 2A and S5, and (ii) a dehydrogenation/annulation process with fusing the helical part and cyclobutadiene formation (see intermediate A2 in Figure S6). The simulations, however, predict the free energy of the A2 intermediate being by about 1 eV lower than A1. Thus, the first reaction channel is considered to be more favorable and is discussed below.

The course of the initial step of the reaction, in particular, what benzene ring will first planarize during the dehydrogenation of methyl groups,³⁰ is directed by their asymmetric position imposed by the underlying surface, i.e., the distances of the bonds, labeled as d1 and d2 (see Figure S7), to be formed between the carbon atoms of methyl groups and matching central C atoms of fluorene. The relevant analysis includes the determination of the kinetic control over the reaction, i.e., the calculation of the activation energies for the two products. Such an approach, however, requires considering multiple dehydrogenations, which greatly complicates and questions the reliability of such calculations. Alternatively, probabilities of these steps can be determined using an assumption that the reaction rates depend on the reaction coordinates' behavior around the equilibrium position of the initial state. In other words, the rates of the two reaction pathways can be qualitatively compared based on the time-course distribution of d1 and d2 distances along the reaction coordinates at a given temperature. For this purpose, molecular dynamics (MD) simulations, employing the hybrid quantum mechanics/molecular mechanics (QM/MM) methods,^{31–33} were performed to obtain temporal evolution of d1 and d2 reaction coordinates (Figure S7) and the probability distribution for the given intermediate (Figure S7). In these simulations, the precursor and intermediates are treated at the QM level, while the metallic surface is described at the MM level. The histogram of d1 and d2 distances (Figure S7) shows a significantly shorter time-average distance between the methyl carbon and the central fluorene carbon located on the helical part of the molecule closer to the metallic surface (d1 in Figure S7). The resulting reaction channel thus leads to A1 (Figures 2A, S6, and S7), i.e., the formation of the six-membered ring on the side of the molecule relevant to the shorter d1 distance and, consequently, planarization of the appropriate part of the molecule. The planarization stabilizes the system by additional dispersion attractive forces due to a newly formed ring with π -electrons interacting with the substrate. It is noteworthy that this reaction step determines the resulting chirality of the P1. We also carried out similar MD simulations without the substrate (see Figure S10), which enables us to estimate an increase of the free energy by 10.5 kcal/mol due to the presence of substrate.

The decisive step determining the formation of P1 or P4 product represents the dehydrogenation/annulation process with planarization of the second phenyl ring, which involves the methyl group (see Figure 2B and C). This bifurcation point occurs either prior to or after the dehydrogenation/annulation process with fusing the helical part, i.e., at intermediate A1 or B3 (see Figure S6). The two possible

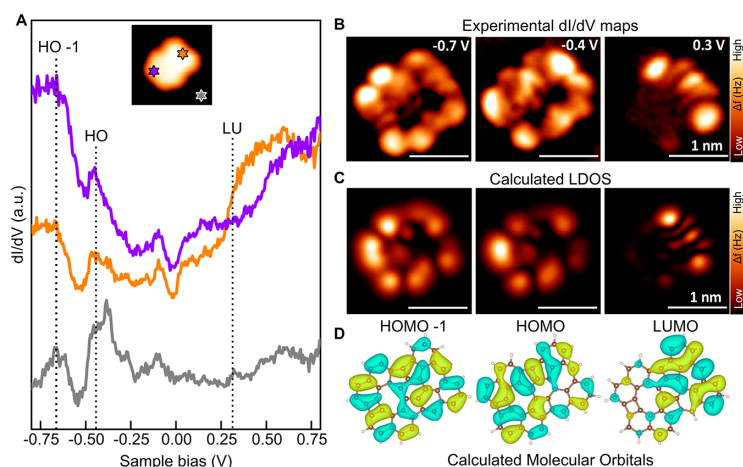


Figure 3. Electronic structure of the product P1. (A) Experimental dI/dV spectra acquired on different sites of the P1 product (see inset); (B) experimental dI/dV maps acquired at three different bias voltages (-0.7 , -0.4 , and 0.3 V); (C) calculated dI/dV maps for canonical DFT orbitals of HOMO-1, HOMO, and LUMO shown in (D).

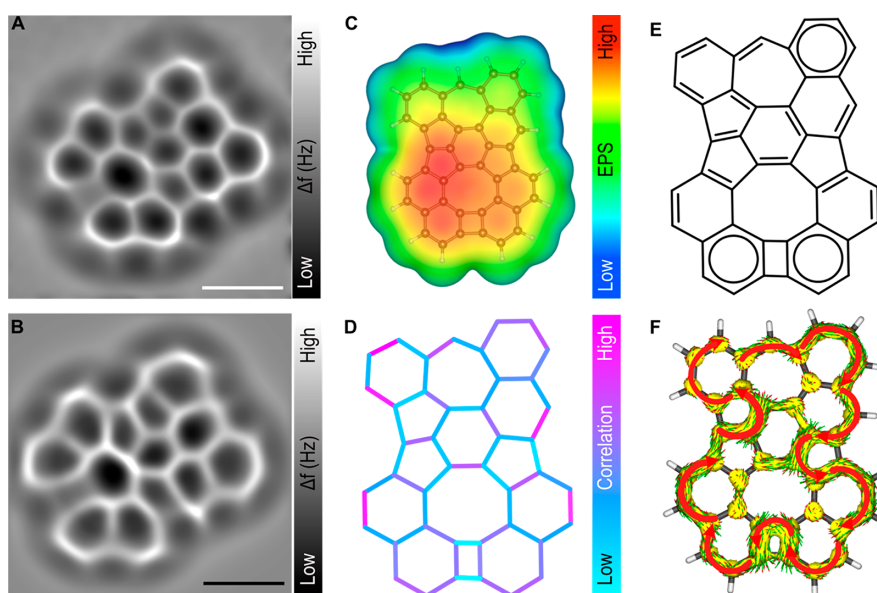


Figure 4. Analysis of the structure and aromaticity of the product P1. Experimental (A) and simulated (B) high-resolution nc-AFM images of the product P1 obtained with the CO-tip (both with an adopted Laplace filter); (C) DFT-calculated electrostatic potential map of P1; (D) plot of mutual information on individual bonds obtained from DMRG calculations of the product P1; (E) corresponding resonance structure of P1 derived from the mutual information DMRG; (F) plot of calculated ACID of P1 product (red darts show orientation of the peripheral ring current).

channels, related to the seven- or six-membered rings' construction, describe the phenyl ring planarization. Similar to the first step, the surface-imposed asymmetrical arrangement of the methyl group in A1 or B3 to adjacent benzene or fluorene determines the probabilities of the two channels and the course of the reaction. From A1, these channels lead to either seven-membered (B1 intermediate) or six-membered (B2 intermediate) ring construction, and, consequently, the probabilities of $A1 \rightarrow B1$ and $A1 \rightarrow B2$ processes determine the relative yield of P1 and P4, as shown in Figure 2.

The MD simulations (see Figures 2D and S8 for the results of the distance–time distributions) predict B1 is more likely than B2; thus, P1 is preferred over P4. From B3, the alternative channels for P1 and P4 formation are $B3 \rightarrow C2 \rightarrow P1$ and $B3 \rightarrow P4$, respectively. Like in the previous case, MD simulations predict the formation of the seven-membered ring (Figure S8), i.e., following the former reaction path, which is more feasible due to the shorter d1 reaction coordinate. These observations rationalize the larger abundance of P1 over the more stable P4.

As for the formation of P5, it can be formed from P4 by a simple 1,2-shift or from P1 by a series of 1,2-shifts (Figure S3).

The effect of the substrate on the course of the reaction can be rationalized with the help of MD simulations performed in the absence of the surface. Figures S10–S12 show the time-average distance of reaction coordinates and free energy profiles for the precursor and A1 and B3 intermediates in the absence of the surface, previously considered to play a decisive role for the formation of P4. The results show very similar values of d1 and d2 distances and the corresponding free energy profiles, highlighting the importance of the substrate for the formation of thermodynamically less favorable P4.

Probing the Electronic Structure of a Nonalternant Non-Benzenoid Aromatic Compound Containing Four- to Eight-Membered Rings. Figure 3A presents constant-height dI/dV spectra acquired over two different positions of the P1 shown in the inset. The dI/dV spectra reveal three distinct peaks at -700 , -400 , and 300 meV respectively assigned to HOMO-1, HOMO, and LUMO (HOMO and LUMO stand for the highest occupied and lowest unoccupied molecular orbitals, respectively) and providing a molecular band gap of 0.7 eV. The calculated DFT-PBE0^{27,34} band gap of ~ 1.4 eV of the free-standing P1 product concurs well with the experimental observation. We expect that in the presence of the underlying metallic surface these values decrease.³⁵ The experimental dI/dV spectra lack any zero-bias peak or inelastic electron tunneling signal, which indicates the closed-shell ground state of P1. Its closed-shell character is also confirmed by DFT-PBE0 and density matrix renormalization group (DMRG) calculations of the free-standing molecule. The DMRG^{36,37} calculations were performed with the active space constructed from a full π -orbital space (42 electrons in 42 orbitals), resulting in the occupancies of the highest occupied and lowest unoccupied natural orbitals of 1.80 and 0.23, respectively.

Figure 3B shows the constant-current dI/dV maps at the corresponding energies resolving spatial localization of electron density of the frontier orbitals. Namely, dI/dV maps of the LUMO reveal strong spatial localization in the vicinity of the seven-membered ring. This picture is fully supported by the DFT-calculated dI/dV map³⁸ of the canonical LUMO (see Figure 3D), showing the same localization pattern (see Figure 3C). The remaining calculated maps of occupied frontier orbitals show fairly good agreement with their experimental counterparts as well, thus confirming the orbital assignment.

High-resolution nc-AFM imaging allows direct visualization of the chemical structure of the P1 product revealing the presence of all four- to eight-member rings; see Figure 4A. Namely, the presence of the seven-membered ring can be unambiguously determined from a careful analysis of bond lengths in the nc-AFM images of the P1 and P4 products (Figure S13). The presence of multiple non-benzenoid rings (namely, an azulene 5–7 ring segment) causes the localization of molecular orbitals at distinct parts of P1, introducing an internal charge transfer within the molecule (Figure 4C). Thus, the submolecular contrast seen in the high-resolution nc-AFM images is heavily affected by the electrostatic interaction between the CO-tip and P1,³⁹ altering the apparent C–C bond lengths with respect to real ones and making the bond-order analysis⁴⁰ from the nc-AFM images ambiguous. Despite a good overall agreement between experimental and calculated nc-AFM images (see Figure 4A,B and Figure S14), the

comparison of the experimental and calculated apparent bond lengths is not fully conclusive.

Analysis of the Aromaticity. To assign the most representative resonant structure of P1, we adopted an alternative approach employing the mutual information on atomic-like orbitals that form π -bonds (see SI). Mutual information on individual bonds (Figure 4D) was obtained from DMRG calculations. The resulting structure (Figure 4E) contains three disjointed Clar's sextets, i.e., benzenoid moieties.⁴¹ Alternative resonant structures consisting of more of such sextets (five being the maximum number; see Figure S15) lead to the biradical character of the structure, increasing its instability. Note that similar resonant structure can be derived from the bond distances of the fully optimized DFT structure (Figure S14), except the 4-ring, in which the bond length of two C–C bonds connecting benzene rings corresponds to double-bond character.

The concept of aromaticity is well understood for benzenoid PAH compounds. Its extension to non-benzenoid nonalternant compounds is however still under debate. It is thus interesting to analyze the aromatic character of P1 with respect to different criteria. In particular, for systems consisting of several fused rings, the aromaticity criteria can be applied either to the whole system, i.e., counting all π -electrons in the systems, or considering only π -electrons on the periphery, thus distinguishing between the global and peripheral aromaticity (see, e.g., ref 42). Application of the most popular Hückel's⁴³ and Baird's rules⁴⁴ on P1 in the closed-shell ground state configuration provides contradictory results: the global aromaticity (42, i.e., $(4n + 2)$ π -electrons) and peripheral antiaromaticity (28, i.e. $(4n)$ π -electrons). Despite the frequent use of these rules, generalized by Soncini and Fowler,⁴⁵ they hold strictly for monocyclic systems and can be violated in polycyclic systems. Table S1 summarizes results based on the local aromaticity of individual rings obtained with the following approaches: the generalized harmonic oscillator model (HOMA)^{46,47} using the mutual information⁴⁹ of atomic-like orbitals forming π -bonds from DMRG (see Table S1), the nucleus-independent chemical shifts (NICS),⁴⁸ and the isotropic magnetic shielding (IMS)⁴⁹ (see Figures S16 and S17). NICS and IMS methods agree on strong antiaromaticity of the four-membered ring and weak antiaromaticities of the seven- and eight-membered rings, respectively, as well as one aromatic (5-II) and two antiaromatic (5-I, 5-III) five-membered rings. Agreement of NICS and IMS results is also reached for aromaticity indexes of the six-membered rings. These values are, however, in contrast with the HOMA results. In particular, NICS and IMS methods predict the strong aromaticity of the inner ring (6-IV, see Figure S16 and Table S1), while its aromaticity is very low according to the HOMA-DMRG calculations. Interestingly, the results of NICS and IMS calculations, i.e., the strong aromaticity and Clar's sextet in 6-IV, contradict the existence of the closed-shell resonant structure, hence the experimental, as well as theoretical DFT and DMRG results.

The concept of conjugated circuits⁵⁰ predicts that P1 is partially aromatic, with the aromaticity degree of 95% (see Figure S18 for details). Probably the most complex picture of the aromaticity character of P1 is obtained by the calculations of the anisotropy of the induced current density (ACID).⁵¹ The ACID map (Figure 4F) reveals the interactions of ring currents of each individual ring, enhancing or suppressing the boundary with neighboring rings, depending on their mutual orientations. Indeed, the strong negative (aromatic) NICS and

ISM values on the inner 6-IV ring are caused by the presence of synergic antiaromatic currents on two adjacent 5-rings; see Figure 4F. Similarly, IMS and NICS values predict the weak antiaromaticity of the 8-ring in contrast to its weak aromatic character predicted with ACID. The latter result originates from the current enhancement due to the similarly oriented current on joint edges with 6-IV and 4-rings and weakening by the opposite current directions on the neighboring 5- and 6-rings (see Figure S19).

The ACID map also shows the clockwise direction of the main current ring on the P1 periphery revealing its aromatic character. Although in disagreement with $4n + 2$ rule of aromaticity, all π -electrons²⁹ are involved in this current. The aromaticity and, thus, the stabilization in the closed-shell electronic structure are maintained by avoiding peripheral bonds of antiaromatic 4, 5-I, and 5-III rings. This indicates that the closed-shell ground state character in nonalternant non-benzenoid aromatic compounds can be reached via the development of a complex peripheral ring current excluding certain molecular parts and suppressing the local aromatic/antiaromatic character of rings.

CONCLUSION

We have demonstrated that the internal molecular stress imposed by the presence of the underlying surface can impose a kinetic control of on-surface reactions forming thermodynamically less stable final products. We anticipate that the on-surface chemical approach employing internal stress of nonplanar molecules on surfaces is capable of establishing a new synthetic strategy to form new non-benzenoid PAH compounds, not available via traditional synthetic methods in solution or on surfaces.

Such non-benzenoid PAH nanostructures offer a rich playground to reach interesting optical and magnetic properties of carbon-based nanostructures with closed-shell or radical character. So far, nonalternant non-benzenoid aromatic compounds often feature an open-shell antiaromatic character, which makes them more vulnerable to a chemical transformation. Interestingly, the P1 product consisting of four- to eight-membered rings has a closed-shell aromatic character, enhancing its chemical stability. Moreover, it also shows a strong localization of the LUMO on the seven-membered ring, similarly to a prototypical nonalternant azulene compound. Such spatial electronic localization makes it attractive in view of potential in optoelectronic applications of such nontrivial aromatic systems, e.g., enhancing a charge separation in organic solar cells.

Thus, we believe that this novel synthetic route not only is a synthetic curiosity but can stimulate further research effort to form non-benzenoid PAH complexes, including polymers, which can open new routes to design novel spintronics and optoelectronics devices.

ASSOCIATED CONTENT

Supporting Information

The Supporting Information is available free of charge at <https://pubs.acs.org/doi/10.1021/jacs.1c06168>.

Materials and methods; Figures S1 to S20; Table S1; synthesis of the starting material (PDF)

AUTHOR INFORMATION

Corresponding Authors

Bruno de la Torre – Regional Centre of Advanced Technologies and Materials, Czech Advanced Technology and Research Institute (CATRIN), Palacký University Olomouc, 783 71 Olomouc, Czech Republic; Institute of Physics, Czech Academy of Sciences, 162 00 Prague, Czech Republic; orcid.org/0000-0002-6462-6833; Email: bruno.de@upol.cz

Dana Nachtigallová – Regional Centre of Advanced Technologies and Materials, Czech Advanced Technology and Research Institute (CATRIN), Palacký University Olomouc, 783 71 Olomouc, Czech Republic; Institute of Organic Chemistry and Biochemistry, Czech Academy of Sciences, 162 00 Prague, Czech Republic; orcid.org/0000-0002-9588-8625; Email: dana.nachtigallova@uochb.cas.cz

Libor Veis – J. Heyrovský Institute of Physical Chemistry, Czech Academy of Sciences, 182 23 Prague, Czech Republic; orcid.org/0000-0002-4229-6335; Email: libor.veis@jh-inst.cas.cz

Martin Katora – Department of Organic Chemistry, Charles University, 128 00 Prague, Czech Republic; orcid.org/0000-0003-4491-7091; Email: katora@natur.cuni.cz

Pavel Jelínek – Regional Centre of Advanced Technologies and Materials, Czech Advanced Technology and Research Institute (CATRIN), Palacký University Olomouc, 783 71 Olomouc, Czech Republic; Institute of Physics, Czech Academy of Sciences, 162 00 Prague, Czech Republic; orcid.org/0000-0002-5645-8542; Email: jelinekp@fzu.cz

Authors

Benjamin Mallada – Regional Centre of Advanced Technologies and Materials, Czech Advanced Technology and Research Institute (CATRIN), Palacký University Olomouc, 783 71 Olomouc, Czech Republic; Institute of Physics, Czech Academy of Sciences, 162 00 Prague, Czech Republic; orcid.org/0000-0002-8209-9977

Jesús I. Mendieta-Moreno – Institute of Physics, Czech Academy of Sciences, 162 00 Prague, Czech Republic

Adam Matěj – Regional Centre of Advanced Technologies and Materials, Czech Advanced Technology and Research Institute (CATRIN), Palacký University Olomouc, 783 71 Olomouc, Czech Republic; Institute of Physics, Czech Academy of Sciences, 162 00 Prague, Czech Republic

Mikulas Matoušek – J. Heyrovský Institute of Physical Chemistry, Czech Academy of Sciences, 182 23 Prague, Czech Republic

Pingo Mutombo – Institute of Physics, Czech Academy of Sciences, 162 00 Prague, Czech Republic

Jiri Brabec – J. Heyrovský Institute of Physical Chemistry, Czech Academy of Sciences, 182 23 Prague, Czech Republic

Timothée Cadart – Department of Organic Chemistry, Charles University, 128 00 Prague, Czech Republic

Complete contact information is available at: <https://pubs.acs.org/10.1021/jacs.1c06168>

Author Contributions

[†]B.M. and B.T. contributed equally to this work.

Notes

The authors declare no competing financial interest.

ACKNOWLEDGMENTS

M.K. dedicates this work to Professor Tamotsu Takahashi on the occasion of his retirement. B.T. dedicates this work to the memory of José María Gómez-Rodríguez. This work has been supported by Praemium Academie of the Academy of Science of the Czech Republic, GACR 20-13692X (P.J., P.M., B.M.), 19-27454X (D.N.), GACR 18-18940Y (L.V.), and GACR 18-17823S (M.K.). A.M. and B.M. acknowledge the support from the Internal Student Grant Agency of the Palacký University in Olomouc, Czech Republic, IGA_PrF_2021_033 and IGA_PrF_2021_032. We acknowledge CzechNanoLab Research Infrastructure supported by MEYS CR (LM2018110) and the support of the Operational Programme for Research, Development and Education of the European Regional Development Fund (Project No. CZ.02.1.01/0.0/0.0/16_019/0000754). Some of the computations were carried out on the Salomon and Barbra supercomputers in Ostrava; the authors would therefore like to acknowledge the support by the Czech Ministry of Education, Youth and Sports from the Large Infrastructures for Research, Experimental Development and Innovations project "IT4Innovations National Supercomputing Center-LM2015070".

REFERENCES

- (1) Ehrenfreund, P.; Rasmussen, S.; Cleaves, J.; Chen, L. Experimentally Tracing the Key Steps in the Origin of Life: The Aromatic World. *Astrobiology* **2006**, *6* (3), 490–520.
- (2) Anthony, J. E. Functionalized Acenes and Heteroacenes for Organic Electronics. *Chem. Rev.* **2006**, *106*, 5028–5048.
- (3) Anthony, J. E. The Larger Acenes: Versatile Organic Semiconductors. *Angew. Chem., Int. Ed.* **2008**, *47* (3), 452–483.
- (4) Wang, Y.; Liu, B.; Koh, C. W.; Zhou, X.; Sun, H.; Yu, J.; Yang, K.; Wang, H.; Liao, Q.; Woo, H. Y.; Guo, X. Facile Synthesis of Polycyclic Aromatic Hydrocarbon (PAH)-Based Acceptors with Fine-Tuned Optoelectronic Properties: Toward Efficient Additive-Free Nonfullerene Organic Solar Cells. *Adv. Energy Mater.* **2019**, *9* (24), 1803976.
- (5) Zhang, X. S.; Huang, Y. Y.; Zhang, J.; Meng, W.; Peng, Q.; Kong, R.; Xiao, Z.; Liu, J.; Huang, M.; Yi, Y.; Chen, L.; Fan, Q.; Lin, G.; Liu, Z.; Zhang, G.; Jiang, L.; Zhang, D. Dicyclohepta[*ijkluvwx*]Rubicene with Two Pentagons and Two Heptagons as a Stable and Planar Non-Benzenoid Nanographene. *Angew. Chem., Int. Ed.* **2020**, *59* (9), 3529–3533.
- (6) Konishi, A.; Horii, K.; Shiomi, D.; Sato, K.; Takui, T.; Yasuda, M. Open-Shell and Antiaromatic Character Induced by the Highly Symmetric Geometry of the Planar Heptalene Structure: Synthesis and Characterization of a Nonalternant Isomer of Bisanthene. *J. Am. Chem. Soc.* **2019**, *141* (26), 10165–10170.
- (7) Clair, S.; De Oteyza, D. G. Controlling a Chemical Coupling Reaction on a Surface: Tools and Strategies for On-Surface Synthesis. *Chem. Rev.* **2019**, *119* (7), 4717–4776.
- (8) Wang, T.; Zhu, J. Confined On-Surface Organic Synthesis: Strategies and Mechanisms. *Surf. Sci. Rep.* **2019**, *74*, 97–140.
- (9) Hou, I. C. Y.; Sun, Q.; Eimre, K.; Di Giovannantonio, M.; Urgel, J. I.; Ruffieux, P.; Narita, A.; Fasel, R.; Müllen, K. On-Surface Synthesis of Unsaturated Carbon Nanostructures with Regularly Fused Pentagon-Heptagon Pairs. *J. Am. Chem. Soc.* **2020**, *142* (23), 10291–10296.
- (10) Ogawa, N.; Yamaoka, Y.; Takikawa, H.; Yamada, K. I.; Takasu, K. Helical Nanographenes Embedded with Contiguous Azulene Units. *J. Am. Chem. Soc.* **2020**, *142* (31), 13322–13327.
- (11) Lohr, T. G.; Urgel, J. I.; Eimre, K.; Liu, J.; Di Giovannantonio, M.; Mishra, S.; Berger, R.; Ruffieux, P.; Pignedoli, C. A.; Fasel, R.; Feng, X. On-Surface Synthesis of Non-Benzenoid Nanographenes by Oxidative Ring-Closure and Ring-Rearrangement Reactions. *J. Am. Chem. Soc.* **2020**, *142*, 13565.
- (12) Fan, Q.; Martin-Jimenez, D.; Ebeling, D.; Krug, C. K.; Brechmann, L.; Kohlmeyer, C.; Hilt, G.; Hieringer, W.; Schirmeisen, A.; Gottfried, J. M. Nanoribbons with Nonalternant Topology from Fusion of Polyazulene: Carbon Allotropes beyond Graphene. *J. Am. Chem. Soc.* **2019**, *141* (44), 17713–17720.
- (13) Nobusue, S.; Fujita, K.; Tobe, Y. Skeletal Rearrangement of Twisted Polycyclic Aromatic Hydrocarbons under Scholl Reaction Conditions. *Org. Lett.* **2017**, *19* (12), 3227–3230.
- (14) Han, Y.; Xue, Z.; Li, G.; Gu, Y.; Ni, Y.; Dong, S.; Chi, C. Formation of Azulene-Embedded Nanographene: Naphthalene to Azulene Rearrangement During the Scholl Reaction. *Angew. Chem., Int. Ed.* **2020**, *59* (23), 9026–9031.
- (15) Su, J.; Wu, X.; Song, S.; Telychko, M.; Lu, J. Substrate Induced Strain for On-Surface Transformation and Synthesis. *Nanoscale* **2020**, *12* (14), 7500–7508.
- (16) Telychko, M.; Su, J.; Gallardo, A.; Gu, Y.; Mendieta-Moreno, J. I.; Qi, D.; Tadich, A.; Song, S.; Lyu, P.; Qiu, Z.; Fang, H.; Koh, M. J.; Wu, J.; Jelínek, P.; Lu, J. Strain-Induced Isomerization in One-Dimensional Metal-Organic Chains. *Angew. Chem., Int. Ed.* **2019**, *58* (51), 18591–18597.
- (17) Stone, A. J.; Wales, D. J. Theoretical Studies of Icosahedral C₆₀ and Some Related Species. *Chem. Phys. Lett.* **1986**, *128* (S–6), 501–503.
- (18) Brayfindley, E.; Irace, E. E.; Castro, C.; Karney, W. L. Stone-Wales Rearrangements in Polycyclic Aromatic Hydrocarbons: A Computational Study. *J. Org. Chem.* **2015**, *80* (8), 3825–3831.
- (19) Stetsovych, O.; Svec, M.; Vacek, J.; Chocholoušová, J. V.; Janík, A.; Rybáček, J.; Kosmider, K.; Stará, I. G.; Jelínek, P.; Starý, I. From Helical to Planar Chirality by On-Surface Chemistry. *Nat. Chem.* **2017**, *9* (3), 213–218.
- (20) Shiotari, A.; Nakae, T.; Iwata, K.; Mori, S.; Okujima, T.; Uno, H.; Sakaguchi, H.; Sugimoto, Y. Strain-Induced Skeletal Rearrangement of a Polycyclic Aromatic Hydrocarbon on a Copper Surface. *Nat. Commun.* **2017**, *8* (1), 16089.
- (21) Shiotari, A.; Tanaka, K.; Nakae, T.; Mori, S.; Okujima, T.; Uno, H.; Sakaguchi, H.; Sugimoto, Y. Chiral Discrimination and Manipulation of Individual Heptahelicene Molecules on Cu(001) by Noncontact Atomic Force Microscopy. *J. Phys. Chem. C* **2018**, *122* (9), 4997–5003.
- (22) Zhang, H.; Liu, H.; Shen, C.; Gan, F.; Su, X.; Qiu, H.; Yang, B.; Yu, P. Chiral Recognition of Hexahelicene on a Surface via the Forming of Asymmetric Heterochiral Trimers. *Int. J. Mol. Sci.* **2019**, *20* (8), 2018.
- (23) Mairena, A.; Mendieta, J. I.; Stetsovych, O.; Terfort, A.; Stará, I. G.; Starý, I.; Jelínek, P.; Ernst, K. H. Heterochiral Recognition among Functionalized Heptahelicenes on Noble Metal Surfaces. *Chem. Commun.* **2019**, *55* (71), 10595–10598.
- (24) Kaiser, R. P.; Nečas, D.; Cadart, T.; Gyepes, R.; Císařová, I.; Mosinger, J.; Pospíšil, L.; Kotora, M. Straightforward Synthesis and Properties of Highly Fluorescent [5]- and [7]-Helical Dispiroindeno-[2,1-c] Fluorenes. *Angew. Chem., Int. Ed.* **2019**, *58* (48), 17169–17174.
- (25) Gross, L.; Mohn, F.; Moll, N.; Liljeroth, P.; Meyer, G. The Chemical Structure of a Molecule Resolved by Atomic Force Microscopy. *Science (Washington, DC, U. S.)* **2009**, *325* (5944), 1110–1114.
- (26) Jelínek, P. High Resolution SPM Imaging of Organic Molecules with Functionalized Tips. *J. Phys.: Condens. Matter* **2017**, *29* (34), 343002.
- (27) Blum, V.; Gehrke, R.; Hanke, F.; Havu, P.; Havu, V.; Ren, X.; Reuter, K.; Scheffler, M. Ab Initio Molecular Simulations with Numeric Atom-Centered Orbitals. *Comput. Phys. Commun.* **2009**, *180* (11), 2175–2196.
- (28) Hapala, P.; Kichin, G.; Wagner, C.; Tautz, F. S.; Temirov, R.; Jelínek, P. Mechanism of High-Resolution STM/AFM Imaging with Functionalized Tips. *Phys. Rev. B: Condens. Matter Mater. Phys.* **2014**, *90* (8). DOI: 10.1103/PhysRevB.90.085421.
- (29) Eisenhut, F.; Lehmann, T.; Viertel, A.; Skidin, D.; Krüger, J.; Nikipar, S.; A. Ryndyk, D.; Joachim, C.; Hecht, S.; Moresco, F.;

Cuniberti, G. On-Surface Annulation Reaction Cascade for the Selective Synthesis of Diindenopyrene. *ACS Nano* **2017**, *11* (12), 12419–12425.

(30) Su, J.; Telychko, M.; Hu, P.; Macam, G.; Mutombo, P.; Zhang, H.; Bao, Y.; Cheng, F.; Huang, Z. Q.; Qiu, Z.; Tan, S. J. R.; Lin, H.; Jelínek, P.; Chuang, F. C.; Wu, J.; Lu, J. Atomically Precise Bottom-up Synthesis of -Extended [5]Triangulene. *Sci. Adv.* **2019**, *5* (7), DOI: 10.1126/sciadv.aav7717.

(31) Mendieta-Moreno, J. I.; Walker, R. C.; Lewis, J. P.; Gómez-Puertas, P.; Mendieta, J.; Ortega, J. Fireball/Amber: An Efficient Local-Orbital DFT QM/MM Method for Biomolecular Systems. *J. Chem. Theory Comput.* **2014**, *10* (5), 2185–2193.

(32) Heinz, H.; Lin, T. J.; Kishore Mishra, R.; Emami, F. S. Thermodynamically Consistent Force Fields for the Assembly of Inorganic, Organic, and Biological Nanostructures: The INTERFACE Force Field. *Langmuir* **2013**, *29* (6), 1754–1765.

(33) Lewis, J. P.; Jelínek, P.; Ortega, J.; Demkov, A. A.; Trabada, D. G.; Haycock, B.; Wang, H.; Adams, G.; Tomfohr, J. K.; Abad, E.; Wang, H.; Drabold, D. A. Advances and Applications in the FIREBALL Ab Initio Tight-Binding Molecular-Dynamics Formalism. *Phys. Status Solidi B* **2011**, *248* (9), 1989–2007.

(34) Becke, A. D. Density-Functional Thermochemistry. III. The Role of Exact Exchange. *J. Chem. Phys.* **1993**, *98* (7), 5648–5652.

(35) Neaton, J. B.; Hybertsen, M. S.; Louie, S. G. Renormalization of Molecular Electronic Levels at Metal-Molecule Interfaces. *Phys. Rev. Lett.* **2006**, *97* (21), DOI: 10.1103/PhysRevLett.97.216405.

(36) Brabec, J.; Brandejs, J.; Kowalski, K.; Xantheas, S.; Legeza, Ö.; Veis, L. Massively Parallel Quantum Chemical Density Matrix Renormalization Group Method. *J. Comput. Chem.* **2021**, *42* (8), 534–544.

(37) Chan, G. K. L.; Sharma, S. The Density Matrix Renormalization Group in Quantum Chemistry. *Annu. Rev. Phys. Chem.* **2011**, *62* (1), 465–481.

(38) Krejčí, O.; Hapala, P.; Ondráček, M.; Jelínek, P. Principles and Simulations of High-Resolution STM Imaging with a Flexible Tip Apex. *Phys. Rev. B: Condens. Matter Mater. Phys.* **2017**, *95* (4), DOI: 10.1103/PhysRevB.95.045407.

(39) Hapala, P.; Švec, M.; Stetsovych, O.; Van Der Heijden, N. J.; Ondráček, M.; Van Der Lit, J.; Mutombo, P.; Swart, I.; Jelínek, P. Mapping the Electrostatic Force Field of Single Molecules from High-Resolution Scanning Probe Images. *Nat. Commun.* **2016**, *7* (1), 11560.

(40) Gross, L.; Mohn, F.; Moll, N.; Schuler, B.; Criado, A.; Guitián, E.; Peña, D.; Gourdon, A.; Meyer, G. Bond-Order Discrimination by Atomic Force Microscopy. *Science (Washington, DC, U. S.)* **2012**, *337* (6100), 1326–1329.

(41) Clar, E. *The Aromatic Sextet*; Wiley-Interscience: London, 1972.

(42) Miyoshi, H.; Nobusue, S.; Shimizu, A.; Tobe, Y. Non-Alternant Non-Benzenoid Kekulenes: The Birth of a New Kekulene Family. *Chem. Soc. Rev.* **2015**, *44*, 6560–6577.

(43) Hückel, E. Quantentheoretische Beiträge Zum Benzolproblem - I. *Eur. Phys. J. A* **1931**, *70* (3–4), 204–286.

(44) Baird, N. C. Quantum Organic Photochemistry II Resonance and Aromaticity in the Lowest $3\pi\pi^*$ State of Cyclic Hydrocarbons. *J. Am. Chem. Soc.* **1972**, *94* (14), 4941–4948.

(45) Soncini, A.; Fowler, P. W. Ring-Current Aromaticity in Open-Shell Systems. *Chem. Phys. Lett.* **2008**, *450* (4–6), 431–436.

(46) Kruszewski, J.; Krygowski, T. M. Definition of Aromaticity Basing on the Harmonic Oscillator Model. *Tetrahedron Lett.* **1972**, *13* (36), 3839–3842.

(47) Ostrowski, S.; Dobrowolski, J. C. What Does the HOMA Index Really Measure? *RSC Adv.* **2014**, *4* (83), 44158–44161.

(48) Chen, Z.; Wannere, C. S.; Corminboeuf, C.; Puchta, R.; von Ragué-Schleyer, P. Nucleus-Independent Chemical Shifts (NICS) as an Aromaticity Criterion. *Chem. Rev.* **2005**, *3842*–3888.

(49) Lampkin, B. J.; Karadakov, P. B.; VanVeller, B. Detailed Visualization of Aromaticity Using Isotropic Magnetic Shielding. *Angew. Chem., Int. Ed.* **2020**, *59* (43), 19275–19281.

(50) Randić, M. Conjugated Circuits and Resonance Energies of Benzenoid Hydrocarbons. *Chem. Phys. Lett.* **1976**, *38* (1), 68–70.

(51) Geuenich, D.; Hess, K.; Köhler, F.; Herges, R. Anisotropy of the Induced Current Density (ACID), a General Method To Quantify and Visualize Electronic Delocalization. *Chem. Rev.* **2005**, *105* (10), 3758–3772.

(52) Riss, A.; Paz, A. P.; Wickenburg, S.; Tsai, H. Z.; De, O. D. G.; Bradley, A. J.; Ugeda, M. M.; Gorman, P.; Jung, H. S.; Crommie, M. F.; Rubio, A.; Fischer, F. R. Imaging single-molecule reaction intermediates stabilized by surface dissipation and entropy. *Nat. Chem.* **2016**, *8* (7), 678–83.

3.2 Magnetic anisotropy of one-dimensional porphyrin coordination polymers

3.2.1 Introduction

One-dimensional organic magnets with regularly spaced magnetic centers have gained attention for their potential use in spintronic devices due to their extended spin coherence length, mechanical flexibility[58, 59], and the intrinsic array-like geometry, which can be advantageous for industrial applications[60]. However, the synthesis of 1D polymeric molecular spintronics remains challenging[59]. One possible approach to overcoming this challenge is through the use of well-defined, straight, conjugated polymers, such as porphyrin molecules with coordinated transition metal atoms. Porphyrins have high thermal stability and tend to form well-ordered assemblies on solid surfaces, making them ideal for on-surface synthesis of 1D organometallic polymers and to be incorporated in graphene nanoribbons [61].

When ligands surround a metal ion, they create a region of negative charge that interacts with the positively charged metal ion, splitting the d-orbitals of the metal ion into two energy levels, with some orbitals becoming higher in energy than others. The magnetic anisotropy, or the preferred orientation of magnetic moments, of the central metal atom is determined by the ligand field coordination with it, and therefore it may potentially be controlled by modifying either the coordinated metal atom or the ligand, such as by altering the molecular backbone. Tailoring the coupling between the molecular ligand field and the magnetic anisotropy of the metal atom could create new opportunities for spintronic applications in arrays of organometallic systems containing magnetic atoms.

This section outlines the results of synthesizing two types of polymers on Au(111) using the same precursor, Iron(III) 5,15-(di-4-bromophenyl)porphyrin chloride (**2BrFeDPP-Cl**)

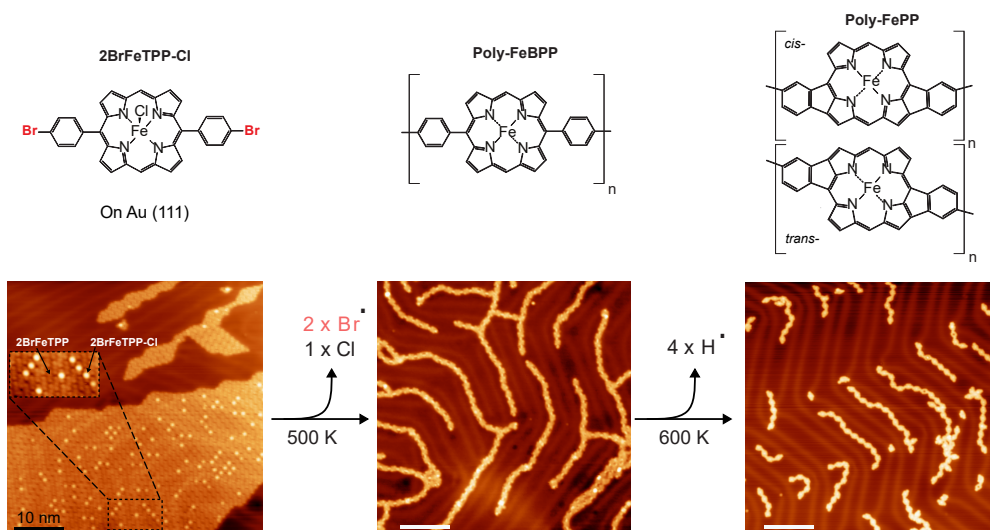


Figure 3.7: The reaction proceeds in three stages: first, the material is deposited at room temperature; next, the temperature is raised to 500 K to induce the formation of non-planar polymers; and finally, the temperature is further increased to 600 K to promote the formation of planar polymers.

under ultra-high vacuum (UHV) conditions. Upon deposition on the surface, **2BrFeDPP-Cl** forms ordered, closely packed islands (as shown in Fig. 3.7) with both Cl-containing and Cl-free molecules present in a random distribution. The twisted phenyl groups with Br atoms are clearly visible in AFM as bright, saddle-like structures, while the porphyrin core is not resolved due to its lower height (see Fig. 3.8).

To induce the first reaction, the sample is annealed at 500 K for 30 minutes. During this process, the precursor compound **2BrFeDPP-Cl** undergoes debromination and then an aryl-aryl coupling between monomers of FeDPP, resulting in the formation of covalently bonded molecular wires known as Poly-FeDPP. However, due to steric hindrance, the aryl-aryl linkers are twisted and obscure the visualization of the lower porphyrin core (see Fig. 3.8). As a second step, the sample is annealed at 600 K for 30 minutes, which induces intramolecular rearrangements of the aryl groups through dehydrogenation and cyclization of the aryl and pyrrolic groups of the porphyrins in the polymer (**Poly-FePP**). This rearrangement leads to intermolecular rearrangement of the monomers (**FePP**) into

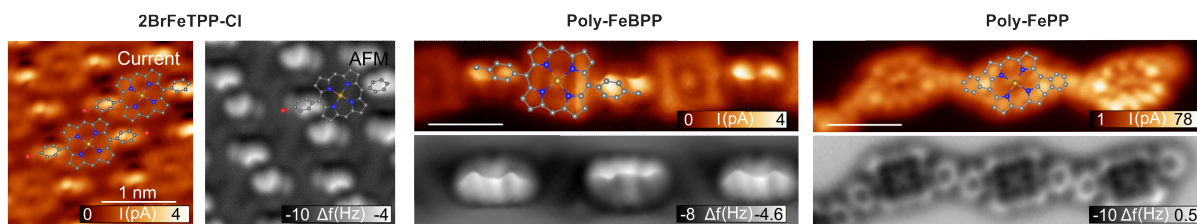


Figure 3.8: High-resolution imaging with CO-tip in constant height mode for the three steps of the reaction.

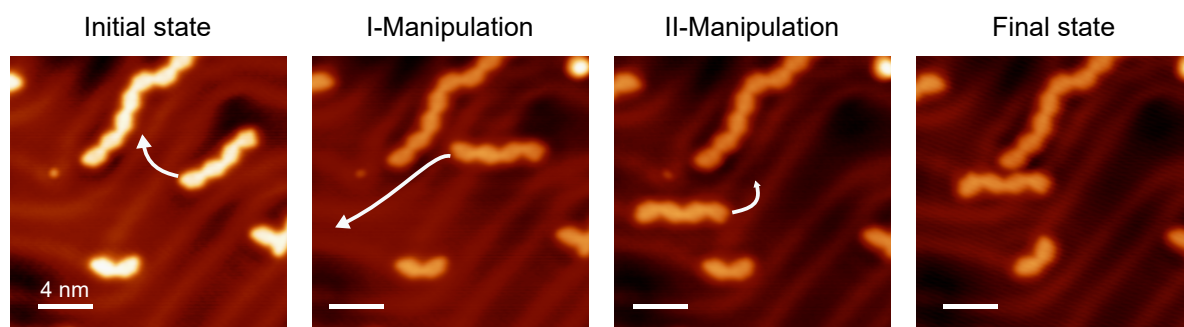


Figure 3.9: The planar polymers are connected by covalent bonds and can be controlled using the STM tip ($V_{Bias} = 100$ mV, $I_{set} = 50$ pA).

isoindole groups, resulting in the planarization of the polymer. The planarization process keeps the covalent bonds between monomers intact (see Fig. 3.9) and produces an equivalent amount of cis (52%) and trans (48%) **FePP** units, incorporated into large wires of up to 50 nm (Fig. 3.10)

In the three steps of the reaction, the magnetic anisotropy of the coordinated Fe is affected by the local chemical and geometrical environment. Initially, the **2BrFeDPP-Cl** has a net spin of $S=3/2$ while the dechlorinated **2BrFeDPP** (naturally dechlorinated in the sublimation process or by tip-induced manipulation) has a lower oxidation state of the iron, from Fe^{+3} to Fe^{+2} , leading to a total spin of $S=1$. To measure the magnetic anisotropy in STM, we experimentally measure the inelastic spin excitation in the dI/dV curves of the Fe atoms. The FWHM of the curve is proportional to $2 \cdot D$, where D represents the total magnetic anisotropy.

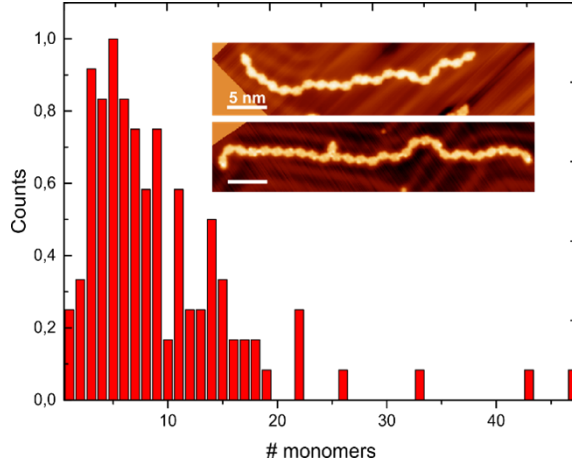


Figure 3.10: Statistical distribution of chain lengths upon annealing the sample up to 600 K ($N=114$). Two STM images of large poly-FePP polymers are displayed in the inset.

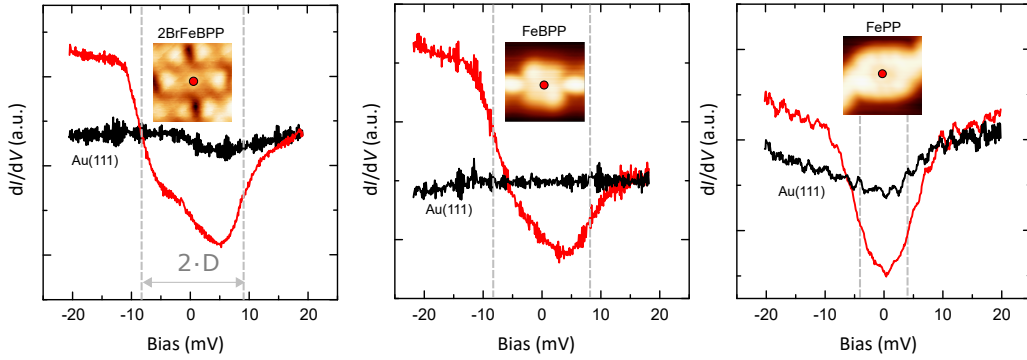


Figure 3.11: dI/dV spectra recorded on the center (red) of single 2BrFeDPP , poly- FeDPP and poly- FePP wires.

Once the first polymerization starts, it can be observed that the experimental magnetic anisotropy D in both single 2BrFeDPP and the linked monomers of FeDPP is minimally affected by the polymerization process (Fig. 3.11). This is indicated by the similarity between the excitation onsets or extremes of FWGM for both molecules, with $V_{2\text{BrFeDPP}} = \pm 8.5$ mV and $V_{\text{FeDPP}} = \pm 7.5$ mV, respectively, and a difference below the experimental resolution of 2 mV. This phenomenon is consistent with a triple with $S=1$.

However, planarization of FePP does have an effect on the spectra, leading to a reduction in the onset of excitations to $V_{2\text{BrFeDPP}} = \pm 3.5$ mV while still retaining the single-step

dI/dV profile and the spin $S=1$. The observed reduction in magnetic anisotropy, as also evidenced in DFT calculated spin occupation levels, can be attributed to the breaking of square-planar symmetry and subsequent charge redistribution during the planarization process, resulting in a variation in the ligand field.

3.2.2 Author's contribution to the published work

In this work, I prepared and conducted the polymeric reactions and performed the experimental acquisition of STM and nc-AFM. I also performed the statistical analysis of the length of polymers, the cis/trans populations, and the analysis of the STS spectra. I also discussed both experimental and simulated findings, began drafting the manuscript, prepared the figures, and participated in the discussion and interpretation of the data with my collaborators.

On-Surface Synthesis of One-Dimensional Coordination Polymers with Tailored Magnetic Anisotropy

Benjamin Mallada, Piotr Błoński,* Rostislav Langer, Pavel Jelínek, Michal Otyepka, and Bruno de la Torre*



Cite This: *ACS Appl. Mater. Interfaces* 2021, 13, 32393–32401



Read Online

ACCESS |

Metrics & More

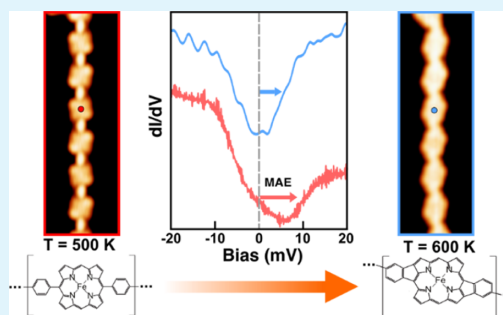
Article Recommendations

Supporting Information

ABSTRACT: One-dimensional (1D) metalloporphyrin polymers can exhibit magnetism, depending on the central metal ion and the surrounding ligand field. The possibility of tailoring the magnetic signal in such nanostructures is highly desirable for potential spintronic devices. We present low-temperature (4.2 K) scanning tunneling microscopy and spectroscopy (LT-STM/STS) in combination with high-resolution atomic force microscopy (AFM) and a density functional theory (DFT) study of a two-step synthetic protocol to grow a robust Fe-porphyrin-based 1D polymer on-surface and to tune its magnetic properties. A thermally assisted Ullmann-like coupling reaction of Fe(III)diphenyl-bromine-porphyrin (2BrFeDPP-Cl) on Au(111) in ultra-high vacuum results in long (up to 50 nm) 1D metal–organic wires with regularly distributed magnetic and (electronically) independent porphyrins units, as confirmed by STM images.

Thermally controlled C–H bond activation leads to conformational changes in the porphyrin units, which results in molecular planarization steered by 2D surface confinement, as confirmed by high-resolution AFM images. Spin-flip STS images in combination with DFT self-consistent spin–orbit coupling calculations of porphyrin units with different structural conformations reveal that the magnetic anisotropy of the triplet ground state of the central Fe ion units drops down substantially upon intramolecular rearrangements. These results point out to new opportunities for realizing and studying well-defined 1D organic magnets on surfaces and demonstrate the feasibility of tailoring their magnetic properties.

KEYWORDS: coordination-polymer, on-surface chemistry, metal-porphyrin, magnetic anisotropy, scanning probe microscopy



1. INTRODUCTION

The synthesis and functionalization of molecular spintronic nanostructures have attracted considerable interest due to their great potential for being beneficial to the next generation of electronic devices.^{1–5} Among others, organic nanostructures enabling to tailor the spin-polarized signal is a burgeoning area of spintronic research.⁵ One-dimensional (1D) polymeric organic magnets with regularly distributed magnetic centers are desirable networks, thanks to their long spin coherence length and mechanical flexibility.⁶ Till date, several 1D molecular wires with transition-metal (TM) atoms have been proposed, including 1D TM-cyclopentadienyl,⁷ TM-benzene,⁸ TM-anthracene,⁹ TM-phthalocyanine,¹⁰ TM-metallocene,¹¹ TM-benzoquinonediimines,¹² and TM-naphthalene.¹³ However, despite significant efforts, the experimental realization of such 1D polymeric molecular spintronics still remains a significant challenge. Nevertheless, the fabrication of novel frameworks that could be fashioned by a simple synthetic method is urgently required. To make progress in this field, it is important to choose a suitable functional molecule for making a large 1D polymeric framework.

Porphyrin molecules with coordinated TM atoms emerge as a promising candidate for constructing molecular spintronics because they combine inherent optical, redox, and magnetic properties of the intervening metal centers with those of the purely organic materials.^{14–22} In such coordination polymer complexes, the ligand field coordinated with the central metal atom governs its magnetic anisotropy due to spin–orbit coupling (SOC).^{23,24} Additionally, porphyrins exhibit high thermal stability and propensity to form well-ordered assemblies on a variety of solid surfaces.^{25–27} Commonly, peripheral ligands are attached to the porphyrin macrocycle in specific positions in order to steer the intermolecular bonding.²⁸ Thus, arrays of conjugated porphyrin with delocalized electronic networks have been intensively explored

Received: March 12, 2021

Accepted: June 18, 2021

Published: July 6, 2021



Chart 1. Thermal Reaction Sequence of 2BrFeDPP-Cl on Au(111) Obtained in the First Step of Annealing: Dehalogenation and Subsequent On-Surface Homocoupling Polymerization upon Annealing up to 500 K, and Furthermore, Cyclodehydrogenation into cis- and trans-Polymers upon Annealing up to 600 K

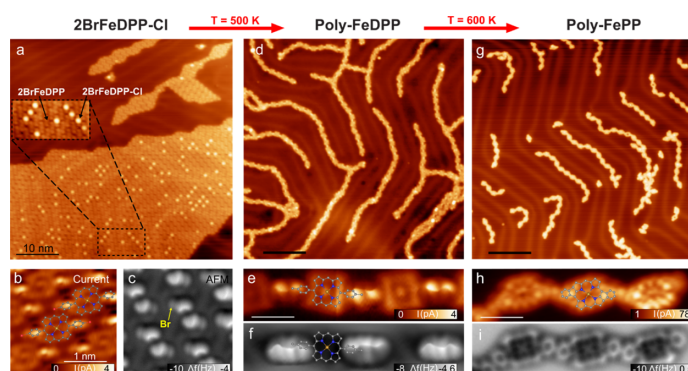
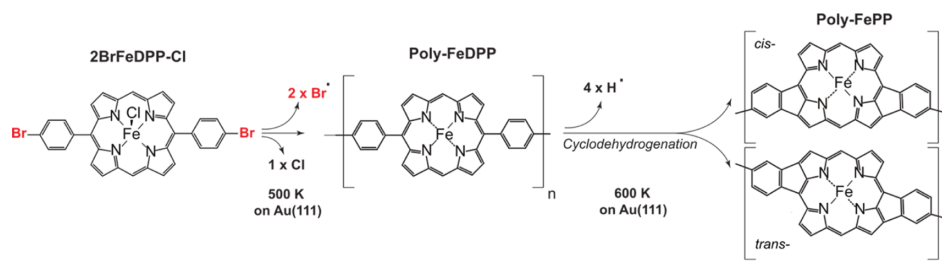


Figure 1. (a) STM topography upon deposition of 2BrFeDPP-Cl on Au(111) at RT ($V_{\text{bias}} = -200$ mV, $I_{\text{set}} = 20$ pA). (b,c) Detailed STM/nc-AFM constant height images with CO-tip. (d) STM topography upon sample annealing to 500 K ($V_{\text{bias}} = 100$ mV, $I_{\text{set}} = 20$ pA). (e,f) Corresponding detailed STM/nc-AFM constant height images with CO-tip of FeDPP molecular wires. (g) STM topography upon sample annealing to 600 K ($V_{\text{bias}} = -500$ mV, $I_{\text{set}} = 50$ pA). (h,i) Corresponding detailed STM/nc-AFM constant height images with CO-tip of the FePP molecular wires. The scale bar corresponds to 10 nm in (a,d,g) and to 1 nm in (b,c,e,f,h,i).

over the last two decades.^{29–32} For example, the 1D Zn-porphyrin arrays have been already obtained experimentally, and they may find promising applications as a conducting molecule.³³

However, such large structures are difficult to form by traditional chemical synthesis and to deposit on surfaces for further characterization and application onto devices; therefore, only oligomers formed by a few porphyrin units have been investigated so far. Recently, the emerging field of on-surface synthesis has enabled to overcome the limitation of both solubility and reactivity found in the solution synthesis, along with allowing in situ atomic-scale characterization by means of scanning tunneling microscopy/non-contact atomic force microscopy (STM/nc-AFM).³⁴ Furthermore, the 2D confinement imposed by the substrate during the polymerization process may result in molecular structure rearrangements, which would be otherwise difficult to induce as molecular planarization.

Here, we report a thorough investigation into the on-surface synthesis of large (up to 50 nm) metal-porphyrin based 1D molecular wires with regularly distributed magnetic and thermally adjustable anisotropy signals by means of low-temperature STM and high-resolution nc-AFM with CO-tip³⁵ complemented with theoretical calculations. Importantly, the formation of such long 1D chains have not been observed so far. Porphyrin building blocks are functionalized by bromine atoms in both phenyls at the para position, which steer an

thermally induced intermolecular Ullman-like coupling reaction of aryl-halides, giving rise to 1D molecular wires, and further intramolecular transformations (planarization) at higher temperatures, allowing stepwise thermal control of chemical reactions.

We show that the adsorption of iron(III) 5,15-(di-4-bromophenyl)porphyrin-chloride molecules on Au(111) leads to the dechlorination of a large portion of molecules, which reduces the total spin of the molecule. Subsequent annealing to 500 K induces debromination, which gives rise to 1D molecular structures of covalently linked iron porphyrin molecules driven by aryl–aryl intermolecular coupling. A second step of annealing to 600 K affords intramolecular dehydrogenation and ring closure reactions as a consequence of activation at such a temperature of both C–H bonds of the aryl and porphyrin moieties, which results in molecular wires formed by iron-metaled planarized porphyrin molecules. Inelastic spin excitation experiments in combination with DFT calculations reveal a substantial modification of the magnetic anisotropy energy (MAE) at the iron atom upon porphyrin planarization due to the adjustment of the electron density at d and π orbitals.

We envision that our investigation into the magnetic anisotropy dependence and the spin–spin coupling in porphyrin-based molecular wires can provide insights into the magnetism, spin delocalization, metal–ligand d- π mixing,

and pathways for transmitting spin effects in 1D molecular nanostructures.^{36–40}

2. RESULTS

2.1. Structural Characterization. Chart 1 shows the chemical structure of the iron(III)-chlorine biphenyl porphyrin archetype [iron(III) 5,15-(di-4-bromophenyl)porphyrin chloride, hereafter referred to as 2BrFeDPP-Cl], we used as a molecular precursor in this study. This porphyrin species possesses phenyl moieties functionalized with C–Br groups at the para position to facilitate the linearity of the intermolecular coupling reaction product upon dehalogenation on the Au(111) substrate. Initial step-by-step structural characterization of the on-surface reaction was conducted by scanning probe microscopy (SPM) measurements to identify the distinct molecular structures present on the sample. Subsequently, after each sample annealing step, the sample is transferred and cooled to 5 K in ultra-high vacuum (UHV) conditions for SPM inspection.

2.1.1. Structure at 300 K. Upon adsorption at room temperature, 2BrFeDPP-Cl porphyrins were arranged into spatially extended close-packed islands with a majority of molecules appearing with a dim center, as depicted by STM images (cf. Figure 1). They correspond to the dechlorinated (loss of the Cl ligand) species 2BrFeDPP, which adopt a saddle conformation with twisted aryl moieties.^{25,41} 2BrFeDPP molecules can be controllably realized by removing the Cl ligand from the 2BrFeDPP-Cl molecules using tunneling electrons over the Cl position⁴¹ or by gently annealing the substrate ($T < 500$ K). The nc-AFM constant high images with CO-tip of assembled 2BrFeDPP molecules displayed a bonded Br atom as bright features (see Figure 1c), which correspond to strong repulsive force contributions, corroborating the preservation of bromine at the termini of both twisted phenyl moieties (cf. Figure 1b,c). According to the 2BrFeDPP optimized structure on Au(111) from DFT calculations (see Figure S1), the single molecule adsorbed preferentially on the Au(111) surface in a way that the Fe ion was directly above the Au atom of the top-most layer, with the adsorption energy of -77.4 kcal/mol at the Fe–Au distance of 3.53 Å. The in-plane rotation of the molecule, which decreased the Br–Br distance, increased the adsorption energy by at most 7.7 kcal/mol.

2.1.2. Structure at 500 K. A first step of the sample annealing to $T \sim 500$ K for 30 min led to the development of large 1D molecular wires extended over the surface (cf. Figure 1d). As illustrated by high-resolution STM/nc-AFM images, the molecular wires were composed of covalently bonded iron-porphyrin molecules that lost their coordinated chlorine atoms (cf. Figure 1e,f). Thus, we denote the subunits within the 1D structure as FeDPP, indicating the structural relationship with the precursor molecule. The annealing resulted in the cleavage of the C–Br bonds and the subsequent formation of 1D supramolecular structures upon surface-assisted aryl–aryl cross-coupling of adjacent porphyrin molecules. A wise choice of molecular functionalization in para positions at the porphyrin precursor allowed linearity during the intermolecular coupling process, which led to molecular wires with lengths that extend up to ~ 40 monomers with no appreciable structural defects.

Importantly, the connecting aryl–aryl pairs were twisted owing to the steric hindrance, similar to unreacted 2BrFeTTP molecules on Au(111). Moieties at the same monomer were twisted differently; thus, consecutive bridges with opposite

twist angle were observed within the 1D structures (cf. Figure 1e,f). In consequence, the non-planar configuration of the monomers hindered the submolecular resolution of the porphyrin centers by means of constant height nc-AFM imaging; therefore, only the linker moieties, which protruded further out of the surface, are featured in nc-AFM images (cf. Figures 1f and S2).

Finally, the loose end of the molecular wires was passivated by bromine or residual hydrogen atoms, precluding further polymerization. Interestingly, FeDPP molecular wires were easily manipulated with the SPM tip both vertically and laterally over the surface, which demonstrates the robustness of the nanostructure (see Figure S3).

2.1.3. Structure at 600 K. Following the thermal annealing of the molecule-decorated sample to $T \sim 600$ K for 30 min, molecular units within the wires underwent an intramolecular reaction through dehydrogenation and electrocyclic ring closure of their aryl termini and the macrocyclic pyrroles. This process led to the formation of isoindole motifs, which induced planarization of the porphyrin monomers on the surface (hereafter referred to as FePP units, Figure 1g), as unambiguously corroborated by high-resolution STM and nc-AFM images shown in Figure 1h,i. Therefore, the Fe atom at the center of the porphyrin unit is displayed as a cross-like feature in nc-AFM images, similar to the nc-AFM contrast observed on other metal phthalocyanines and porphyrin complexes.^{42–44}

The ring closure of aryl moieties toward the macrocycle gave rise either to trans- or cis-configurations of the molecular repeating units (Chart 1). Statistically (over hundreds of monomer units counted on several samples), we observed equivalent abundance of the intramolecular cis (52%) and trans (48%) motifs, pointing out that both configurations are equally favorable. Interestingly, we found two effects regarding the substrate reconstruction: (1) the FePP molecular chains aligned along the herringbone, and, (2) frequently, the molecular chains terminated at the elbow sites. Thus, the segments that showed repeated cis or trans motifs were found with a maximum length of five units.

The intramolecular- versus intermolecular-induced reaction observed at different temperatures is rationalized by theoretical calculations of the dissociation energy (BDE) for various C–H and C–Br bonds of a single porphyrin specie on the Au(111) surface. Our theoretical calculations revealed that the activation energy for bromine abstraction was lower than that of hydrogen abstraction (C–H₁ and C–H₂, see bond labeling shown in Figure 2) by at least 30 kcal/mol (see Table 1). Upon adsorption, this value dropped up to 15 kcal/mol due to surface-assisted molecular structure stabilization. The initial removal of the Br atom further reduced the bond dissociation energies of the C–H₁, which favored H abstraction at higher temperatures, resulting in the ring closure of aryl moieties

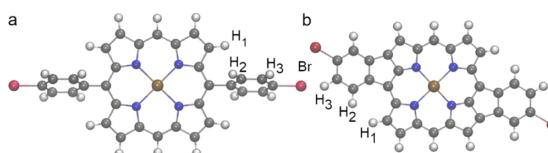


Figure 2. Stick-ball model for 2BrFeDPP (a) and 2BrFePP (b). BDEs of the labeled bonds are gathered in Table 1. C atoms are shown in gray, H in white, N in blue, Fe in orange, and Br in red.

Table 1. BDEs (in kcal/mol) of C–Br and C–H Bonds Labeled in Figure 2a

bond	2BrFeDPP		2BrFePP	
	freestanding	on Au(111)	freestanding	on Au(111)
C–Br	99.3	102.1	85.3	102.8
C–H ₁	133.2 (104.1)	117.9 (116.5)		118.5
C–H ₂	129.5 (101.7)	128.2	128.1	117.8
C–H ₃	129.8		116.2	115.8

^aBDEs of selected C–H bonds after the removal of the Br atom are shown in brackets. See also note 1 in SOM of the calculated adsorption of 2BrFeDPP and 2BrFePP on Au(111).

steered by the 2D confinement of the surface. Thus, the stepwise annealing of 2BrFeDPP first allowed the formation of poly-FeDPP structures through Ullmann-like coupling of arylhalides and, subsequently, the emergence of poly-FePP planar structures at higher temperatures. Interestingly, we found shorter molecular chains upon the planarization process (annealing at 600 K) in average (4–11 monomers). This may be due to thermally induced polymer breaking. However, molecular chains containing up to 50 nm can be found on the sample (see Figure S4).

Accordingly, annealing the sample at intermediate temperatures in the range of $T \sim 500$ –600 K, that is, at 550 K, for 30 min, partially activated the ring closure reaction, thus yielding molecular wires with a mixture of FeDPP and FePP units (see Figure S5). Notably, no trace of intramolecular dehydrogenation was observed at temperatures below 550 K. Indeed, no dehydrogenation reaction was identified prior to the polymerization process of the molecular precursor.

On the other hand, annealing to elevated temperatures ($T > 600$ K) resulted in molecular wires fused together, which reduced the 1D character of the nanostructures. These structures were formed by the dissociation of the C–H bonds at the periphery of the porphyrin units and by the subsequent fusion of the nearby polymer, as depicted in STM/nc-AFM images (see Figure S6).

2.2. Experimental Spin Features. Next, we focused on spin characteristics of 2BrFeDPP-Cl molecules upon adsorption, dechlorination, polymerization (poly-FeDPP), and intramolecular planarization (poly-FePP) by means of inelastic spin excitation spectroscopy with STM.^{45–47} Figure 3 plots specific site spectra of the differential conductance (dI/dV) around the Fermi level with the STM tip placed on the Fe center (red) for both single 2BrFeDPP-Cl (Figure 3a) and 2BrFeDPP (Figure 3b) and on FeDPP (Figure 3c) and FePP (Figure 3d) units in a molecular wire as well. Reference spectroscopy on the bare Au(111) surface (featureless) is plotted with black lines, as shown in Figure 3.

In the case of 2BrFeDPP-Cl molecules, we identified a prominent dip feature at the Fermi level (cf. Figure 3a). In similar FeTTP-Cl molecules, step-like features at ± 1.7 meV associated with spin-flip excitations have been reported.⁴⁸ However, due to the thermal broadening at the temperature at which we conducted our experiments (4.2 K), we cannot unequivocally distinguish whether the observed feature represents a spin-flip excitation or a Kondo resonance. The change in contrast between 2BrFeDPP-Cl and 2BrFeDPP (see Figure S7) is consistent with the same process in FeTTPCl (see, e.g., ref 41). In contrast, the spectra acquired on the Fe center of the dechlorinated 2BrFeDPP (cf. Figure 3b),

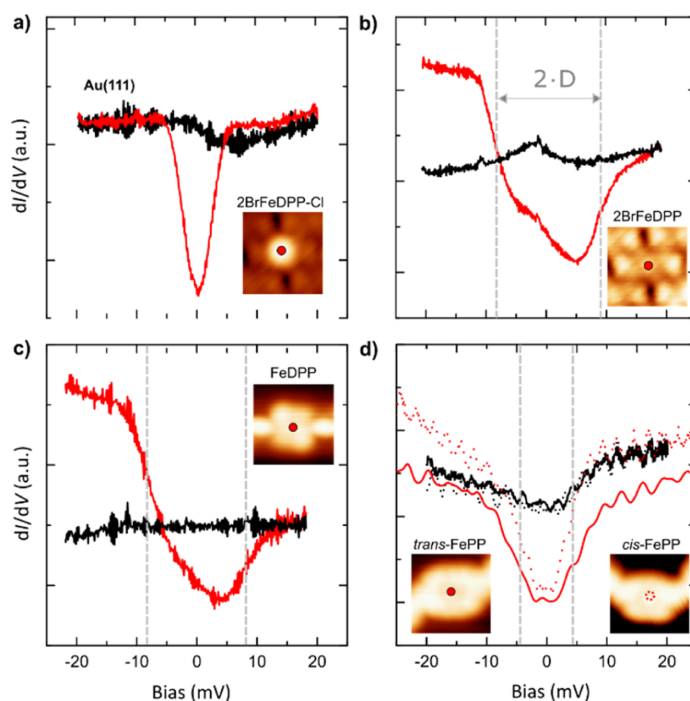


Figure 3. dI/dV spectra recorded on the center (red) of single 2BrFeDPP-Cl (a), on 2BrFeDPP (b), on monomer in poly-FeDPP wire, (c) on cis- (dash-shaped) and trans- (line-shaped) monomer in poly-FePP wire, and (d) corresponding reference spectra on the bare substrate (black).

polymerized FeDPP (cf. Figure 3c), and FePP (cf. Figure 3d) molecules revealed stepwise increments in conductance at symmetric bias values. Consistent with previous studies on similar Fe-TPP on Au(111), we ascribed this feature to the spin-flip inelastic excitation process.^{48,49}

Notably, the removal of the coordinated chlorine atom from the 2BrFeDPP-Cl molecules reduced the Fe-oxidation state from Fe³⁺ to Fe²⁺ and consequently lowered the total spin from $S = 3/2$ to $S = 1$.⁴¹ The spin reduction was confirmed by the current SP-DFT calculations. Furthermore, the calculations predicted MAE of -4.1 meV for 2BrFeDPP-Cl, where the negative MAE represented the easy-axis system, which was in contrast with the MAE of dechlorinated 2BrFeDPP (cf. Section 3). Upon dechlorination, the degenerated triplet state splits into the ground spin state $m_s = 0$ and the doubly degenerated $m_s = \pm 1$ excited states due to the spin-orbit interaction. This splitting is referred to as zero-field splitting and occurs even in the absence of a magnetic field.⁵⁰ In the first approximation, the spin excitation is determined by the magnetic anisotropy of the molecule on the surface, which is well described by a spin Hamiltonian $HS_O = DS_z^2 + E(S_x^2 - S_y^2)$, where D is vertical magnetic anisotropy (origin of the zero-field splitting) and E is in-plane magnetic anisotropy, which typically vanishes for planar molecules. Therefore, we attributed the inelastic spin excitation spectra to the triplet $S = 1$, and the excitation energy corresponded to the axial anisotropy constant. It should be noted that very similar spectra were also obtained for an Fe-tetraphenyl-porphyrin molecule,⁴⁹ which was attributed to inelastic spin excitation of the $S = 1$ spin state as well.

The spectra acquired on the 2BrFeDPP molecules and FeDPP monomers showed excitation voltage onsets at $V_s = \pm 8.5$ mV and $V_s = \pm 7.5$ mV (see Figure S8), respectively (similar to previously reported values of D for FeDPP complexes⁴⁹). It is worth noting that the difference in the excitation onset observed for 2BrFeDPP and FeDPP was lower than that in our experimental resolution (2 mV). Interestingly, the excitation spectra on both the 2BrFeDPP molecule and the FeDPP unit showed similar steps with asymmetric line shapes. Such asymmetries have been previously attributed to the characteristic particle-hole excitation symmetry in Fe-tetraphenyl porphyrin complexes.⁴⁸

Based on this data and in accordance with our theoretical calculations (see below), we conclude that the polymerization process (aryl-aryl coupling) hardly affects the magnetic anisotropy of the FeDPP molecule (similar energy onset and line shape of the spin excitation). This result can be attributed to the lack of large distortions of the molecular ligand field upon the formation of poly-FeDPP chains, as confirmed by our calculations.

On the other hand, although the planarization process from poly-FeDPP toward poly-FePP did not change the overall character of the stepped spectrum (step-like shape), it decreased the onset of the excitation energy to $V_s = \pm 3.5$ mV ($D = 3.5$ meV). Additionally, the excitation in the FePP features had a more symmetric line shape than that in FeDPP. All together hint toward a change in the magnetic polarization of the spin state upon molecular planarization, as will be discussed below.

For comparison, we analyzed isolated FePP molecules, which were often found on the surface after annealing the sample to 600 K. They displayed identical characteristics to the corresponding FePP units in molecular wires (see Figure S9),

confirming that the observed change in the MAE from FeDPP ($D = 7.5$ meV) to FePP ($D = 3.5$ meV) units was induced by planarization and the subsequent ligand field variation. Thus, we assume that the structure of the ligand field ruled the magnetic anisotropy of the wire units rather than that of the polymer bridges. This observation was further corroborated by measurements on a molecular chain composed of a mixture of FeDPP and FePP (see Figure S5), where we observed that the magnetic anisotropy of every molecular unit was not affected by being connected to either a planar or a non-planar unit. This result was expected due to the low degree of electronic delocalization of the single C-C bond connecting the monomers.

3. DISCUSSION

To gain a deeper insight into the origin of the reduction of MAE of the planarized FePP molecules observed experimentally, we performed spin-polarized DFT calculations including a self-consistent treatment of SOC. While the theoretical calculations of the MAE hinge on several inevitable approximations including the choice of an exchange-correlation functional, the degree of optimization of the geometry of the adsorbate/substrate complex, and the MAE calculated either self-consistently or via the magnetic force theorem, leading to a lower bound of the actual MAE, the theory still provides a sound physical picture of the MAE.⁵¹ We examined the magnetic properties of the single molecules of 2BrFeDPP and 2BrFePP and polymers of FeDPP and FePP, both freestanding and supported on Au(111).

Scalar relativistic (SR) calculations predict the spin-triplet ground state for both the freestanding and Au(111)-supported molecules and chains, while the spin-singlet is at least ~ 0.4 eV higher in energy. The total magnetic moment is localized mostly on the Fe ion and, to a much lesser extent, on the four coordinating N atoms (see Figure S10).

Table 2 gathers the theoretical MAE of all the systems considered. While the theoretical MAE of 2BrFeDPP and

Table 2. MAE (in meV) of Freestanding and Au(111)-Supported 2BrFeDPP and 2BrFePP

	2BrFeDPP		2BrFePP	
	freestanding	on Au(111)	freestanding	on Au(111)
single molecule	6.2	2.0	1.0	0.3
dimer	4.8		1.1	
wire	1.5	3.7	0.4	1.7

^aPositive MAE corresponds to an easy-plane system. The in-plane MAE of all systems was negligible.

2BrFePP is reduced by polymerization, the trend is reversed for the Au(111)-supported counterparts, due to the interaction with the substrate. The relative reduction of the MAE of the Au(111)-supported molecules and chains due to planarization is, however, similar and amounts to 1.7 and 2.0 meV, respectively. Thus, the reduction of MAE for the planarized molecules is in semi-quantitative agreement with the experimental observation, regardless of whether they were deposited on the Au(111) surface or/and polymerized. This indicates that the origin of the MAE reduction must be viewed in the differences in the symmetry of the Fe environment, which may lead to a different occupation scheme of the central Fe atom.

Indeed, in the 2BrFeDPP molecule, all Fe–N distances were equal to 2.01 Å. Occupations of the Fe 3d levels were similar for the SR limit and for the axial (hard) direction of magnetization after adding SOC (Figure S11). The rotation of magnetic moments in the in-plane (easy) direction led to the lifting of the degeneracy of the $d\pi$ states and the reordering and change in the occupation of the 3d levels.

In the 2BrFePP molecule, the square-planar symmetry was broken with two short and two long Fe–N bonds in the length of 1.94 and 2.04 Å, respectively, and the lifting of the degeneracy of the $d\pi$ states was already observed in the SR limit (see Figure S11). With SOC, no significant changes occurred in the occupation of the Fe 3d levels upon the rotation in the direction of magnetization between the axial (hard) and in-plane (easy) direction. This explains the reduced MAE in planarized 2BrFePP.

For a single molecule of 2BrFeDPP supported on Au(111), an in-plane magnetic direction is favored; as for a free-standing molecule (Table 2), with the spin/orbital moment of 2.361/0.113 μ_B . The perpendicular hard magnetic direction is disfavored by 2.0 meV with the spin/orbital moments reduced to 2.358/0.009 μ_B . The internal cyclization (planarization) reduced the MAE only to 0.3 meV, which is in line with the experimental observation. We identified the spin/orbital moments of 2.005/0.119 μ_B for the easy magnetic direction and 2.002/0.025 μ_B for the hard magnetic axis. It should be in line with the reduced anisotropy of the orbital moments, compared to the 2BrFeTPP/Au(111) system.

Densities of states of 2BrFeDPP/Au(111) and 2BrFePP/Au(111) projected on the Fe-d orbitals are shown in Figure 4a,b (see also Figures S12 and S13), and the corresponding occupation schemes of the Fe 3d levels are shown in Figure 4c,d. The $d_{x^2-y^2}$ and d_{xy} -derived states, which were localized and narrow due to their weak interaction with the Au substrate, were fully occupied and empty, respectively. While the spin-down d_z^2 and $d\pi$ -derived states were occupied in both systems, for 2BrFeDPP/Au(111), the spin-up counterparts were partially occupied and empty, respectively. For planarized 2BrFePP/Au(111), the spin-up d_z^2 and d_{xz} -derived states were both partially occupied, and, moreover, the d_z^2 and $d\pi$ -derived states were slightly broadened because of their larger hybridization with the substrate. Accordingly, projected density of states (PDOS) indicates that the spin polarization originated predominantly from the contribution of d_z^2 and $d\pi$. As for the freestanding molecules, the degeneracy of $d\pi$ was largely broken for planarized 2BrFePP/Au(111) (Figures S12 and S13). In addition, the effect of SOC on the occupations of the 3d electronic states for the supported molecules was lower than that of the freestanding molecules (cf. Figure S11) as a consequence of the hybridization with the substrate and according to lower MAE⁵¹ (cf. Table 2).

The occupation scheme of the 3d electronic states of the infinite chain of FeDPP and FePP supported on Au(111) corresponds well to those for the supported molecules (as shown in Figure 4c,d) and, accordingly, the MAE is in semi-qualitative agreement with the experimental findings. A slightly larger MAE, compared to the single-molecule counterparts, may be due to the intrachain interactions; this being at the expense of the interaction with the substrate.

4. CONCLUSIONS

In conclusion, we have synthesized large 1D metal-porphyrin wires on-surface and have investigated their conformational

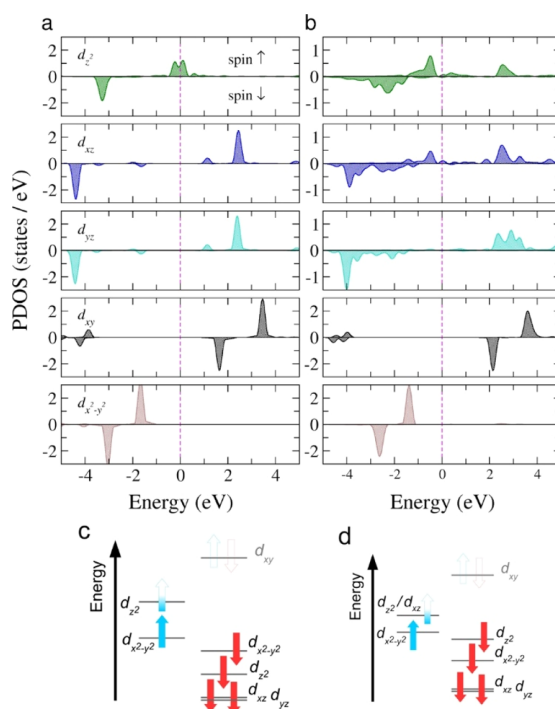


Figure 4. PDOS of the d orbitals of Fe for the Au(111)-supported 2BrFeDPP (a) and 2BrFePP (b). The corresponding PDOS-derived occupation schemes of the Fe 3d levels are shown in (c,d). Due to two unpaired Fe-d electrons, the systems have $S = 1$ ground state (cf. Figures S12 and S13).

and intrinsic magnetic characteristics. High-resolution AFM images confirmed that annealing the 2BrFeDPP-Cl-decorated Au(111) sample to $T \approx 500$ K led to 1D polymers with regular Fe-porphyrins and surface-assisted intramolecular planarization upon sample annealing to $T \approx 600$ K. Such intramolecular planarization resulted in substantial adjustment of the magnetic properties of porphyrin's metal atom, as confirmed by spin-flip STS measurements and DFT-SOC calculations. Upon planarization, the MAE from the triplet ground state of the Fe ion dropped down due to a reduction of the ligand field symmetry and subsequent charge redistribution. We anticipate that the large flexibility of porphyrin compounds to incorporate different TM atoms and linkers into the macrocycle, together with the synthetic protocols presented here to control inter- and intramolecular on-surface reactions, may open new opportunities for designing π -d 1D nanostructures with desirable magnetic properties.

5. METHODS

5.1. Experimental Section. Experiments were performed in a custom-designed LT-STM/AFM UHV system (Createc GmbH) at 4.2 K with a base pressure below 5×10^{-10} mbar. STM/nc-AFM images were taken with sharpened focus ion beam Pt/Ir tips. STM images were acquired in the constant current mode with a bias voltage applied to the sample. For the spectroscopic measurements, specific site dI/dV were taken by a conventional lock-in technique with a modulation of 0.5 mV at 937 Hz. For nc-AFM imaging, the tip was functionalized with a single CO molecule picked up from the bare metal substrate and operated in the frequency-modulation mode

(oscillated with a constant amplitude of 50 pm; resonant frequency ≈ 30 kHz; stiffness ≈ 1800 N/m). All nc-AFM images were acquired in a constant height mode with a bias voltage of 1 mV. All images were subject to a standard process using WSxM software.⁵²

The Au(111) substrate was prepared by repeated cycles of Ar⁺ sputtering (1 keV) and subsequent annealing. A molecular precursor (commercial from PorphyChem) was deposited by organic molecular-beam epitaxy from a tantalum pocket maintained at 625 K onto a clean Au(111) held at room temperature. When annealed to the desired temperature, the samples were transferred to the STM stage, which was maintained at 4.2 K.

5.2. Theoretical Calculations. DFT calculations^{53,54} were performed with the Perdew–Burke–Ernzerhof exchange and correlation functional,⁵⁵ projected augmented wave potentials representing atomic cores,^{56,57} and zero-damping DFT-D3 method of Grimme⁵⁸ to account for the dispersion corrections. The Hubbard $U - J = 4$ eV parameter⁵⁹ was applied for Fe. Occupations of the Fe 3d levels of freestanding molecules were re-examined by using non-local correlation functional optB86b + U .⁶⁰ The plane-wave basis set contained waves with kinetic energy lower than 500 eV. The Brillouin zone samplings were restricted to Γ point as the supercell dimensions were sufficiently large. Bond dissociation energies were computed by employing PBE0 hybrid functional^{54,55,61} (see also Sen et al.⁶²). The Au(111) surface was modeled using 7×7 supercells consisting of four Au layers, the bottom two layers of which were kept constrained in all structural relaxations. The vacuum layer of ~ 15 Å was applied along the off-planar direction to ward off spurious interactions with the periodic images. Structural optimizations were performed employing a quasi-Newton algorithm until the residual atomic forces were below 25 meV Å⁻¹. Simultaneously, the electronic and magnetic degrees of freedom were converged to an energy of less than 10^{-6} eV. MAEs were computed in the noncollinear mode following implementations of Hobbs et al.⁶¹ and Marsman and Hafner.⁶³ The adsorption energy E_{ad} of the BrFeDPP and 2BrFePP molecules on the Au(111) surface was calculated using the formula

$$E_{\text{ad}} = E_{\text{tot}} - E_{\text{slab}} - E_{\text{molecule}}$$

where E_{tot} represents the total energy of the entire surface-adsorbed system, E_{slab} is the total energy of the Au(111) slab, and E_{molecule} is the total energy of the gas-phase 2BrFeDPP or 2BrFePP. In this convention, negative adsorption energy means that the adsorption is energetically favorable, and lower adsorption energy denotes higher energetic stability of the surface-adsorbed system.

ASSOCIATED CONTENT

Supporting Information

The Supporting Information is available free of charge at <https://pubs.acs.org/doi/10.1021/acsami.1c04693>.

Optimized structures of 2BrFeTPP [and 2BrFePP on Au(111)]; nc-AFM constant height images simulated using a DFT-calculated FeDPP dimer structure; lateral manipulation of FeDPP molecular chains; statistical distribution of chain lengths upon annealing the sample up to 600 K; overview after annealing the molecule decorated sample to 550 K; overview upon sample annealing to temperatures higher than 600 K; dechlorination of 2BrFeDPP-Cl molecule; measurements of the onset of magnetic anisotropy using the first derivative of the dI/dV spectra; characterization of single FePP molecule; isosurface of the spin density calculated for the 2BrFeDPP/Au(111) system; simplified scheme of the occupation of Fe 3d levels of the freestanding 2BrFeDPP and 2BrFePP; and spin- and orbital-resolved PDOS on Fe and N of 2BrFeDPP supported on Au(111) (PDF)

AUTHOR INFORMATION

Corresponding Authors

Piotr Błoński – Regional Centre of Advanced Technologies and Material, Czech Advanced Technology and Research Institute (CATRIN), Palacký University Olomouc, 783 71 Olomouc, Czech Republic; orcid.org/0000-0002-7072-232X; Email: piotr.blonski@upol.cz

Bruno de la Torre – Regional Centre of Advanced Technologies and Material, Czech Advanced Technology and Research Institute (CATRIN), Palacký University Olomouc, 783 71 Olomouc, Czech Republic; Institute of Physics, The Czech Academy of Sciences, 162 00 Prague, Czech Republic; orcid.org/0000-0002-6462-6833; Email: bdelatorre@fzu.cz

Authors

Benjamin Mallada – Regional Centre of Advanced Technologies and Material, Czech Advanced Technology and Research Institute (CATRIN), Palacký University Olomouc, 783 71 Olomouc, Czech Republic; Institute of Physics, The Czech Academy of Sciences, 162 00 Prague, Czech Republic; orcid.org/0000-0002-8209-9977

Rostislav Langer – Regional Centre of Advanced Technologies and Material, Czech Advanced Technology and Research Institute (CATRIN), Palacký University Olomouc, 783 71 Olomouc, Czech Republic; Department of Physical Chemistry, Faculty of Science, Palacký University Olomouc, 78371 Olomouc, Czech Republic; orcid.org/0000-0003-1703-6707

Pavel Jelínek – Regional Centre of Advanced Technologies and Material, Czech Advanced Technology and Research Institute (CATRIN), Palacký University Olomouc, 783 71 Olomouc, Czech Republic; Institute of Physics, The Czech Academy of Sciences, 162 00 Prague, Czech Republic; orcid.org/0000-0002-5645-8542

Michal Otyepka – Regional Centre of Advanced Technologies and Material, Czech Advanced Technology and Research Institute (CATRIN), Palacký University Olomouc, 783 71 Olomouc, Czech Republic; IT4Innovations, Technical University of Ostrava, 708 00 Ostrava-Poruba, Czech Republic; orcid.org/0000-0002-1066-5677

Complete contact information is available at: <https://pubs.acs.org/10.1021/acsami.1c04693>

Notes

The authors declare no competing financial interest.

ACKNOWLEDGMENTS

B.T. dedicates this work to the memory of José María Gómez-Rodríguez. The authors gratefully acknowledge support of the Operational Programme for Research, Development and Education of the European Regional Development Fund (project no. CZ.02.1.01/0.0/0.0/16_019/0000754). B.M. acknowledges support from the Internal Student Grant Agency of the Palacký University in Olomouc, Czech Republic (IGA_PrF_2021_032). R.L. acknowledges support from the Internal Student Grant Agency of the Palacký University in Olomouc, Czech Republic (IGA_PrF_2021_031). P.J. acknowledges support from the Praemium Academie of the Academy of Science of the Czech Republic and GACR (project no. 20-13692X).

REFERENCES

- (1) Wolf, S. A. Spintronics: A Spin-Based Electronics Vision for the Future. *Science* **2001**, *294*, 1488–1495.
- (2) Žutić, I.; Fabian, J.; Das Sarma, S. Spintronics: Fundamentals and Applications. *Rev. Mod. Phys.* **2004**, *76*, 323–410.
- (3) Maslyuk, V. V.; Bagrets, A.; Meded, V.; Arnold, A.; Evers, F.; Brandbyge, M.; Bredow, T.; Mertig, I. Organometallic Benzene-Vanadium Wire: A One-Dimensional Half-Metallic Ferromagnet. *Phys. Rev. Lett.* **2006**, *97*, 097201.
- (4) Wang, L.; Cai, Z.; Wang, J.; Lu, J.; Luo, G.; Lai, L.; Zhou, J.; Qin, R.; Gao, Z.; Yu, D.; Li, G.; Mei, W. N.; Sanvito, S. Novel One-Dimensional Organometallic Half Metals: Vanadium-Cyclopentadienyl, Vanadium-Cyclopentadienyl-Benzene, and Vanadium-Anthracene Wires. *Nano Lett.* **2008**, *8*, 3640–3644.
- (5) Xiong, Z. H.; Wu, D.; Vally Vardeny, Z.; Shi, J. Giant Magnetoresistance in Organic Spin-Valves. *Nature* **2004**, *427*, 821–824.
- (6) Tsukagoshi, K.; Alphenaar, B. W.; Ago, H. Coherent Transport of Electron Spin in a Ferromagnetically Contacted Carbon Nanotube. *Nature* **1999**, *401*, 572–574.
- (7) Zhang, X.; Tian, Z.; Yang, S.-W.; Wang, J. Magnetic Manipulation and Half-Metal Prediction of One-Dimensional Bimetallic Organic Sandwich Molecular Wires [CpTM 1 CpTM 2] ∞ (TM 1 = Ti, Cr, Fe; TM 2 = Sc–Co). *J. Phys. Chem. C* **2011**, *115*, 2948–2953.
- (8) Xiang, H.; Yang, J.; Hou, J. G.; Zhu, Q. One-Dimensional Transition Metal–Benzene Sandwich Polymers: Possible Ideal Conductors for Spin Transport. *J. Am. Chem. Soc.* **2006**, *128*, 2310–2314.
- (9) Parida, P.; Kundu, A.; Pati, S. K. One-Dimensional Organometallic V–Anthracene Wire and Its B–N Analogue: Efficient Half-Metallic Spin Filters. *Phys. Chem. Chem. Phys.* **2010**, *12*, 6924.
- (10) Ma, Y.; Dai, Y.; Zhang, Z.; Yu, L.; Huang, B. Magnetic Properties of Phthalocyanine-Based Organometallic Nanowire. *Appl. Phys. Lett.* **2012**, *101*, 062405.
- (11) Santhini, V. M.; Stetsovych, O.; Ondráček, M.; Mendieta Moreno, J. I.; Mutombo, P.; Torre, B.; Švec, M.; Klívar, J.; Stará, I. G.; Vázquez, H.; Starý, I.; Jelinek, P. On-Surface Synthesis of Polyferrocenylene and its Single-Chain Conformational and Electrical Transport Properties. *Adv. Funct. Mater.* **2020**, *31*, 2006391.
- (12) Santhini, V. M.; Wäckerlin, C.; Cahlik, A.; Ondráček, M.; Pascal, S.; Matěj, A.; Stetsovych, O.; Mutombo, P.; Lazar, P.; Siri, O.; Jelinek, P. 1D Coordination π -d Conjugated Polymers with Distinct Structures Defined by the Choice of the Transition Metal: Towards a New Class of Antiaromatic Macrocycles. *Angew. Chem., Int. Ed.* **2021**, *60*, 439–445.
- (13) Telychko, M.; Su, J.; Gallardo, A.; Gu, Y.; Mendieta-Moreno, J. I.; Qi, D.; Tadich, A.; Song, S.; Lyu, P.; Qiu, Z.; Fang, H.; Koh, M. J.; Wu, J.; Jelinek, P.; Lu, J. Strain-Induced Isomerization in One-Dimensional Metal–Organic Chains. *Angew. Chem., Int. Ed.* **2019**, *58*, 18591–18597.
- (14) Kang, B. K.; Aratani, N.; Lim, J. K.; Kim, D.; Osuka, A.; Yoo, K.-H. Length and Temperature Dependence of Electrical Conduction through Dithiolated Porphyrin Arrays. *Chem. Phys. Lett.* **2005**, *412*, 303.
- (15) Tagami, K.; Tsukada, M.; Matsumoto, T.; Kawai, T. Electronic Transport Properties of Free-Base Tape-Porphyrin Molecular Wires Studied by Self-Consistent Tight-Binding Calculations. *Phys. Rev. B: Condens. Matter Mater. Phys.* **2003**, *67*, 245324.
- (16) Long, M.-Q.; Chen, K.-Q.; Wang, L.; Qing, W.; Zou, B. S.; Shuai, Z. Negative Differential Resistance Behaviors in Porphyrin Molecular Junctions Modulated with Side Groups. *Appl. Phys. Lett.* **2008**, *92*, 243303.
- (17) Ribeiro, F. J.; Lu, W.; Bernholc, J. Doping-Dependent Negative Differential Resistance in Hybrid Organic/Inorganic Si–Porphyrin–Si Junctions. *ACS Nano* **2008**, *2*, 1517–1522.
- (18) Holten, D.; Bocian, D. F.; Lindsey, J. S. Probing Electronic Communication in Covalently Linked Multiporphyrin Arrays. A Guide to the Rational Design of Molecular Photonic Devices. *Acc. Chem. Res.* **2002**, *35*, 57–69.
- (19) Yamaguchi, Y. Time-Dependent Density Functional Calculations of Fully π -Conjugated Zinc Oligoporphyrins. *J. Chem. Phys.* **2002**, *117*, 9688–9694.
- (20) Chen, Y.; Prociuk, A.; Perrine, T.; Dunitz, B. D. Spin-Dependent Electronic Transport through a Porphyrin Ring Ligating an Fe(II) Atom: An Ab Initio Study. *Phys. Rev. B: Condens. Matter Mater. Phys.* **2006**, *74*, 245320.
- (21) Abel, M.; Clair, S.; Ourdjini, O.; Mossoyan, M.; Porte, L. Single Layer of Polymeric Fe-Phthalocyanine: An Organometallic Sheet on Metal and Thin Insulating Film. *J. Am. Chem. Soc.* **2011**, *133*, 1203–1205.
- (22) Zhou, J.; Sun, Q. Magnetism of Phthalocyanine-Based Organometallic Single Porous Sheet. *J. Am. Chem. Soc.* **2011**, *133*, 15113–15119.
- (23) Carlin, R. L. Paramagnetism: Zero-Field Splittings. *Magnetochemistry*; Springer-Verlag: Berlin, 1986.
- (24) Getzlaff, M. Magnetic Anisotropy Effects. *Fundamentals of Magnetism*; Springer-Verlag: Berlin, 2008.
- (25) Auwärter, W.; Ćija, D.; Klappenberger, F.; Barth, J. V. Porphyrins at Interfaces. *Nat. Chem.* **2015**, *7*, 105.
- (26) Marbach, H. Surface-Mediated in Situ Metalation of Porphyrins at the Solid–Vacuum Interface. *Acc. Chem. Res.* **2015**, *48*, 2649–2658.
- (27) Gottfried, J. M. Surface Chemistry of Porphyrins and Phthalocyanines. *Surf. Sci. Rep.* **2015**, *70*, 259–379.
- (28) Jurow, M.; Schuckman, A. E.; Batteas, J. D.; Drain, C. M. Porphyrins as Molecular Electronic Components of Functional Devices. *Coord. Chem. Rev.* **2010**, *254*, 2297–2310.
- (29) Tanaka, T.; Osuka, A. Conjugated Porphyrin Arrays: Synthesis, Properties and Applications for Functional Materials. *Chem. Soc. Rev.* **2015**, *44*, 943–969.
- (30) Judd, C. J.; Nizovtsev, A. S.; Plougmann, R.; Kondratuk, D. V.; Anderson, H. L.; Besley, E.; Saywell, A. Molecular Quantum Rings Formed from a π -Conjugated Macrocyclic. *Phys. Rev. Lett.* **2020**, *125*, 206803.
- (31) Svatek, S. A.; Perdigo, L. M. A.; Stannard, A.; Wieland, M. B.; Kondratuk, D. V.; Anderson, H. L.; O’Shea, J. N.; Beton, P. H. Mechanical Stiffening of Porphyrin Nanorings through Supramolecular Columnar Stacking. *Nano Lett.* **2013**, *13*, 3391–3395.
- (32) Saywell, A.; Browning, A. S.; Rahe, P.; Anderson, H. L.; Beton, P. H. Organisation and Ordering of 1D Porphyrin Polymers Synthesised by On-Surface Glaser Coupling. *Chem. Commun.* **2016**, *52*, 10342–10345.
- (33) Tsuda, A. Fully Conjugated Porphyrin Tapes with Electronic Absorption Bands That Reach into Infrared. *Science* **2001**, *293*, 79–82.
- (34) Grill, L.; Hecht, S. Covalent On-Surface Polymerization. *Nat. Chem.* **2020**, *12*, 115–130.
- (35) Jelinek, P. High Resolution SPM Imaging of Organic Molecules with Functionalized Tips. *J. Phys.: Condens. Matter* **2017**, *29*, 343002.
- (36) Iwamura, H.; Koga, N. Studies of Organic Di-, Oligo-, and Polyradicals by Means of Their Bulk Magnetic Properties. *Acc. Chem. Res.* **1993**, *26*, 346–351.
- (37) Ung, V. A.; Cargill Thompson, A. M. W.; Bardwell, D. A.; Gatteschi, D.; Jeffery, J. C.; McCleverty, J. A.; Totti, F.; Ward, M. D. Roles of Bridging Ligand Topology and Conformation in Controlling Exchange Interactions between Paramagnetic Molybdenum Fragments in Dinuclear and Trinuclear Complexes. *Inorg. Chem.* **1997**, *36*, 3447–3454.
- (38) Pardo, E.; Carrasco, R.; Ruiz-García, R.; Julve, M.; Lloret, F.; Muñoz, M. C.; Journaux, Y.; Ruiz, E.; Cano, J. Structure and Magnetism of Dinuclear Copper(II) Metallacyclophanes with Oligoacenebis(Oxamate) Bridging Ligands: Theoretical Predictions on Wirelike Magnetic Coupling. *J. Am. Chem. Soc.* **2008**, *130*, 576–585.
- (39) Ferrando-Soria, J.; Castellano, M.; Yuste, C.; Lloret, F.; Julve, M.; Fabelo, O.; Ruiz-Pérez, C.; Stiriba, S.-E.; Ruiz-García, R.; Cano, J. Long-Distance Magnetic Coupling in Dinuclear Copper(II) Com-

- plexes with Oligo-Para-Phenylenediamine Bridging Ligands. *Inorg. Chim. Acta* **2010**, *363*, 1666–1678.
- (40) Castellano, M.; Fortea-Pérez, F. R.; Stiriba, S.-E.; Julve, M.; Lloret, F.; Armentano, D.; De Munno, G.; Ruiz-García, R.; Cano, J. Very Long-Distance Magnetic Coupling in a Dicationic(II) Metal-lacyclophane with Extended π -Conjugated Diphenylethyne Bridges. *Inorg. Chem.* **2011**, *50*, 11279–11281.
- (41) Gopakumar, T. G.; Tang, H.; Morillo, J.; Berndt, R. Transfer of Cl Ligands between Adsorbed Iron Tetrphenylporphyrin Molecules. *J. Am. Chem. Soc.* **2012**, *134*, 11844.
- (42) Kaiser, K.; Gross, L.; Schulz, F. A Single-Molecule Chemical Reaction Studied by High-Resolution Atomic Force Microscopy and Scanning Tunneling Microscopy Induced Light Emission. *ACS Nano* **2019**, *13*, 6947–6954.
- (43) Chutora, T.; de la Torre, B.; Mutombo, P.; Hellerstedt, J.; Kopeček, J.; Jelínek, P.; Švec, M. Nitrous Oxide as an Effective AFM Tip Functionalization: A Comparative Study. *Beilstein J. Nanotechnol.* **2019**, *10*, 315–321.
- (44) Doležal, J.; Merino, P.; Redondo, J.; Ondič, L.; Cahlik, A.; Švec, M. Charge Carrier Injection Electroluminescence with CO-Functionalized Tips on Single Molecular Emitters. *Nano Lett.* **2019**, *19*, 8605–8611.
- (45) Heinrich, A. J.; Gupta, J. A.; Lutz, C. P.; Eigler, D. M. Single-Atom Spin-Flip Spectroscopy. *Science* **2004**, *306*, 466.
- (46) Madhavan, V. Tunneling into a Single Magnetic Atom: Spectroscopic Evidence of the Kondo Resonance. *Science* **1998**, *280*, 567–569.
- (47) Ternes, M. Spin Excitations and Correlations in Scanning Tunneling Spectroscopy. *New J. Phys.* **2015**, *17*, 063016.
- (48) Rubio-Verdú, C.; Sarasola, A.; Choi, D.-J.; Majzik, Z.; Ebeling, R.; Calvo, M. R.; Ugeda, M. M.; Garcia-Lekue, A.; Sánchez-Portal, D.; Pascual, J. I. Orbital-Selective Spin Excitation of a Magnetic Porphyrin. *Commun. Phys.* **2018**, *1*, 15.
- (49) Li, J.; Merino-Díez, N.; Carbonell-Sanromà, E.; Vilas-Varela, M.; De Oteyza, D. G.; Peña, D.; Corso, M.; Pascual, J. I. Survival of Spin State in Magnetic Porphyrins Contacted by Graphene Nanoribbons. *Sci. Adv.* **2018**, *4*, No. eaq0582.
- (50) Tsukahara, N.; Noto, K.-i.; Ohara, M.; Shiraki, S.; Takagi, N.; Takata, Y.; Miyawaki, J.; Taguchi, M.; Chainani, A.; Shin, S.; Kawai, M. Adsorption-Induced Switching of Magnetic Anisotropy in a Single Iron(II) Phthalocyanine Molecule on an Oxidized Cu(110) Surface. *Phys. Rev. Lett.* **2009**, *102*, 167203.
- (51) Błoński, P.; Hafner, J. Density-Functional Theory of the Magnetic Anisotropy of Nanostructures: An Assessment of Different Approximations. *J. Phys.: Condens. Matter* **2009**, *21*, 426001.
- (52) Horcas, I.; Fernández, R.; Gómez-Rodríguez, J. M.; Colchero, J.; Gómez-Herrero, J.; Baro, A. M. WSXM: A Software for Scanning Probe Microscopy and a Tool for Nanotechnology. *Rev. Sci. Instrum.* **2007**, *78*, 013705.
- (53) Kresse, G.; Hafner, J. Ab Initio Molecular Dynamics for Liquid Metals. *Phys. Rev. B: Condens. Matter Mater. Phys.* **1993**, *47*, 558–561.
- (54) Kresse, G.; Furthmüller, J. Efficiency of Ab-Initio Total Energy Calculations for Metals and Semiconductors Using a Plane-Wave Basis Set. *Comput. Mater. Sci.* **1996**, *6*, 15–50.
- (55) Perdew, J. P.; Burke, K.; Ernzerhof, M. Generalized Gradient Approximation Made Simple. *Phys. Rev. Lett.* **1996**, *77*, 3865–3868.
- (56) Blöchl, P. E. Projector Augmented-Wave Method. *Phys. Rev. B: Condens. Matter Mater. Phys.* **1994**, *50*, 17953.
- (57) Kresse, G.; Joubert, D. From Ultrasoft Pseudopotentials to the Projector Augmented-Wave Method. *Phys. Rev. B: Condens. Matter Mater. Phys.* **1999**, *59*, 1758–1775.
- (58) Grimme, S.; Antony, J.; Ehrlich, S.; Krieg, H. A Consistent and Accurate Ab Initio Parametrization of Density Functional Dispersion Correction (DFT-D) for the 94 Elements H-Pu. *J. Chem. Phys.* **2010**, *132*, 154104.
- (59) Dudarev, S. L.; Botton, G. A.; Savrasov, S. Y.; Humphreys, C. J.; Sutton, A. P. Electron-Energy-Loss Spectra and the Structural Stability of Nickel Oxide: An LSDA+U Study. *Phys. Rev. B: Condens. Matter Mater. Phys.* **1998**, *57*, 1505–1509.
- (60) Klimeš, J.; Bowler, D. R.; Michaelides, A. Van Der Waals Density Functionals Applied to Solids. *Phys. Rev. B: Condens. Matter Mater. Phys.* **2011**, *83*, 195131.
- (61) Hobbs, D.; Kresse, G.; Hafner, J. Fully Unconstrained Noncollinear Magnetism within the Projector Augmented-Wave Method. *Phys. Rev. B: Condens. Matter Mater. Phys.* **2000**, *62*, 11556–11570.
- (62) Sen, D.; Błoński, P.; Torre, B. d. l.; Jelínek, P.; Otyepka, M. Thermally Induced Intra-Molecular Transformation and Metalation of Free-Base Porphyrin on Au(111) Surface Steered by Surface Confinement and Ad-Atoms. *Nanoscale Adv.* **2020**, *2*, 2986.
- (63) Marsman, M.; Hafner, J. Broken Symmetries in the Crystalline and Magnetic Structures of γ -Iron. *Phys. Rev. B: Condens. Matter Mater. Phys.* **2002**, *66*, 224409.

3.3 Characterization of defects in 1D-anthracene conjugated polymers

3.3.1 Introduction

Recently, on-surface synthesis has emerged as a new protocol for designing nanomaterials with atomic precision and customized electronic properties. This bottom-up approach has been shown to produce atomically-precise large conjugated polymers under ultra-high vacuum (UHV) conditions, not accessible in solution chemistry, with examples including the synthesis of ethynylene-bridged polymers derived from anthracene[62], pentacene and bisanthene[44, 45]. These one-dimensional polymers exhibit two resonance forms (see Fig. 3.12): either fully aromatic acenes with ethynylene bridges or quinoid acenes with cumulene bridges. The ground state is a combination of both forms, and the dominant resonance structure depends on the interplay between repulsive electron-electron interaction and electron-phonon coupling[44].

One of the ways of affecting the electronic properties of these polymers is by the introduction of atomic-scale defects. In the case of anthracene wires as the ones described in Fig. 3.12, defects can alter the electronic conjugation across the polymer structure, resulting in reduced electron mobility, changing the intrinsic band structure (see Fig. 3.12-c) or leading to the rearrangement of atoms and the formation of open-shell configurations with nontrivial π -magnetism. From this point of view, understanding the engineering of defects can provide deep insight into the synthetic limitations of π -conjugated polymers. In the present section, it will be shown the consequences of introducing on-purpose defects on anthracene ethynylene bridged polymers by thermal annealing.

The initial step the is deposition of the molecular precursor 11,11,12,12-tetrabromoanthracene(4BrAn) onto a clean Au(111) surface,carried out using organic molec-

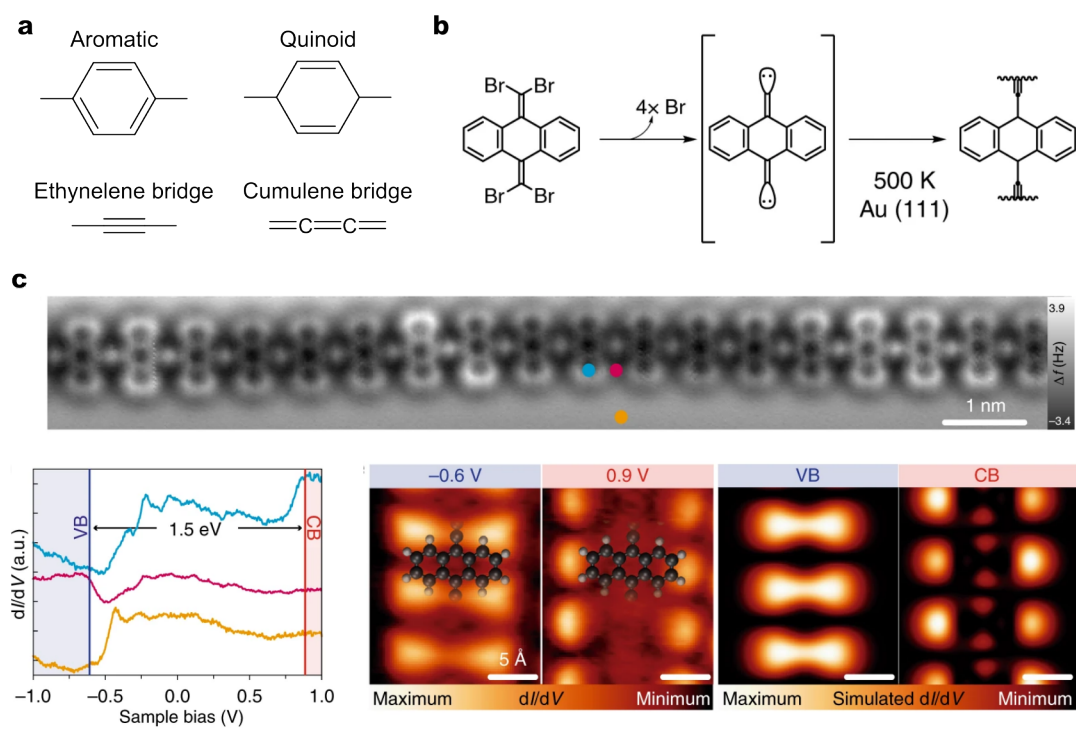


Figure 3.12: a, Aromatic and quinoid structures. b, The synthesis of anthracene wires. c, (Top) Constant height nc-AFM image of an anthracene wire on Au(111). (left) Experimental determination of E_{gap} with STS acquired at the positions depicted by the coloured dots in the AFM image. (right) Constant current dI/dV maps acquired at the approximate energies of the valence band (VB) and conducting band (CB) with the corresponding simulated maps.

ular beam epitaxy with a tantalum pocket maintained at 370 K. The next step is the annealing of the sample at 500 K for 30 minutes in UHV, for promoting the synthesis of ethynylene-bridged anthracene polymers. From this pristine wires, the introduction of defects is achieved by heating up the sample. For instance, annealing the surface at 500 K results in distorted molecular wires with a significantly higher density of structural defects (Fig. 3.13). Statistical analysis reveals a clear trend between defect density and annealing temperature, with a drastic increase in intramolecular defects (i.e. between monomers) observed at 500 K. Subsequent annealing up to 700 K introduces intermolecular defects (i.e. between polymers) into the anthracene wires, usually in the form of laterally fused chains (Fig. 3.14).

In-plane joints or kinks between pristine ethynylene-bridged anthracene segments with a measurable angle primarily ranging from 60° to 80° were observed in the molecular wires. These joints were later classified as type A and B defects, as indicated by white arrows in Fig. 3.13-b and c. The statistical analysis (see Fig. 3.13-d) revealed that these defects constituted the majority compared to those maintaining polymer linearity (type C) or exhibiting slight bending (type D). These defects can be rationalized in terms of the incorporation of one extra C atom (such as in type A), the polymer diffusion in the surface at high temperatures, but also the relative stiffness of the ethynylene bridge that promotes mostly reactions in the longitudinal direction as has been explained elsewhere[44]. The effect of these defects on the electronic structure has different degrees of impact, for example, type A disrupts locally the band structure of the wire, while defect type B does not contribute to the perturbation of the polymer[63]. The effect of these molecular rearrangements can be better observed by examining the effect of the number of closed rings in the most dominant defects.

Type A defects consist of two six-membered rings and one five-membered ring. Non-AFM images (Fig. 3.15) reveal a bright spot in the center of the linker in neighboring

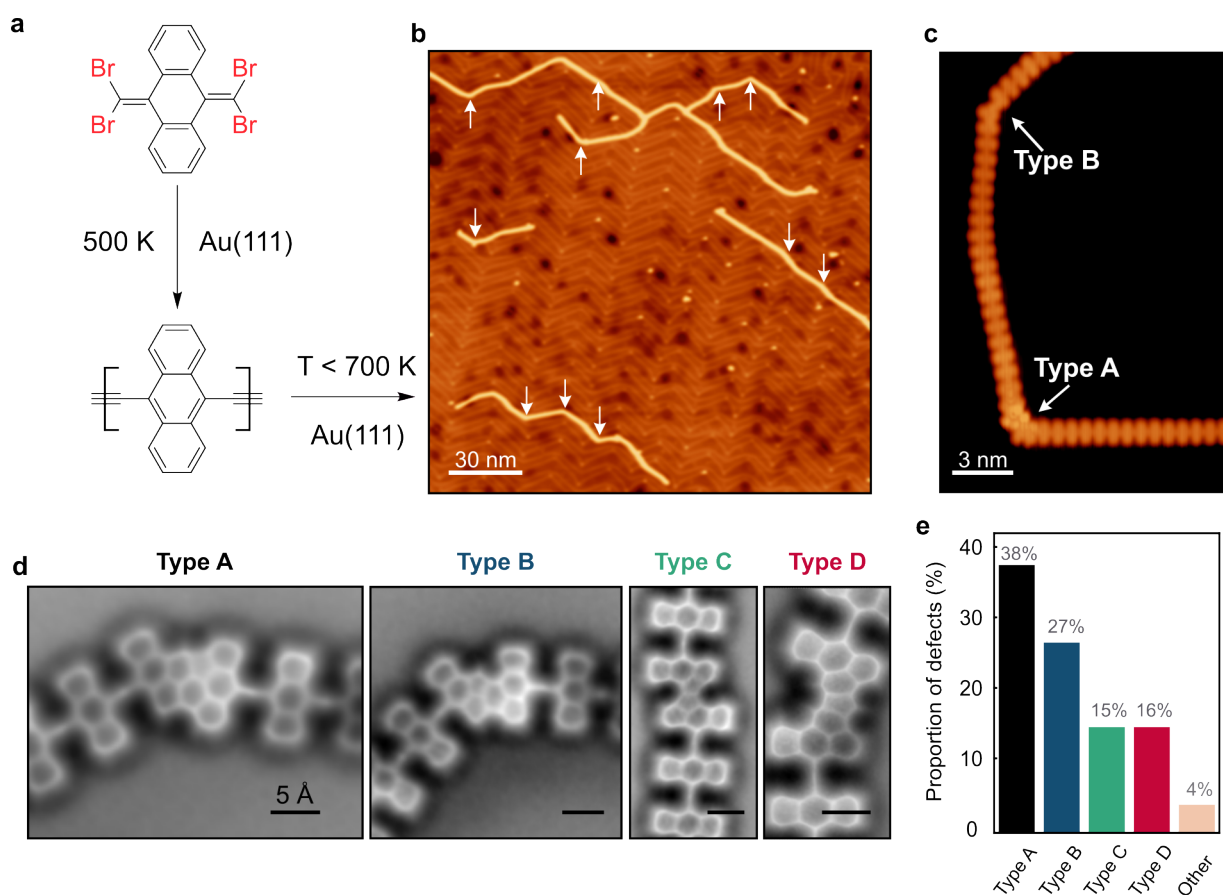


Figure 3.13: a, Scheme of the reaction sequence of 4BrAn wires and the incorporation of defects. b, STM topography ($V_{Bias} = 200$ mV, $I_{set} = 5$ pA) showing the defects as kinks in the wires. c) Detail ($V_{Bias} = 5$ mV, $I_{set} = 10$ pA) of two kinks incorporating the most common defects type A and B. d) Constant height nc-AFM with CO-tip (Laplacian filtered) images of the most common defects. e) Histogram of relative abundance of the most common defects.

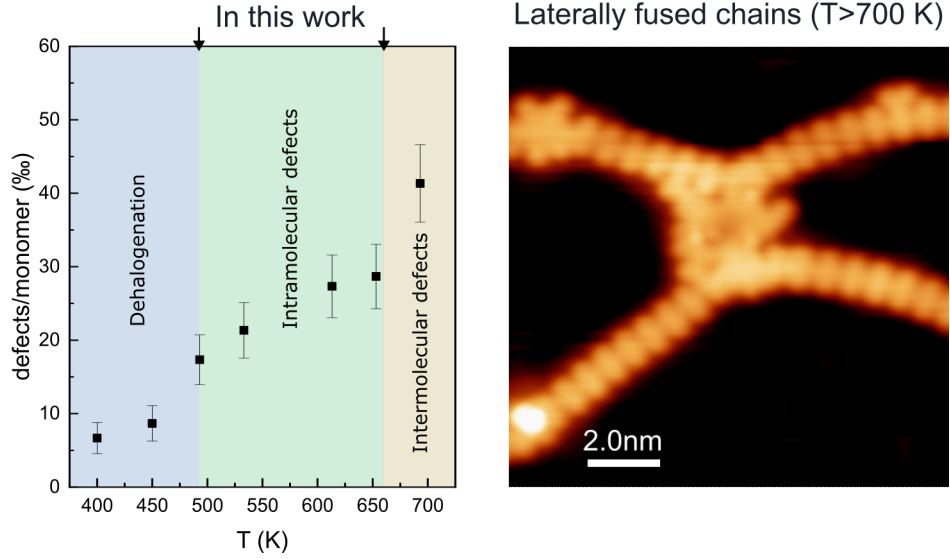


Figure 3.14: (Left) Proportion of defects as a function of temperature. (Right) An example of fused polymers at high temperatures.

monomers, indicating the ethynylene character of these linkers. STM images at low bias voltage show enhanced LDOS near the Fermi level around type A defects. Spectroscopic dI/dV measurements demonstrate the presence of a sharp zero-bias peak (ZBP) at the junction and adjacent anthracene monomers, attributed to a Kondo resonance resulting from the screening of a magnetic moment (unpaired electron) by conduction electrons in the Au(111). The width of the ZBP increases with temperature, exhibiting characteristic behavior of a weakly coupled Kondo system[6]. The existence of an unpaired spin density in the defect is confirmed by spin-polarized density functional theory (DFT) calculations. Type B defects, on the other hand, involve the constitution of six- and five-membered rings at the junction. Nc-AFM images and dI/dV spectra of type B defects (Fig. 3.16) show featureless characteristics, indicating the absence of extra charge localization at the junction. DFT calculations suggest that type B defects adopt a closed-shell structure, possibly with cumulene-like bridges maximizing the number of disjointed Clar's π -sextets.

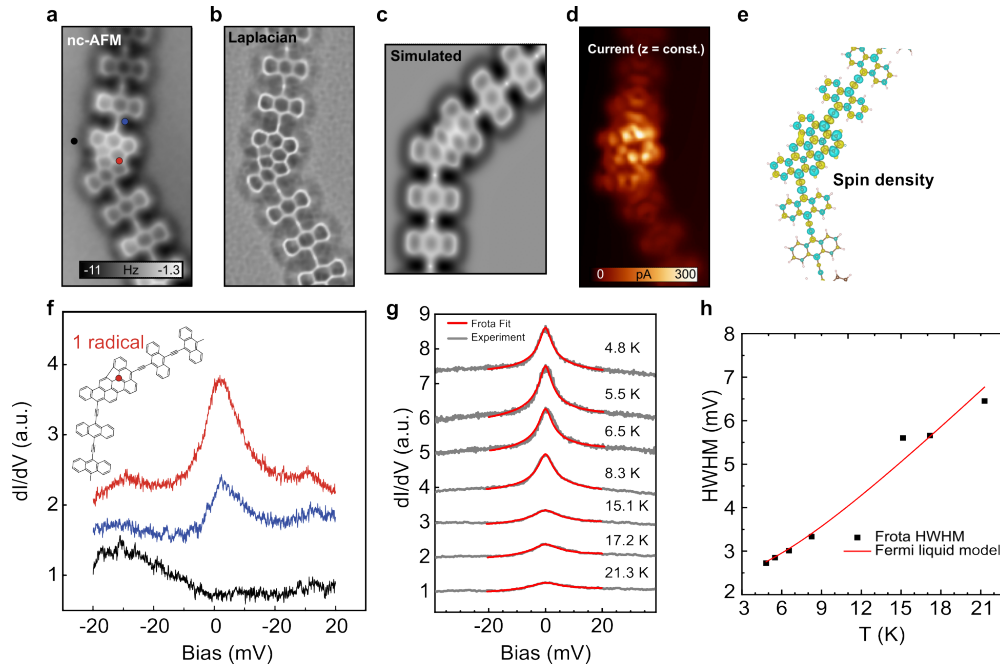


Figure 3.15: a) Constant height nc-AFM with CO-tip imaging of the type A defect showing the presence of the characteristic enhanced electron density of the triple bonds as bright dots. b) Laplace filtered nc-AFM image. c) Simulated AFM image of the defect with the probe particle model. e) Spin density calculated by DFT. f) STS spectroscopy showing a Zero Bias Peak on the defect site. In the inset, conjugation of the anthracene-ethynylene polymer with type A defect. d). g) Temperature evolution of the Zero Bias Peak (gray line) fit with a Frota function (red line) obtained on the defect site. h) Half width at the half maximum (HWHM) values extracted from the Fano fit of the Zero Bias Peak as a function of the temperature.

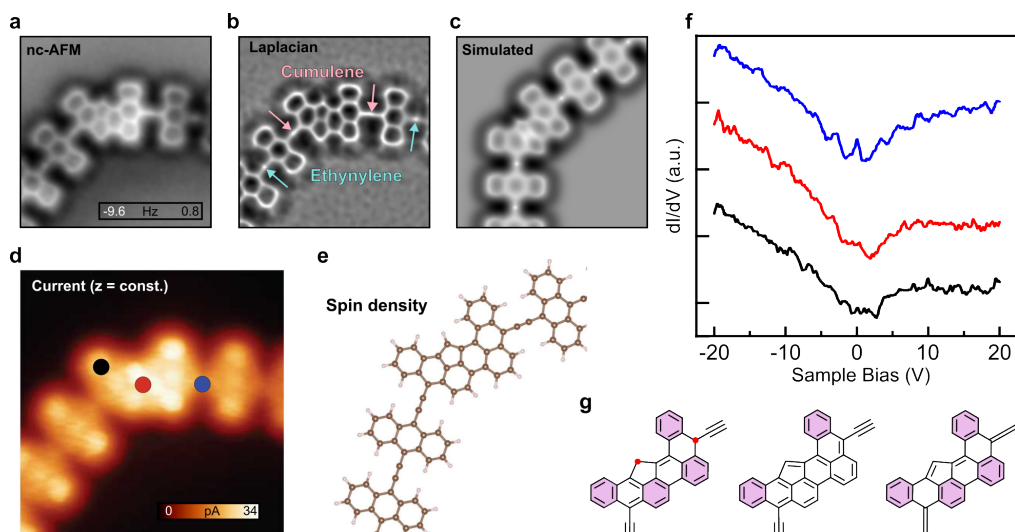


Figure 3.16: a-b) AFM Constant height current images with CO-functionalized tip of the type B defect. b) Laplace filtered nc-AFM image showing the transition from cumulene linkers in the vicinity of the defect to the ethynylene bridges of the unaltered polymers. c) Simulated AFM image with probe particle of the type B defect. d) High resolution constant height current image of the defect with the positions of the spectroscopies. e) Spin density calculated by DFT. f) STS spectroscopy near Fermi for selected regions (red, blue and black dots) of the defective polymer. e) Conjugation models for the type B defect.

The formation of these defects could be controlled hypothetically by an external source of atomic carbon atoms during the polymerization reaction. Transforming type B defects into type A defects can be achieved through a hypothetical experiment involving the introduction of atomic carbon atoms in an ultra-high vacuum. While a detailed understanding of the defect formation mechanism requires complex quantum molecular mechanics calculations, our findings shed light on the role of these defects in the conjugation of anthracene-ethynylene polymers on Au(111).

3.3.2 Author's contribution to the published work

In this work, I prepared and conducted the polymeric reactions and performed the experimental acquisition of STM and nc-AFM. I also performed the statistical analysis of the defects and the analysis of the STS spectra. I also discussed both experimental and

simulated findings, began drafting the manuscript, prepared the figures, and participated in the discussion and interpretation of the data with my collaborators.

Resolving Atomic-Scale Defects in Conjugated Polymers On-Surfaces

Benjamín Mallada,^[a, b, c] Qifan Chen,^[c] Taras Chutora,^[a, e] Ana Sánchez-Grande,^[d] Borja Cirera,^[d] José Santos,^[d] Nazario Martín,^[d] David Ecija,^[d] Pavel Jelínek,^[a, c] and Bruno de la Torre*^[a, c]

Abstract: Atomic scale defects significantly affect the mechanical, electronic, and optical properties of π -conjugated polymers. Here, isolated atomic-scale defects are deliberately introduced into a prototypical anthracene-ethynylene π -conjugated polymer, and its local density of states is carefully examined on the atomic scale to show how individual defects modify the inherent electronic and magnetic properties of this one-dimensional systems. Scanning tunneling and atomic force microscopy experiments, supplemented with density functional theory calculations, reveal the existence of a sharp

electronic resonance at the Fermi energy around certain defects, which is associated with the formation of a local magnetic moment accompanied by substantial mitigation of the mobility of charge carriers. While defects in traditionally synthesized polymers lead to arbitrary conformations, the presented results clearly reflect the preferential formation of low dimensional defects at specific polymer sites, which may introduce the possibility of engineering macroscopic defects in surface-synthesized conjugated polymers.

Introduction

The synthesis of conjugated polymers aims to improve their beneficial properties, such as high charge carrier mobility, unique light absorption, and emission characteristics,^[1] which is useful for different technological applications, including light-emitting devices, solar cells, organic field-effect transistors, photocatalysis, and biosensors.^[2,3] As a result of their strong structure-to-property correlations, defects play a central role in the physical properties of conjugated polymers. For example, it has been observed that structural and chemical defects disturb electronic conjugation throughout the polymer structure by

reshaping the π electron lattice, resulting in: (i) potential confinement of electronic excitations on small subunits that act as chromophores and, (ii) significantly reduced electron mobility.^[4–9] Although the role played by these defects has been extensively addressed by theory,^[10–14] reported experimental data refer to statistical properties of the entire heterogeneous collection of defects generated in the polymerization process.^[8,12,15–20]

Recently, on-surface synthesis^[21–24] has emerged as a new synthetic protocol for designing nanomaterials with atomic precision and customized electronic properties. Taking advantage of the two-dimensional confinement of a surface, polymerization reactions can lead to the formation of unprecedented large polymers under ultra-high vacuum (UHV) conditions, not accessible in solution chemistry. Particular attention has been paid to π -conjugated materials,^[25] illustrated by the bottom-up synthesis of graphene nanoribbons.^[24,26] Lately, the approach has shown the potential to design well-defined π -conjugated materials with exotic electronic properties, such as non-trivial band topology^[27–30] or π -magnetism.^[31] Furthermore, on-surface synthesis allows the characterization of these systems by combining surface science techniques such as scanning tunneling microscopy (STM) and high-resolution atomic force microscopy in a non-contact (nc-AFM) regime. This blend of techniques has the ability to resolve not only the topographic shape but the backbone of individual molecules^[32] allowing the identification of the reaction products for each on-surface reaction step^[33–35] together with their microscopic electronic structure via scanning tunneling spectroscopy (STS).

Such nanostructures are often subject to comprise atomic-scale defects arising from the synthesis process.^[36,37] Importantly, defects can tailor intrinsic characteristics of the π -conjugated material by atomic rearrangement, resulting in stabilized open-shell configurations that feature nontrivial π -


[a] B. Mallada, Dr. T. Chutora, Dr. P. Jelínek, Dr. B. de la Torre
Regional Centre of Advanced Technologies and Materials
Czech Advanced Technology and Research Institute (CATRIN)
Palacký University Olomouc
78371 Olomouc (Czech Republic)
E-mail: bruno.de@upol.cz

[b] B. Mallada
Department of Physical Chemistry,
Faculty of Science
Palacký University
78371 Olomouc (Czech Republic)

[c] B. Mallada, Q. Chen, Dr. P. Jelínek, Dr. B. de la Torre
Institute of Physics,
Academy of Sciences of the Czech Republic
Prague (Czech Republic)

[d] Dr. A. Sánchez-Grande, Dr. B. Cirera, Dr. J. Santos, Prof. N. Martín, Dr. D. Ecija
IMDEA Nanociencia, Ciudad Universitaria de Cantoblanco
Madrid (Spain)

[e] Dr. T. Chutora
Current address: Department of Physics, University of Alberta
Edmonton, Alberta,
T6G 2J1 (Canada)

 Supporting information for this article is available on the WWW under
<https://doi.org/10.1002/chem.202200944>

magnetism.^[38–40] Even though defect engineering was a striking success story in inorganic semiconductors,^[41,42] both for their mechanical and electronic properties, and also applied to organic hard materials, defect engineering has rarely been used in the design of soft matter so far. Thus, for further development of protocols for understanding and engineering defects in such structures, a detailed characterization of the electronic and geometric structure of low-dimensional defects in π -conjugated polymers is demanded.

In the following, we have deliberately introduced atomic-scale defects in on-surface synthesized polymers and deeply investigated their nature by using STM/STS, nc-AFM, and density functional theory (DFT). We study the prototypical anthracene-ethynylene π -conjugated polymer on Au(111) following our recently developed synthetic protocol.^[29,43] Then, we induce formation of atomic-scale defects that can be harnessed to a given extent by increasing the annealing temperature during reaction processes. In particular, we identified statistically more abundant defects consisting of both atomic rearrangements and incorporation of atomic species and examined their impact on the electronic structure of the

polymer. Interestingly, we show that while some conformational defects hardly affect the intrinsic electronic structure of the polymer, certain atomically defined defect motifs can harbor localized spins at specific sites, which is revealed by the presence of a Kondo resonance^[44,45] in the STS spectroscopy.

Results

Synthesis of defects-containing ethynylene-bridged anthracene polymers

The one-dimensional conjugated nanostructure, and its low-dimensional defects studied here, are synthesized directly on the Au(111) surface by thermal annealing after molecular deposition in ultra-high vacuum. Deposition of the molecular precursor 11,11,12,12-tetrabromoanthra-*p*-quinodimethane (hereafter 4BrAn, see the sketch in Figure 1a) on a clean Au(111) surface and subsequent annealing at 500 K for 30 minutes in UHV, results in the formation of a low-bandgap (≈ 1.5 eV) ethynylene-bridged anthracene polymer (see Figure 1b, and ref.

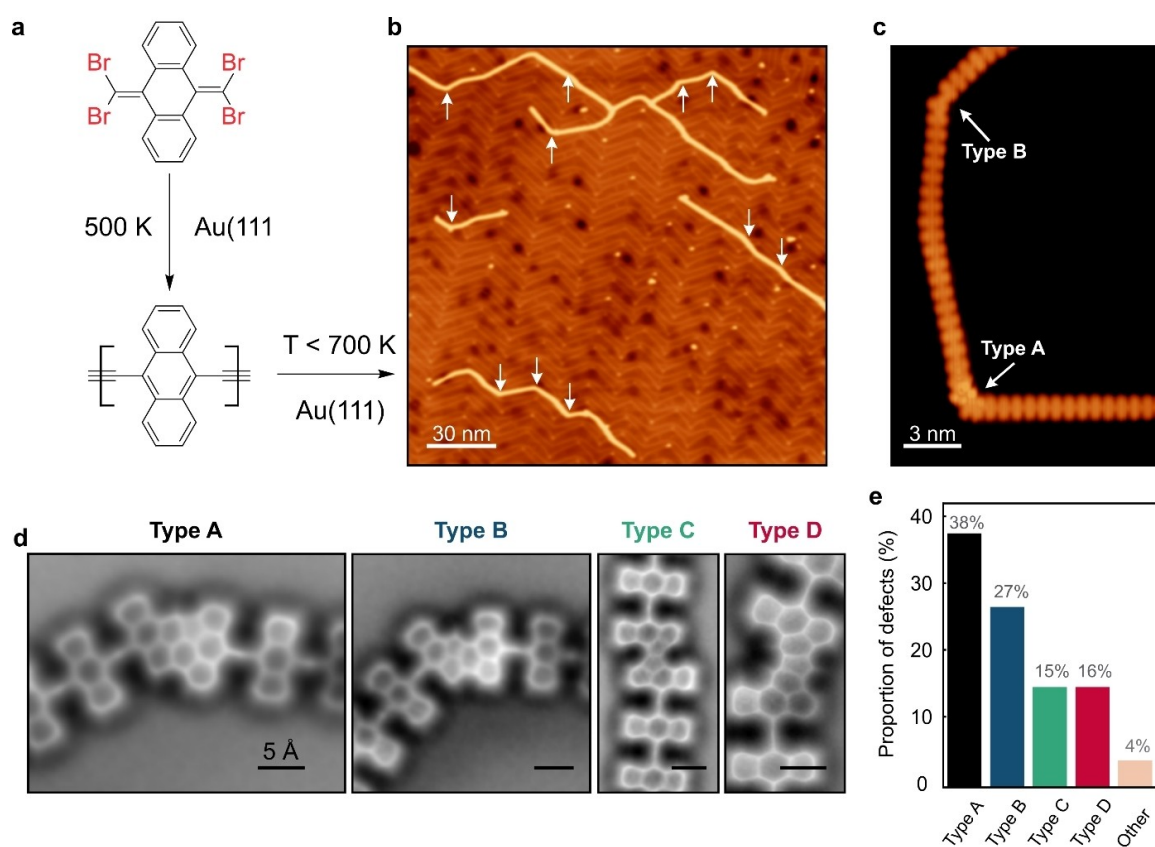


Figure 1. Low-dimensional structural defects in anthracene-ethynylene polymer on Au(111). a) Scheme of the reaction sequence of 4BrAn (11,11,12,12-tetrabromoanthra-*p*-quinodimethane) precursor after being deposited on Au(111) and annealed. b) Topographic overview ($I_t = 5$ pA, $V_{\text{Bias}} = 200$ mV) of the polymer-decorated sample upon annealing below 700 K. c) Close-up topography of a polymer containing kinks ($I_t = 10$ pA, $V_{\text{Bias}} = 5$ mV). d) nc-AFM (Laplacian filtered) elucidation and statistics of the most found low-dimensional defects. e) Histogram of relative abundance of defects (77 defects were counted in total).

[43] for a detailed characterization of its pristine properties). Defects in such polymers are rare and pristine polymeric segments up to hundreds of nanometers can be found routinely.

Subsequent annealing of the surface leads to distorted molecular wires with a much greater number of structural defects. Statistical analysis of the defect density at different temperatures produces a clear trend with annealing temperature (Figure S1). The number of intermolecular defects drastically increases upon annealing the sample at 500 K, indicating the onset of the defect formation. Further annealing up to 700 K gradually introduces intramolecular defects into the polymers. The overview and detailed STM topographies upon annealing <700 K, shown in Figures 1b, c, display the on-surface synthesized ethynylene-bridged anthracene wires as a result of successful polymerization. In addition, the molecular wires comprise in-plane (plane of the surface) joints between pristine ethynylene-bridged anthracene segments with a measurable angle mainly in a narrow range from 60° to 80°, which will be later identified as type A and B defects (marked by white arrows in Figures 1b, c). These defects are the majority over those that preserve the linearity of the polymer (type C, see below) and those featuring a small bending angle (type D, see below) as manifested in the statistical analysis (see Figure 1d, e). Recently, we reported that at the polymerization temperature ($T > 500$ K), molecular vibrations are triggered both in the monomer unit and the linker,^[46] inducing carbon rearrangements.^[47] In such pristine ethynylene-bridged anthracene-polymers, the relative longitudinal stiffness of the ethynylene bridge promotes bending of the polymer over longitudinal reactions, while preserving the chemical structure of the monomer, unlike polymers with cumulene-like bridges.^[46] Thus, the featured kinks in anthracene-ethynylene polymers can be rationalized by such structural bending in the linker moiety together with increased diffusion of the polymer on the surface at elevated temperatures, facilitating the backbone realignment. In addition, as we will explain below, for type A defect, it is necessary the incorporation of an extra single atom.

Post-annealing of the substrate to higher temperatures ($T > 700$ K) results in a sample with predominantly lateral bonds between polymers due to the activation of the C–H bonds at the periphery of the monomers and the high lateral mobility of the species on the surface (see Figure S2) which largely increases the density of defects (Figure S1).

Structural characterization

We attained structural characteristics of more prominent defects at the atomic level employing non-contact AFM measurements with a CO-functionalized tip^[32] (Figure 1d and Figure S3). Statistic of defects observed in several experimental sessions, reveals that two distinct types of low-dimension structural defects (labeled A and B in Figure 1c,d) are the most frequently encountered in our experiments for all investigated annealing temperatures. Thus, below, we focus our discussion on a detailed comparison of polymers with type A and B defects

that are by far the most representative ($\approx 38\%$ and $\approx 27\%$ of the total number of defects, respectively). As illustrated by the high-resolution nc-AFM image (see Figure 1d), the type A defect consists of two hexagons and a single pentagon formed at the junction between two adjacent anthracene monomers instead of the ethynylene bridge found in pristine polymers. On the other hand, type B (see Figure 1d) consist of both six- and five-membered rings at the junction.

Type B defect can be rationalized by a bare frustrated transformation reaction from ethynylene- towards pentalene-bridged polymer, whereas the incorporation of an additional atom to the polymeric linker is required to account for the formation of defect type A. nc-AFM images allow to identify heteroatoms in the chemical structure due to their distinct van der Waals radii, bonding geometry, electron density, and substrate interaction.^[48] Our nc-AFM images lead to atomic features with rather similar contrast which points to the formation of such defects with only carbon atoms. Individual carbon atoms are common residues in surface chemistry experiments with organic compounds. In our case, the cleavage of $=CBr_2$ at the ends of the polymer provides the system with a reservoir of residual. The growth of type A and B defects involves rearrangement of the carbon atoms and π -conjugation around the ethynylene-bridge along with final cyclodehydrogenation reactions.

Electronic characterization

Next, we turn the attention to the effect of such low dimensional type A and B defects on the intrinsic electronic properties of the polymers. The addition of an extra carbon to the bridge (type A defect) leads to significant differences in charge distribution at the junction, in addition to the structural rearrangement described above. To give a clearer picture it is worth to comparatively discuss both defects. To probe the electronic properties of polymeric sections featuring type A or type B defects, we performed scanning tunneling point spectroscopy (STS) measurements and differential conductance (dI/dV) mapping on both types of defects and adjacent pristine segments. These measurements directly probe the energy- and spatial dependence of the local density of states (LDOS) of each carbon nanostructure.

In agreement with our previous reports,^[43] two frontier resonances at -0.6 eV and 0.8 eV are distinguished in STS data collected in pristine polymeric segments (cf Figure 2a), which are close to the onset of valence (VB) and conduction (CB) bands respectively (see Ref. [42]). The dI/dV map of the VB has states over the bridges and notably on the voids adjacent to the links. The dI/dV map of the CB shows states located on the edges of the anthracene moieties.

As expected, the dI/dV maps acquired on the defects show significant differences when compared to pristine ones. For type A defect, dI/dV map at 0.8 eV (i.e. at the CB) exhibits that signal barely changes around the defect, with bright features localized at the outermost anthracene edges (cf Figure 2a). Contrary, the map at the VB shows dim contrast at the defect

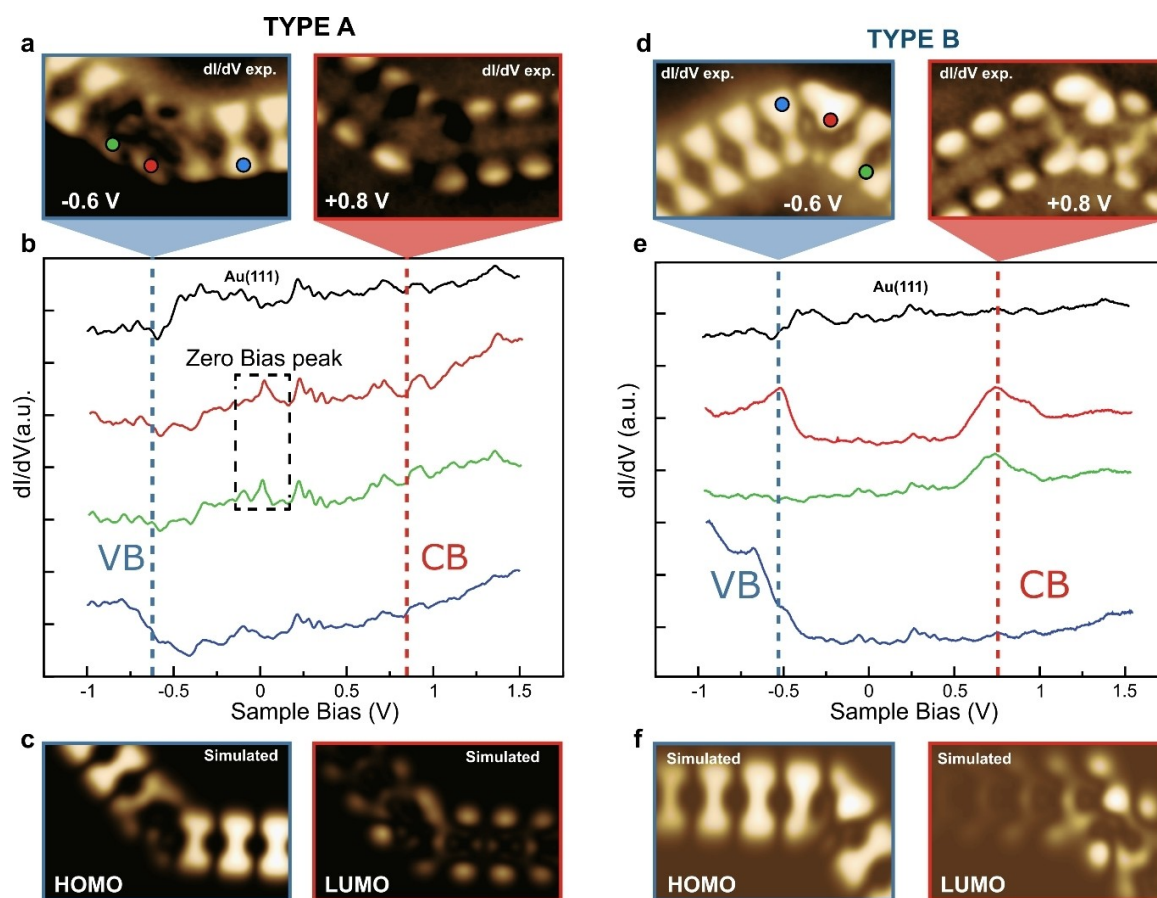


Figure 2. Conductance maps of type A and B defects. (a–d) Experimental dI/dV maps ($V_{\text{mod}} = 20$ mV, 613 Hz) were acquired on the defect type A and B at two bias voltages (-0.6 V and 0.8 V); (b–e) Experimental dI/dV spectra acquired on different sites of the defects type A and type B; (c–f) Calculated dI/dV maps for canonical DFT orbitals of HOMO and LUMO.

site and at the nearest anthracene units (Figure 2a,b), which may indicate a strong hybridization of the defect-induced electronic states with the polymer orbitals. The experimental findings are well supported by DFT-calculated dI/dV maps of a finite defective polymer (Figure 2c). However, for a detailed description, we have to look at the spin-polarized electronic states localized at the defect A and their corresponding energy alignment with the VB and CB of the polymer. Our DFT spin-polarized calculations of defect type A (see Figure S4) display both single-occupied (SO) and single-unoccupied (SU) states laying very close to the VB and CB respectively. Although this may affect the resolution of the VB and CB, our calculations mimic the important features, i.e. the lower contrast around defect for the VB and the high contrast at the features localized at the outermost anthracene edges for the CB.

On the other hand, spectra acquired at the junction of a type B defect exhibits resonances at both 0.8 eV and -0.6 eV (Figure 2e), and the CB and VB maps of the junction display a substantial charge density at the defect site. Importantly, dI/dV maps of both VB and CB (cf Figure 2d) show that the spatial

distribution of the band structure is barely disturbed around the defect. The images display that the band structure is not affected by the presence of the defect, indicating a low impact of such defect on the electronic properties of the polymer, at least for the frontier orbitals. Again, the DFT-simulated dI/dV maps (cf Figure 2f) are in good agreement with the experimental data reproducing the aforementioned features.^[37]

Discussion

Thus, in the following, we will discuss the impact of both defects on the conjugation of the polymer. For such a purpose, we employ high-resolution nc-AFM imaging with a CO-tip that has demonstrated the ability to resolve not only the chemical structure of individual molecules but also the bonding character. As discussed earlier, type A defect consists of two six-member and one five-member ring. Nc-AFM images of the defect clearly resolve a bright spot in the center of the linker in neighboring monomers (Figure 3a–c), which has been ascribed

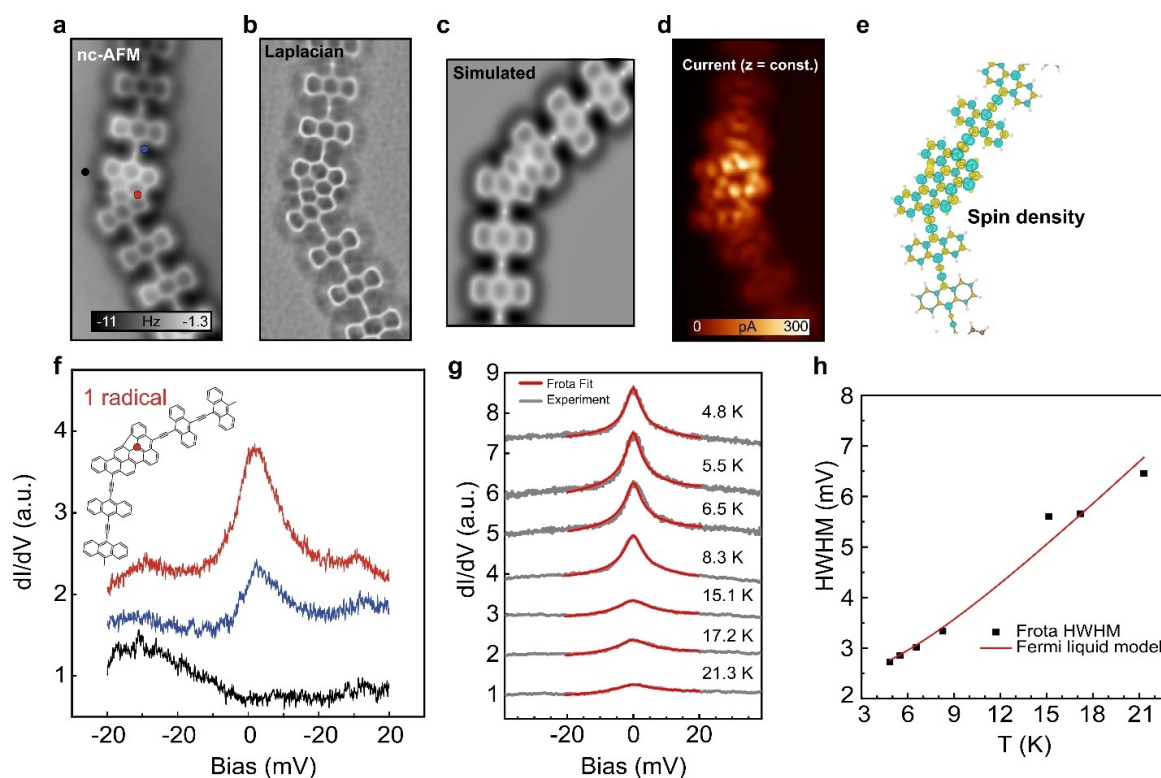


Figure 3. Structural characterization of type A defect. a) Constant height nc-AFM with CO-tip imaging of the type A defect. b) Laplace filtered nc-AFM image. c) Simulated AFM image of the defect with the probe particle model. d) Spin density calculated by DFT. e) STS spectroscopy near Fermi level showing a Zero Bias Peak on the defect site. In the inset, conjugation of the anthracene-ethynylene polymer with type A defect. f) STS spectroscopy near Fermi level showing a Zero Bias Peak (gray line) fit with a Frota function (red line) obtained on the defect site. g) Temperature evolution of the Zero Bias Peak as a function of the temperature. The Kondo temperature is extracted from the Fermi-liquid model: $\Gamma = \frac{1}{2} \sqrt{(\alpha K_B T)^2 + (2K_B T_K)^2}$ with an empirical parameter of $\alpha = 6.9 \pm 0.3$ and a Kondo temperature of $T_K = 27 \pm 2$.

to the large electron density of the triple bond, thus demonstrating the ethynylene character of such linkers. Meaningfully, in such a form of π -conjugation, the defect should harbor a single localized unpaired electron. In fact, STM constant height images at low bias voltage (0.005 V) show brighter contrast around type A defects (Figure 3d) compared to the straight polymeric segment, reflecting enhancements of the local density of states (LDOS) near the Fermi level. Though these bright regions extend over the closest anthracene monomers and their junction as well, the brighter signal can be located in the anthracene closest to the pentagon moiety. Comparatively, such low-energy LDOS enhancements are absent in type B defects (see Figure 4d).

A better understanding of the origin of these LDOS differences in type A defects can be achieved by recording the spectroscopic differential conductance (dI/dV) around Fermi level with the STM tip positioned at different sites above the defect. Spectra acquired on the type A defect reveals the presence of a sharp zero-bias peak (ZBP) (Figure 3f) located at the junction and adjacent anthracene monomers, rapidly vanishing into neighboring anthracene moieties. The shape of the ZBP is close to that of a Lorentzian with a line width of

approximately 3.5 mV. The narrow width of the ZBP rules out the direct association of this peak with a molecular resonance. The zero-bias features can be well fit with a Frota (see Figure 3g) or Fano (see Figure S5) functions^[49,50] and thus are attributed to a Kondo resonance arising from the screening of magnetic moment (unpaired electron) by the conduction electrons residing in the Au(111), as already expected from the chemical resonance form of the defect. The relationship between the observed ZBP and the Kondo effect is further demonstrated by measurements of dI/dV spectra at different temperatures (Figure 3c). The width of the resonance line increases with temperature following the characteristic behavior of a weakly coupled Kondo system with a Kondo temperature $T_K = 27 \pm 2$ K, and a multiplicative factor $\alpha = 6.9 \pm 0.3$, in line with a quenching of the ZBP with temperatures above 21 K (Figure 3g-h).^[51,52] Remarkably, we found that also Fano function fits well our data leading a Kondo temperature of $T_K = 38 \pm 2$ K (see Figure S5).

The existence of an unpaired spin density in the defect is corroborated by theoretical calculations of a free-standing polymeric section comprising one type A defect. Spin-polarized DFT reveals significant spin density at the defect site which

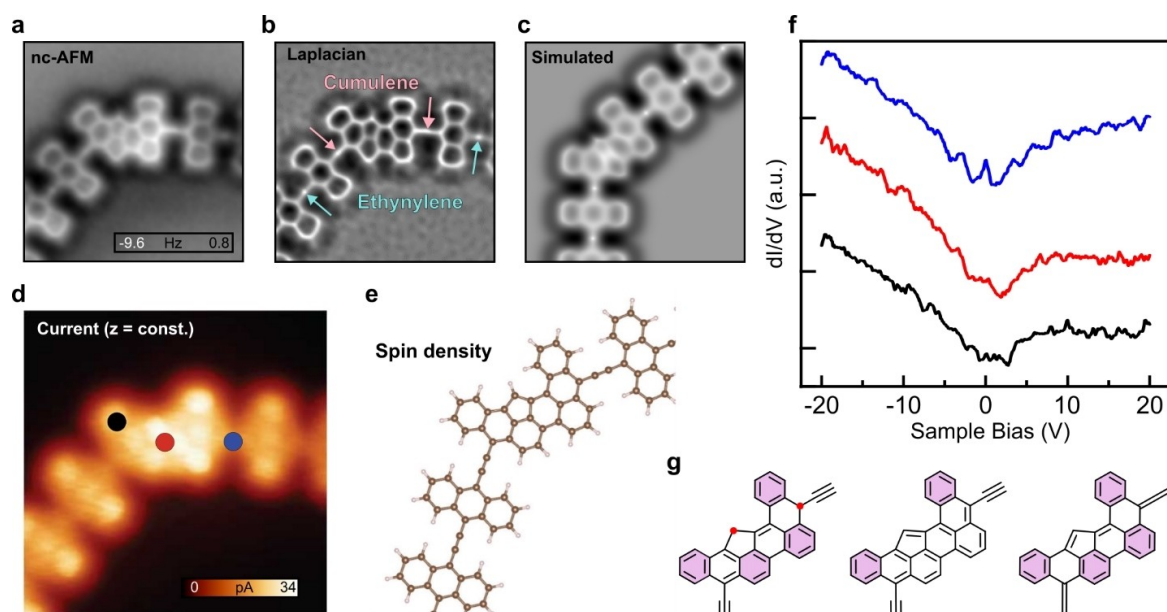


Figure 4. Structural characterization of type B defect. a-b) AFM Constant height current images with CO-functionalized tip of the type B defect. b) Laplace filtered nc-AFM image. c) Simulated AFM image with probe particle of the type B defect. d) High resolution constant height current image of the defect with the positions of the spectroscopies. e) Spin density calculated by DFT. f) STS spectroscopy near Fermi for selected regions (red, blue and black dots) of the defective polymer. g) Conjugation models for the type B defect with Clar's sextets highlighted: open-shell (left), close-shell ethynylene (center), and close-shell cumulene (right).

extends towards the monomers nearby (Figure 3e). Hence, the bright regions in STM images near Fermi energy are caused by the localization of a single magnetic moment around the defect site. According to our measurements, such polarized spin density survives on the Au(111) surface and gives rise to the ZBP due to the Kondo phenomenon, as previously encountered in other magnetic carbon-based nanomaterials.^[38]

Next, an analysis of nc-AFM images of type B defect shows distinct characteristics from its type A counterpart. The formation of type B defect, which involves the constitution of six- and five-membered rings at the junction, can give rise to distinct resonance forms of the π -conjugation: (i) an open-shell structure that leads to two unsaturated bonds (radicals) in the defect junction, or (ii) a closed-shell structure leading to saturated bonds. However, after examining the DFT-calculated spin-density of finite ethynylene-anthracene monomer (see Figure 4e), it becomes clear that defect type B is associated with the closed-shell structure. In fact, both constant height STM image and dI/dV spectra acquired above the junction and adjacent anthracene monomer sites of a defect type B are featureless, similarly to that of defect at low energy (Figure 4f), pointing to the absence of extra charge localization at the junction.

Here two resonance forms can be considered for the close-shell structure regarding the conjugation of the adjacent linkers, leading to ethynylene or cumulene bridges (see Figure 4g). Two arguments suggest that the defect type B may adopt the cumulene-like structure. First, our nc-AFM images display lower

contrast and more elongated feature at the adjacent linkers compared to those at farther distances (cf Figure 4b). This intramolecular contrast is the result of the short-ranged Pauli repulsion being maximized in the areas of higher electron density so that minor variations in electron density assigned to specific bonding order can be resolved in nc-AFM images as features with different brightness or shape, thus pointing to an alternation in the character of the bond. On the other hand, such features can be further varied due to anisotropic charge distribution in the molecular backbone,^[53] distinct interaction with the surface^[54] and varying with the tip-sample distance. Second, Clar's aromatic π -sextet rule states that a resonance structure of polycyclic aromatic hydrocarbons with the maximal number of nonadjacent π -sextets represents the most stable form or the major resonance contributor. If we apply this rule in a local viewpoint in defect type B, we found that the cumulene transition increases the number of nonadjacent π -sextets from 2 (for the ethylene form) to 4 (cf Figure 4g).

Although a fully characterization of the mechanism behind the particular formation of such defects is beyond the scope of this article because it would involve complex quantum molecular mechanics calculations,^[46,55] our findings suggest a mechanism to engineer low-dimensional defects in such polymers by placing an external source in UHV, which provides the system with atomic carbon atoms in a controllable manner during the polymerization reaction. In such a hypothetical experiment, one should expect to largely transform type B defects into type A.

Conclusions

In conclusion, we report a strategy for thermally inducing low-dimensional structural defects that can imprint an open-shell character in on-surface synthesized π -conjugated polymers. High-resolution non-contact atomic force microscopy clarifies the structure of these defects, being those labeled type A and type B the most observed by far. We characterized the impact of these defects in the electronic properties of the polymer using a combination of scanning tunneling microscopy/spectroscopy experiments complemented with state-of-the-art density functional theory calculations. While the type B defect hardly affects the electronic structure of the polymer, the type A defect shows an intrinsic open-shell character which is of potential relevance for fundamental science, as well as in view of its potential applications, in materials chemistry and, particularly, in quantum electronic devices. The low bandgap of the polymer, and in particular, the proximity of the VB to the Fermi level, is a crucial aspect to stabilize the radical ground state of the type A defect. Our results show the growth and characterization of structural defects in π -conjugated polymers that address relevant electronic properties, thus contributing to the development of the field of on-surface chemistry and guiding the defect engineering of modern low-band-gap polymers.

Methods

Experimental Section

Experiments were performed in an ultra-high vacuum with a base pressure below 5×10^{-10} mbar system hosting a STM/nc-AFM (Createc GmbH) operated at 4.2 K. STM images were acquired in constant current mode with a bias voltage applied to the sample. For the spectroscopic measurements, specific site dI/dV were taken with the conventional lock-in technique with a modulation ranging from 0.5 mV to 10 mV at 937 Hz. STM/nc-AFM images were taken with sharpened by focus ion beam (FIB) Pt/Ir tips mounted on a qPlus sensor. In nc-AFM imaging, the tip was functionalized with a single CO molecule picked up from the bare metal substrate and operated in frequency-modulation mode (oscillated with a constant amplitude of 50 pm; resonant frequency ≈ 30 kHz; stiffness ≈ 1800 N/m). All nc-AFM images were acquired in constant height mode with a bias voltage of 1 mV. All images were subject to standard process using WSxM software.^[56]

The Au(111) substrate was prepared by repeated cycles of Ar⁺ sputtering (1 keV) and subsequent annealing. The molecular precursor was deposited by organic molecular beam epitaxy from a tantalum pocket maintained at 370 K onto a clean Au(111) held at room temperature. Whenever necessary samples were annealed to the desired temperature and subsequently transferred to the STM stage, which was kept at 4.2 K. For the temperature dependent STS data displayed in figures 3 g,h, the sample was heated up from 4.8 K by using a Zener diode mounted to the baseplate of the STM. The temperature was increased in a rate of 0.05–0.1 K / min. After reaching the temperature of interest, the system was thermalized for about 30–60 min.

Synthesis of molecular precursor 11,11,12,12-tetrabromoanthraquinodimethane is introduced elsewhere.^[43]

Theoretical Calculations

Computational details

Density functional theory (DFT) calculations were performed using the FHI-AIMS code^[57] within XC PBE0 functional^[58,59] to describe the electronic properties of different gas-phase molecules. In all the calculations, we employed the light settings for the atomic basis sets. The atomic structures were relaxed until the total forces were smaller than 10^{-2} eVÅ⁻¹. The relaxed structures were found by exploring different initial conditions and selecting the one with the lowest potential energy. Only the Γ -point was used for integration in the Brillouin zone.

A. dI/dV simulations in the gas phase

Frontiers molecular orbitals were obtained from DFT calculations using the FHI-AIMS code within hybrid exchange-correlation functional PBE0^[58,59] for the gas phase molecule. We employed Probe Particle Scanning Probe Microscopy (PP-SPM) code^[59,60] to simulate constant-height dI/dV maps and CO-tip was represented by a linear combination of s-like (15%) and px,py-like (85%) orbitals without tip relaxation at tip-sample distance 5 Å.

B. AFM Simulations

The AFM images were calculated using the probe particle model.^[59] The parameters of the tip were chosen to mimic a CO-tip, using a quadrupole charge moment of $-0.2 e \cdot \text{Å}^2$ ^[58,61] and the lateral stiffness of the CO molecule is set to 0.25 Nm^{-1} . The electrostatic interaction was described in the AFM calculations using the potential calculated by DFT. To simulate the probe dynamics, we used typical values of a qPlus sensor, oscillation amplitude $A = 100$ pm, sensor stiffness $k = 3600$ N/m, and eigenfrequency $f_0 = 30$ kHz.

Author contributions

B.T. conceived and designed the experiments. D.E., P.J., and B.T. supervised the project and led the collaboration efforts. B.M., T.Ch., A.S.-G., B.C., and B.T. carried out the experiments and obtained the data. J.S. and N.M. synthesized the precursors. The experimental data were analyzed by B.M., D.E., P.J., and B.T., and discussed by all the authors. Q.Ch. and P.J. performed the theoretical calculations. The manuscript was written by B.M., D.E., P.J. and B.T., with contributions from all the authors.

Acknowledgements

The authors gratefully acknowledge the support of the Operational Programme for Research, Development, and Education of

the European Regional Development Fund (Project No. CZ.02.1.01/0.0/0.0/16_019/0000754). Q. Ch, B.M., and P.J. acknowledge the support of GACR 20–13692X. B.M. acknowledges the support from the Internal Student Grant Agency of the Palacký University in Olomouc, Czech Republic IGA_PrF_2021_032 and the Fischer Scholarship. This project has received funding from Comunidad de Madrid [projects QUIMTRONIC-CM (Y2018/NMT-4783)], and Ministerio de Ciencia, Innovación y Universidades (projects PID2019-108532GB-I00). IMDEA Nanociencia is appreciative of support from the “Severo Ochoa” Programme for Centers of Excellence in R&D (MINECO, grant SEV-2016-0686).

Conflict of Interest

The authors declare no conflict of interest.

Data Availability Statement

The data that support the findings of this study are available from the corresponding author upon reasonable request.

Keywords: atomic force microscopy · conjugated polymers · on-surface synthesis · scanning tunneling microscopy

- [1] A. Kraft, A. C. Grimsdale, A. B. Holmes, *Angew. Chem. Int. Ed.* **1998**, *37*, 402–428; *Angew. Chem.* **1998**, *110*, 416–443.
- [2] Z. Qiu, B. A. G. Hammer, K. Müllen, *Prog. Polym. Sci.* **2020**, *100*, 101179.
- [3] J. Roncali, *Macromol. Rapid Commun.* **2007**, *28*, 1761–1775.
- [4] Y. Zhang, B. de Boer, P. W. M. Blom, *Phys. Rev. B: Condens. Matter Mater. Phys.* **2010**, *81*, 085201.
- [5] H. T. Nicolai, M. Kuik, G. A. H. Wetzelaer, B. de Boer, C. Campbell, C. Risko, J. L. Brédas, P. W. M. Blom, *Nat. Mater.* **2012**, *11*, 882–887.
- [6] D. Abbaszadeh, A. Kunz, N. B. Kotadiya, A. Mondal, D. Andrienko, J. J. Michels, G. J. A. H. Wetzelaer, P. W. M. Blom, *Chem. Mater.* **2019**, *31*, 6380–6386.
- [7] L. G. Kaake, P. F. Barbara, X. Y. Zhu, *J. Phys. Chem. Lett.* **2010**, *1*, 628–635.
- [8] R. Meng, Y. Li, K. Li, K. Gao, S. Yin, L. Wang, *Phys. Chem. Chem. Phys.* **2017**, *19*, 24971–24978.
- [9] L. Romaner, A. Pogantsch, P. S. de Freitas, U. Scherf, M. Gaal, E. Zojer, E. J. W. List, *Adv. Funct. Mater.* **2003**, *13*, 597–601.
- [10] V. I. Arkhipov, P. Heremans, E. v. Emelianova, H. Bässler, *Phys. Rev. B* **2005**, *71*, 045214.
- [11] M. Silver, L. Pautmeier, H. Bässler, M. Silver, L. Pautmeier, H. Bässler, *SSCom* **1989**, *72*, 177–180.
- [12] V. I. Arkhipov, H. von Seggern, E. v. Emelianova, *Appl. Phys. Lett.* **2003**, *83*, 5074.
- [13] V. I. Arkhipov, E. v. Emelianova, G. J. Adriaenssens, *Phys. Rev. B* **2001**, *64*, 125125.
- [14] D. Hu, J. Yu, K. Wong, B. Bagchi, P. J. Rossky, P. F. Barbara, *Nature* **2000**, *405*, 1030–1033.
- [15] Z. Liang, A. Nardes, D. Wang, J. J. Berry, B. A. Gregg, *Chem. Mater.* **2009**, *21*, 4914–4919.
- [16] C. Tanase, P. W. M. Blom, D. M. de Leeuw, E. J. Meijer, *Phys. Status Solidi A* **2004**, *201*, 1236–1245.
- [17] L. Xu, J. Wang, J. W. P. Hsu, *Phys. Rev. Appl.* **2016**, *6*, 064020.
- [18] J. Yu, D. Hu, P. F. Barbara, *Science* **2000**, *289*, 1327–1330.
- [19] J. M. Lupton, P. Schouwink, P. E. Keivanidis, A. C. Grimsdale, K. Müllen, *Adv. Funct. Mater.* **2003**, *13*, 154–158.
- [20] P. A. Troshin, D. K. Susarova, Y. L. Moskvin, I. E. Kuznetsov, S. A. Ponomarenko, E. N. Myshkovskaya, K. A. Zakharcheva, A. A. Balakai, S. D. Babenko, V. F. Razumov, *Adv. Funct. Mater.* **2010**, *20*, 4351–4357.
- [21] L. Grill, S. Hecht, *Nat. Chem.* **2020**, *12*, 115–130.
- [22] Q. Shen, H. Y. Gao, H. Fuchs, *Nano Today* **2017**, *13*, 77–96.
- [23] S. Clair, D. G. de Oteyza, *Chem. Rev.* **2019**, *119*, 4717–4776.
- [24] J. Cai, P. Ruffieux, R. Jaafar, M. Bieri, T. Braun, S. Blankenburg, M. Muoth, A. P. Seitsonen, M. Saleh, X. Feng, K. Müllen, R. Fasel, *Nature* **2010**, *466*, 470–473.
- [25] G. Galeotti, F. de Marchi, E. Hamzehpoor, O. MacLean, M. Rajeswara Rao, Y. Chen, L. v. Besteiro, D. Dettmann, L. Ferrari, F. Frezza, P. M. Sheverdyeva, R. Liu, A. K. Kundu, P. Moras, M. Ebrahimi, M. C. Gallagher, F. Rosei, D. F. Perepichka, G. Contini, *Nat. Mater.* **2020**, *19*, 874–880.
- [26] P. Ruffieux, S. Wang, B. Yang, C. Sanchez-Sanchez, J. Liu, T. Dienel, L. Talirz, P. Shinde, C. A. Pignedoli, D. Passerone, T. Dumslaff, X. Feng, K. Müllen, R. Fasel, *Nature* **2016**, *531*, 489–492.
- [27] D. J. Rizzo, G. Veber, T. Cao, C. Bronner, T. Chen, F. Zhao, H. Rodriguez, S. G. Louie, M. F. Crommie, F. R. Fischer, *Nature* **2018**, *560*, 204–208.
- [28] O. Gröning, S. Wang, X. Yao, C. A. Pignedoli, G. Borin Barin, C. Daniels, A. Cupo, V. Meunier, X. Feng, A. Narita, K. Müllen, P. Ruffieux, R. Fasel, *Nature* **2018**, *560*, 209–213.
- [29] B. Cirera, A. Sánchez-Grande, B. de la Torre, J. Santos, S. Edalatmanesh, E. Rodríguez-Sánchez, K. Lauwaet, B. Mallada, R. Zbořil, R. Miranda, O. Gröning, P. Jelínek, N. Martín, D. Eciija, *Nat. Nanotechnol.* **2020**, *15*, 437–443.
- [30] A. Sánchez-Grande, J. I. Urgel, A. Cahlik, J. Santos, S. Edalatmanesh, E. Rodríguez-Sánchez, K. Lauwaet, P. Mutombo, D. Nachtigallová, R. Nieman, H. Lischka, B. de la Torre, R. Miranda, O. Gröning, N. Martín, P. Jelínek, D. Eciija, *Angew. Chem. Int. Ed.* **2020**, *59*, 17594–17599; *Angew. Chem.* **2020**, *132*, 17747–17752.
- [31] J. Lawrence, P. Brandimarte, A. Berdonces-Layunta, M. S. G. Mohammed, A. Grewal, C. C. Leon, D. Sánchez-Portal, D. G. de Oteyza, *ACS Nano* **2020**, *14*, 4499–4508.
- [32] L. Gross, F. Mohn, N. Moll, P. Liljeroth, G. Meyer, *Science* **2009**, *325*, 1110–1114.
- [33] L. Gross, B. Schuler, N. Pavliček, S. Fatayer, Z. Majzik, N. Moll, D. Peña, G. Meyer, *Angew. Chem. Int. Ed.* **2018**, *57*, 3888–3908; *Angew. Chem.* **2018**, *130*, 3950–3972.
- [34] D. G. de Oteyza, P. Gorman, Y. C. Chen, S. Wickenburg, A. Riss, D. J. Mowbray, G. Etkin, Z. Pedramrazi, H. Z. Tsai, A. Rubio, M. F. Crommie, F. R. Fischer, *Science* **2013**, *340*, 1434–1437.
- [35] A. Riss, A. P. Paz, S. Wickenburg, H. Z. Tsai, D. G. de Oteyza, A. J. Bradley, M. M. Ugeda, P. Gorman, H. S. Jung, M. F. Crommie, A. Rubio, F. R. Fischer, *Nat. Chem.* **2016**, *8*, 678–683.
- [36] A. Berdonces-Layunta, J. Lawrence, S. Edalatmanesh, J. Castro-Esteban, T. Wang, M. S. G. Mohammed, L. Colazzo, D. Peña, P. Jelínek, D. G. de Oteyza, *ACS Nano* **2021**, *15*, 5610–5617.
- [37] H. González-Herrero, J. I. Mendieta-Moreno, S. Edalatmanesh, J. Santos, N. Martín, D. Eciija, B. de la Torre, P. Jelínek, *Adv. Mater.* **2021**, *33*, 2104495.
- [38] J. Li, S. Sanz, M. Corso, D. J. Choi, D. Peña, T. Frederiksen, J. I. Pascual, *Nat. Commun.* **2019**, *10*, 200.
- [39] S. Mishra, D. Beyer, R. Berger, J. Liu, O. Gröning, J. I. Urgel, K. Müllen, P. Ruffieux, X. Feng, R. Fasel, *J. Am. Chem. Soc.* **2020**, *142*, 1147–1152.
- [40] Y. Zheng, C. Li, C. Xu, D. Beyer, X. Yue, Y. Zhao, G. Wang, D. Guan, Y. Li, H. Zheng, C. Liu, J. Liu, X. Wang, W. Luo, X. Feng, S. Wang, J. Jia, *Nat. Commun.* **2020**, *11*.
- [41] P. T. Landsberg in *Recombination in Semiconductors*, Cambridge University Press, Cambridge, **1991**.
- [42] R. Smith in *Semiconductors*, Cambridge University Press, Cambridge, **1959**.
- [43] A. Sánchez-Grande, B. de la Torre, J. Santos, B. Cirera, K. Lauwaet, T. Chutora, S. Edalatmanesh, P. Mutombo, J. Rosen, R. Zbořil, R. Miranda, J. Björk, P. Jelínek, N. Martín, D. Eciija, *Angew. Chem. Int. Ed.* **2019**, *58*, 6559–6563; *Angew. Chem.* **2019**, *131*, 6631–6635.
- [44] J. Kondo, *Prog. Theor. Phys.* **1964**, *32*, 37–49.
- [45] M. Ternes, A. J. Heinrich, W. D. Schneider, *J. Condens. Matter Phys.* **2008**, *21*, 053001.
- [46] B. de la Torre, A. Matěj, A. Sánchez-Grande, B. Cirera, B. Mallada, E. Rodríguez-Sánchez, J. Santos, J. I. Mendieta-Moreno, S. Edalatmanesh, K. Lauwaet, M. Otyepka, M. Medved, Á. Buendía, R. Miranda, N. Martín, P. Jelínek, D. Eciija, *Nat. Commun.* **2020**, *11*, 4567.
- [47] B. Schuler, S. Fatayer, F. Mohn, N. Moll, N. Pavliček, G. Meyer, D. Peña, L. Gross, *Nat. Chem.* **2016**, *8*, 220–224.
- [48] P. Zahl, Y. Zhang, *Energy Fuels* **2019**, *33*, 4775–4780.
- [49] H. O. Frota, *Phys. Rev. B* **1992**, *45*, 1096–1099.
- [50] O. Újsághy, J. Kroha, L. Szunyogh, A. Zawadowski, *Phys. Rev. Lett.* **2000**, *85*, 2557–2560.

- [51] Y. H. Zhang, S. Kahle, T. Herden, C. Stroh, M. Mayor, U. Schlickum, M. Ternes, P. Wahl, K. Kern, *Nat. Commun.* **2013**, *4*.
- [52] K. Nagaoka, T. Jamneala, M. Grobis, M. F. Crommie, *Phys. Rev. Lett.* **2002**, *88*.
- [53] B. Mallada, B. de la Torre, J. I. Mendieta-Moreno, D. Nachtigallová, A. Matěj, M. Matoušek, P. Mutombo, J. Brabec, L. Veis, T. Cadart, M. Kotora, P. Jelinek, *J. Am. Chem. Soc.* **2021**, *143*, 14694–14702.
- [54] S. Kawai, S. Nakatsuka, T. Hatakeyama, R. Pawlak, T. Meier, J. Tracey, E. Meyer, A. S. Foster, *Sci. Adv.* **2018**, *4*.
- [55] Y. Morita, S. Suzuki, K. Sato, T. Takui, *Nat. Chem.* **2011**, *3*, 197–204.
- [56] I. Horcas, R. Fernández, J. M. Gómez-Rodríguez, J. Colchero, J. Gómez-Herrero, A. M. Baro, *Rev. Sci. Instrum.* **2007**, *78*, 013705.
- [57] V. Blum, R. Gehrke, F. Hanke, P. Havu, V. Havu, X. Ren, K. Reuter, M. Scheffler, *Computer Comput. Phys. Commun.* **2009**, *180*, 2175–2196.
- [58] A. D. Becke, *Chem. Phys.* **1993**, *98*, 5648–5652.
- [59] P. Hapala, G. Kichin, C. Wagner, F. S. Tautz, R. Temirov, *P. Phys. Rev. B* **2014**, *90*, 085421.
- [60] O. Krejčí, P. Hapala, M. Ondráček, P. Jelinek, *Phys. Rev. B* **2017**, *95*.
- [61] J. Peng, J. Guo, P. Hapala, D. Cao, R. Ma, B. Cheng, L. Xu, M. Ondráček, P. Jelinek, E. Wang, Y. Jiang, *Nat. Commun.* **2018**, *9*.

Manuscript received: March 28, 2022

Accepted manuscript online: June 10, 2022

Version of record online: July 6, 2022

Chapter 4

Charge distribution visualization with KPFM

Charge and its spatial distribution at the atomic and molecular scale, play a critical role in the behavior of many physical and chemical systems. In the biological world, several processes are mediated by the interplay of electrostatic interactions between charged regions of molecules. One of the most significant processes is protein folding, where the electrostatic interactions between charged amino acid residues can significantly influence the stability and function of the protein structure, regulating the formation of secondary and tertiary structures[64]. Several well known systems can be found in biology, such as the transport of ions across cell membranes, nerve impulses, muscle contraction, or in photosynthesis where the localization of charges plays a significant role.

The understanding at the atomic level of the mechanisms driving electrostatic interactions and the influence of charge distribution in surfaces and molecular systems and surfaces have numerous consequences, from the study of proteins[65, 66] to the experimental realization of theoretical predictions[20]. Atomic force microscopy (AFM) has been established as an effective tool for achieving atomic-scale imaging of surfaces and molecules. One specific

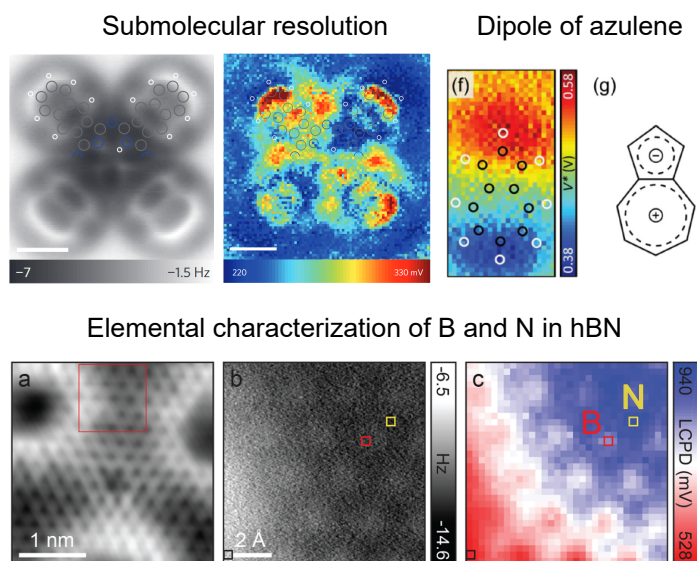


Figure 4.1: Submolecular resolution of the charge distribution of a naphthalocyanine molecule[67] (top, left), visualization of the azulene dipole [68] (top, right) and the elemental identification (bottom) of boron and nitrogen atoms in epitaxial hBN[70] (Note: color scales are not consistent across the literature, however in all of them, a minimum of LCPD means positive charges and a maxima negative charges). Adapted with permission. 2012 Springer Nature, 2019 American Physical Society, 2018 American Chemical Society.

application of AFM, Kelvin probe force microscopy (KPFM), has attracted significant attention for its ability to visualize the distribution of electrical charges on surfaces. Several studies have demonstrated the utility of KPFM for imaging charge distributions at the atomic scale. For example, it has achieved submolecular resolution of the charge distribution of individual naphthalocyanine molecules using KPFM[67], measurement of the dipole moment of individual azulene molecules[68], characterization of charge states of single gold atoms[69], or the element discrimination in epitaxial hBN[70].

In this chapter, I will explore the different systems where the charge distribution plays a significant role at the atomic or molecular level and their subsequent visualization in real space using KPFM. In Section 4.1 is introduced the atomic-scale charge distribution of single substitutional p- (boron) and n-type (nitrogen) dopants in graphene. Using combined AFM and KPFM measurements, supported with DFT simulations, I will demonstrate the

divergent chemical activity of nitrogen and boron atoms incorporated into graphene as substitutional dopants, providing a deeper insight into the precise chemical functionalization of graphene derivatives at the atomic level. In Section 4.2, it will be explored the possibility of achieving subatomic resolution of anisotropic charge distributions within single halogen atoms using KPFM. In this experiment, I will explore two equivalent systems where one halogen atom, bromine, should exhibit a σ -hole and is compared to another halogen atom, fluorine, that should not exhibit a σ -hole. These results provide direct evidence of the existence of σ -holes and direct quantification of properties of non-covalent interactions between atoms functionalizing the tip and the halogen atoms. This approach, as will be seen in this section, open a path for extending the capabilities of KPFM in imaging with atomic precision complex molecular or surface systems with inhomogeneous polarizability, dipolar moments, or charged states. Finally, in Section 4.3, the experimental evidence of the existence of π -holes in organic molecular systems and their influence on electrostatic interactions between the molecule and a metallic surface is presented. Real-space imaging of the π -hole is achieved using KPFM on a single fluorinated anthracene and compared to its non-fluorinated counterpart anthracene. Altogether, these experiments demonstrate the potential of scanning microscopy for studying the internal charge distribution in molecules, which fundamentally affects their physical and chemical properties, with submolecular or even atomic spatial resolution.

4.1 Charge Distribution of single boron and nitrogen dopants in graphene

4.1.1 Introduction

The discovery of graphene, the first isolated 2D material[71], was rapidly followed by a complete characterization of its mechanical and electronic properties[72]. It was observed early, that the range of tools for the control of its chemical and electronic behaviour was severely hindered by some of its own strengths. The monoelemental character of graphene and its regular honeycomb lattice originate from the overlap of three sp^2 hybridized carbon orbitals bonding through σ -bonds, while the non-hybridized p_z -orbitals in each carbon interact with the other p_z -orbitals forming two half-filled bands of π delocalized electrons. This structural and electronic scaffold generates the emergence of exotic properties such as the Dirac cones, anomalous quantum Hall effect, ballistic transport[73], or by the interaction with other 2D materials[74], including graphene such as in the recent discovery of superconductivity in graphene sheets, emerging from overlapping two graphene sheets in a relative angle called *magic angle*[75].

On the other hand, these properties provide graphene with an inert character that constrains the precise control of its chemical properties and other desirable properties such as tuning the density of charge carriers[76, 77], plasmon mobility[78], or magnetic behavior[79]. The incorporation of heteroatoms into the graphene lattice, more specifically boron and nitrogen atoms, could lead to a similar path of development as the one followed by the silicon-based semiconductors doped with positive (p) and negative (n)-type heteroatoms[80]. In the work presented in this section, it is reported the growth of graphene (G) supported on SiC(0001) and the subsequent low-concentration doping and characterization in UHV of single nitrogen and boron graphitic dopants by means of STM, AFM,

and KPFM. The atomically-precise capabilities of the SPM techniques at low temperature (5 K) with a CO-functionalized tip provide a broader perspective on the chemical reactivity of graphene when doped with atoms neighbouring carbon in the periodic table and the extension of the charge distribution surrounding the boron and nitrogen substitutional dopants.

The starting point is the growth of graphene on a SiC(0001) substrate in vacuum conditions. By heating the SiC(0001) to a temperature of around 900°C, Si atoms start to sublime, promoting the growth of epitaxial graphene from the top to the bulk of SiC(0001) in a reactor kept at vacuum conditions. Monitoring the time of the process allow precise control of the growth of graphene in monolayer, double-layer, or multiple-layer graphene. In this work, it is reported monolayer graphene, and further details on the growth and doping have been described elsewhere [80, 81]. The doping with boron and nitrogen follows a two-step preparation, where the boron is sublimated on the previously grown graphene and then the whole system is heated up to temperatures of 1200° to incorporate the boron atoms into the graphene lattice (B-G). The nitrogen is incorporated utilizing ionized N_2 and then sputtered onto the B-doped graphene surface (BN-G). The initial characterization by STM with CO-tips shows the random implantation of the dopants in low concentration as bright objects with three-fold symmetry (see Fig. 4.2).

However, as mentioned earlier, STM is a technique that images the convolution of the density of states of the tip, and effects such as the electron scattering by the dopants/defects do not lead to direct atomic identification. Using constant-height high-resolution AFM imaging with a CO-tip, the honeycomb structure of carbon atoms was clearly resolved, and boron and nitrogen atoms were observed to be brighter and darker, respectively, than the surrounding carbon atoms regardless of the tip-sample distance as seen in Fig. 4.3. This noticeable contrast was accompanied by a significant local bond length distortion of the carbons surrounding nitrogen and boron and observed as an increased bond length

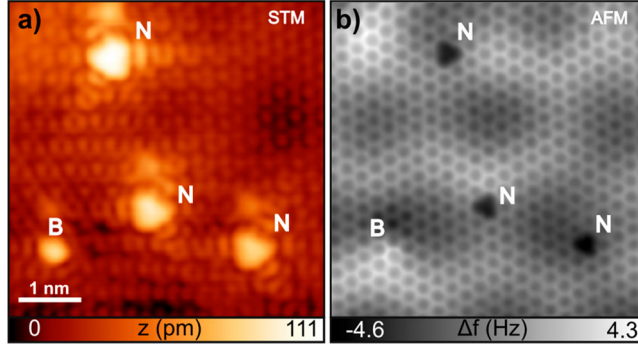


Figure 4.2: a, STM topography ($V_{Bias}=200$ mV, $I_{tunnel}=0$ pA) of a graphene region containing one boron and three nitrogen substitutional dopants. b, Constant-height (nc-AFM) image where the boron dopant appears as a bright feature in the bottom left-hand corner, while the nitrogen dopants are observed as dark features.

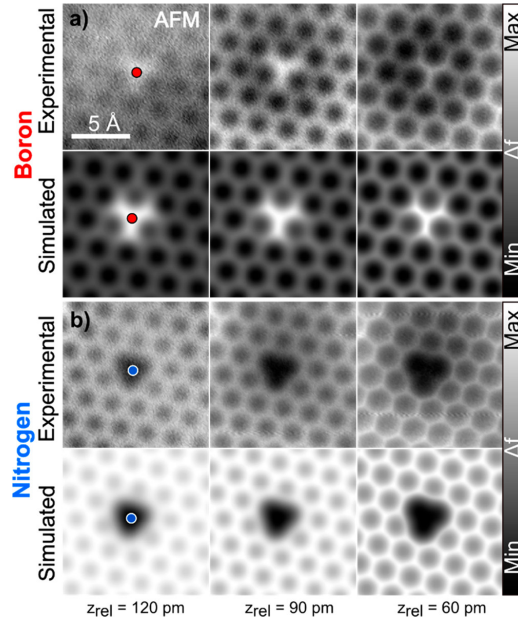


Figure 4.3: Constant height nc-AFM images obtained with CO-tip of boron (a) and nitrogen (b) dopants in substitutional positions.

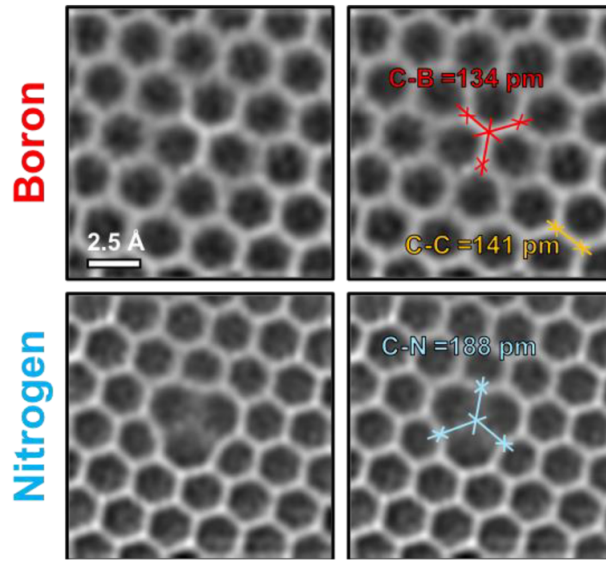


Figure 4.4: Bond length analysis of the B and N dopants from Laplace filtered constant height nc-AFM images measured with CO-tip.

for C-N (188 ± 8) and a shortening for the B-N (134 ± 4) relative to a typical C-C (141 ± 2) of the pristine lattice (Fig. 4.4). The distortion of the lattice was attributed to localized electrostatic charges on the dopants that were characterized using KPFM (Fig. 4.5).

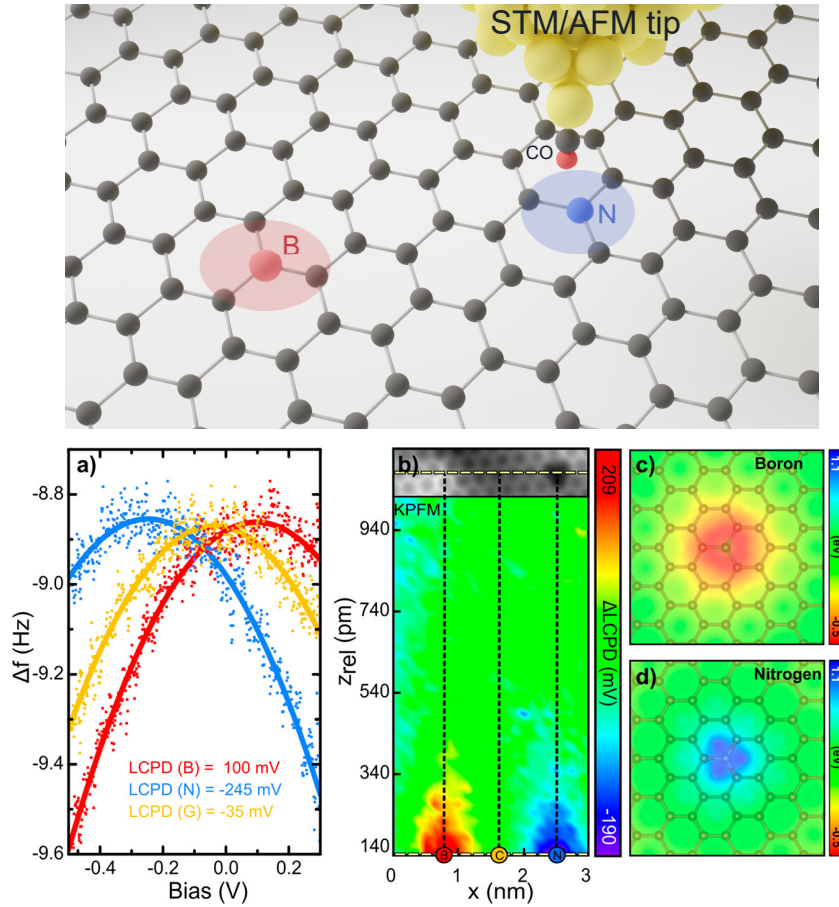


Figure 4.5: Schematic of the BN-G system. The CO-tip, with the STM feedback open, acquires single KPFM spectroscopies (a) on B (red), N (blue), and C (yellow). By repeating the process along a line in the plane defined by the lattice (b), and then moving the tip in the z positions, a set of parabolas can be acquired covering the XZ plane (see Fig. 1.7 for more details). Red represents a positive LCPD (negative charge) and blue a negative shift (positive charge). The graphene background (black dashed line over C atom in (b)) was subtracted column by column from the total map to enhance the contrast. The DFT calculated Hartree potentials for both dopants (d) confirms the experimental results where B/N behave as negative/positive point-like charges confined to the surroundings of the dopants.

The LCPD over the dopants was shifted to a higher or lower value depending on the surface dipole induced by the dopant, which reflects an increase (N) or decrease (B) in the local work function. The sign of the LCPD difference between the dopants reflects the localization of positive and negative net charges on nitrogen and boron sites, respec-

tively. The magnitude of the LCPD difference indicates a comparable level of opposite charge doping by boron and nitrogen. The net charge on the dopants originates from the acceptance/donation of an electron to the graphene π -band and the subsequent electronic redistribution around the dopants.

In addition, DFT calculations show the presence of a negative/positive net charge on boron/nitrogen dopants in the Hartree potential images, which is consistent with the spatial confinement of the charge observed in the experimental LCPD map. Finally, the chemical properties of each dopant were assessed by measuring the experimental interaction between the CO tip and the dopants, confirming the DFT prediction that the interaction is mostly driven by weak electrostatic interactions with strength in the order of ≈ 10 -30 pN.

4.1.2 Author's contribution to the published work

The preparation of the sample in an external reactor, the transfer to an STM-compatible sample plate, the dual-doping with boron and nitrogen in UHV, and the subsequent degassing of the sample were performed by me. The experimental STM and nc-AFM acquisition, including the force spectroscopies and the bond length analysis, in addition to the KPFM acquisition were performed by me. The data acquisition, curation, processing, and analysis of the KPFM maps were done with Python scripts developed by me.

Atomic-Scale Charge Distribution Mapping of Single Substitutional p- and n-Type Dopants in Graphene

Benjamin Mallada, Shayan Edalatmanesh, Petr Lazar, Jesus Redondo, Aurelio Gallardo, Radek Zbořil, Pavel Jelínek,* Martin Švec,* and Bruno de la Torre*

Cite This: *ACS Sustainable Chem. Eng.* 2020, 8, 3437–3444

Read Online

ACCESS |



Metrics & More



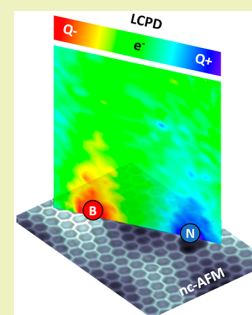
Article Recommendations



Supporting Information

ABSTRACT: Tuning the chemical properties of graphene by controlled doping is a widely investigated strategy. The effect of a substitutional single dopant on graphene local reactivity is much less explored. To improve the understanding of the role of p- and n-type dopants in graphene's local chemical activity and quantification of its interaction with single molecules, we report an atomic-scale investigation of single boron (B) and nitrogen (N) dopants in graphene and their interactions with CO molecules by means of atomic force microscopy (AFM) and Kelvin probe force microscopy (KPFM) experiments and theoretical calculations. We infer that N/B doping significantly increases/lowers the chemical interaction of graphene with individual CO molecules as a result of weak electrostatic forces induced by distinct charge distribution around the dopant site. High-resolution AFM images allow dopant discrimination and their atomic-scale structural characterization, which may be crucial for the atomic-scale design of graphene derivatives with relevant potential applications in molecular sensing and catalysis.

KEYWORDS: Graphene, Nitrogen doping, Boron doping, Graphene chemistry, Noncovalent interactions, CO–graphene interaction, Scanning probe microscopy, Density functional theory



INTRODUCTION

The fundamental understanding of the physical and chemical properties of individual dopants incorporated in graphene is crucial for a successful application in graphene-based devices. Doping with heteroatoms has become one of the most successful routes for addressing desirable functionalities in graphene. In particular, incorporation of substitutional boron and nitrogen atoms in the graphene lattice creates acceptor and donor centers, due to the different number of valence electrons with respect to carbon.^{1–4} The size and electronic structure similar to carbon provide them with specific advantages for their substitution into the graphene sheet with minimal strain, maintaining the overall graphene structure. Such dopants affect graphene charge transport^{5,6} and plasmon mobility⁷ and induce magnetism.^{6,8} Great efforts have also been dedicated to address their specific chemical functionalities.^{9,10} Due to the inertness of the pristine graphene, incorporation of atomic and molecular species in the two-dimensional lattice provides enhanced chemical activity of doped graphene, offering a multitude of applications.¹¹

Recent investigation of nitrogen- and boron-doped graphene derivatives^{12–16} has been focused on the dopant physicochemical properties at the atomic level. A comprehensive experimental structure elucidation and charge distribution of the N- and B-doped carbon sheet at the atomic scale are still missing. It is worth mentioning that numerous theoretical studies addressing the electronic and chemical properties of the

dopant sites reported dopant charges, which differ widely in magnitude and even in sign.^{17–20} A Bader charge analysis of theoretical data predicted that the N dopant gains 1.2 e[−] rather than losing charge as expected for an n-type dopant.^{21,22} The real charge redistribution is crucial for understanding the modification of graphene chemistry upon doping,^{23,24} i.e., of the interaction of boron and nitrogen dopants with molecules and other functional moieties. The in-plane component of the dopant electrostatic force field plays a significant role in graphene charge carrier scattering,^{7,25,26} while the out-of-plane component dominates the chemical interaction and may be useful for creating selective sites for graphene functionalization with organic molecules.^{27–30}

Here, we report on a low-temperature noncontact atomic force microscopy (nc-AFM) and Kelvin probe force microscopy (KPFM) investigation with a functionalized CO-tip³¹ of individual nitrogen and boron dopants implanted in a graphene monolayer grown on SiC(0001), complemented by theoretical calculations. We evaluate the noncovalent interactions of nitrogen and boron dopants with CO molecules attached to the apex of an AFM tip with respect to the

Received: December 20, 2019

Revised: February 5, 2020

Published: February 6, 2020



graphene substrate. We map the redistribution of electron densities at C–N and C–B bonds that accompanies the incorporation of sp^2 nitrogen and boron dopants in graphene. This gives rise to net positive and negative static charges localized a few angstroms around the nitrogen and boron sites, respectively, which determine the doped graphene chemical activity through weak electrostatic forces.

METHODS

Experimental Methods. 6H-SiC(0001) samples were cut from TankeBlue research grade wafers using a diamond scribe and PEEK tipped tweezers. The samples were degassed up to 900 °C in UHV and subsequently exposed to a Si flux for 40 min. Once a sharp 3×3 LEED pattern was acquired, the graphene was grown by annealing up to 1300 °C, increasing 50 °C every 5 min. Boron doping³² was achieved by sublimating B from a commercial evaporator on the already-grown graphene at RT (a flux of 26 nA for 20 s was enough to obtain a low concentration of dopants) and a final annealing at 1150 °C for 20 min. The growth and the doping were monitored by means of LEED and STM. The temperature was controlled using a Micro-Epsilon 2MH-CF3 thermometer of a 1.6 μm spectral range with an emissivity of 0.9. N atom implantation was achieved by sputtering the graphene sample with N atoms accelerated at 120 eV and subsequent annealing to approximately 800 °C.

STM/AFM measurements were carried out in a UHV chamber equipped with a low-temperature STM/AFM with qPlus tuning fork sensor operated at 5 K (Createc GmbH). During the AFM measurements, a Pt/Ir tip mounted onto the sensor (frequency ≈ 30 kHz; stiffness ≈ 1800 N/m) was oscillated with a constant amplitude of 50 pm. To obtain high-resolution AFM/STM images, prior to the experiment, the tip was functionalized with a CO molecule gathered from a Au(111) surface. Before transfer of the CO-tip to graphene, we did several approach/retract (up to few micrometers) experiments on Au(111) to select only highly stable CO-tips for transfer to graphene. On graphene, we benchmarked CO presence at the tip apex by constant height AFM atomic-scale images at various tip-sample distances. CO-tip images lead characteristic honeycomb features of graphene whereas metallic tips display hexagonal pattern⁴⁷ (see Figure S5).

For the local contact potential difference (LCPD) mapping in the XZ plane on both dopants, 1250 KPFM measurements were performed with a bias range [–500 mV, 300 mV] in a grid of size of 3 nm \times 1 nm. The acquisition time for each parabola was 30 s. The mapping was generated by fitting each parabola by the formula $a(x-LCPD)^2 + c$ with a Python script and assigning the fitted value of the LCPD for every (x,z) position to a 25×50 grid of pixels. STM/AFM images were analyzed using WSxM software.³³

DFT Methods. Density functional theory calculations were performed using the projector-augmented wave method in the Vienna Ab initio Simulation Package (VASP).^{34,35} The surface of graphene was modeled using a supercell of 5×5 elementary cells (50 carbon atoms). The tip was modeled by the CO molecule attached to the apex gold atom of a triangular pyramid Au cluster (10 Au atoms) having Au(111) faces. The outer layer of the Au cluster and two atoms of graphene were fixed, while the rest of the system (CO molecule and adjacent Au atoms, graphene atoms beneath the tip) was allowed to fully relax.

The $3 \times 3 \times 1$ k -point grid was used to sample the Brillouin zone. The periodically repeated supercells were separated by 25 Å of vacuum. The energy cutoff for the plane-wave expansion was set to 400 eV. We used the optimized van der Waals functional optB86b-vdW³⁶ in all calculations, which provided a balanced description of van der Waals and covalent bonding in our previous studies.^{37,38} We tested also the many-body dispersion method MBD+rscs and empirical dispersion DFT+D2. In order to test robustness of our theoretical calculation, we used also the many-body dispersion MBD@rscs functional.³⁹ The interaction energies and their order for the tip above a C, N, B atoms were very similar to those obtained

using optB86b-vdW (Figure S2). The plots of the induced charge density isosurface were prepared using VESTA software⁴⁰

Hartree potential calculations were done by employing FHI-AIMS⁴¹ code, using two geometrically relaxed slabs of 180 atoms with a periodic boundary condition (PBC). The systems were allowed to relax until the remaining atomic forces reached below 10^{-2} eV/Å. The GGA-PBE⁴² functional was used as the exchange–correlation functional and a grid of $4 \times 4 \times 1$ k -points to sample the Brillouin Zone.

AFM images were calculated using the probe particle model.⁴³ The parameters of the tip were chosen to mimic a CO-tip. Namely, charge distribution of the CO molecule was mimicked by a quadrupole moment⁴⁴ with a value of $-0.1e$ and lateral stiffness of the probe particle of 0.25 N m^{-1} . The electrostatic interaction between the tip and the sample was included in the AFM calculations using the Hartree potential obtained from fully optimized total energy DFT calculations using the VASP code.³⁴ These DFT calculations were done using a $6 \times 6 \times 1$ k -point reciprocal grid in a 7×7 supercell. To simulate the dynamic of the tip, we used typical values of a qPlus sensor, oscillation amplitude $A = 100$ pm, sensor stiffness $k = 3600$ N/m, and eigenfrequency $f_0 = 30$ kHz.

RESULTS AND DISCUSSION

Structural Characterization of B- and N-Doped Graphene. We have carried out combined low-temperature (5 K) STM/nc-AFM experiments on atomically well-defined graphene, doped with single nitrogen and boron atoms in a substitutional configuration. A graphene monolayer is grown on a SiC(0001) substrate and subsequently doped with boron and nitrogen atoms in a stepwise process in ultrahigh vacuum (see Methods for details). Both boron and nitrogen atoms were implanted in low concentrations, which facilitates the study of individual dopant sites on the surface. All the experiments were performed with an STM/AFM tip-apex functionalized with a single CO molecule picked up from a nearby Au(111) substrate.

A typical STM topography of a graphene region which comprises three nitrogen dopants and one boron dopant is shown in Figure 1a. Dopants are featured as three-fold protrusions distributed randomly on the surface with no apparent preference of incorporation in the graphene lattice. Characteristics in STM features of graphene dopants are strongly dependent on the tip termination.^{4,45} We have found that functionalization of the tip with CO molecules provides a very reproducible STM contrast for several experimental

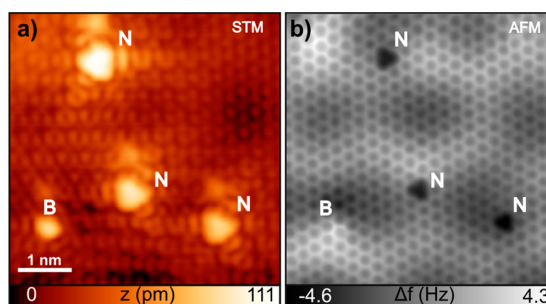


Figure 1. Graphitic boron and nitrogen dopants in graphene. STM topography (a) and constant-height nc-AFM (b) images of a graphene area with one boron and three nitrogen substitutional dopants. In nc-AFM images, boron (bottom left-hand) and nitrogen dopants are resolved as bright and dark features, respectively. STM image parameters: 200 mV, 50 pA.

sessions. The assignment of graphitic nitrogen and boron dopants is corroborated by constant-height high-resolution AFM imaging with a CO-tip of the same graphene area (Figure 1b). The periodic honeycomb structure of carbon atoms is clearly resolved together with the graphene moiré pattern on a larger length scale, which is the $6\sqrt{3} \times 6\sqrt{3}$ -R30° quasiperiodic structure of the buffer layer and is observed in both STM and AFM images, pointing out its topographic origin. The use of a nonreactive CO-tip allows us to evaluate the true topographic corrugation^{46,47} of the moiré from direct comparison of the AFM contrast at several tip-sample distances for high and low graphene areas, similarly as reported by Schwarz et al.⁴⁸ (Figure S1). With this method, we reach an estimate of 20–30 pm in good agreement with previous room-temperature AFM⁴⁹ experiments on the same surface. Interestingly, for an adequate tip-sample height, a pronounced variation of the atomic-scale contrast is observed at the dopant sites; i.e., boron and nitrogen atoms are brighter and darker than the surrounding carbon atoms, respectively. This is observed regardless of localization of the dopants in the moiré superlattice, thus allowing us to rule out any influence of the dopant hybridization with the substrate.

Next, we focus on the contrast of boron and nitrogen dopants in AFM images. Figure 2 shows a series of detailed experimental AFM images of boron (top) and nitrogen (bottom) in graphene as a function of the tip-sample separation. Hereinafter, the closest tip-sample separation

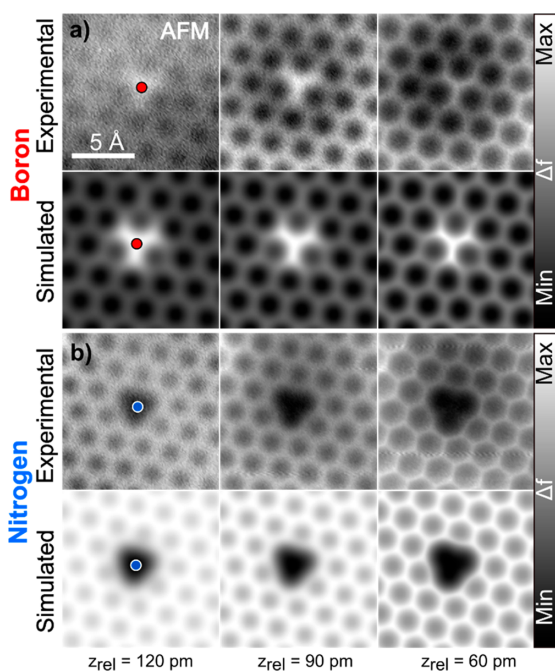


Figure 2. High-resolution AFM images on dopants with a CO-tip. Experimental (top row) and simulated (bottom row) constant-height AFM images of a single boron dopant (a) and nitrogen dopant (b) as a function of the tip-sample separation. Tip-sample distance decreases from left to right. Red and blue dots point to the position of the boron and nitrogen atoms, respectively. In the experiment, the closest tip-sample separation $z_{\text{rel}} = 0$ corresponds to a tip approach of 150 pm from the STM point (−500 mV, 50 pA).

($z_{\text{rel}} = 0$ pm) is referred to as a tip approach of 150 pm from STM point (−500 mV, 50 pA). At the largest separation (left-hand panel; $z_{\text{rel}} = 120$ pm), bright (less negative frequency shift) and dark (more negative frequency shift) features are observed at boron (red dot) and nitrogen (blue dot) sites. Upon the tip approach (centered panel; $z_{\text{rel}} = 90$ pm), the carbon hexagons of graphene are clearly resolved. The three C–B bonds around the boron atom are comparatively brighter than the surrounding C–C bonds. In contrast, no marks of C–N bonds are observed at the same tip-sample distance. At $z_{\text{rel}} = 60$ pm, all the three C–N bonds start to be resolved, while the C–B bonds appearance becomes similar to that of the C–C bonds. Interestingly, the AFM image at a close distance reveals a distortion of the carbon rings in the proximity of the dopants. Previously, similar lateral distortions were attributed to spatial variations of electrostatic potential within a molecule,⁵⁰ thus suggesting localization of electrostatic charges around dopants, as we discuss later. These characteristic contrast features in the AFM images have been observed with several different CO-tips and on dopants located at distinct moiré sites, which proves that the types of contrasts are intrinsic and unique to the doping element. Similar characteristics have been reported recently in AFM images with a CO-tip on boron- and nitrogen-doped graphene nanoribbons on Au(111)⁵¹ and attributed to the modulated local electron density caused by the substitution. Qualitatively, we observed a C–N bond length of 188 ± 8 pm and C–B bond length of 134 ± 4 pm, which differ from the observed bond length of unperturbed C–C bonds of 141 ± 2 pm (Figure S4), in perfect agreement with similar observations in B- and N-doped nanoribbons.⁵¹

We performed AFM simulations⁴³ using the optimized atomic structure and Hartree potential of boron- and nitrogen-doped graphene obtained from total energy DFT calculations (see Methods for more details and Figure 3c for visualization of the Hartree potential). The simulated AFM images are in excellent agreement with the experimental observations and fully capture the contrast of the C–B and C–N bonds (Figure 2) as a function of the tip-sample separation. The optimized structure has negligible out-of-plane relaxation of the dopant, which allows us to exclude any role of topographic effects in the AFM contrast. To understand the origin of the contrast difference between boron and nitrogen dopants, the mechanism of high-resolution imaging has to be considered.^{43,52,53} The CO-tip brought in the vicinity of the sample is sensitive to the total charge density distribution within the inspected system, and its variation can significantly affect the contrast. Intuitively, one can simplify the complex CO-tip charge distribution as a negatively effective charged tip. Thus, when probing an inhomogeneous charge distribution, the tip is repelled (less negative frequency shift) from sites of excess electron density, whereas it is attracted (more negative frequency shift) to those which have a positive charge. Therefore, the apparent contrast in the AFM images shows a substantial modification of the charge density localized at the C–B and C–N bonds.

Charge Distribution at Dopant Sites. This notion is substantiated by our KPFM measurements, also performed with a CO-tip. Figure 3a displays Kelvin parabolas, $\Delta f(V, z_{\text{const}})$, acquired at a constant height over boron (red), nitrogen (blue), and carbon (yellow) atoms. We observe a strong variation of the local potential difference (LCPD) measured above the dopant atoms, compared to carbon atoms

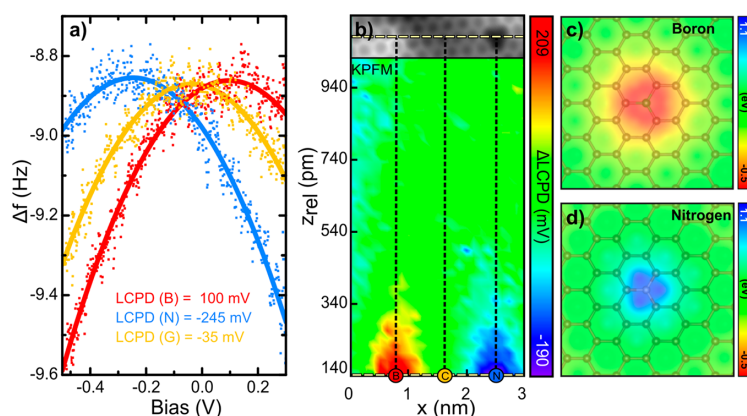


Figure 3. Net charge at the dopant sites in graphene. (a) KPFM parabolas above boron (red), carbon (yellow), and nitrogen (blue) atoms at the same tip–sample distance. KPFM plots are fitted with a parabolic dependence to obtain the LCPD value. (b) LCPD x - z map at different tip–sample separations z along a line crossing boron and nitrogen atoms (yellow dashed line in the inset AFM image). Each pixel corresponds with the fitted LCPD value of the KPFM parabola acquired in every (x , z) position. Errors in LCPD fittings are about 1.5 mV. (c, d) Calculated Hartree potential of single boron- and nitrogen-dopants in graphene.

of graphene, which we attribute primarily to the interaction of the CO-tip with inhomogeneous charge distribution. The LCPD over the boron/nitrogen dopant is shifted to a higher/lower value reflecting a decrease/increase of the local work function, respectively, induced by variation of the surface dipole around the dopants.^{54,55}

To probe the spatial distribution of the net charges around the dopants, we acquired $\Delta f(V, x, z)$ spectra at different tip–sample separations z in the plane perpendicular to graphene and along the line crossing boron and nitrogen dopants (top AFM image in Figure 3b). In a posterior analysis, for each $\Delta f(V)$ curve, we determined the LCPD values by fitting. To extract the local impact of the dopants with respect to pristine graphene, we intentionally subtract the background LCPD signal obtained on pristine graphene areas. After such processing, we plotted a LCPD difference x - z map with respect to graphene (Δ LCPD x - z). At tip–sample height $z_{\text{rel}} = 140$ pm, the boron and nitrogen atoms show almost equal magnitudes of Δ LCPD but with opposite signs (Figure 3b). The sign reflects localization of positive and negative net charges on nitrogen and boron sites, respectively. On the other hand, the similar magnitude indicates a comparable level of opposite charge doping by boron and nitrogen, in good agreement with previous observations.^{2,3} Quantitatively, LCPD values crucially depend on the mesoscopic tip termination due to long-range electrostatic forces,⁵⁶ but in repeated experimental sessions, we observed similar qualitative LCPD as described above, i.e., equal but opposite values for nitrogen and boron with respect to graphene, since the shift is always determined by the direction of the dipole induced by the dopant.^{57,58}

In addition, at the selected separations, a negligible charge redistribution or transfer is observed through the CO molecule–dopant contact (Figure S3). Thus, we unambiguously interpret the observed contrast as a variation of the work function in the vicinity of the dopants. The Δ LCPD value on both dopants decreases continuously upon tip separations larger than $z_{\text{rel}} = 290$ pm, where the average graphene work function prevails. The Δ LCPD x - z map shows the lateral and

vertical confinement of a net positive/negative charge in a small volume centered on the dopant atom.

These experimental observations are fully supported by the total energy DFT calculations. The presence of a negative/positive net charge on boron/nitrogen dopants is evident from the calculated Hartree potential (Figure 3c,d). However, a quantitative agreement between KPFM experiments and theoretical analysis is still missing and beyond the scope of this study. These charges are localized at the atom sites and extend only a few angstroms into the graphene basal plane, which is fully consistent with the spatial confinement of the charge observed in the LCPD map. The net charge on the boron/nitrogen dopants originates from acceptance/donation of an electron to the graphene pi-band^{32,59} and subsequent electronic redistribution.

Chemical Properties of Individual Dopants. Finally, we focus on the chemical properties of the dopants. The force interaction between the CO molecule attached to the AFM tip apex and the incorporated dopants is investigated by means of site-specific $\Delta f(z)$ spectroscopy. $\Delta f(z)$ values above nitrogen (blue) and boron (red) atoms are displayed in Figure 4a and b, respectively, in addition to a reference $\Delta f(z)$ above a nearby carbon atom (yellow). No significant difference between the dopants and the reference carbon is seen in the Δf at larger distances ($z_{\text{rel}} > 250$ pm). For smaller separations, a difference in Δf becomes apparent. This difference is the largest at the minima of Δf for each atom (z_{rel} about 75 pm). Qualitatively, we found that the minimum Δf on nitrogen shows a more negative frequency shift, followed by carbon and boron atoms. At closer separations where Pauli repulsion starts affecting the total interaction, the Δf measured on dopants converges to that of nearby carbon, due to the interplay of electrostatic interaction and Pauli repulsion plus the different van der Waals radii of the atoms.⁵¹ The $\Delta f(z)$ spectroscopy fully agrees with the observed atomic-scale contrast on dopants shown in Figure 2.

We quantify the effect of doping on graphene chemical properties by calculating the forces from the experimental $\Delta f(z)$ plot.⁶⁰ Dopant-independent force components were removed by subtraction of the $\Delta f(z)$ measured on top of a

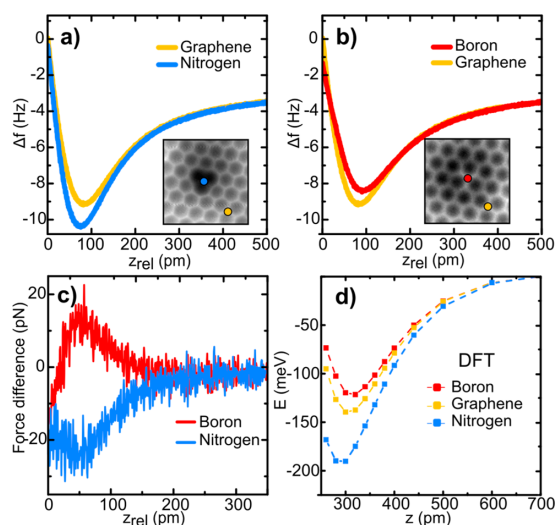


Figure 4. Quantification of interaction of graphene dopants with CO molecule. (a, b) Site-specific $\Delta f(z)$ plots on nitrogen (blue), boron (red), and carbon (yellow) atoms with a CO-tip. Colored circles indicate the exact site of acquisition in the corresponding AFM images in the insets. (c) Force difference between the CO-tip and the boron (red) and nitrogen dopants (blue), with the CO-carbon reference subtracted. (d) DFT-calculated interaction energies between a CO-tip and nitrogen (blue), boron (red), and carbon (yellow) atoms in graphene. Here, the z coordinate indicates the distance between the graphene layer and the oxygen atom in the CO-tip.

carbon atom before the calculation process. Figure 4c shows the force difference of nitrogen (blue line) and boron (red line) dopants with respect to carbon atoms, sensed by the CO-tip. We observe the augmented interaction of CO with graphitic nitrogen by approximately 25 pN. On the other hand, the interaction of CO with the boron dopant is reduced by approximately 15 pN. Despite these rather small force differences, AFM with a CO-tip demonstrates being a technique sensitive enough to visualize single dopants in graphene and their chemical activity.

This observation is in line with DFT+vdW calculations of the tip–graphene interaction. We mimic the experimental setup by the Au(111)-CO pyramidal-tip above a 5×5 graphene lattice in which single nitrogen and boron atoms are localized at graphitic sites. Figure 4d displays the vertical component for the calculated tip–sample interaction energy which reproduces the experimental findings. The calculation yields the highest interaction energy for the CO-tip above the nitrogen atom ($E_N \approx 190$ meV) followed by the carbon atom ($E_C \approx 140$ meV) and the boron atom ($E_B \approx 120$ meV). Note that the tip–graphene system is allowed to fully relax; i.e., only the last plane of the tip Au atoms and carbon atoms distant from the tip are fixed during the calculation. The exact value of the calculated interaction energy is quantitatively sensitive to the choice of the functional used for a description of the van der Waals interaction, which is not covered by standard exchange–correlation functionals as a generalized gradient approximation (GGA). Nevertheless, the order $E_N > E_C > E_B$ and energetic difference between the atoms remain the same for various inspected functionals (see Figure S2 and Methods for more details). Moreover, the calculation shows that the van

der Waals interaction is very uniform above the doped graphene. The differences in the interaction are thus governed by electrostatic forces between the tip and charge density localized around the respective atomic site.

CONCLUSIONS

In summary, we have investigated the physicochemical properties of single substitutional N and B dopants in a graphene monolayer at the atomic-scale by means of combined AFM and KPFM measurements corroborated with DFT simulations. The very good agreement of our theoretical calculations with the experimental findings provides a detailed understanding of the local charge distribution of single dopants. We evaluated the weak chemical interactions of nitrogen and boron dopants with single CO molecules attached to the tip-apex by means of experimental measurements of site-specific force spectroscopy and DFT calculations. Our results demonstrate the divergent chemical activity of nitrogen and boron impurities incorporated into graphene and provide a deeper insight for a precise chemical functionalization of graphene derivatives.

ASSOCIATED CONTENT

Supporting Information

The Supporting Information is available free of charge at <https://pubs.acs.org/doi/10.1021/acssuschemeng.9b07623>.

Figure S1: Moiré corrugation estimation. Figure S2: Comparison of interaction energy and force for different vdW functional. Figure S3: Analysis of the charge redistribution in the CO–dopant junction. Figure S4: Analysis of bond distortion. Figure S5: AFM with metallic tip. (PDF)

AUTHOR INFORMATION

Corresponding Authors

Pavel Jelínek – Regional Centre of Advanced Technologies and Materials, Faculty of Science, Palacký University Olomouc, 78371 Olomouc, Czech Republic; Institute of Physics, Czech Academy of Sciences, 16200 Prague, Czech Republic;

orcid.org/0000-0002-5645-8542; Email: jelinekp@fzu.cz

Martin Švec – Regional Centre of Advanced Technologies and Materials, Faculty of Science, Palacký University Olomouc, 78371 Olomouc, Czech Republic; Institute of Physics, Czech Academy of Sciences, 16200 Prague, Czech Republic; Email: svec@fzu.cz

Bruno de la Torre – Regional Centre of Advanced Technologies and Materials, Faculty of Science, Palacký University Olomouc, 78371 Olomouc, Czech Republic; Institute of Physics, Czech Academy of Sciences, 16200 Prague, Czech Republic; orcid.org/0000-0002-6462-6833; Email: bdelatorre@fzu.cz

Authors

Benjamin Mallada – Regional Centre of Advanced Technologies and Materials, Faculty of Science, Palacký University Olomouc, 78371 Olomouc, Czech Republic; Institute of Physics, Czech Academy of Sciences, 16200 Prague, Czech Republic; orcid.org/0000-0002-8209-9977

Shayan Edalatmanesh – Regional Centre of Advanced Technologies and Materials, Faculty of Science, Palacký University Olomouc, 78371 Olomouc, Czech Republic

Petr Lazar – Regional Centre of Advanced Technologies and Materials, Faculty of Science, Palacký University Olomouc, 78371 Olomouc, Czech Republic; orcid.org/0000-0002-7312-3656

Jesus Redondo – Institute of Physics, Czech Academy of Sciences, 16200 Prague, Czech Republic; Faculty of Mathematics and Physics, Charles University, 180 00 Prague, Czech Republic; orcid.org/0000-0002-8147-689X

Aurelio Gallardo – Institute of Physics, Czech Academy of Sciences, 16200 Prague, Czech Republic; Faculty of Mathematics and Physics, Charles University, 180 00 Prague, Czech Republic; orcid.org/0000-0001-6544-7637

Radek Zbořil – Regional Centre of Advanced Technologies and Materials, Faculty of Science, Palacký University Olomouc, 78371 Olomouc, Czech Republic; Institute of Organic Chemistry and Biochemistry, Czech Academy of Sciences, 16610 Prague 6, Czech Republic; orcid.org/0000-0002-3147-2196

Complete contact information is available at:

<https://pubs.acs.org/10.1021/acssuschemeng.9b07623>

Author Contributions

The manuscript was written through contributions of all authors. All authors have given approval to the final version of the manuscript.

Notes

The authors declare no competing financial interest.

ACKNOWLEDGMENTS

Work was supported by GACR 18-09914S and Operational Programme Research, Development and Education financed by the European Structural and Investment Funds and the Czech Ministry of Education, Youth and Sports (Project No. CZ.02.1.01/0.0/0.0/16_019/0000754). P.J. acknowledges support from the Praemium Academie of the Academy of Science of the Czech Republic. The authors gratefully acknowledge the support from the EXPRO 19-27454X project from the Czech Science Foundation (GA-CR). M.Š. acknowledges the support of the Czech Grant Agency No. 17-24210Y.

REFERENCES

- (1) Schiros, T.; Nordlund, D.; Palova, L.; Zhao, L.; Levendorf, M.; Jaye, C.; Reichman, D.; Park, J.; Hybertsen, M.; Pasupathy, A. Atomistic Interrogation of B–N Co-Dopant Structures and Their Electronic Effects in Graphene. *ACS Nano* **2016**, *10* (7), 6574–6584.
- (2) Zhao, L.; He, R.; Rim, K. T.; Schiros, T.; Kim, K. S.; Zhou, H.; Gutierrez, C.; Chockalingam, S. P.; Arguello, C. J.; Palova, L.; et al. Visualizing Individual Nitrogen Dopants in Monolayer Graphene. *Science* **2011**, *333* (6045), 999–1003.
- (3) Zhao, L.; Levendorf, M.; Goncher, S.; Schiros, T.; Pálková, L.; Zabet-Khosousi, A.; Rim, K. T.; Gutiérrez, C.; Nordlund, D.; Jaye, C.; et al. Local Atomic and Electronic Structure of Boron Chemical Doping in Monolayer Graphene. *Nano Lett.* **2013**, *13* (10), 4659–4665.
- (4) Telychko, M.; Mutombo, P.; Merino, P.; Hapala, P.; Ondráček, M.; Bocquet, F. C.; Sforzini, J.; Stetsovych, O.; Vondráček, M.; Jelínek, P.; et al. Electronic and Chemical Properties of Donor, Acceptor Centers in Graphene. *ACS Nano* **2015**, *9* (9), 9180–9187.
- (5) Li, J.; Lin, L.; Rui, D.; Li, Q.; Zhang, J.; Kang, N.; Zhang, Y.; Peng, H.; Liu, Z.; Xu, H. Q. Electron–Hole Symmetry Breaking in Charge Transport in Nitrogen-Doped Graphene. *ACS Nano* **2017**, *11* (5), 4641–4650.
- (6) Nigar, S.; Zhou, Z.; Wang, H.; Imtiaz, M. Modulating the Electronic and Magnetic Properties of Graphene. *RSC Adv.* **2017**, *7* (81), 51546–51580.
- (7) Hage, F. S.; Hardcastle, T. P.; Gjerding, M. N.; Kepaptsoglou, D. M.; Seabourne, C. R.; Winther, K. T.; Zan, R.; Amani, J. A.; Hofsaess, H. C.; Bangert, U.; et al. Local Plasmon Engineering in Doped Graphene. *ACS Nano* **2018**, *12* (2), 1837–1848.
- (8) Błoński, P.; Tuček, J.; Sofer, Z.; Mazánek, V.; Petr, M.; Pumera, M.; Otyepka, M.; Zbořil, R. Doping with Graphitic Nitrogen Triggers Ferromagnetism in Graphene. *J. Am. Chem. Soc.* **2017**, *139* (8), 3171–3180.
- (9) Georgakilas, V.; Tiwari, J. N.; Kemp, K. C.; Perman, J. A.; Bourlinos, A. B.; Kim, K. S.; Zbořil, R. Noncovalent Functionalization of Graphene and Graphene Oxide for Energy Materials, Biosensing, Catalytic, and Biomedical Applications. *Chem. Rev.* **2016**, *116* (9), 5464–5519.
- (10) Kuila, T.; Bose, S.; Mishra, A. K.; Khanra, P.; Kim, N. H.; Lee, J. H. Chemical Functionalization of Graphene and Its Applications. *Prog. Mater. Sci.* **2012**, *57* (7), 1061–1105.
- (11) Wang, H.; Maiyalagan, T.; Wang, X. Review on Recent Progress in Nitrogen-Doped Graphene: Synthesis, Characterization, and Its Potential Applications. *ACS Catal.* **2012**, *2* (5), 781–794.
- (12) Agnoli, S.; Favaro, M. Doping Graphene with Boron: A Review of Synthesis Methods, Physicochemical Characterization, and Emerging Applications. *J. Mater. Chem. A* **2016**, *4* (14), 5002–5025.
- (13) Lazar, P.; Zbořil, R.; Pumera, M.; Otyepka, M. Chemical Nature of Boron and Nitrogen Dopant Atoms in Graphene Strongly Influences Its Electronic Properties. *Phys. Chem. Chem. Phys.* **2014**, *16* (27), 14231–14235.
- (14) Panchakarla, L. S.; Subrahmanyam, K. S.; Saha, S. K.; Govindaraj, A.; Krishnamurthy, H. R.; Waghmare, U. V.; Rao, C. N. R. Synthesis, Structure, and Properties of Boron- and Nitrogen-Doped Graphene. *Adv. Mater.* **2009**, *21* (46), 4726–4730.
- (15) Zheng, Y.; Jiao, Y.; Ge, L.; Jaroniec, M.; Qiao, S. Z. Two-Step Boron and Nitrogen Doping in Graphene for Enhanced Synergistic Catalysis. *Angew. Chem., Int. Ed.* **2013**, *52* (11), 3110–3116.
- (16) Rao, C. N. R.; Gopalakrishnan, K.; Govindaraj, A. Synthesis, Properties and Applications of Graphene Doped with Boron, Nitrogen and Other Elements. *Nano Today* **2014**, *9* (3), 324–343.
- (17) Usachov, D.; Vilkov, O.; Gruneis, A.; Haberer, D.; Fedorov, A.; Adamchuk, V. K.; Preobrajenski, A. B.; Dudin, P.; Barinov, A.; Oehzelt, M.; Laubschat, C.; Vyalikh, D. V. Nitrogen-Doped Graphene: Efficient Growth, Structure, and Electronic Properties. *Nano Lett.* **2011**, *11* (12), 5401–5407.
- (18) Velez-Fort, E.; Mathieu, C.; Pallechi, E.; Pigneur, M.; Silly, M. G.; Belkhou, R.; Marangolo, M.; Shukla, A.; Sirotti, F.; Ouerghi, A. Epitaxial Graphene on 4H-SiC(0001) Grown under Nitrogen Flux: Evidence of Low Nitrogen Doping and High Charge Transfer. *ACS Nano* **2012**, *6* (12), 10893–10900.
- (19) Joubert, F.; Tison, Y.; Lagoute, J.; Dumont, J.; Cabosart, D.; Zheng, B.; Repain, V.; Chacon, C.; Girard, Y.; Botello-Mendez, A. R.; Rousset, S.; Sporcken, R.; Charlier, J. C.; Henrard, L. Localized state and charge transfer in nitrogen-doped graphene. *Phys. Rev. B: Condens. Matter Mater. Phys.* **2012**, *85* (16), 161408.
- (20) Schiros, T.; Nordlund, D.; Palova, L.; Prezzi, D.; Zhao, L. Y.; Kim, K. S.; Wurstbauer, U.; Gutierrez, C.; Delongchamp, D.; Jaye, C.; Fischer, D.; Ogasawara, H.; Pettersson, L. G. M.; Reichman, D. R.; Kim, P.; Hybertsen, M. S.; Pasupathy, A. N. Connecting Dopant Bond Type with Electronic Structure in N-Doped Graphene. *Nano Lett.* **2012**, *12* (8), 4025–4031.
- (21) Wood, K. N.; Christensen, S. T.; Nordlund, D.; Dameron, A. A.; Ngo, C.; Dinh, H.; Gennett, T.; O’Hayre, R.; Pylypenko, S. Spectroscopic investigation of nitrogen-functionalized carbon materials. *Surf. Interface Anal.* **2016**, *48* (5), 283–292.
- (22) Muhich, C. L.; Westcott, J. Y.; Morris, T. C.; Weimer, A. W.; Musgrave, C. B. The Effect of N and B Doping on Graphene and the Adsorption and Migration Behavior of Pt Atoms. *J. Phys. Chem. C* **2013**, *117* (20), 10523–10535.

- (23) Zhang, L. P.; Xia, Z. H. Mechanisms of Oxygen Reduction Reaction on Nitrogen-Doped Graphene for Fuel Cells. *J. Phys. Chem. C* **2011**, *115* (22), 11170–11176.
- (24) Zhang, L. P.; Niu, J. B.; Dai, L.; Xia, Z. H. Effect of Microstructure of Nitrogen-Doped Graphene on Oxygen Reduction Activity in Fuel Cells. *Langmuir* **2012**, *28* (19), 7542–7550.
- (25) Marconcini, P.; Cresti, A.; Triozon, F.; Fiori, G.; Biel, B.; Niquet, Y. M.; Macucci, M.; Roche, S. Atomistic Boron-Doped Graphene Field-Effect Transistors: A Route toward Unipolar Characteristics. *ACS Nano* **2012**, *6* (9), 7942–7947.
- (26) Lherbier, A.; Botello-Mendez, A. R.; Charlier, J. C. Electronic and Transport Properties of Unbalanced Sublattice N-Doping in Graphene. *Nano Lett.* **2013**, *13* (4), 1446–1450.
- (27) Kong, X. K.; Chen, C. L.; Chen, Q. W. Doped graphene for metal-free catalysis. *Chem. Soc. Rev.* **2014**, *43* (8), 2841–2857.
- (28) Georgakilas, V.; Otyepka, M.; Bourlinos, A. B.; Chandra, V.; Kim, N.; Kemp, K. C.; Hobza, P.; Zboril, R.; Kim, K. S. Functionalization of Graphene: Covalent and Non-Covalent Approaches, Derivatives and Applications. *Chem. Rev.* **2012**, *112* (11), 6156–6214.
- (29) de la Torre, B.; Svec, M.; Hapala, P.; Redondo, J.; Krejci, O.; Lo, R.; Manna, D.; Sarmah, A.; Nachtigallova, D.; Tucek, J.; Blonski, P.; Otyepka, M.; Zboril, R.; Hobza, P.; Jelinek, P. Non-covalent control of spin-state in metal-organic complex by positioning on N-doped graphene. *Nat. Commun.* **2018**, *9*, 2831.
- (30) Pham, V. D.; Lagoutte, J.; Mouhoub, O.; Joucken, F.; Repain, V.; Chacon, C.; Bellec, A.; Girard, Y.; Rousset, S. Electronic Interaction between Nitrogen-Doped Graphene and Porphyrin Molecules. *ACS Nano* **2014**, *8* (9), 9403–9409.
- (31) Gross, L.; Mohn, F.; Moll, N.; Liljeroth, P.; Meyer, G. The Chemical Structure of a Molecule Resolved by Atomic Force Microscopy. *Science* **2009**, *325* (5944), 1110–1114.
- (32) Sforzini, J.; Telychko, M.; Krejci, O.; Vondracek, M.; Svec, M.; Bocquet, F. C.; Tautz, F. S. Transformation of metallic boron into substitutional dopants in graphene on 6H-SiC(0001). *Phys. Rev. B: Condens. Matter Mater. Phys.* **2016**, *93* (4), 041302.
- (33) Horcas, I.; Fernandez, R.; Gomez-Rodriguez, J. M.; Colchero, J.; Gomez-Herrero, J.; Baro, A. M. WSXM: A software for scanning probe microscopy and a tool for nanotechnology. *Rev. Sci. Instrum.* **2007**, *78* (1), 013705.
- (34) Blochl, P. E. Projector Augmented-Wave Method. *Phys. Rev. B: Condens. Matter Mater. Phys.* **1994**, *50* (24), 17953–17979.
- (35) Kresse, G.; Joubert, D. From ultrasoft pseudopotentials to the projector augmented-wave method. *Phys. Rev. B: Condens. Matter Mater. Phys.* **1999**, *59* (3), 1758–1775.
- (36) Klimes, J.; Bowler, D. R.; Michaelides, A. Van der Waals density functionals applied to solids. *Phys. Rev. B: Condens. Matter Mater. Phys.* **2011**, *83* (19), 195131.
- (37) Lazar, P.; Karlicky, F.; Jurecka, P.; Kocman, M.; Otyepkova, E.; Safarova, K.; Otyepka, M. Adsorption of Small Organic Molecules on Graphene. *J. Am. Chem. Soc.* **2013**, *135* (16), 6372–6377.
- (38) Lazar, P.; Martincova, J.; Otyepka, M. Structure, dynamical stability, and electronic properties of phases in TaS₂ from a high-level quantum mechanical calculation. *Phys. Rev. B: Condens. Matter Mater. Phys.* **2015**, *92* (22), 224104.
- (39) Tkatchenko, A.; DiStasio, R. A.; Car, R.; Scheffler, M. Accurate and Efficient Method for Many-Body van Der Waals Interactions. *Phys. Rev. Lett.* **2012**, *108* (23), 236402.
- (40) Momma, K.; Izumi, F. VESTA 3 for three-dimensional visualization of crystal, volumetric and morphology data. *J. Appl. Crystallogr.* **2011**, *44*, 1272–1276.
- (41) Blum, V.; Gehrke, R.; Hanke, F.; Havu, P.; Havu, V.; Ren, X.; Reuter, K.; Scheffler, M. Ab Initio Molecular Simulations with Numeric Atom-Centered Orbitals. *Comput. Phys. Commun.* **2009**, *180* (11), 2175–2196.
- (42) Perdew, J. P.; Burke, K.; Ernzerhof, M. Generalized Gradient Approximation Made Simple. *Phys. Rev. Lett.* **1996**, *77* (18), 3865–3868.
- (43) Hapala, P.; Kichin, G.; Wagner, C.; Tautz, F. S.; Temirov, R.; Jelinek, P. Mechanism of high-resolution STM/AFM imaging with functionalized tips. *Phys. Rev. B: Condens. Matter Mater. Phys.* **2014**, *90* (8), 085421.
- (44) Peng, J.; Guo, J.; Hapala, P.; Cao, D.; Ma, R.; Cheng, B.; Xu, L.; Ondracek, M.; Jelinek, P.; Wang, E.; et al. Weakly Perturbative Imaging of Interfacial Water with Submolecular Resolution by Atomic Force Microscopy. *Nat. Commun.* **2018**, *9* (1), 2831.
- (45) Martin-Recio, A.; Romero-Muniz, C.; Noug, P.; Perez, R.; Gomez-Rodriguez, J. M. Purely substitutional nitrogen on graphene/Pt(111) unveiled by STM and first principles calculations. *Nanoscale* **2016**, *8* (40), 17686–17693.
- (46) de la Torre, B.; Ellner, M.; Pou, P.; Nicoara, N.; Perez, R.; Gomez-Rodriguez, J. M. Atomic-Scale Variations of the Mechanical Response of 2D Materials Detected by Noncontact Atomic Force Microscopy. *Phys. Rev. Lett.* **2016**, *116* (24), 245502.
- (47) Boneschanscher, M. P.; van der Lit, J.; Sun, Z. X.; Swart, I.; Liljeroth, P.; Vanmaekelbergh, D. Quantitative Atomic Resolution Force Imaging on Epitaxial Graphene with Reactive and Nonreactive AFM Probes. *ACS Nano* **2012**, *6* (11), 10216–10221.
- (48) Schwarz, M.; Riss, A.; Garnica, M.; Ducke, J.; Deimel, P. S.; Duncan, D. A.; Thakur, P. K.; Lee, T. L.; Seitsonen, A. P.; Barth, J. V.; Allegretti, F.; Auwärter, W. Corrugation in the Weakly Interacting Hexagonal-BN/Cu(111) System: Structure Determination by Combining Noncontact Atomic Force Microscopy and X-ray Standing Waves. *ACS Nano* **2017**, *11* (9), 9151–9161.
- (49) Telychko, M.; Berger, J.; Majzik, Z.; Jelinek, P.; Svec, M. Graphene on SiC(0001) inspected by dynamic atomic force microscopy at room temperature. *Beilstein J. Nanotechnol.* **2015**, *6*, 901–906.
- (50) Hapala, P.; Svec, M.; Stetsovych, O.; van der Heijden, N. J.; Ondracek, M.; van der Lit, J.; Mutombo, P.; Swart, I.; Jelinek, P. Mapping the electrostatic force field of single molecules from high-resolution scanning probe images. *Nat. Commun.* **2016**, *7* (1), 11560.
- (51) Kawai, S.; Nakatsuka, S.; Hatakeyama, T.; Pawlak, R.; Meier, T.; Tracey, J.; Meyer, E.; Foster, A. S. Multiple heteroatom substitution to graphene nanoribbon. *Sci. Adv.* **2018**, *4* (4), eaar7181.
- (52) Moll, N.; Gross, L.; Mohn, F.; Curioni, A.; Meyer, G. The mechanisms underlying the enhanced resolution of atomic force microscopy with functionalized tips. *New J. Phys.* **2010**, *12*, 125020.
- (53) Ellner, M.; Pavlicek, N.; Pou, P.; Schuler, B.; Moll, N.; Meyer, G.; Gross, L.; Perez, R. The Electric Field of CO Tips and Its Relevance for Atomic Force Microscopy. *Nano Lett.* **2016**, *16* (3), 1974–1980.
- (54) Mohn, F.; Gross, L.; Moll, N.; Meyer, G. Imaging the charge distribution within a single molecule. *Nat. Nanotechnol.* **2012**, *7* (4), 227–231.
- (55) Gross, L.; Mohn, F.; Liljeroth, P.; Repp, J.; Giessibl, F. J.; Meyer, G. Measuring the Charge State of an Adatom with Noncontact Atomic Force Microscopy. *Science* **2009**, *324* (5933), 1428–1431.
- (56) Bocquet, F.; Nony, L.; Loppacher, C. Polarization effects in noncontact atomic force microscopy: A key to model the tip-sample interaction above charged adatoms. *Phys. Rev. B: Condens. Matter Mater. Phys.* **2011**, *83* (3), 035411.
- (57) Albrecht, F.; Repp, J.; Fleischmann, M.; Scheer, M.; Ondracek, M.; Jelinek, P. Probing Charges on the Atomic Scale by Means of Atomic Microscopy. *Phys. Rev. Lett.* **2015**, *115* (7), 076101.
- (58) Gross, L.; Schuler, B.; Mohn, F.; Moll, N.; Pavlicek, N.; Steurer, W.; Scivetti, L.; Kotsis, K.; Persson, M.; Meyer, G. Investigating atomic contrast in atomic force microscopy and Kelvin probe force microscopy on ionic systems using functionalized tips. *Phys. Rev. B: Condens. Matter Mater. Phys.* **2014**, *90* (15), 155455.
- (59) Sforzini, J.; Hapala, P.; Franke, M.; van Straaten, G.; Stohr, A.; Link, S.; Soubatch, S.; Jelinek, P.; Lee, T. L.; Starke, U.; Svec, M.; Bocquet, F. C.; Tautz, F. S. Structural and Electronic Properties of Nitrogen-Doped Graphene. *Phys. Rev. Lett.* **2016**, *116* (12), 126805.

(60) Giessibl, F. J. A direct method to calculate tip-sample forces from frequency shifts in frequency-modulation atomic force microscopy. *Appl. Phys. Lett.* **2001**, *78* (1), 123–125.

4.2 Direct imaging of σ -hole

This section introduces the first time visualization in the real space of the anisotropic charge distribution known as σ -hole in single Br atoms. The comparison of two equivalent molecular systems, one with a fluorine atom (without σ -hole) and one with a bromine atom displaying σ -hole, provided not only the visualization but also the capstone for a more general theory of KPFM developed in parallel with the experiment. Hence, this section explores the limits of nc-AFM for imaging systems with a rich electrostatic behavior, the potential uses of KPFM in the determination of anisotropic charge distributions in single atoms or molecules, the effect of the tip functionalization, and the need for a solid theoretical understanding of the origin of KPFM signal.

Halogen bonding

Noncovalent interactions (NCIs) play a fundamental role in many chemical systems and are present throughout the natural world. Unlike covalent bonding, which involves the sharing of electrons between atoms, noncovalent interactions are formed without the sharing of electrons. Consequently, these interactions often involve weaker attractive forces, such as hydrogen bonding, electrostatic interactions, van der Waals forces, and halogen bonding, which display more localized and lower energy states in comparison to covalent bonds. Moreover, unlike covalent bonding, which is highly directional, noncovalent interactions can be highly dependent on molecular orientation and can lead to a range of intricate structures within chemical systems. In biology, non-covalent interactions mediate in several critical processes, mostly through hydrogen bonding, involved for example in protein folding[64].

Halogen bonding, a subset of non-covalent interactions involving the interaction of halogen atoms (e.g. F, Cl, Br...) with a Lewis base (i.e. elements containing electron lone pairs), has attracted increasing attention in recent years due to its unique properties in

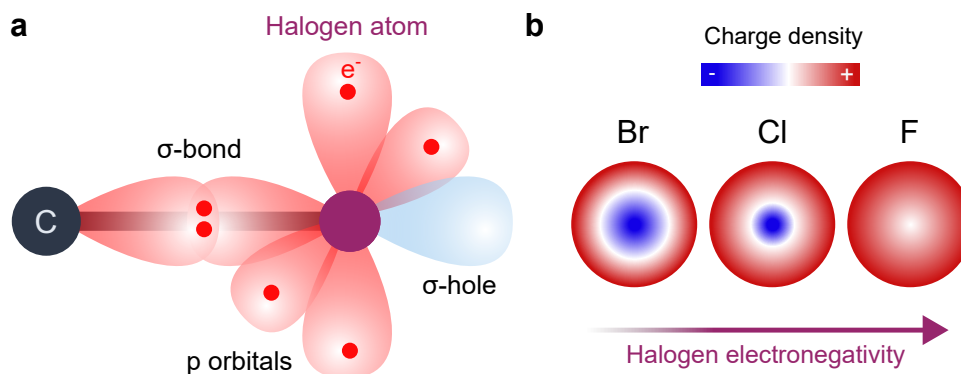


Figure 4.6: **a.** Diagram of the 5 p orbitals of an halogen atom. The four orbitals in xy are occupied with 4 e^- , one orbital in z is bonded with a carbon atom through a σ -bond, and finally, one empty orbital will define the electron-depleted region surrounded by an electron-rich volume, defining the σ -hole. **b.** Pictorial representation of the magnitude of the σ -hole (blue region), visualized in the z direction, as a function of the electronegativity of the halogen atom. More electronegative atoms develop smaller electron-depleted regions. The color scale corresponds with red having more a higher electron density and blue less.

regards of the directionality and strength of the interaction [82]. Halogen bonding involves the electrostatic interaction between a halogen atom and an electron donor, such as a nitrogen or oxygen atom, and shares some common characteristics with hydrogen bonding as the directionality and the electrostatic origin. Halogen bonding has been utilized into drug molecules for increasing their binding affinity to specific receptors, as demonstrated in the design of HIV-1 integrase inhibitors[83].

Halogen bonding and σ -hole

The origin of the halogen bond can be traced down to the formation of an electron-depleted region on the halogen atom, covalently bonded to another element, usually carbon, where the σ -hole, emerges as an electrophilic site that can interact with negatively charged Lewis bases (i.e. nucleophilic groups, atoms with single lone pairs, etc). The σ -hole arises due to the anisotropy of the electron distribution around the halogen atom, which creates a region of the positive electrostatic potential on the direction of the covalent bond axis as shown in Fig. 4.6. The σ -hole is responsible for the high directionality and specificity of halogen

bonding between electron-depleted halogens and electron-rich groups in other molecules [82]. The interaction that stems from the development of σ -holes is strongest with small and electronegative halogen atoms, such as iodine or bromine, which have a larger and more positive σ hole. However, a direct evidence of its existence has been missing since its conception roughly 20 years ago in the works of Clark, Auffinger and Politzer [82, 84, 85]. In this section, it will be introduced the experimental setup, based on STM, ncAFM and KPFM, that provides a real-space resolution of the σ -hole, using a tetragonal molecule with phenyl groups where each phenyl contains one halogen (bromine or fluorinated) joined by a single bond to the phenyl group. This configuration provides a scaffold of 1 nm of height, where an isolated halogenated atom points upwards the σ -hole in such a way that is perpendicular to the surface

The tetrakis-configured precursors, tetrakis(4-bromophenyl) methane (4BrPhM) and tetrakis(4-fluorophenyl) methane (4FPhM), were individually deposited using thermal sublimation using two separate tantalum pockets maintained at 450 K on an Ag(111) surface, held at room temperature in UHV. To obtain an accurate visualization of the σ -hole without interference from surface corrugation, the Ag(111) surface was chosen. Other surfaces, such as Au(111) with its alternating fcc and hcp of the herringbone reconstruction, or Cu(111) known for its high catalytic reactivity that leads to molecule dehalogenation, could potentially impact the molecule's adsorption. To ensure the integrity of the experiments and prevent cross-contamination, the molecules were deposited separately at different times and each experiment was conducted independently. The coverage of each molecule type was adjusted to approximately 20-30% of the surface leading to the formation of rectangular islands driven primarily by electrostatic interactions as can be seen in STM topography images (Fig. 4.7). Both molecules conduct poorly, mostly because of their 3D character and the subsequent distance from the Ag (111) surface (around 1 nm). 4BrPhM and 4FPhM molecules exhibit a subtle height difference between them, with the

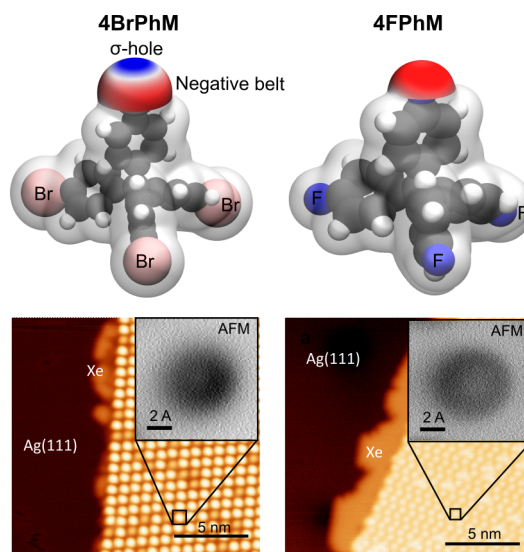


Figure 4.7: (Top row) The molecular models of 4BrPhM and 4FPhM, each containing 4 halogen atoms, three of them acting as a supporting scaffold, and one protruding out of the plane. (Bottom row) STM topography image of the molecules ordering in self-assembled ordered islands. The insets show the lack of features in nc-AFM for both cases.

first having a distance between the surface and the uppermost atom of $z = 1050$ pm and the second molecule $z = 980$ pm (see Fig. 4.8-a,b). This height difference originates in the different sizes of the halogen atoms, but it is also influenced by the different structural arrangements of the other three legs of the molecule touching the surface.

The nc-AFM characterization using CO-tips did not reveal any subatomic features associated with the presence of a σ -hole in either 4BrPhM or 4FPhM. The AFM contrast observed at close tip-sample distances showed no discernible subatomic features that could be attributed to the expected charge anisotropy distribution of the σ -hole as seen in Fig. 4.8-c. Theoretical analysis using the probe particle SPM model confirmed that the AFM contrast was predominantly governed by attractive dispersion forces and Pauli interactions, which exhibited a spherical nature. In contrast, the contribution of the electrostatic interaction energy responsible for the anisotropic charge distribution of the σ -hole was significantly weaker, approximately one order of magnitude weaker than the combined contribution of dispersion and Pauli interactions. Consequently, the visualization of the σ -

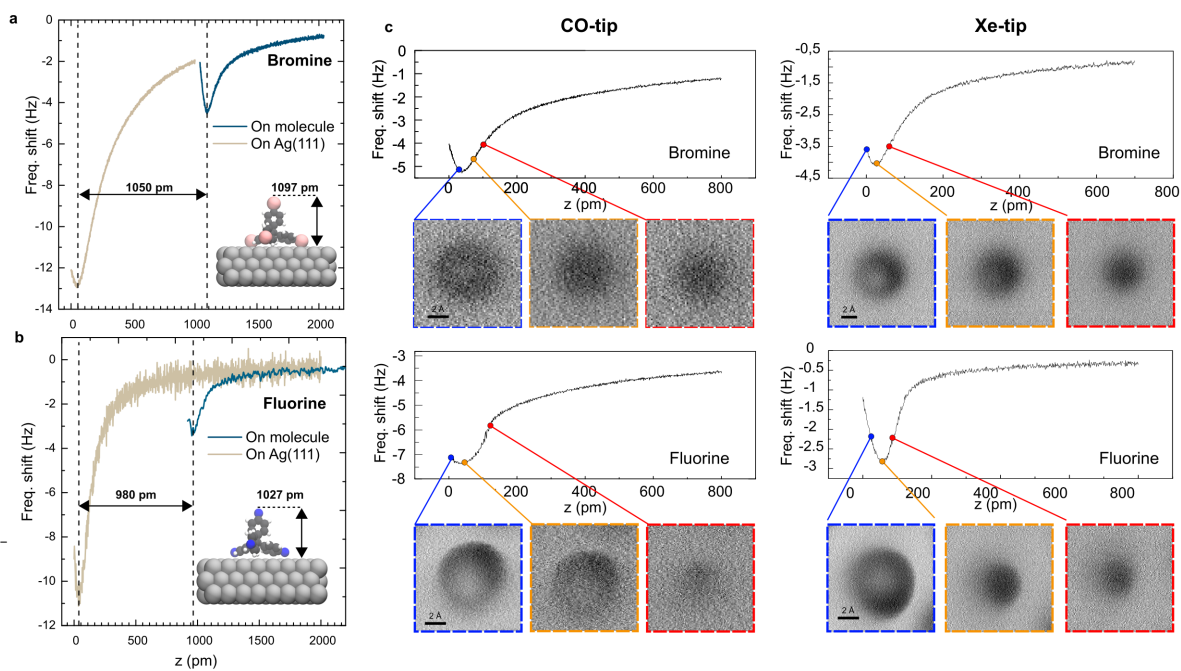


Figure 4.8: (Right) The experimental adsorption heights for 4BrPhM/4FPhM with respect to the surface of Ag(111). In the inset, are the calculated heights of the frontier atoms. (Left) Series of constant height nc-AFM images, at different tip-sample distances, acquired with CO and Xe tips for the bromine/fluorine belonging to the 4BrPhM/4FPhM molecules.

hole using AFM was impeded by the overwhelming dominance of these interactions over the expected anisotropic charge distribution.

To enhance the electrostatic interaction between the tip and the molecules, Kelvin probe force microscopy (KPFM) was employed due to its sensitivity to electrostatic interactions. Initially, using CO-tips resulted in donut-shaped charge distributions in the local contact potential difference (LCPD) maps for both 4BrPhM and 4FPhM. KPFM images obtained with the CO-tip on 4FPhM, where the σ -hole was not expected, exhibited a ring-like configuration with reduced LCPD values at the core of the fluorine atom. This contrast arose from the interaction between the spherical polarized charge of the fluorine atom and the quadrupole charge distribution of the CO-tip. Similarly, 4BrPhM also exhibited a ring-shaped charge anisotropy in KPFM images, with lower LCPD values at the core compared to the surrounding area. The observed ambiguity in the contrast of both atom types, despite displaying the same experimental charge anisotropy distribution, originated from the robust quadrupolar charge distribution of the CO-tip, which introduced undesired spatial variations in the voltage-dependent LCPD as confirmed by KPFM simulations using the probe particle model. To address this issue, the CO-tip was replaced with a Xe-tip (see Section 2.2), featuring a significantly spherical charge distribution that facilitated a direct depiction of the σ -hole charge distribution through KPFM.

The Xe-tip allowed then to create experimental LCPD maps (see details of acquisition in Section 1.3) of 4BrPhM exhibiting the σ -hole at different heights (Fig. 4.9) as a region of negative LCPD (blue) with an approximate width of 200 pm in the core of the Br atom, surrounded by a positive LCPD region with a ring shape. This scenario corresponds with an electron-depleted region, the σ -hole, with an approximate width of 200 pm, surrounded by a crown of a more electron-rich region. As commented in earlier sections, the LCPD maps are sensitive to the tip-sample distance of acquisition and can only be reliably trusted to stem from an electrostatic origin between the minima of interaction (Fig. 4.9, green line

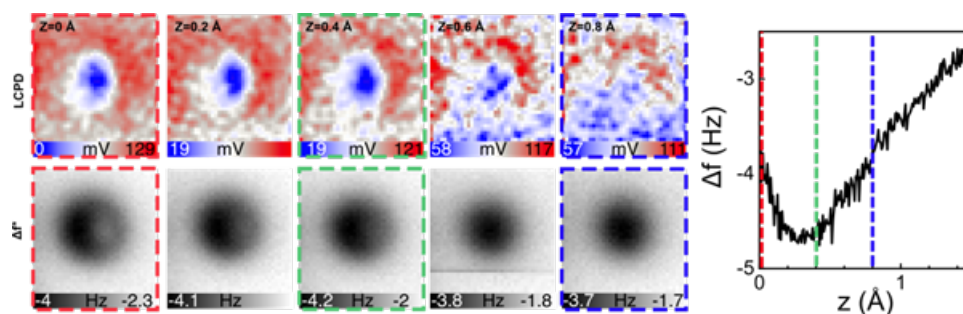


Figure 4.9: Experimental LCPD maps of the bromine of 4BrPhM for different tip-sample distances. The onset of the development of the contrast is in the characteristic distances where only electrostatics and dispersion are sensed by the tip (dotted green and blue lines). Beyond that (dotted red line) the tip starts also to experiment the Pauli repulsion.

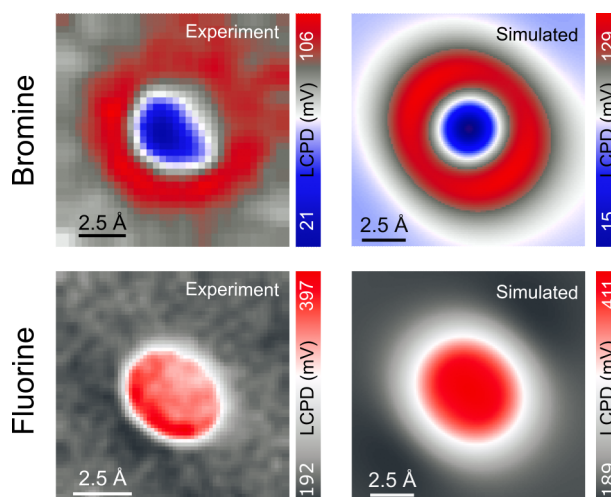


Figure 4.10: Experimental and PP-simulated LCPD maps of the σ -hole in Br (top row) and its absence in F (bottom row).

) and the onset of the dispersion sources where resolution is lost (Fig. 4.9, blue line). In the case of the 4FPhM molecule, the LCPD exhibited a positive shift over the atom exhibiting an almost homogeneous charge distribution as seen in Fig. 4.10. In addition, the shape of the feature in the KPFM image provided additional information about the internal arrangement of the molecule on the surface as the displayed elliptical shape is a consequence of the influence of the neighboring positively charged hydrogen atoms in the underlying phenyl group.

Finally, the expected non-covalent character of the interaction of the CO and the Xe

tips with the halogenated atoms, was experimentally measured with $\Delta f(z)$ spectroscopies to be in the order of below 1 kcal/mol, corresponding to the scale of energies expected by a system dominated by dispersion and electrostatics interactions and confirmed by computational methods such as CCSD(T) and ω B97X-V.

4.2.1 Author's contribution to the published work

In this section, I performed the experimental measurements using nc-AFM, STM and KPFM. The data acquisition, curation, processing, and analysis of the KPFM and nc-AFM maps were done with Python scripts developed by me. I also prepared the figures for the publication, collaborated in the draft and discussed the theoretical results with my colleagues.

SPECTROSCOPY

Real-space imaging of anisotropic charge of σ -hole by means of Kelvin probe force microscopyB. Mallada^{1,2,3†}, A. Gallardo^{2,4†}, M. Lamanec^{3,5†}, B. de la Torre^{1,2}, V. Špirko^{5,6}, P. Hobza^{5,7*}, P. Jelinek^{1,2*}

An anisotropic charge distribution on individual atoms, such as σ -holes, may strongly affect the material and structural properties of systems. However, the spatial resolution of such anisotropic charge distributions on an atom represents a long-standing experimental challenge. In particular, the existence of the σ -hole on halogen atoms has been demonstrated only indirectly through the determination of the crystal structures of organic molecules containing halogens or with theoretical calculations, consequently calling for its direct experimental visualization. We show that Kelvin probe force microscopy with a properly functionalized probe can image the anisotropic charge of the σ -hole and the quadrupolar charge of a carbon monoxide molecule. This opens a new way to characterize biological and chemical systems in which anisotropic atomic charges play a decisive role.

The observation of molecular structures with the unusual atomic arrangement of possessing two adjacent halogens or a pair of halogen atoms and electron donor motifs (oxygen, nitrogen, sulfur, ...), found in different crystals in the second half of the 20th century (1–4), represented a long-standing puzzle in supramolecular chemistry. Both halogens and electron donors are electronegative elements that carry a negative charge. Thus, close contacts of these atoms should theoretically cause highly repulsive electrostatic interaction. Counterintuitively, such atoms are frequently found to form intermolecular bonds, called latter halogen bonds, that stabilize the molecular crystal structure. An elegant solution offered by Auffinger *et al.* (5), Clark *et al.* (6), and Politzer *et al.* (7, 8) showed that the formation of a covalent bond between certain halogen atoms (chlorine, bromine, and iodine) and a more electronegative atom (such as carbon) gives rise to a so-called σ -hole that has an anisotropic charge distribution on the halogen atom. Thus, a physical observable corresponding electrostatic potential around the halogen atom is not uniform (as considered within all empirical force fields) but exhibits an electropositive distal to covalently bound carbon

crown surrounded by an electronegative belt (Fig. 1A).

Consequently, halogen bonding is attributed to attractive electrostatic interaction between a halogen's electropositive σ -hole and an electronegative belt of the other halogen or an electronegative atom with negative charge. The International Union of Pure and Applied Chemistry (IUPAC) definition of a halogen bond (9) states that a halogen bond “occurs when there is evidence of a net attractive interaction between an electrophilic region associated with a halogen atom in a molecular entity and a nucleophilic region in another, or the same, molecular entity.” Stability of the σ -hole bonding is comparable with that of hydrogen-bonded complexes, and attraction in both types of noncovalent complexes was originally assigned to electrostatic interaction. Although this scenario is basically true for H-bonded complexes, in the case of halogen-bonded systems, the importance of dispersion interaction (10) was highlighted. The importance of the dispersion interaction is not surprising because close contact takes place between two heavy atoms with high polarizability in halogen-bonded complexes.

The concept of halogen bonding was later generalized to a σ -hole bonding concept. In particular, the halogen (group 17), chalcogen (group 16), pnictogen (group 15), tetrel (group 14), and aerogen bonding (group 18) were established according to the name of the electronegative atom bearing the positive σ -hole. The existence of a σ -hole in atoms of the mentioned groups of elements has a common origin in the unequal occupation of valence orbitals.

The σ -hole bonding plays a key role in supramolecular chemistry (11), including the engineering of molecular crystals or in biological macromolecular systems (5). Despite its relevance and intensive research devoted to σ -hole bonding, the existence of the σ -hole itself was confirmed only indirectly with quantum calcu-

lations (5–8) or crystal structures of complexes containing σ -hole donors and electron acceptors (11–15). However, a direct visualization of this entity allowing for the resolution of its peculiar shape has thus far been missing.

The cause of the σ -hole is the anisotropic distribution of the atomic charge on a halogen atom. The imaging of anisotropic atomic charge represents an unfulfilled challenge for experimental techniques, including scanning probe microscopy (SPM), electron microscopy, and diffraction methods. Thus, we sought a technique in which the imaging mechanism relies on the electrostatic force to facilitate the visualization of the anisotropic charge distribution on a halogen atom with a sub-ångström spatial resolution. We show that real-space visualization of the σ -hole can be achieved through Kelvin probe force microscopy (KPFM) under ultrahigh vacuum (UHV) conditions (16, 17) with unprecedented spatial resolution.

KPFM belongs to a family of SPM techniques that routinely provide real-space atomic resolution of surfaces. In the KPFM technique, the variation of the frequency shift Δf of an oscillating probe on applied bias voltage V with the quadratic form $\Delta f \sim V^2$ is recorded (18). The vertex of the Kelvin parabola $\Delta f(V)$ determines the difference between work functions of tip and sample, also called the contact potential difference V_{CPD} . Moreover, the spatial variation of the contact potential difference V_{CPD} across the surface allows the mapping of local variation of surface dipole on the sample (V_{LCDP}) (17). Recent developments of the KPFM technique operating in UHV conditions made it possible to reach true atomic resolution on surfaces (19, 20) to image intramolecular charge distribution (21), to control single-electron charge states (22), to resolve bond polarity (23), or to discriminate charge (24).

The atomic contrast in KPFM images originates from a microscopic electrostatic force between static (ρ_0) and polarized charge densities ($\delta\rho$) located on frontier atoms from the tip apex and sample when an external bias is applied (17). There are two dominant components of this force: the interaction between the polarized charge on the apex $\delta\rho_t$, which is linearly proportional to the applied bias voltage (V), and the static charge on sample ρ_s^0 . The second term consists of the electrostatic interaction between the polarized charge on the sample $\delta\rho_s$ and the static charge on tip ρ_t^0 . Consequently, these two components cause local variation of the contact potential difference V_{LCDP} (a detailed description of the mechanism is provided in the supplementary materials), thus providing atomic-scale contrast.

Results

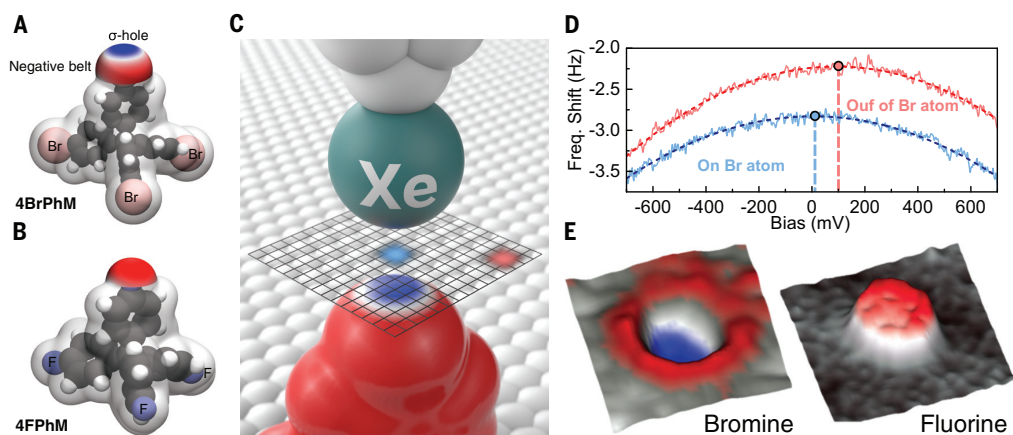
Consequently, KPFM appears to be the tool of choice for imaging anisotropic charge distribution within a single atom, such as the

¹Regional Centre of Advanced Technologies and Materials, Czech Advanced Technology and Research Institute (CATRIN), Palacký University Olomouc, 78371 Olomouc, Czech Republic. ²Institute of Physics, Academy of Sciences of the Czech Republic, Prague, Czech Republic. ³Department of Physical Chemistry, Palacký University Olomouc, tr. 17. listopadu 12, 771 46 Olomouc, Czech Republic. ⁴Department of Condensed Matter Physics, Faculty of Mathematics and Physics, Charles University, V Holešovičkách 2, 180 00 Prague, Czech Republic. ⁵Institute of Organic Chemistry and Biochemistry, Czech Academy of Sciences, Flemingovo náměstí 542/2, 16000 Prague, Czech Republic. ⁶Department of Chemical Physics and Optics, Faculty of Mathematics and Physics, Charles University in Prague, Ke Karlovu 3, 12116 Prague, Czech Republic. ⁷IT4Innovations, VSB-Technical University of Ostrava, 17. listopadu 2172/15, 70800 Ostrava-Poruba, Czech Republic.

*Corresponding author. Email: pavel.hobza@uochb.cas.cz (P.H.); jelinekp@fzu.cz (P.J.)

†These authors contributed equally to this work.

Fig. 1. Schematic view of the KPFM measurements to image a σ -hole. (A and B) Models of 4BrPhM and 4FPhM molecules, including corresponding electrostatic potential map on outermost Br/F atom. They reveal the presence of the σ -hole on a Br atom, and there is an isotropic negative charge on the F atom. (C) Schematic view of the acquisition method of the KPFM measurement with a functionalized Xe-tip on a 2D grid. (D) Corresponding $\Delta f(V)$ parabolas acquired in the central part (blue) of the 2D grid and on the periphery (red). Vertical dashed lines indicate the value of V_{LCPD} for the given $\Delta f(V)$ parabola, which forms the 2D KPFM image. (E) 3D representation of the KPFM images (V_{LCPD} maps) acquired with an Xe-tip over bromide and fluoride atoms of 4BrPhM and 4FPhM molecules. Blue indicates low values of V_{LCPD} , and red indicates high values of V_{LCPD} .



σ -hole. To test this hypothesis, we deliberately chose tetrakis(4-bromophenyl) methane (4BrPhM) and tetrakis(4-fluorophenyl) methane (4FPhM) compounds (Fig. 1, A and B). The skeleton arrangement of these compounds facilitates a tripodal configuration once deposited onto a surface with a single bromine-fluorine atom oriented outward from the surface (fig. S1). This arrangement facilitated direct inspection of the σ -hole on a halogen atom by the front-most atom of a scanning probe, (Fig. 1C). Deposition of the molecules in low coverage (less than 1 monolayer) on the Ag(111) surface held at room temperature under UHV conditions led to the formation of well-ordered, self-assembled molecular arrangements in a rectangular formation (Fig. 2, A and B). Bromine atoms of the 4BrPhM molecule have a substantial positive σ -hole (Fig. 1A), and fluorine atoms possess an isotropic negative charge (Fig. 1B). This enabled us to perform comparative measurements on similar systems with and without the presence of the σ -hole.

Shown in Fig. 2, C and D, is a substantial contrast between two-dimensional (2D) constant-height KPFM maps acquired over Br and F front-most atoms of the molecular compounds with an Xe-decorated tip. In the case of the 4FPhM molecule, we observed a monotonous elliptical increase of the V_{LCPD} signal over the fluorine atom. In comparison, the KPFM image over the 4BrPhM molecule featured a notable ring-like shape. The 2D KPFM maps were recorded in the attractive tip-sample interaction regime near the minimum of the Δf - z curve (fig. S2) to avoid undesired topographic cross-talk (fig. S3 and supplementary text) or the effect of lateral bending of the functionalized probe due to repulsive forces (25) that could cause image distortions. Evolution of the contrast of the KPFM image of the σ -hole

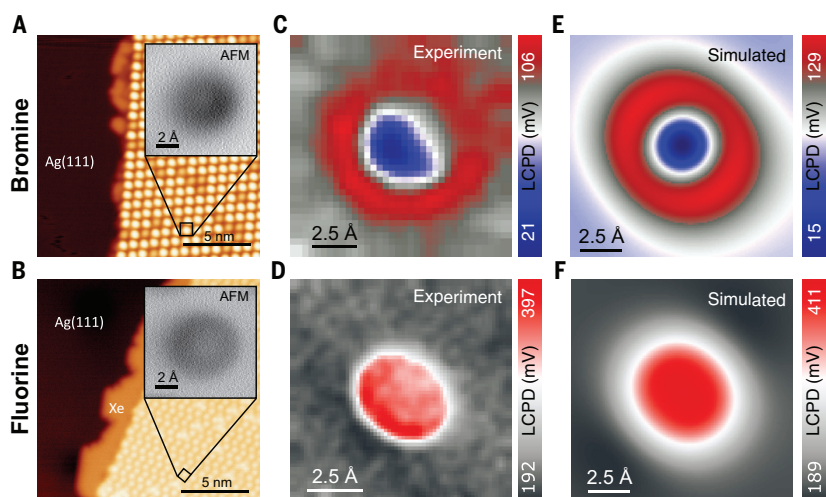


Fig. 2. KPFM imaging of 4BrPhM and 4FPhM molecules with an Xe-tip. (A and B) STM images of a molecular self-assembled submonolayer of 4BrPhM and 4FPhM molecules on an Ag(111) surface. (Insets) AFM images acquired on a single molecule with a Xe tip at the minima of the frequency shift. (C and D) Experimental KPFM images obtained with a functionalized Xe tip over bromine and fluoride atoms of single 4BrPhM and 4FPhM molecules. (E and F) Calculated KPFM images with a functionalized Xe tip of single 4BrPhM and 4FPhM molecules. Blue indicates low values of V_{LCPD} and red indicates high values of V_{LCPD} .

on the front-most Br atom with the tip-sample distance is shown in fig. S4.

Discussion

To confirm the origin of the anisotropic contrast observed experimentally on the Br atom, we carried out KPFM simulations using static ρ_0 and polarized $\delta\rho$ charges of Br and F-terminated molecules and Xe-tip models obtained from density functional theory (DFT) calculations (fig. S5). Simulated KPFM maps that are perfectly matched to the experimental

maps are shown in Fig. 2, E and F. Our theoretical model allowed us to decompose the two leading contributions: the electrostatic interaction of the polarized charge on tip $\delta\rho_t$ with the static charge on the molecule and the counterpart term of the electrostatic interaction between the polarized charge on molecule $\delta\rho_s$ with the ρ_t^0 static charge of the tip (fig. S5). We found that the anisotropic contrast obtained on the Br-terminated molecule can be rationalized from a variation of the microscopic electrostatic interaction between

atomic-scale charges of tip and sample. On the periphery of the Br atom, the positive shift of V_{CPD} is given by the electrostatic interaction of the spherical polarized charge, $\delta\rho_r$, of the Xe-tip apex, with the belt of negative charge surrounding the positive σ -hole. By contrast, in the central part, the electrostatic interaction with the positive crown of the σ -hole turned the V_{LCPD} value with respect to that on the peripheral region. In the case of the 4FPhM molecule, both terms provided a trivial contrast with a positive shift of the V_{LCPD} over the atom. The term corresponding to the static charge ρ_s^0 on the molecule revealed an elliptical shape originating from neighbor positively charged hydrogen atoms in the underlying phenyl group of the 4FPhM molecule. Therefore, the shape of the feature presented in the KPFM image provided additional information about the internal arrangement of the molecule on the surface.

We deliberately used a single Xe atom to functionalize the tip apex instead of the more commonly used carbon monoxide (CO). As discussed above, the Xe tip allowed us to optimize the imaging conditions of the σ -hole because static charge density ρ_0 on the apex of the CO-tip had a strong quadrupolar character (Fig. 3A), and the charge on the Xe tip was highly spherical (fig. S5). This choice eliminated spurious spatial variation of the V_{LCPD} signal, which did not belong directly to the σ -hole. In particular, a component of the microscopic electrostatic interaction between static charge ρ_t^0 of the tip and polarized charge on sample $\delta\rho_s$ needs to be abolished. In the case of the Xe-tip, the spatial variation of the local V_{CPD} was dominated by the component that includes the interaction of a spherically polarized charge on the Xe atom $\delta\rho_r$ with the anisotropic electrostatic field of the σ -hole. This enabled a direct mapping of the spatial charge distribution of the σ -hole by means of the KPFM technique.

Thus, it is instructive to look at the KPFM images acquired with the CO tip on the 4FPhM molecule as well. Despite the frontier fluorine atom of the 4FPhM molecule having an isotropic charge distribution, the experimental KPFM image (Fig. 3B) features a nontrivial ringlike shape with lower values of the V_{LCPD} signal on the center of the fluorine atom. Our KPFM simulation using a CO-tip (Fig. 3C) coincided qualitatively with the experimental counterpart. From a detailed analysis of the electrostatic components (fig. S6), we found that the contrast arose from the interaction of the spherical polarized charge $\delta\rho_s$ on a fluorine atom with the static quadrupole charge on a CO tip, composed of a negative crown of density on an oxygen atom surrounded by a positive charge belt (Fig. 3A). Thus, the KPFM features resolved on the 4FPhM molecule re-

flected the quadrupolar charge distribution of the CO tip. Thus, from the spatial variation of the V_{LCPD} signal, we could determine the sign of the quadrupole of the CO molecule on the tip. The shift of V_{LCPD} toward lower values in the central part of the KPFM image was caused by the negative charge crown of the quadrupole charge localized at oxygen (Fig. 3A). The enhanced V_{LCPD} value on the periphery reflects the positively charged belt of the quadrupole charge of the CO molecule. This reverse shift of V_{LCPD} with respect to the previous case of the σ -hole was caused by our inspection of the anisotropic charge on the tip instead of the sample. A detailed explanation of the origin and sign of V_{LCPD} shift is available in the supplementary materials.

Alternatively, some works reported subatomic features in noncontact atomic force microscopy (nc-AFM) (26) images with CO functionalized tips (27). However, the origin of such contrast and their interpretation of the physical meaning are under debate (28, 29). Additionally, nc-AFM has demonstrated unprecedented chemical resolution of single molecules (30) or their charge distribution (31). Thus, we were intrigued by the possibility of imaging the σ -hole by means of nc-AFM with functionalized tips (27).

A series of high-resolution nc-AFM images acquired at a wide range of tip-sample distances are shown in fig. S7 with a CO tip and Xe tip, respectively. At the onset of the atomic contrast in nc-AFM mode, the tip-sample interaction was dominated by an attractive dispersion. The resulting AFM contrast for both 4FPhM and 4BrPhM molecules had a similar spherical character that lacks any subatomic feature. Also, in close tip-sample distances, the AFM contrast remained similar for both molecular compounds, featuring a bright spot in the center caused by the Pauli repulsion. Thus, we found that the AFM images did not

reveal any signature of the σ -hole in the whole range of tip-sample distances covering both an attractive and repulsive interaction regime.

To understand in detail this experimental observation, we performed theoretical analysis of the nc-AFM images with a CO tip using the probe particle SPM model (25). Shown in figs. S8 and S9 are lateral cross sections of different force components of the interaction energy acting between the CO tip and the outermost F and Br atoms of the 4FPhM and 4BrPhM molecules, respectively. The calculated AFM images showed similar atomic contrast, ruling out the possibility to image the σ -hole with a CO tip. From the analysis, we inferred that the AFM contrast was dominated by dispersive and Pauli interaction, both of which have a highly spherical character. On the other hand, the electrostatic interaction possesses an anisotropic character caused by the presence of both a σ -hole on the Br atom and a quadrupolar charge distribution on the apex of the CO-tip (Fig. 3A). Nevertheless, the magnitude of the electrostatic interaction was about one order smaller than the competing dispersion and Pauli interactions, which made the σ -hole hard to image in the AFM technique. From this analysis, we could conclude that the resolution of anisotropic atomic charges requires a technique such as KPFM, whose contrast mechanism is mastered by the electrostatic interaction that maps the charge distribution on the forefront atoms.

Next, we investigated the influence of the σ -hole on the noncovalent intermolecular interaction energies. The nc-AFM technique provided the distinctive possibility to explore interaction energies between individual atoms and molecules placed on the tip apex and sample by means of site-specific force spectroscopies (32–35). Apart from a quantitative evaluation of the interaction energies between well-defined entities, the nc-AFM

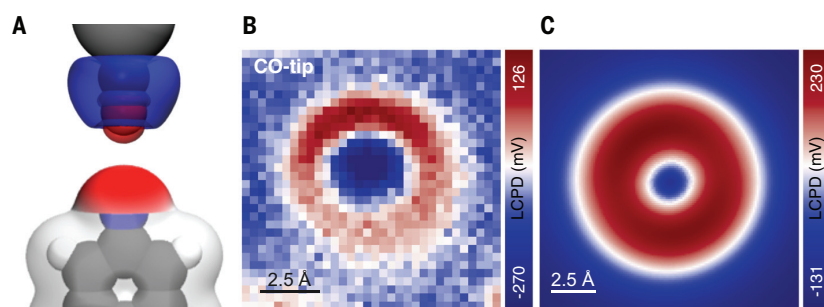


Fig. 3. KPFM imaging of a 4FPhM molecule with a CO tip. (A) Schematic view of a CO tip above a 4FPhM molecule with a superimposed calculated differential charge density of the CO tip, revealing (top) a quadrupole charge of a CO-tip model and (bottom) calculated electrostatic potential of 4FPhM molecule showing an isotropic negative charge on the frontier fluorine atom in 4FPhM. (B) Experimental KPFM image acquired over the frontier fluorine atom with a CO tip. (C) Simulated KPFM image of a 4FPhM molecule with a CO tip. Blue indicates low values of V_{LCPD} , and red indicates high values of V_{LCPD} .

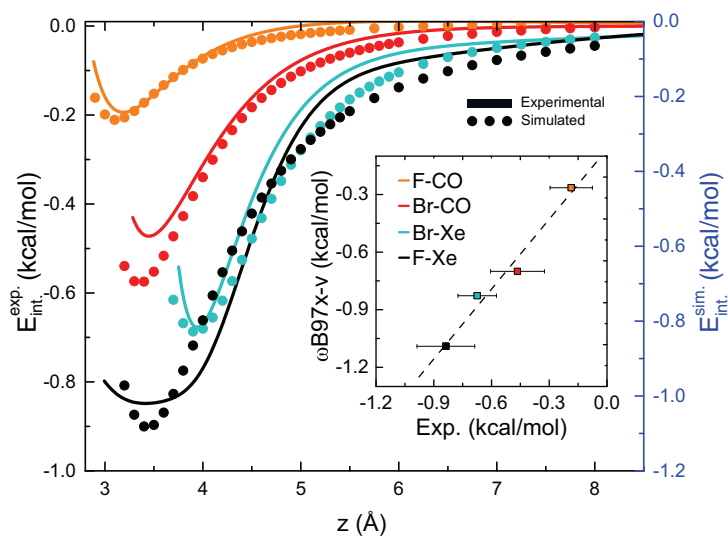


Fig. 4. Comparison of experimental and theoretical interaction energies of four complexes. Experimental (solid curves) and calculated (dots, obtained with DFT/ ω B97X-V) energy curves versus tip-sample distance between 4FPhM and 4BrPhM molecules and Xe and CO tips. (Inset) The correlation between experimental and theoretical values [coefficient of determination (R^2) = 0.98] of the energy minima for all complexes. Bars indicate an estimated experimental error of the energy minima calculated as the difference between a polynomial fit and the experimental energy (fig. S12).

technique also gave an invaluable opportunity to benchmark the accuracy of different theoretical methods to describe these weak noncovalent interactions (34–36).

Tip functionalization offered an opportunity to explore distinct scenarios of the interaction mechanisms with molecular complexes. The Xe tip has a positive net charge and large polarizability, but the CO tip possesses a quadrupolar charge (O and C carry negative and positive net charge, respectively) and a relatively small polarizability. Their interaction energies are shown in Fig. 4, with the 4FPhM and 4BrPhM molecules as a function of the tip-sample distance. Small values of the maximum energies of 0.2 to 0.83 kcal/mol revealed a noncovalent bonding mechanism. In general, the complexes with an Xe-tip are more stable than the complexes with a CO tip, which may be rationalized by a larger dispersion interaction caused by an Xe tip. We observed that the Xe-4BrPhM complex was less stable than the Xe-4FPhM complex (by 0.67 and 0.83 kcal/mol, respectively) despite the larger polarizability of Br that determines the magnitude of the polarization interaction. This effect was caused by the presence of the repulsive electrostatic interaction between the positive σ -hole on a Br atom and the positively charged Xe tip, which partially cancelled the attractive dispersive interaction in the Xe-4BrPhM complex. On the other hand, the dispersive and electrostatic forces are both attractive in the case of the Xe-4FPhM complex, resulting

in a larger total interaction energy. This observation not only supported the presence of the positive σ -hole on the Br atom, it also explained the origin of a peculiar intermolecular orientation of halogen-bonded molecular systems (12–15).

Recently, a vigorous effort has been devoted to the development of computational methods based on DFT with dispersion correction that are able to reliably describe intermolecular interactions in noncovalent complexes (37). But their transferability is still limited owing to adopted approximations, and thus, careful benchmarking is desired. From this perspective, the above-described complexes represent interesting noncovalent systems for benchmarks with a complex interplay between the dispersion and the electrostatic interaction. The maximum interaction energies measured were below 1 kcal/mol, which used to be considered as the limit of chemical accuracy, further strengthening the benchmark.

Accurate interaction energies for different types of noncovalent complexes could be obtained from a nonempirical coupled-cluster method covering triple-excitations [CCSD(T)]. Unfortunately, its large computational demands made it impossible to apply this method to a system of the size of the molecules we investigated in the present work.

To circumvent this problem, we performed the CCSD(T) calculations on smaller reference model systems consisting of F- and Br-benzene, exhibiting similar characteristics as

4BrPhM and 4FPhM molecules (supplementary materials). We compared the calculated CCSD(T) interaction energies to interaction energies obtained with several popular DFT functionals (table S3). We found that the range-separated ω B97X-V functional (38) that implicitly covers dispersion energy provided good agreement with the benchmarked dataset (table S3). Because this functional was also shown to provide the best results among other popular DFT functionals for various types of systems with noncovalent interactions (38), we selected this functional for further use.

To check its transferability to our larger molecular systems, we calculated the interaction energies between 4FPhM and 4BrPhM molecules and Xe- and CO-tip models. Excellent agreement between the ω B97X-V interaction energies and the experimental data results is shown in Fig. 4. The calculated energy minima for all complexes fit the measured values perfectly within the experimental error (Fig. 4, inset). The PBE0 functional (39) with the D3 correction (40) reproduced the CCSD(T) results on small-model systems as well (table S3 and fig. S10). However, its transferability on the large systems was no longer as good as the range-separated ω B97X-V functional (fig. S11).

The ω B97X-V functional describes well the interaction trend for all considered systems (Fig. 4, inset), with the caveat that it systematically slightly overestimates the interaction energy by ~ 0.1 kcal/mol. The perfect agreement between theoretical and experimental values could not be expected because calculations were limited to free-standing 4FPhM and 4BrPhM molecules interacting with Xe- and CO-tip model, and in the experiment, 4FPhM and 4BrPhM molecules were adsorbed at Ag(111) surface. The results confirmed good transferability of the ω B97X-V functional toward larger systems. Moreover, the good agreement between calculated and experimental datasets obtained for all four complexes also gave confidence in the multiscale benchmark technique that uses small-model complexes with the Xe-tip model. Therefore, this approach makes it possible to accurately describe systems whose size does not allow for the direct application of the accurate coupled-cluster technique (or a similar technique), or when other direct experimental measurements are currently not feasible.

Conclusions

We report the possibility of achieving the spatial resolution of anisotropic atomic charge with the KPFM technique, which not only provided direct evidence of the existence of σ -holes but is expected to substantially extend the possibility to characterize charge distribution in complex molecular systems and on surfaces. We anticipate that this technique could

be further extended to provide invaluable information about the local inhomogeneous polarizability of individual atoms on surfaces or within molecules with unprecedented spatial resolution in chemical and biologically relevant systems.

REFERENCES AND NOTES

- N. Ramasubbu, R. Parthasarathy, P. Murray-Rust, *J. Am. Chem. Soc.* **108**, 4308–4314 (1986).
- O. Hassel, J. Hvostlef, E. H. Vihovde, N. A. Sørensen, *Acta Chem. Scand.* **8**, 873–873 (1954).
- O. Hassel *et al.*, *Acta Chem. Scand.* **13**, 275–280 (1959).
- O. Hassel *et al.*, *Acta Chem. Scand.* **12**, 1146–1146 (1958).
- P. Auffinger, F. A. Hays, E. Westhof, P. S. Ho, *Proc. Natl. Acad. Sci. U.S.A.* **101**, 16789–16794 (2004).
- T. Clark, M. Hennemann, J. S. Murray, P. Politzer, *J. Mol. Model.* **13**, 291–296 (2007).
- T. Brinck, J. S. Murray, P. Politzer, *Int. J. Quantum Chem.* **44** (S19), 57–64 (1992).
- P. Politzer, P. Lane, M. C. Concha, Y. Ma, J. S. Murray, *J. Mol. Model.* **13**, 305–311 (2007).
- G. R. Desiraju *et al.*, *Pure Appl. Chem.* **85**, 1711–1713 (2013).
- K. E. Riley, P. Hobza, *Phys. Chem. Chem. Phys.* **15**, 17742–17751 (2013).
- L. C. Gilday *et al.*, *Chem. Rev.* **115**, 7118–7195 (2015).
- Z. Han *et al.*, *Science* **358**, 206–210 (2017).
- J. Tschakert *et al.*, *Nat. Commun.* **11**, 5630 (2020).
- S. Kawai *et al.*, *ACS Nano* **9**, 2574–2583 (2015).
- H. Huang *et al.*, *ACS Nano* **10**, 3198–3205 (2016).
- M. Nonnenmacher, M. P. O’Boyle, H. K. Wickramasinghe, *Appl. Phys. Lett.* **58**, 2921–2923 (1991).
- T. Glatzel, S. Sadewasser, Eds., *Kelvin Probe Force Microscopy* (Springer, 2018), vol. 65.
- W. Melitz, J. Shen, A. C. Kummel, S. Lee, *Surf. Sci. Rep.* **66**, 1–27 (2011).
- L. Nony, A. S. Foster, F. Bocquet, C. Loppacher, *Phys. Rev. Lett.* **103**, 036802 (2009).
- S. Sadewasser *et al.*, *Phys. Rev. Lett.* **103**, 266103 (2009).
- F. Mohn, L. Gross, N. Moll, G. Meyer, *Nat. Nanotechnol.* **7**, 227–231 (2012).
- L. Gross *et al.*, *Science* **324**, 1428–1431 (2009).
- F. Albrecht *et al.*, *Phys. Rev. Lett.* **115**, 076101 (2015).
- B. Mallada *et al.*, *ACS Sustain. Chem. Eng.* **8**, 3437–3444 (2020).
- P. Hapala *et al.*, *Phys. Rev. B Condens. Matter Mater. Phys.* **90**, 085421 (2014).
- T. R. Albrecht, P. Grütter, D. Horne, D. Rugar, *J. Appl. Phys.* **69**, 668–673 (1991).
- P. Jelinek, *J. Phys. Condens. Matter* **29**, 343002 (2017).
- F. Huber *et al.*, *Science* **366**, 235–238 (2019).
- M. Emmrich *et al.*, *Science* **348**, 308–311 (2015).
- L. Gross, F. Mohn, N. Moll, P. Liljeroth, G. Meyer, *Science* **325**, 1110–1114 (2009).
- P. Hapala *et al.*, *Nat. Commun.* **7**, 11560 (2016).
- M. A. Lantz *et al.*, *Science* **291**, 2580–2583 (2001).
- Y. Sugimoto *et al.*, *Nature* **446**, 64–67 (2007).
- S. Kawai *et al.*, *Nat. Commun.* **7**, 11559 (2016).
- Z. Sun, M. P. Boneschanscher, I. Swart, D. Vanmaekelbergh, P. Liljeroth, *Phys. Rev. Lett.* **106**, 046104 (2011).
- C. Wagner *et al.*, *Nat. Commun.* **5**, 5568 (2014).
- S. Grimme, A. Hansen, J. G. Brandenburg, C. Bannwarth, *Chem. Rev.* **116**, 5105–5154 (2016).
- N. Mardirossian, M. Head-Gordon, *Phys. Chem. Chem. Phys.* **16**, 9904–9924 (2014).
- C. Adamo, V. Barone, *J. Chem. Phys.* **110**, 6158–6170 (1999).
- S. Grimme, J. Antony, S. Ehrlich, H. Krieg, *J. Chem. Phys.* **132**, 154104 (2010).
- B. Mallada *et al.*, Data for “Real-space imaging of anisotropic charge of σ -hole by means of Kelvin probe force microscopy”. *Zenodo* (2020); doi:10.5281/zenodo.5172233.

ACKNOWLEDGMENTS

We acknowledge fruitful discussions with A. Růžička and P. Hapala. M.L. acknowledges inspirational advice from his previous supervisor, J. Kuchár. P.J. and B.d.I.T. dedicate this manuscript to the memory of J. M. Gómez-Rodríguez. **Funding:** This work was supported by the Czech Science Foundation GACR 20-13692X (A.G., B.M., and P.J.) and 19-27454X (P.H.); Praemium Academie of the Academy of Science of the Czech Republic (A.G.); Palacký University Internal Grant Association IGA_PrF_2021_031 (M.L.); Palacký University Internal Grant Association IGA_PrF_2021_034 (B.M.); and CzechNanoLab Research Infrastructure, supported by MEYS CR (LM2018110). **Author contributions:** Conceptualization: P.J. Methodology: B.M., A.G., B.d.I.T., and P.J. Theoretical calculations: A.G., M.L., V.Š., P.J., and P.H. Experimental: B.M. and B.d.I.T. Funding acquisition: P.H. and P.J. Supervision: B.d.I.T., P.H., and P.J. Writing, original draft: B.M., A.G., B.d.I.T., P.H., and P.J. **Competing interests:** The authors declare that they have no competing interests. **Data and materials availability:** All data needed to evaluate the conclusions in the paper are present in the paper or the supplementary materials. Data can be found at Zenodo (41).

SUPPLEMENTARY MATERIALS

science.org/doi/10.1126/science.abk1479
Materials and Methods
Supplementary Text
Figs. S1 to S20
Tables S1 to S3
References (42–55)
24 June 2021; resubmitted 28 July 2021
Accepted 20 September 2021
10.1126/science.abk1479

Real-space imaging of anisotropic charge of #-hole by means of Kelvin probe force microscopy

B. MalladaA. GallardoM. LamanecB. de la TorreV. ŠpirkoP. HobzaP. Jelinek

Science, 374 (6569), • DOI: 10.1126/science.abk1479

Resolution of the #-hole

Anisotropic distribution of charges on atoms plays an important role in intermolecular interactions, yet direct experimental imaging remains a long-standing challenge. A good example is the #-hole, an anisotropic charge distribution on a halogen atom covalently linked to carbon atoms. The #-hole gives rise to the halogen-bonding mechanism, which is well known in supramolecular chemistry despite its existence being confirmed only indirectly. Mallada *et al.* developed Kelvin probe force microscopy with a specifically functionalized tip and report direct real-space visualization of the #-hole, revealing its strong anisotropic charge distribution. The authors show that this technique, which relies entirely on electrostatic interactions, may be a powerful tool with which to study anisotropic atomic charge distributions. —YS

View the article online

<https://www.science.org/doi/10.1126/science.abk1479>

Permissions

<https://www.science.org/help/reprints-and-permissions>

Use of this article is subject to the [Terms of service](#)

Science (ISSN) is published by the American Association for the Advancement of Science. 1200 New York Avenue NW, Washington, DC 20005. The title *Science* is a registered trademark of AAAS.
Copyright © 2021 The Authors, some rights reserved; exclusive licensee American Association for the Advancement of Science. No claim to original U.S. Government Works

4.3 Direct imaging of π -hole

Introduction

This section is dedicated to one of the most recent results in our group in the topic of anisotropic charge visualization with submolecular resolution in halogenated systems. As it has been already introduced in Section 4.2, the submolecular charge distribution in single atoms or molecules profoundly impacts the physical-chemical properties of molecules and their intermolecular interactions. One intriguing manifestation of an anisotropic charge distribution is the presence of a π -hole, which refers to a π -electron-deficient cavity found in certain halogen-substituted polyaromatic hydrocarbon compounds [86].

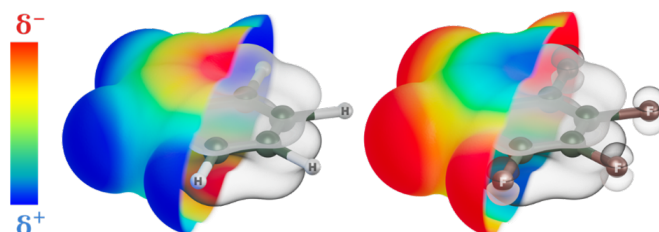


Figure 4.11: Concept of π -hole. The spatial distribution of the highest occupied molecular orbitals (HOMO) (grey-shaded volumes) of benzene (C_6H_6) on left and hexafluorobenzene (C_6F_6) on right overlapped with the electrostatic potential map (colored surface from red (negative charge) to blue (positive charge)). In the case of C_6F_6 , the occupied orbitals are delocalized over both carbon and fluorine atoms. In contrast, in the case of C_6H_6 molecule, they are predominantly localized on carbon atoms only, as seen in the grey surfaces.

The electron distribution within these molecules is strongly influenced by the electronegativity of peripheral halogenated substituents, such as fluorine or chlorine, resulting in an electron withdrawal from the carbon atoms towards the halogens and the subsequent change in the occupied orbitals, leading to a depletion of electron density in the central π -system on the carbon atoms (see Fig. 4.11). This electron-deficient area, located in the same plane as the π electrons of the hydrocarbon compound, can influence the stabi-

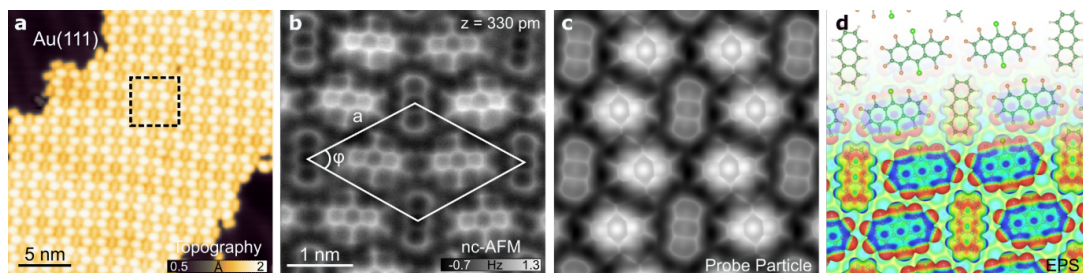


Figure 4.12: a, STM ($V_{Bias}=500$ mV, $I_{tunnel}=10$ pA) topography overview of the ordered self-assembly structure of An and FCl-An molecules on Au(111). b, Constant height nc-AFM with CO-tip of the unit cell of the self-assembly ($a=1.85 \pm 0.02$ nm, $\phi = 122 \pm 0.6^\circ$). c, Probe Particle simulated nc-AFM image. d, Model of the self-assembly of An and FCl-An (top) and the electrostatic potential map of the optimized supramolecular structure (bottom).

lization of intermolecular π stacking interactions between hydrocarbon molecules such as benzene and hexafluorobenzene dimers. For instance, the homodimer formed from the π stacking of two benzenes (C_6H_6) or two hexafluorobenzenes (C_6F_6) is predominantly stabilized through dispersion interactions, while the heterodimers benefit from both attractive electrostatic quadrupole-quadrupole interactions and substantial dispersion interactions.

Although the description of the π -hole is relatively recent[86], similar to the case of the σ -hole, the influence of the π -hole on non-covalent intermolecular interactions is particularly noteworthy. For example, the stability of helical DNA structures heavily relies on intermolecular stacking interactions, which can be significantly affected by the presence of a π -hole[87] and could potentially influence the architecture of molecular self-assemblies. However, until very recently, the existence of these -holes had only been theoretically established, with direct experimental observation remaining elusive. In this section, it will be presented the visualization in real space with KPFM of the π -hole in a molecule of Dichlorooctafluoroanthracene $C_{14}F_8C_{12}$ (FCl-An) and compared at the same time with another molecule of anthracene $C_{14}H_{10}$ (An) that does not develop a π -hole. The experiment is started by depositing 9,10-Dichlorooctafluoroanthracene (FCl-An) and anthracene (An) molecules with two Knudsen cells simultaneously in UHV conditions at RT on the

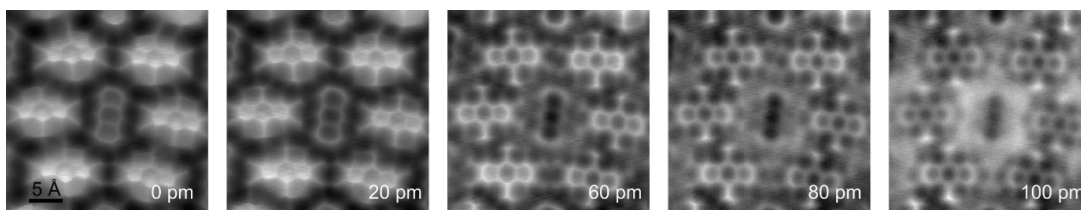


Figure 4.13: Constant height nc-AFM with CO-tip of FCl-An and An as a function of distance.

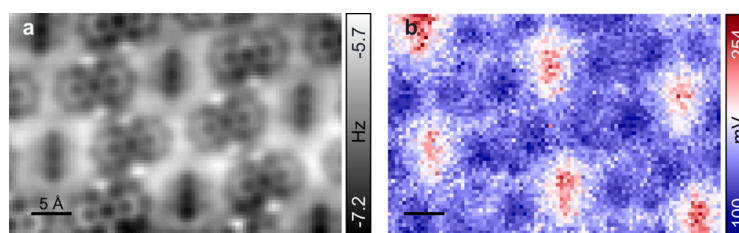


Figure 4.14: (Left) Constant height nc-AFM with CO-tip of FCl-An and An. (Right) Constant height LCPD map with a CO-tip of FCl-An and An.

sample of Au (111) for 15 s. In these conditions, the An and FCl-An order in a periodic fashion with a rhombic self-assembly as can be seen in Fig. 4.12-a. This ordering is mostly driven by electrostatic intermolecular interactions between the two species. Upon characterization with a CO-tip in nc-AFM (Fig. 4.12-b), two species are clearly identified, in a proportion of one An and two FCl-An molecules in the unit cell. The molecules of FCl-An have an adsorption height approximately 30 pm higher than those of An, resulting in the visualized slight difference of contrast between both molecules, as the FCl-An is probed in a slightly closer regime (Fig. 4.13). In order to visualize the π -hole, a purely electrostatic phenomenon, without the effects of dispersion, Pauli repulsion or artefacts introduced by the bending of the tip, KPFM was used to visualize the charge distribution within each molecule. In big-scale LCPD maps (see Fig. 4.14), it can be observed simultaneously the difference of contrast between them, with the molecules of FCl-An observed as a bow-tie shape of negative LCPD and the An observed as uniform, more positive, LCPD corresponding with a negative charge distribution.

These experimental results are more clearly visualized in the high-resolution LCPD

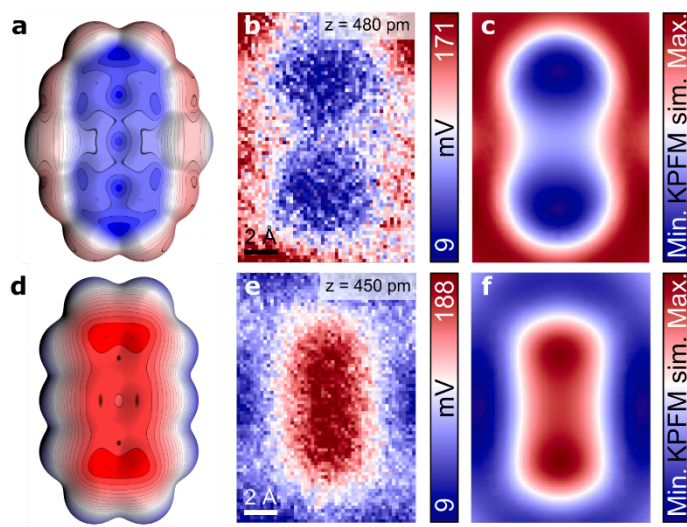


Figure 4.15: (a, d), Electrostatic potential maps of free-standing FCl-An and An molecules. (b, e), Experimental LCPD maps of An and FCl-An acquired with the same CO-tip in constant height mode. (c, f), Probe Particle simulated LCPD maps of FCl-An and An.

image of single molecules, supported by KPFM simulations (Fig. 4.15), demonstrating the distinct charge distribution patterns between anthracene (An) and fluorinated anthracene (FCl-An) molecules. The LCPD contrast exhibited a shift to higher or lower values for An or FCl-An, respectively, in both experiments and simulations, consistent with a scenario where the aromatic anthracene molecule has all the π -electrons fully delocalized and as a consequence has a uniformly distributed electron density. On the other hand, the FCl-An counterpart exhibits an anisotropic charge distribution stemming from the migration of electrons towards the halogenated atoms. In particular, the addition of Cl in the 9,10 positions, with a different electronegativity than F, results in the formation of a σ -hole, pointing outwards and in the sample plane as the molecular backbone, contributing to an uneven depletion in the middle section of the molecule and creating the characteristic bow-tie shape.

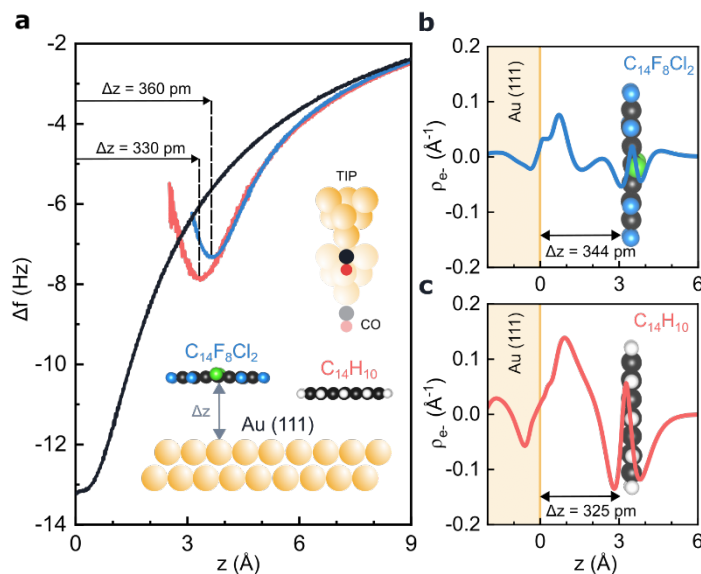


Figure 4.16: a Experimental adsorption heights measured with f - z spectroscopy in the middle hexagon of the molecules (inset) FCl-An (blue line) and An (red line) with respect to Au(111) substrate (black-line). (b, c) Calculated induced electron density of FCl-An (top, blue line) on Au(111) and An (bottom, red line) as a function of the distance between the surface and the molecule.

Finally, the presence of a π -hole was found to impact the adsorption of molecules on a metallic substrate. As commented earlier, constant height AFM images showed submolecular contrast on FCl-An molecules, indicating different adsorption heights compared to An. Specific-site force-distance spectroscopy revealed a 30 pm difference in the Δf - z curves, reflecting the variation in adsorption height (see Fig. 4.16). DFT calculations showed that there is a more significant induced electron density in the interface between An molecule and metallic substrate compared to FCl-An/Au(111) interface, with both molecules being physisorbed with negligible hybridization of molecular orbitals. The induced charge density is a consequence of attractive electrostatic interaction between the molecule and the surface. In particular, for the case of FCl-An molecule, the presence of π -hole increases the ionization potential and consequently suppresses the charge density induction at the molecule/metal interface. For the case of An, the HOMO orbital is found close to the Fermi level of metal, which facilitates the charge induction upon the adsorption, rationalizing the

lower adsorption distance compared to the FCI-An.

4.3.1 Author's contribution to the published work

As in the case of the Section 4.2, in this section, I performed the experimental measurements using nc-AFM, STM and KPFM. The data acquisition, curation, processing, and analysis of the KPFM and nc-AFM maps were done with Python scripts developed by me. I also prepared the figures for the publication, collaborated on the draft and discussed the theoretical results with my colleagues. This publication is currently under review and I am collaborating in the answering to the referees and the edition of the manuscript.

Visualization of π -hole in molecules by means of Kelvin probe force microscopy

B. Mallada^{1,2,4†}, M. Ondráček^{1†}, M. Lamanec^{3,4†}, A. Gallardo¹, A. Jiménez-Martín^{1,2}, B. de la Torre^{1,2*}, P. Hobza^{3,5*}, P. Jelínek^{1,2*}

¹Institute of Physics, Academy of Sciences of the Czech Republic, Prague, Czech Republic.

²Regional Centre of Advanced Technologies and Materials, Czech Advanced Technology and Research Institute (CATRIN), Palacký University Olomouc, 78371 Olomouc, Czech Republic.

³Institute of Organic Chemistry and Biochemistry, Czech Academy of Sciences, Flemingovo náměstí 542/2, 16000 Prague, Czech Republic

⁴Department of Physical Chemistry, Palacký University Olomouc, tr. 17. listopadu 12, 771 46 Olomouc, Czech Republic.

⁵IT4Innovations, VŠB – Technical University of Ostrava, 17. listopadu 2172/15, 708 00 Ostrava-Poruba, Czech Republic

† These authors contributed equally to this work and can be considered as the first author

*Corresponding author. Email: bruno.de@upol.cz, pavel.hobza@uochb.cas.cz, jelinekp@fzu.cz

Abstract (300 words)

Submolecular charge distribution significantly affects the physical-chemical properties of molecules and their mutual interaction. One example is the presence of a π -electron-deficient cavity in halogen-substituted polyaromatic hydrocarbon compounds, the so-called π -holes, the existence of which was predicted theoretically, but the direct experimental observation is still missing. Here we present the resolution of the π -hole on a single molecule using the Kelvin probe force microscopy, which confirms the theoretical prediction of its existence. In addition, experimental measurements supported by theoretical calculations show the importance of π -holes in the process of adsorption of molecules on solid-state surfaces. This study expands our understanding of the π -hole systems and, at the same time, opens up possibilities for studying the influence of submolecular charge distribution on the chemical properties of molecules and their mutual interaction.

Main

Non-covalent interactions are crucial in many chemical and biological processes, such as supramolecular assembling, ion recognition, and protein stability. The nature of non-covalent intermolecular bonds is determined, among others, by dispersion and electrostatic forces. While the dispersion force is always attractive and directionless, the electrostatic component can be attractive or repulsive and is highly directional. The nature of the electrostatic interaction is intimately linked to the internal charge distribution within the molecule. Therefore, precise knowledge of the charge distribution in molecules is a fundamental requirement for comprehending non-covalent interactions¹.

For instance, in the most prevalent category of molecular species, polycyclic aromatic hydrocarbons (PAHs), the larger electronegativity of carbon compared to the peripheral hydrogen results in an accumulation of electron density in the delocalized/conjugated π -bonds on the carbon skeleton. This electron-rich delocalized/conjugated π -bond system, which is evenly distributed above and below the molecular plane, generates a negative quadrupole moment for the PAH molecules, see **Fig. 1**. However, substituting peripheral hydrogens with other substituents that are more electronegative than carbon, such as fluorine or chlorine, reverses the electron population of the π -bond system to make it electron-deficient, see **Fig. 1**. Consequently, the quadrupole moment of such a molecule becomes positive². The presence of a π -electron-deficient cavity in the central part of the molecule is called a π -hole³.

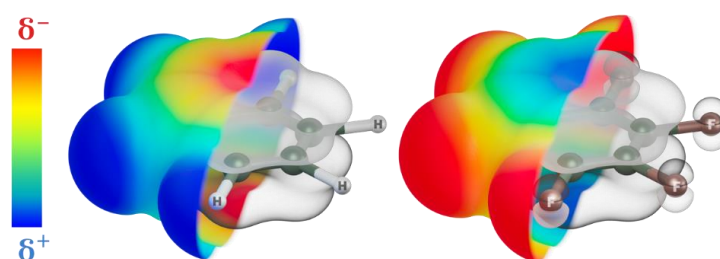


Fig. 1 | Schematic description of the concept of π -hole. The spatial distribution of the highest occupied molecular orbitals (HOMO) (grey-shaded volumes) of benzene (C_6H_6) on left and hexafluorobenzene (C_6F_6)

on right overlapped with the electrostatic potential map (colored surface from red (negative charge) to blue (positive charge)).

The π -hole concept can be vividly illustrated by comparing the electron distribution of benzene, C_6H_6 , and hexafluorobenzene, C_6F_6 . In benzene, electrons are localized within the aromatic carbon skeleton, as depicted in the electrostatic potential map shown in **Fig. 1**. Conversely, in hexafluorobenzene, the higher electronegativity of fluorine results in electron withdrawal from carbon atoms towards halogens, leading to a depletion of electron density in the central π -system on the carbon atoms. The origin of the distinct localization of the electron density in both systems is closely associated with the different character of occupied molecular orbitals. Namely, in the case of C_6F_6 , the occupied orbitals are delocalized over both carbon and fluorine atoms. In contrast, in the case of C_6H_6 molecule, they are predominantly localized on carbon atoms only, as seen in the grey surfaces in **Fig 1**.

As discussed above, the presence of a positively charged π -hole significantly affects non-covalent intermolecular interactions. For example, intermolecular stacking interactions⁴, which play an essential role in the stabilization of the helical structure of DNA bases, can be strongly affected by the presence of a π -hole. The decisive role of the electrostatic interaction on the stacked structure can be well documented for the simplest stacked aromatic systems, dimers of benzene C_6H_6 and/or hexafluorobenzene, C_6F_6 . In the case of homodimers, their stabilization is entirely caused by dispersion interaction, as the electrostatic quadrupole-quadrupole interaction is repulsive. However, in the case of heterodimers, the situation changes due to the attractive electrostatic quadrupole-quadrupole interaction, which allows a close approach of the aromatic rings resulting in significant dispersion interaction and, consequently, resulting in substantial stabilization of the heterodimers².

It is evident that the presence of π -hole may strongly affect the physicochemical properties of molecular systems. So far, the concept of π -hole has been developed exclusively on a theoretical basis using quantum calculations. Experimentally, the existence of π -hole has only been proven indirectly based on measured data, the interpretation of which can only explain the presence of π -hole⁵ However, a direct experimental observation that would clearly prove the existence of the π -hole has been lacking so far.

Of all the experimental techniques, scanning probe microscopy (SPM) emerges as the most appropriate tool for the direct visualization of π -holes in molecular systems. In recent years, the development of SPM with a functionalized probe^{6,7} has enabled the unprecedented spatial resolution not only of the chemical⁶ and spin⁸ structure of molecules on the surfaces but also of the anisotropic atomic charge on individual atoms, the so-called sigma-hole⁹. In this article, we will show that the Kelvin probe force microscopy (KPFM) method, which enabled us to resolve the sigma-hole for the first time, is an ideal imaging tool for the real space observation of the π -hole system as well.

Results and discussion

Here, we experimentally confirm the existence of the π -hole in 9,10-Dichlorooctafluoroanthracene $C_{14}F_8Cl_2$ (FCI-An) molecule and, at the same time, its absence in anthracene $C_{14}H_{10}$ (An). As discussed above, the presence of different substituents rules the charge transfer between π -orbitals of the carbon skeleton and the substituents. Fig. S1 displays selected occupied orbitals of An and FCI-An, whose comparison reveals their different shape. Similarly, as in the case of C_6H_6 and C_6F_6 , the molecular orbitals in An are localized only at the carbon skeleton, while these in FCI-An are also extended at all halogen substituents. In the latter case, this gives rise to the presence of π -hole localized on the carbon skeleton.

Here we investigated heterogeneous molecular self-assemblies consisting of FCI-An and An molecule. **Fig. 2a** displays the molecular self-assembly grown by simultaneous sublimation of the two compounds on an atomically clean Au (111) surface kept at room temperature in an ultrahigh vacuum. Scanning tunnelling microscopy (STM) images, acquired at a base temperature of 4.8 K, reveal large-scale ordered molecular islands composed of both molecular species alternating in a periodic fashion (**Fig. 2a,b**).

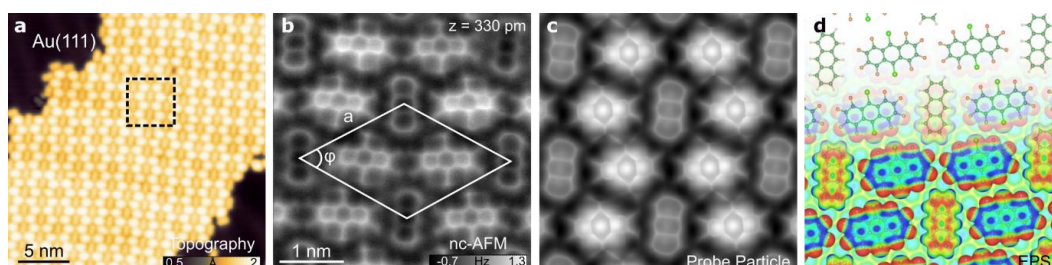


Fig.2 | Overview and description of the system. **a**, STM ($V_{\text{Bias}}=500$ mV, $I_{\text{tunnel}}=10$ pA) topography overview of the ordered self-assembly structure of An and FCI-An molecules on Au(111). **b**, Constant height nc-AFM with CO-tip of the unit cell of the self-assembly ($a=1.85 \pm 0.02$ nm, $\varphi = 122 \pm 0.6^\circ$). **c**, Probe Particle simulated nc-AFM image. **d**, Model of the self-assembly of An and FCI-An (top) and the electrostatic potential map of the optimized supramolecular structure (bottom).

To determine the detailed arrangement of the molecular species in the assembly, we use noncontact atomic force microscopy (nc-AFM) with a functionalized carbon monoxide (CO) tip. The high-resolution nc-AFM images acquired at a constant height mode in **Fig. 2b** clearly distinguish two different molecular species. To gain insight into the self-assembly structure, we carried out total energy density functional theory (DFT) calculations as well as AFM imaging of the supramolecular structure on the Au (111) surface. The perfect agreement between experimental and theoretical nc-AFM images allowed us to unambiguously resolve the chemical structure of both An and FCI-An molecules, as well as their arrangement. The supramolecular assembly comprises a rhombic periodic structure with one An and two FCI-An molecules in the unit cell, as shown in **Fig. 2b,c**. The arrangement is dictated by attractive intermolecular electrostatic interactions between negatively charged fluorine atoms, sigma-hole on chlorine, and positively charged hydrogen atoms (**Fig. 2d**). This scenario is supported by the fact that the mere deposition of An on the surface does not result in the formation of self-organized molecular structures, as shown in **Fig. S2**.

Notably, the high-resolution AFM images show, apart from the difference in the apparent size of the molecular species, a relatively similar contrast of the carbon skeleton for both types of molecules. In addition, AFM images show that FCI-An molecules are systematically imaged brighter than An molecules due to a topographic effect, as we will discuss below. Thus, the AFM images apparently do not provide any direct experimental evidence of π -hole.

Therefore, we employed Kelvin Probe Force Microscopy, which records the spatial variation of the local contact potential difference (LCPD) across the surface¹⁰. At short tip-sample distances, the magnitude of the LCPD is affected by a short-range electrostatic interaction acting between the tip apex and surfaces, which enables us to map the charge distribution (See **Fig. 3a,d**) with atomic resolution^{9,11}. The KPFM technique was employed to investigate the charge distribution at the atomic and molecular levels. This

technique is useful for detection of single electron charge states of individual atoms¹² and molecule¹³, mapping charge distribution within molecules¹⁴, resolving molecular dipolar moments¹⁵, and visualizing the anisotropic charge distributions in single atoms⁹. In previous work, we demonstrate that the sensitivity of the KPFM method can be substantially enhanced^{9,16} using functionalized probes.

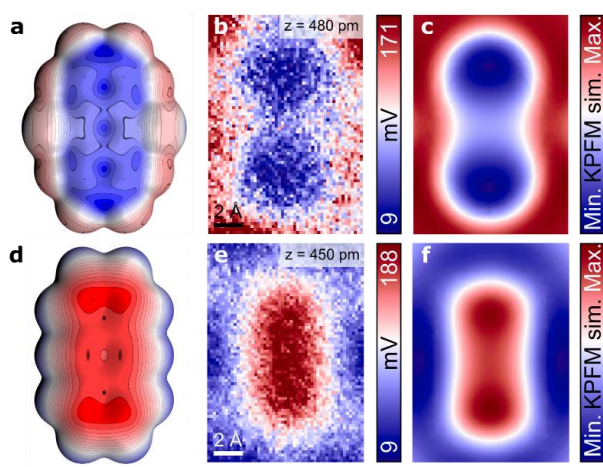


Fig. 3 | Simulated and experimental charge distributions of An and FCI-An. (a, d), Electrostatic potential maps of free standing FCI-An and An molecules. **(b, e),** Experimental LCPD maps of An and FCI-An acquired with the same CO-tip in constant height mode. **(c, f),** Probe Particle simulated LCPD maps of FCI-An and An.

Fig. 3b and **3e** depict constant height KPFM maps conducted with the same CO-terminated tip of individual An and FCI-An molecules, respectively. These maps reveal a striking difference in the LCPD contrast between the two molecular species. Specifically, the LCPD signal over An/FCI-An molecule is shifted to a higher/lower value, indicating a decrease/increase in the local work function. The anthracene molecule possesses a uniform positive LCPD signal, representing a negative charge distribution, while the fluorinated counterpart exhibits a bow-tie shape of negative LCPD, indicating a positive charge distribution. Large KPFM images (**Fig. S3**) of molecules adsorbed at various sites demonstrate the same trend, suggesting that the observed effects are not attributable to spatial variations in the LCPD of the substrate.

In terms of KPFM measurements, it is important to note that the obtained contrast is highly dependent on the tip-sample distance, as illustrated in **Fig. S4**. Specifically, when the tip-sample distance is far, the KPFM images do not exhibit intramolecular features. As the tip-sample distance decreases, submolecular contrast becomes increasingly pronounced. Nonetheless, at shorter tip-sample distances, tip relaxations can noticeably influence the KPFM signal and generate measurement artifacts. In contrast to nc-AFM imaging, where tip-relaxations improve the submolecular resolution, in KPFM measurement, such relaxations cause a noticeable deviation in the LCPD signal from its parabolic shape¹⁷. Therefore, we opt for a tip-sample height close to the Δf minima on both molecules, which ensures the absence of tip relaxation and enhances the contrast. This choice is further supported by the absence of submolecular resolution in Δf^* images (Δf^* corresponds to the $\Delta f(V)$ maximum that is, Δf at compensated LCPD, see Methods) for either An or FCI-An, as shown in **Fig. S4 and S5**.

To rationalize the experimental KPFM images, we performed KPFM simulations using the optimized supramolecular structures obtained from DFT calculations using PP-AFM code^{9,18}. The simulated KPFM images shown in **Fig. 3c,f** match very well with the experimental evidence. In particular, they also reproduce submolecular variation of the LCPD signal with the characteristic bow-tie pattern presented in the central part of FCI-An molecule. This internal variation of the LCPD signal also nicely matches the distribution of the electrostatic potential calculated for a free-standing FCI-An molecule, shown in **Fig. 3a**. This effect is associated with the heterogeneous charge distribution of the π -hole due to the different electronegativity of fluorine and chlorine modulating the charge transfer from the π -system locally.

We already mentioned that the presence of a π -hole can substantially change the stacking interaction. Thus, we analysed how the presence of π -hole affects the adsorption of the molecules on a metallic substrate. A series of constant height AFM images, shown in **Fig. S6**, reveal that submolecular contrast first emerges on FCI-An molecules independently of their adsorption site. This observation suggests different adsorption heights of the FCI-An and An molecules on the Au(111) surface. To analyse in more detail the different adsorption heights of the molecules, we carried out specific-site force-distance spectroscopy. **Fig. 4a** displays Δf -z spectroscopy acquired with the same CO-tip above the central benzene unit of both An and FCI-An molecules. The difference between the minima of two Δf -z curves of

30 pm can be directly related to the difference in the adsorption height of the molecule. Moreover, we also acquired Δf -z spectroscopy over the bare Au(111) surface, which enables us to determine the relative height of the molecules above the Au(111) surface, to be 330 and 360 pm for An and FCI-An, respectively. These values match reasonably well with the adsorption height obtained from the total energy DFT calculations of molecular assembly on Au(111) surface (325 and 344 pm, respectively).

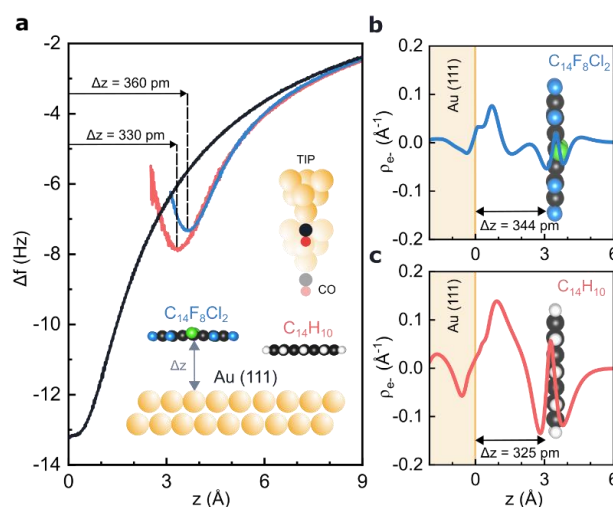


Fig. 4 | Charge transfer and π -hole effect on the adsorption height. **a**, Experimental adsorption heights measured with Δf -z spectroscopies in the middle hexagon of the molecules (inset) FCI-An (blue line) and An (red line) respect to Au(111) substrate (black-line). **(b, c)** Calculated induced electron density of FCI-An (top, blue line) on Au(111) and An (bottom, red line) as a function of the distance between the surface and the molecule.

One may argue that the greater adsorption height of FCI-An molecule is caused by the presence of chlorine atoms in FCI-An. A larger atomic radius of chlorine atoms (1.75 Å (Cl) and 1.47 Å (F)) may enhance Pauli repulsion pushing the molecule out of the Au(111) surface. However, the total energy DFT simulation of the fully fluorinated molecule provides a remarkably similar adsorption height of 343 pm over the Au(111) surface, see **Table S1** Thus, the presence of chlorine atoms does not influence the adsorption height. Next, we looked at the character of bonding interaction between the molecules and metallic substrate. According to DFT calculations, both molecules are physisorbed with negligible hybridization of molecular orbitals

(see **Fig. S7 and S8**), and the interaction is dominated by dispersion interaction, see **Table S2**. **Fig. 4 b,c** represents calculated induced electron density between An and FCI-An molecules and the Au (111) surfaces. We observe that there is more significant induced electron density in the interface between An molecule and metallic substrate compared to FCI-An/Au(111) interface. The induced charge density is a consequence of attractive electrostatic interaction between the molecule and the surface. In the case of An molecule, HOMO orbital is found close to the Fermi level of metal, which facilitates the charge induction upon the adsorption (**Fig. S7**). However, in the case of FCI-An molecule, the presence of π -hole increases the ionization potential and consequently suppresses the charge density induction at the molecule/metal interface.

To get more detailed insight into the adsorption energy, we perform the symmetry-adapted perturbation treatment (SAPT0), which provides the interaction energy decomposition scheme¹⁹. The SAPT0 analysis was performed on a cluster model, which gives very similar results to the slab model. It is also worth noting that DFT and SAPT0 calculations give very similar results of adsorption energies of molecules on Au(111), see **Table S2**. **Table S3** presents the SAPT0 energy decomposition for all three molecules. It is evident that in all cases, the attractive interaction dominates the dispersion energy compared to the electrostatic and induction terms. Importantly, the induction energy describing stabilization energy due to electrostatic interaction between permanent charge multipoles and the induced charge is larger for An than for FCI-An molecule. This trend fully agrees with the above-mentioned findings on the relative magnitude of induced electron densities in An and FCI-An predicted by the DFT slab calculation, see **Fig. 4b,c**.

Conclusions

Here, we presented the experimental evidence of the existence of π -hole in molecular systems by its real space imaging on a single molecule by means of Kelvin probe force microscopy. We showed that the presence of π -hole also influences the electrostatic interaction between the molecule and a metallic surface and, consequently, the adsorption height of the molecule. Namely, the π -hole increases the ionization potential of the molecule, which inhibits the induction of the charge density at the molecule/metal interface. This results in weakened induced electrostatic interactions and, consequently, in larger adsorption height

of the molecule. This study shows the potential of scanning microscopy for studying the internal charge distribution in molecules, which fundamentally affects their physical and chemical properties.

Methods

Experimental methods

The experiments were conducted at a temperature of 4.2 K using a commercial STM/nc-AFM microscope (Createc GmbH). Pt/Ir tips, sharpened by focused ion beam (FIB), were utilized and were further cleaned and shaped by gentle indentation (~1 nm) in the bare metallic substrate. STM topography was acquired in constant current mode with the bias voltage applied to the sample. In nc-AFM imaging, a qPlus sensor (resonant frequency \approx 30 kHz; stiffness \approx 1800 N/m) was operated in frequency modulation mode with an oscillation amplitude of 200 pm. Both nc-AFM and KPFM images were captured in constant height mode. The Au(111) substrate was prepared by repeated cycles of Ar⁺ sputtering (1 keV) and subsequent annealing at ~800 K. The STM/nc-AFM/KPFM images were processed using WSxM software ²⁰.

Molecular deposition

9,10-Dichlorooctafluoroanthracene (FCI-An) and anthracene (An) molecules were sublimated with two Knudsen cells simultaneously in UHV conditions at RT on the sample of Au (111) for 15 s.

KPFM characterization and analysis

LCPD maps were obtained by fitting a parabolic expression to frequency shift vs bias spectroscopies ($\Delta f(V, x, y)$) collected at all the points of a 64 x 80 pixels rectangular grid of size 3 nm x 5 nm. The data was collected at constant height using the same CO functionalized tip for both anthracene and chlorinated molecules. Each data point was acquired in approximately 3 seconds, with each parabola containing 600 points. Following the acquisition, we fitted the data with a parabolic expression of the form $\Delta f(V) = a \times (V - \text{LCPD})^2 + \Delta f^*$. The LCPD value, which corresponds to the bias at which the parabola has a maximum, and the Δf^* parameter, which is the maximum frequency shift value, were extracted from the fitted

parabolas and plotted separately in the (x, y) grids to generate maps. The data did not exhibit any significant distortion or deviation from expected parabolic behaviour within the bias range of (-150, 400) mV for either molecule or tip. The acquisition height was chosen to be in the attractive regime in order to maximize the electrostatic contribution for both molecules.

Theoretical methods

The optimized geometries of free-standing molecules, individual molecules adsorbed on the Au(111) surface, and the supramolecular assembly, both free standing and on-surface, were calculated using DFT-based methods implemented in the FHI-AIMS (Fritz Haber Institute Ab-Initio Materials Simulation) code²¹. Local atom-centred basis set consisted of the “light” default basis sets (the version from 2010) for individual species as distributed with FHI-AIMS. The PBE²² version of the GGA was employed for the exchange-correlation functional. The surface Brillouin zone was represented by only one k-point (Γ). This lightweight setup – “light” basis, PBE functional, no k-grid – was needed to cope with the relatively large supercells in calculations that involved the Au(111) surface. For individual free-standing molecules, calculations with the hybrid PBE0^{23,24} functional and the “tight” basis have also been carried out without substantial changes in either the geometry or charge distribution. The Au(111) slab consisted of 4 atomic layers. The size of the surface supercell intended to represent isolated molecules on the surface corresponded to the 6×6 unit cell of the unreconstructed Au(111) surface. In the case of the supramolecular structure, we first optimized the size of the supercell without the Au surface. Then, we constructed a $\sqrt{39}\times\sqrt{39}$ surface cell of Au(111) and deformed it somewhat (stretched by 1.20 % in one main crystallographic direction, compressed by 1.06 % in the other, and reduced the angle between the two directions from 60° to 56.3°) so as to exactly match 2 optimal unit cells of the supramolecular structure. During geometry optimization, the free-standing molecules were forced to remain planar while for molecules on the surface, all atoms in the system except the bottom layer Au atoms were allowed to relax. Van der Waals correction of interatomic forces based on the Tkatchenko-Scheffler method with Hirshfeld partitioning²⁵ was applied to the molecular structures on the surface, excluding direct Au-Au interaction. The geometries were considered fully optimized when all forces except those corresponding to a constraint were under 2 meV/Å.

The AFM and KPFM images have been simulated using the Probe Particle (PP) model¹⁸ adapted to a CO-terminated tip. The elastic deflection of the CO molecule has been modelled using the lateral (along the surface) spring constant of 0.25 N/m. DFT-calculated electron densities of the sample surface have been used in the PP model to evaluate the Pauli repulsion²⁶. Furthermore, DFT-calculated maps of electrostatic potential and electrical polarizability (derived from the difference of electron densities in the external field of 0.1 eV/Å and without the external field, respectively) have been employed to generate the simulated KPFM maps⁹ while assuming the d_z^2 -like charge quadrupole of $-0.2 e/\text{Å}^2$ for the CO tip termination.

The molecular orbitals, as well as the electrostatic potential maps of isolated An and FCI-An were calculated for MP2/cc-pVTZ²⁷ optimized geometries. The cluster calculations used for SAPT0 analysis consisted of a single molecule An and FCI-An and surface represented by one layer made of 38 gold atoms with (111) orientation. Both studied molecules were optimized on the gold layer using PBE0²³ functional with Grimme's D3²⁸ dispersion correction using the Becke-Johnson damping²⁹ and def2-TZVPP³⁰ basis set. The molecule was fully relaxed while the atoms of the gold layer were fixed. All these calculations were carried out by ORCA quantum chemistry program package³¹. SAPT0 calculations were made on the cluster models by PSI4³² program in cc-pVDZ (cc-pwCVDZ-PP³³ for Au) basis set.

Bibliography

1. Müller-Dethlefs, K. & Hobza, P. Noncovalent Interactions: A Challenge for Experiment and Theory. *Chem Rev* **100**, (2000).
2. Pluháčková, K., Jurečka, P. & Hobza, P. Stabilisation energy of C₆H₆...C₆X₆ (X = F, Cl, Br, I, CN) complexes: Complete basis set limit calculations at MP2 and CCSD(T) levels. *Physical Chemistry Chemical Physics* **9**, (2007).
3. Murray, J. S., Lane, P., Clark, T., Riley, K. E. & Politzer, P. σ -Holes, π -holes and electrostatically-driven interactions. *J Mol Model* **18**, (2012).
4. Řezáč, J. & Hobza, P. Benchmark Calculations of Interaction Energies in Noncovalent Complexes and Their Applications. *Chemical Reviews* vol. **116** (2016).
5. Wang, H., Wang, W. & Jin, W. J. σ -Hole Bond vs π -Hole Bond: A Comparison Based on Halogen Bond. *Chemical Reviews* vol. **116** (2016).

6. Gross, L., Mohn, F., Moll, N., Liljeroth, P. & Meyer, G. The chemical structure of a molecule resolved by atomic force microscopy. *Science (1979)* **325**, 1110–1114 (2009).
7. Jelínek, P. High resolution SPM imaging of organic molecules with functionalized tips. *Journal of Physics: Condensed Matter* **29**, 343002 (2017).
8. Wäckerlin, C. *et al.* Role of the Magnetic Anisotropy in Atomic-Spin Sensing of 1D Molecular Chains. *ACS Nano* **16**, 16402–16413 (2022).
9. Mallada, B. *et al.* Real-space imaging of anisotropic charge of σ -hole by means of Kelvin probe force microscopy. *Science (1979)* **374**, 863–867 (2021).
10. *Kelvin Probe Force Microscopy*. vol. 65 (Springer International Publishing, 2018).
11. Sadewasser, S. *et al.* New Insights on Atomic-Resolution Frequency-Modulation Kelvin-Probe Force-Microscopy Imaging of Semiconductors. *Phys Rev Lett* **103**, 266103 (2009).
12. Gross, L. *et al.* Measuring the Charge State of an Adatom with Noncontact Atomic Force Microscopy. *Science (1979)* **324**, 1428–1431 (2009).
13. Berger, J. *et al.* Quantum dissipation driven by electron transfer within a single molecule investigated with atomic force microscopy. *Nat Commun* **11**, (2020).
14. Mohn, F., Gross, L., Moll, N. & Meyer, G. Imaging the charge distribution within a single molecule. *Nat Nanotechnol* **7**, 227–231 (2012).
15. Klein, B. P. *et al.* Molecular Topology and the Surface Chemical Bond: Alternant Versus Nonalternant Aromatic Systems as Functional Structural Elements. *Phys Rev X* **9**, 011030 (2019).
16. Mallada, B. *et al.* Atomic-Scale Charge Distribution Mapping of Single Substitutional p- and n-Type Dopants in Graphene. *ACS Sustain Chem Eng* **8**, 3437–3444 (2020).
17. Albrecht, F. *et al.* Probing Charges on the Atomic Scale by Means of Atomic Force Microscopy. *Phys Rev Lett* **115**, 076101 (2015).
18. Hapala, P. *et al.* Mechanism of high-resolution STM/AFM imaging with functionalized tips. *Phys Rev B Condens Matter Mater Phys* **90**, 085421 (2014).
19. Gonthier, J. F. & Sherrill, C. D. Density-fitted open-shell symmetry-adapted perturbation theory and application to π -stacking in benzene dimer cation and ionized DNA base pair steps. *Journal of Chemical Physics* **145**, (2016).
20. Horcas, I. *et al.* WSXM: A software for scanning probe microscopy and a tool for nanotechnology. *Review of Scientific Instruments* **78**, 013705 (2007).
21. Blum, V. *et al.* Ab initio molecular simulations with numeric atom-centered orbitals. *Comput Phys Commun* **180**, 2175–2196 (2009).
22. Perdew, J. P., Burke, K. & Ernzerhof, M. Generalized Gradient Approximation Made Simple. *Phys Rev Lett* **77**, 3865–3868 (1996).
23. Adamo, C. & Barone, V. Toward reliable density functional methods without adjustable parameters: The PBE0 model. *J Chem Phys* **110**, 6158 (1999).

24. Ren, X. *et al.* Resolution-of-identity approach to Hartree-Fock, hybrid density functionals, RPA, MP2 and GW with numeric atom-centered orbital basis functions. *New J Phys* **14**, (2012).
25. Tkatchenko, A. & Scheffler, M. Accurate molecular van der Waals interactions from ground-state electron density and free-atom reference data. *Phys Rev Lett* **102**, 073005 (2009).
26. Krejčí, O., Hapala, P., Ondráček, M. & Jelínek, P. Principles and simulations of high-resolution STM imaging with a flexible tip apex. *Phys Rev B* **95**, (2017).
27. Dunning, T. H. Gaussian basis sets for use in correlated molecular calculations. I. The atoms boron through neon and hydrogen. *J Chem Phys* **90**, 1007–1023 (1989).
28. Grimme, S., Antony, J., Ehrlich, S. & Krieg, H. A consistent and accurate ab initio parametrization of density functional dispersion correction (DFT-D) for the 94 elements H-Pu. *J Chem Phys* **132**, 154104 (2010).
29. Grimme, S., Ehrlich, S. & Goerigk, L. Effect of the damping function in dispersion corrected density functional theory. *J Comput Chem* **32**, 1456–1465 (2011).
30. Weigend, F. & Ahlrichs, R. Balanced basis sets of split valence, triple zeta valence and quadruple zeta valence quality for H to Rn: Design and assessment of accuracy. *Physical Chemistry Chemical Physics* **7**, 3297 (2005).
31. Neese, F., Wennmohs, F., Becker, U. & Riplinger, C. The ORCA quantum chemistry program package. *Journal of Chemical Physics* **152**, (2020).
32. Smith, D. G. A. *et al.* P SI4 1.4: Open-source software for high-throughput quantum chemistry. *Journal of Chemical Physics* **152**, (2020).
33. Peterson, K. A. & Puzzarini, C. Systematically convergent basis sets for transition metals. II. Pseudopotential-based correlation consistent basis sets for the group 11 (Cu, Ag, Au) and 12 (Zn, Cd, Hg) elements. *Theor Chem Acc* **114**, (2005).

Author contributions

Conceptualization: P.J., P.H.

Methodology: B.M., B.T., P.J.

Theoretical calculations: M.O., A.G., M.L., P.J., P.H.

Experimental: B.M., A. J-M. B.T.

Funding acquisition: P.H., P.J.

Supervision: B.T., P.H., P.J.

Writing – original draft: B.M., B.T., P.H., P.J.

Acknowledgments

We acknowledge the financial support of Czech Science Foundation GACR 20-13692X (A.G., B.M., M.O., P.J.), 19-27454X (P.H.), 23-06781M (B.T.) and CzechNanoLab Research Infrastructure supported by

MEYS CR (LM2023051). B.M. and M.L. acknowledge support from the Internal Student Grant Agency of the Palacký University in Olomouc, Czech Republic, IGA_PrF_2022_026 (B.M.) and IGA_PrF_2023_018 (M.L.). B.M. also acknowledges the Fischer scholarship. The authors gratefully acknowledge the support of the Operational Programme for Research, Development, and Education of the European Regional Development Fund (Project No. CZ.02.1.01/0.0/0.0/16_019/0000754)

Competing interests

The authors declare no competing interests

What we observe as material bodies and forces are nothing but shapes and variations in the structure of space. Particles are just *schaumkommen* (appearances). The world is given to me only once, not one existing and one perceived. Subject and object are only one.

—Life and Thought, Cambridge U. Press, p327 (1989)

Erwin Schrodinger

Chapter 5

Conclusions and outlook

In this thesis, I have presented a selection of results obtained since 2017 using SPM techniques in the field of on-surface synthesis and the visualization of charge distributions in single atoms/molecules using KPFM. Within the field of OSS, my research has primarily focused on exploring the impact of intramolecular and intermolecular rearrangements on the production of diverse objects, including polymers and individual molecules. The first work presented in this thesis describes the temperature-dependent intramolecular rearrangements that mediate the magnetic properties of iron porphyrin polymers. As already commented, the presence of non-planar regions or entirely planar polymers plays a pivotal role in properties such as the magnetic anisotropy, a property fundamentally influenced by molecular geometry and its impact on the crystal field.

In the field of synthesis of π -conjugated polymers derived from acene precursors, I present one result involving the incorporation of defects into quasi-metallic anthracene ethynylene-bridged polymers. This investigation revealed that internal rearrangements between monomers can significantly disrupt or modify electronic and magnetic properties by affecting the conjugation of π -electrons. Additionally, I have participated in the synthesis of other polymers, where the precise engineering of acene size in monomers facilitated the

tailoring of topological order and π -conjugation to engineer quasi-metallic polymers[44, 45, 88]. However, during my studies, I have also participated in the exploration of other options for tailoring the properties of polymers, such as using monomers with vibronic modes compatible with certain chemical paths (e.g. the synthesis of bisanthene polymers with pentalene ladderized linkers[44]). Additionally, the hydrogenation of polymers has been explored by introducing hydrogen through the SPM head, followed by subsequent cleaning and manipulation using the STM tip. This process allows the creation of polymer regions with or without additional hydrogens with changing electronic properties.

Moreover, I have also dedicated time to the study of single polyaromatic hydrocarbons with non-benzenoid regions, in particular, the role of strain in helical molecules in the possible reaction on the surface. The molecule "All-in," encompassing cyclic groups ranging from four to eight-membered rings, demonstrated the role of strain, particularly in helical compounds, in synthesizing non-benzenoid regions with potential optoelectronic properties. The presence of azulene moieties, among others, perturbed the electronic properties of the molecule, resulting in areas with permanent dipolar moments.

The majority of my research efforts, however, have been devoted to visualizing charge distributions in single atoms, such as the impact of boron and nitrogen dopants in graphene or the presence of the σ -hole in bromine atoms. In particular, the study of σ -hole was performed over the course of three years, where it was explored a range of molecules containing different halogen atoms in various molecular scaffolds. Ultimately, we successfully compared a system with a σ -hole (Br and F in a tetrakis scaffold) to one without it. Although our initial intention was to employ nc-AFM to observe the σ -hole, we achieved direct observation of the anisotropic charge distribution using KPFM and by switching from a CO-tip to a Xe-tip in order to remove imaging artefacts from the quadrupole of the CO. Considering this, the observed properties of the σ -hole aligned perfectly with theoretical predictions. It is noteworthy that the experiment was enriched by the parallel

development of the Probe Particle model, which facilitated the generation of simulated KPFM images. This iterative process of experimental and theoretical collaboration led to the development of an atomistic theory explaining the origin of signals in KPFM. In this sense, I anticipate that KPFM, despite its time-intensive nature and the requirement for low-level noise in the AFM signal, will become a more common tool for characterizing systems ranging from the atomic scale to molecules, particularly for describing the polarizability of single atoms or molecules. Thus, one of the extensions of the developed work during the characterization of the σ -hole has been already applied in the characterization and observation of the related phenomenon of the π -hole in molecules such as FCl-An.

During my studies, in parallel with the projects presented in this thesis, I have also conducted research focusing on addressing the limitations of the on-surface synthesis methods and leveraging the benefits of wet chemistry through electrospray ion beam deposition (ES-IBD). ES-IBD, a widely recognized technique in mass spectrometry, involves the vaporization of a liquid solution into a fine spray using high electric fields. Through successive fragmentation, the solvent-containing solute droplets are reduced in size until the desired solute remains, which can then be adsorbed onto a surface under ultra-high vacuum (UHV) conditions.

After three years of research using a basic ES-IBD commercial setup, we have achieved successful depositions of systems that were previously unattainable through thermal sublimation due to their high molecular weight. Examples include zinc-based porphyrin rings comprising up to 12 monomers, as well as fragile organic molecules of significant biological interest, such as the highly delicate RP4a polyene essential in the immune response against Group B Streptococcus (GBS) diseases. Additionally, we have obtained structural insights, using the high-resolution capabilities of nc-AFM, of the adsorption behaviour of complex carbohydrates, such as β -cyclodextrin on metallic surfaces.

ES-IBD is expected to enable the deposition of complex biologically-relevant molecules

and complex precursors for on-surface synthesis, overcoming the molecular weight limitation of thermal evaporation. Toy-model experiments with real-time, real-space resolution could approximate biological processes, such as charge dynamics and their localization in complex molecules, such as dyes, proteins and chlorophyll relatives among others. Additionally, structural, mechanical, magnetic, and electrostatic information can be extracted from the conformation of biological molecules on surfaces. Although current surfaces are mostly metallic, a transition to insulators or semiconductors is inevitable. The utilization of these surfaces holds significant potential to enhance our understanding of intricate systems. This arises from the reduced impact of hybridization and charge transfer from the surface to the molecules, providing valuable insights into the conformation and dynamics of electrons within single molecules. Addressing challenges associated with these surfaces (e.g., graphene, MgO, KBr, NaCl, BN, metallic oxides) requires careful consideration of factors such as surface preparation, limitations of the STM at low temperatures, available reaction mechanisms, heterogeneous chemical environments and the influence of solvents and gases.

Bibliography

- ¹G. Binnig, H. Rohrer, C. Gerber, and E. Weibel, “Tunneling through a controllable vacuum gap”, *Applied Physics Letters* **40**, 178–180 (1982).
- ²J. Bardeen, “Tunnelling from a many-particle point of view”, *Physical Review Letters* **6**, 57–59 (1961).
- ³J. Bardeen, *Semiconductor research leading to the point contact transistor*, 1956.
- ⁴J. Tersoff and D. R. Hamann, “Theory and application for the scanning tunneling microscope”, *Physical Review Letters* **50**, 1998–2001 (1983).
- ⁵J. Tersoff and D. R. Hamann, “Theory of the scanning tunneling microscope”, *Physical Review B* **31**, 805–813 (1985).
- ⁶J. Kondo, “Resistance minimum in dilute magnetic alloys”, *Progress of Theoretical Physics* **32**, 37–49 (1964).
- ⁷C. J. Chen, *Introduction to Scanning Tunneling Microscopy* (Oxford University Press, 2007).
- ⁸G. Binnig, H. Rohrer, C. Gerber, and E. Weibel, “Surface studies by scanning tunneling microscopy”, *Physical Review Letters* **49**, 57–61 (1982).
- ⁹J. Wintterlin, J. Wiechers, H. Brune, T. Gritsch, H. Höfer, and R. J. Behm, “Atomic-resolution imaging of close-packed metal surfaces by scanning tunneling microscopy”, *Phys. Rev. Lett.* **62**, 59–62 (1989).

- ¹⁰G. Binnig, C. F. Quate, and C. Gerber, “Atomic force microscope”, *Physical Review Letters* **56**, 930–933 (1986).
- ¹¹F. J. Giessibl, “Principle of nc-afm”, in *Noncontact atomic force microscopy*, edited by S. Morita, R. Wiesendanger, and E. Meyer (Springer Berlin Heidelberg, Berlin, Heidelberg, 2002), pp. 11–46.
- ¹²T. R. Albrecht, P. Grütter, D. Horne, and D. Rugar, “Frequency modulation detection using highq cantilevers for enhanced force microscope sensitivity”, *Journal of Applied Physics* **69**, 668–673 (1991).
- ¹³Y. Martin, C. C. Williams, and H. K. Wickramasinghe, “Atomic force microscope force mapping and profiling on a sub 100Å scale”, *Journal of Applied Physics* **61**, 4723–4729 (1987).
- ¹⁴J. Welker, E. Illek, and F. J. Giessibl, “Analysis of force-deconvolution methods in frequency-modulation atomic force microscopy”, *Beilstein Journal of Nanotechnology* **3**, 238–248 (2012).
- ¹⁵J. E. Sader and S. P. Jarvis, “Accurate formulas for interaction force and energy in frequency modulation force spectroscopy”, *Applied Physics Letters* **84**, 1801–1803 (2004).
- ¹⁶L. Kelvin, “V.- contact electricity of metals”, *The London, Edinburgh, and Dublin Philosophical Magazine and Journal of Science* **46**, 82–120 (1898).
- ¹⁷M. Nonnenmacher, M. P. O’Boyle, and H. K. Wickramasinghe, “Kelvin probe force microscopy”, *Applied Physics Letters* **58**, 2921–2923 (1991).
- ¹⁸T. Glatzel and S. Sadewasser, eds., *Kelvin probe force microscopy*, Vol. 65 (Springer International Publishing, 2018).

- ¹⁹S. Sadewasser, P. Jelinek, C.-K. Fang, O. Custance, Y. Yamada, Y. Sugimoto, M. Abe, and S. Morita, “New insights on atomic-resolution frequency-modulation kelvin-probe force-microscopy imaging of semiconductors”, *Physical Review Letters* **103**, 266103 (2009).
- ²⁰B. Mallada, A. Gallardo, M. Lamanec, B. de la Torre, V. Pirko, P. Hobza, and P. Jelinek, “Real-space imaging of anisotropic charge of -hole by means of kelvin probe force microscopy”, *Science* **374**, 863–867 (2021).
- ²¹A. J. G. Caparrós, “Theoretical study of charge states in molecular nanostructures on surfaces” (Univerzita Karlova, Matematicko-fyzikální fakulta, 2022).
- ²²A. Zangwill, *Physics at surfaces* (Cambridge University Press, 1988).
- ²³J. I. Mendieta-Moreno, B. Mallada, B. D. L. Torre, T. Cadart, M. Kotora, P. Jelinek, P. Jelínek, J. I. Mendieta-Moreno, B. Mallada, B. D. L. Torre, P. Jelínek,] B. Mallada, T. Cadart, and M. Kotora, “Unusual scaffold rearrangement in polyaromatic hydrocarbons driven by concerted action of single gold atoms on a gold surface”, *Angewandte Chemie International Edition*, 10.1002/ANIE.202208010 (2022).
- ²⁴P. Hapala, G. Kichin, C. Wagner, F. S. Tautz, R. Temirov, and P. Jelnek, “Mechanism of high-resolution STM/AFM imaging with functionalized tips”, *Physical Review B* **90**, 085421 (2014).
- ²⁵G. Binnig, H. Rohrer, C. Gerber, and E. Weibel, “ 7×7 reconstruction on si(111) resolved in real space”, *Physical Review Letters* **50**, 120–123 (1983).
- ²⁶F. J. Giessibl, “Atomic resolution of the silicon (111)-(7x7) surface by atomic force microscopy”, *Science* **267**, 68–71 (1995).
- ²⁷L. Gross, F. Mohn, N. Moll, P. Liljeroth, and G. Meyer, “The chemical structure of a molecule resolved by atomic force microscopy”, *Science* **325**, 1110–1114 (2009).

- ²⁸T. Chutora, B. de la Torre, P. Mutombo, J. Hellerstedt, J. Kopeck, P. Jelnek, and M. vec, “Nitrous oxide as an effective AFM tip functionalization: a comparative study”, *Beilstein Journal of Nanotechnology* **10**, 315–321 (2019).
- ²⁹F. Mohn, B. Schuler, L. Gross, and G. Meyer, “Different tips for high-resolution atomic force microscopy and scanning tunneling microscopy of single molecules”, *Applied Physics Letters* **102**, 073109 (2013).
- ³⁰P. Jelínek, “High resolution spm imaging of organic molecules with functionalized tips”, *Journal of Physics: Condensed Matter* **29**, 343002 (2017).
- ³¹P. Hapala, R. Temirov, F. S. Tautz, and P. Jelnek, “Origin of high-resolution IETS-STM images of organic molecules with functionalized tips”, *Physical Review Letters* **113**, 10.1103/physrevlett.113.226101 (2014).
- ³²A. Gallardo, J. Fanfrlík, P. Hobza, and P. Jelínek, “Nature of binding in planar halogen-benzene assemblies and their possible visualization in scanning probe microscopy”, *The Journal of Physical Chemistry C* **123**, 8379–8386 (2019).
- ³³L. Bartels, G. Meyer, and K.-H. Rieder, “Controlled vertical manipulation of single CO molecules with the scanning tunneling microscope: a route to chemical contrast”, *Applied Physics Letters* **71**, 213–215 (1997).
- ³⁴B. de la Torre, M. vec, G. Foti, O. Krejčí, P. Hapala, A. Garcia-Lekue, T. Frederiksen, R. Zboil, A. Arnau, H. Vázquez, and P. Jelínek, “Submolecular resolution by variation of the inelastic electron tunneling spectroscopy amplitude and its relation to the afm/stm signal”, *Physical Review Letters* **119**, 166001 (2017).
- ³⁵N. Okabayashi, A. Gustafsson, A. Peronio, M. Paulsson, T. Arai, and F. Giessibl, “Relationship between the geometrical structure of a tip apex of a scanning probe microscope and the intensity of the signal in inelastic electron tunneling spectroscopy”, **61**, 651–656 (2018).

- ³⁶M. Chen, J. Shang, Y. Wang, K. Wu, J. Kuttner, G. Hilt, W. Hieringer, and J. M. Gottfried, “On-surface synthesis and characterization of honeycombene oligophenylene macrocycles”, *ACS NANO* **11**, 134–143 (2017).
- ³⁷L. B. Zasada, L. Guio, A. A. Kamin, D. Dhakal, M. Monahan, G. T. Seidler, C. K. Luscombe, and D. J. Xiao, “Conjugated metalorganic macrocycles: synthesis, characterization, and electrical conductivity”, *Journal of the American Chemical Society*, jacs.1c12596 (2022).
- ³⁸J. Zhou and Q. Sun, “Magnetism of phthalocyanine-based organometallic single porous sheet”, *Journal of the American Chemical Society* **133**, 15113–15119 (2011).
- ³⁹J. Su, M. Telychko, P. Hu, G. Macam, P. Mutombo, H. Zhang, Y. Bao, F. Cheng, Z. Q. Huang, Z. Qiu, S. J. Tan, H. Lin, P. Jelínek, F. C. Chuang, J. Wu, and J. Lu, “Atomically precise bottom-up synthesis of π -extended [5]triangulene”, *Science Advances* **5**, 10.1126/sciadv.aav7717 (2019).
- ⁴⁰S. Mishra, D. Beyer, K. Eimre, R. Ortiz, J. FernándezRossier, R. Berger, O. Gröning, C. A. Pignedoli, R. Fasel, X. Feng, and P. Ruffieux, “Collective allcarbon magnetism in triangulene dimers**”, *Angewandte Chemie* **132**, 12139–12145 (2020).
- ⁴¹N. Pavliek, A. Mistry, Z. Majzik, N. Moll, G. Meyer, D. J. Fox, and L. Gross, “Synthesis and characterization of triangulene”, *Nature Nanotechnology* **12**, 308–311 (2017).
- ⁴²S. Mishra, D. Beyer, K. Eimre, J. Liu, R. Berger, O. Groning, C. A. Pignedoli, K. Muellen, R. Fasel, X. Feng, and P. Ruffieux, “Synthesis and characterization of π -extended triangulene”, *JOURNAL OF THE AMERICAN CHEMICAL SOCIETY* **141**, 10621–10625 (2019).
- ⁴³Q. Fan, L. Yan, M. W. Tripp, O. Krejci, S. Dimosthenous, S. R. Kachel, M. Chen, A. S. Foster, U. Koert, P. Liljeroth, and J. M. Gottfried, “Biphenylene network: a nonbenzenoid carbon allotrope”, *SCIENCE* **372**, 852+ (2021).

- ⁴⁴B. de la Torre, A. Matj, A. Sánchez-Grande, B. Cirera, B. Mallada, E. Rodríguez-Sánchez, J. Santos, J. I. Mendieta-Moreno, S. Edalatmanesh, K. Lauwaet, M. Otyepka, M. Medve, Á. Buendía, R. Miranda, N. Martín, P. Jelínek, and D. Écija, “Tailoring π -conjugation and vibrational modes to steer on-surface synthesis of pentalene-bridged ladder polymers”, *Nature Communications* **11**, 4567 (2020).
- ⁴⁵B. Cirera, A. Sánchez-Grande, B. de la Torre, J. Santos, S. Edalatmanesh, E. Rodríguez-Sánchez, K. Lauwaet, B. Mallada, R. Zboil, R. Miranda, O. Gröning, P. Jelnek, N. Martn, and D. Ecija, “Tailoring topological order and π -conjugation to engineer quasi-metallic polymers”, *Nature Nanotechnology* **15**, 437–443 (2020).
- ⁴⁶S. Mishra, D. Beyer, K. Eimre, S. Kezilebieke, R. Berger, O. Gröning, C. A. Pignedoli, K. Müllen, P. Liljeroth, P. Ruffieux, X. Feng, and R. Fasel, “Topological frustration induces unconventional magnetism in a nanographene”, *Nature Nanotechnology* **15**, 22–28 (2019).
- ⁴⁷S. Jiang, T. Neuman, A. Boeglin, F. Scheurer, and G. Schull, “Topologically localized excitons in single graphene nanoribbons”, *Science* **379**, 1049–1054 (2023).
- ⁴⁸L. Grill and S. Hecht, “Covalent on-surface polymerization”, *Nature Chemistry* **12**, 115–130 (2020).
- ⁴⁹B. Mallada, S. Edalatmanesh, P. Lazar, J. Redondo, A. Gallardo, R. Zboil, P. Jelínek, M. vec, and B. de la Torre, “Atomic-scale charge distribution mapping of single substitutional p- and n-type dopants in graphene”, *ACS Sustainable Chemistry & Engineering* **8**, 3437–3444 (2020).
- ⁵⁰B. Mallada, P. Boski, R. Langer, P. Jelínek, M. Otyepka, and B. de la Torre, “On-surface synthesis of one-dimensional coordination polymers with tailored magnetic anisotropy”, *ACS Applied Materials I& Interfaces* **13**, 32393–32401 (2021).

- ⁵¹B. Mallada, B. de la Torre, J. I. Mendieta-Moreno, D. Nachtigallová, A. Matj, M. Matouek, P. Mutombo, J. Brabec, L. Veis, T. Cadart, M. Kotorá, and P. Jelínek, “On-surface strain-driven synthesis of nonalternant non-benzenoid aromatic compounds containing four- to eight-membered rings”, *Journal of the American Chemical Society* **143**, 14694–14702 (2021).
- ⁵²A. Shiotari, K. Tanaka, T. Nakae, S. Mori, T. Okujima, H. Uno, H. Sakaguchi, and Y. Sugimoto, “Chiral discrimination and manipulation of individual heptahelicene molecules on cu(001) by noncontact atomic force microscopy”, *Journal of Physical Chemistry C* **122**, 4997–5003 (2018).
- ⁵³K.-H. Ernst, “Molecular chirality at surfaces”, *physica status solidi (b)* **249**, 2057–2088 (2012).
- ⁵⁴A. Shiotari, T. Nakae, K. Iwata, S. Mori, T. Okujima, H. Uno, H. Sakaguchi, and Y. Sugimoto, “Strain-induced skeletal rearrangement of a polycyclic aromatic hydrocarbon on a copper surface”, *Nature Communications* **8**, 16089 (2017).
- ⁵⁵J. Su, X. Wu, S. Song, M. Telychko, and J. Lu, “Substrate induced strain for on-surface transformation and synthesis”, *Nanoscale* **12**, 7500–7508 (2020).
- ⁵⁶J. I. Mendieta-Moreno, R. C. Walker, J. P. Lewis, P. Gómez-Puertas, J. Mendieta, and J. Ortega, “Fireball / amber: an efficient local-orbital dft qm/mm method for biomolecular systems”, *Journal of Chemical Theory and Computation* **10**, 2185–2193 (2014).
- ⁵⁷S. Szalay, G. Barcza, T. Szilvási, L. Veis, and Ö. Legeza, “The correlation theory of the chemical bond”, *Scientific Reports* 2017 7:1 **7**, 1–10 (2017).
- ⁵⁸I. uti, J. Fabian, and S. D. Sarma, “Spintronics: fundamentals and applications”, *Reviews of Modern Physics* **76**, 323–410 (2004).

- ⁵⁹S. Watanabe, K. Ando, K. Kang, S. Mooser, Y. Vaynzof, H. Kurebayashi, E. Saitoh, and H. Sirringhaus, “Polaron spin current transport in organic semiconductors”, *Nature Physics* **10**, 308–313 (2014).
- ⁶⁰E. C. Ahn, “2d materials for spintronic devices”, *npj 2D Materials and Applications* **4**, 10.1038/s41699-020-0152-0 (2020).
- ⁶¹J. Li, N. M. Díez, E. C. Sanromà, M. Vilas-Varela, D. G. D. Oteyza, D. Peña, M. Corso, and J. I. Pascual, “Survival of spin state in magnetic porphyrins contacted by graphene nanoribbons”, *Science Advances*, 10.1126/sciadv.aag0582 (2018).
- ⁶²A. Sánchez-Grande, B. de la Torre, J. Santos, B. Cirera, K. Lauwaet, T. Chutora, S. Edalatmanesh, P. Mutombo, J. Rosen, R. Zboil, R. Miranda, J. Björk, P. Jelínek, N. Martín, and D. Écija, “On-surface synthesis of ethynylene-bridged anthracene polymers”, *Angewandte Chemie - International Edition* **58**, 6559–6563 (2019).
- ⁶³B. Mallada, Q. Chen, T. Chutora, A. Sanchez-Grande, B. Cirera, J. Santos, N. Martin, D. Ecija, P. Jelinek, and B. de la Torre, “Resolving atomic-scale defects in conjugated polymers on-surfaces”, *Chemistry A European Journal*, 10.1002/CHEM.202200944 (2022).
- ⁶⁴R. W. Newberry and R. T. Raines, “Secondary forces in protein folding”, *ACS Chemical Biology* **14**, PMID: 31243961, 1677–1686 (2019).
- ⁶⁵B. Salna, A. Benabbas, J. T. Sage, J. van Thor, and P. M. Champion, “Wide-dynamic-range kinetic investigations of deep proton tunnelling in proteins”, *Nature Chemistry* **8**, 874–880 (2016).
- ⁶⁶M. F. Perutz, “Electrostatic effects in proteins”, *Science* **201**, 1187–1191 (1978).
- ⁶⁷F. Mohn, L. Gross, N. Moll, and G. Meyer, “Imaging the charge distribution within a single molecule”, *Nature Nanotechnology* **7**, 227–231 (2012).

- ⁶⁸B. P. Klein, N. J. van der Heijden, S. R. Kachel, M. Franke, C. K. Krug, K. K. Greulich, L. Ruppenthal, P. Müller, P. Rosenow, S. Parhizkar, F. C. Bocquet, M. Schmid, W. Hieringer, R. J. Maurer, R. Tonner, C. Kumpf, I. Swart, and J. M. Gottfried, “Molecular topology and the surface chemical bond: alternant versus nonalternant aromatic systems as functional structural elements”, *Phys. Rev. X* **9**, 011030 (2019).
- ⁶⁹L. Gross, F. Mohn, P. Liljeroth, J. Repp, F. J. Giessibl, and G. Meyer, “Measuring the charge state of an adatom with noncontact atomic force microscopy”, *Science* **324**, 1428–1431 (2009).
- ⁷⁰F. Schulz, J. Ritala, O. Krej, A. P. Seitsonen, A. S. Foster, and P. Liljeroth, “Elemental identification by combining atomic force microscopy and kelvin probe force microscopy”, *ACS Nano* **12**, 5274–5283 (2018).
- ⁷¹K. Novoselov, A. Geim, S. Morozov, D. Jiang, Y. Zhang, S. Dubonos, I. Grigorieva, and A. Firsov, “Electric field effect in atomically thin carbon films”, *SCIENCE* **306**, 666–669 (2004).
- ⁷²A. H. Castro Neto, F. Guinea, N. M. R. Peres, K. S. Novoselov, and A. K. Geim, “The electronic properties of graphene”, *REVIEWS OF MODERN PHYSICS* **81**, 109–162 (2009).
- ⁷³X. Du, I. Skachko, A. Barker, and E. Y. Andrei, “Approaching ballistic transport in suspended graphene”, *NATURE NANOTECHNOLOGY* **3**, 491–495 (2008).
- ⁷⁴J.-H. Chen, C. Jang, S. Xiao, M. Ishigami, and M. S. Fuhrer, “Intrinsic and extrinsic performance limits of graphene devices on sio₂”, *NATURE NANOTECHNOLOGY* **3**, 206–209 (2008).
- ⁷⁵Y. Cao, V. Fatemi, S. Fang, K. Watanabe, T. Taniguchi, E. Kaxiras, and P. Jarillo-Herrero, “Unconventional superconductivity in magic-angle graphene superlattices”, *NATURE* **556**, 43+ (2018).

- ⁷⁶J. Sforzini, M. Telychko, O. Krejci, M. Vondracek, M. Svec, F. C. Bocquet, and F. S. Tautz, “Transformation of metallic boron into substitutional dopants in graphene on 6h-sic(0001)”, *PHYSICAL REVIEW B* **93**, 10.1103/PhysRevB.93.041302 (2016).
- ⁷⁷L. Banszerus, M. Schmitz, S. Engels, J. Dauber, M. Oellers, F. Haupt, K. Watanabe, T. Taniguchi, B. Beschoten, and C. Stampfer, “Ultrahigh-mobility graphene devices from chemical vapor deposition on reusable copper”, *SCIENCE ADVANCES* **1**, 10.1126/sciadv.1500222 (2015).
- ⁷⁸Z. Fang, S. Thongrattanasiri, A. Schlather, Z. Liu, L. Ma, Y. Wang, P. M. Ajayan, P. Nordlander, N. J. Halas, and F. Javier Garcia de Abajo, “Gated tunability and hybridization of localized plasmons in nanostructured graphene”, *ACS NANO* **7**, 2388–2395 (2013).
- ⁷⁹H. Gonzalez-Herrero, J. M. Gomez-Rodriguez, P. Mallet, M. Moaied, J. Jose Palacios, C. Salgado, M. M. Ugeda, J.-Y. Veullen, F. Yndurain, and I. Brihuega, “Atomic-scale control of graphene magnetism by using hydrogen atoms”, *SCIENCE* **352**, 437–441 (2016).
- ⁸⁰M. Telychko, P. Mutombo, P. Merino, P. Hapala, M. Ondráek, F. C. Bocquet, J. Sforzini, O. Stetsovych, M. Vondráek, P. Jelínek, and M. vec, “Electronic and chemical properties of donor, acceptor centers in graphene”, *ACS Nano* **9**, PMID: 26256407, 9180–9187 (2015).
- ⁸¹J. Redondo, M. Telychko, P. Procházka, M. Konený, J. Berger, M. Vondráek, J. echal, P. Jelínek, and M. vec, “Simple device for the growth of micrometer-sized monocrystalline single-layer graphene on SiC(0001)”, *Journal of Vacuum Science & Technology A* **36**, 031401, 10.1116/1.5008977 (2018).
- ⁸²P. Politzer, P. Lane, M. C. Concha, Y. Ma, and I. S. Murray, “An overview of halogen bonding”, *Journal of Molecular Modeling* **13**, 305–311 (2007).

- ⁸³X. Z. Zhao, K. Maddali, B. Christie Vu, C. Marchand, S. H. Hughes, Y. Pommier, and T. R. Burke, “Examination of halogen substituent effects on hiv-1 integrase inhibitors derived from 2,3-dihydro-6,7-dihydroxy-1h-isoindol-1-ones and 4,5-dihydroxy-1h-isoindole-1,3(2h)-diones”, *Bioorganic & Medicinal Chemistry Letters* **19**, 2714–2717 (2009).
- ⁸⁴T. Clark, M. Hennemann, I. S. Murray, and P. Politzer, “Halogen bonding: the sigma-hole. proceedings of "modeling interactions in biomolecules ii", prague, september 5th-9th, 2005.”, *Journal of molecular modeling* **13**, 291–6 (2007).
- ⁸⁵P. Auffinger, F. A. Hays, E. Westhof, and P. S. Ho, “Halogen bonds in biological molecules”, *Proceedings of the National Academy of Sciences* **101**, 16789–16794 (2004).
- ⁸⁶J. S. Murray, P. Lane, T. Clark, K. E. Riley, and P. Politzer, “ σ -holes, π -holes and electrostatically-driven interactions”, *Journal of Molecular Modeling* **18**, 541–548 (2011).
- ⁸⁷J. ezá and P. Hobza, “Benchmark calculations of interaction energies in noncovalent complexes and their applications”, *Chemical Reviews* **116**, PMID: 26943241, 5038–5071 (2016).
- ⁸⁸A. SánchezGrande, B. de la Torre, J. Santos, B. Cirera, K. Lauwaet, T. Chutora, S. Edalatmanesh, P. Mutombo, J. Rosen, R. Zboil, R. Miranda, J. Björk, P. Jelínek, N. Martín, and D. Écija, “Onsurface synthesis of ethynylenebridged anthracene polymers”, *Angewandte Chemie* **131**, 6631–6635 (2019).

List of Figures

1.1	The STM energy level diagram.	3
1.2	The STM feedback loop	7
1.3	Diagram of the AFM tip.	11
1.4	The FM-AFM feedback loop.	11
1.5	The capacitor model of KPFM.	14
1.6	The lineal contribution of F_{KPFM}^{SR} to the CPD	15
1.7	KPFM workflow	17
1.8	The imaging region of KPFM.	18
1.9	Degradation of the KPFM signal.	21
1.10	The effect of tip-sample distance in the LCPD maps.	22
2.1	The atomic resolution in STM	25
2.2	The high-resolution of nc-AFM	27
2.3	The STM tip functionalization	28
3.1	On-surface synthesis	31
3.2	Helical strained precursor	34
3.3	High resolution of non-planar objects	35
3.4	The planar non-benzenoid products	35
3.5	The pathway from precursor to all-in	36

3.6	Electronic properties and aromaticity of All-in	37
3.7	Synthesis of Fe porphyrin 1D polymers	49
3.8	High-resolution nc-AFM of porphyrin polymers	50
3.9	Polymer manipulation	50
3.10	Length of the polymers	51
3.11	Experimental magnetic anisotropy	51
3.12	Overview of an anthracene wire	63
3.13	The creation of defects in 4BrAn wires	65
3.14	Proportion of defects as a function of temperature.	66
3.15	Anthracene polymer defect type A	67
3.16	Anthracene polymer defect type B	68
4.1	Charge visualization using KPFM.	80
4.2	Boron and Nitrogen dopants in graphene	84
4.3	nc-AFM images of B and N dopants	84
4.4	Bond length analysis of the dopants	85
4.5	The charge distribution of single B and N dopants.	86
4.6	Definition of the σ -hole.	97
4.7	The models of 4BrPhM/4FPhM and STM topography on Ag(111)	99
4.8	Series of constant height nc-AFM images of 4BrPhM and 4FPhM	100
4.9	LCPD maps vs z of the σ -hole in bromine	102
4.10	Experimental and simulated LCPD maps of the σ -hole in Br.	102
4.11	Concept of π -hole	110
4.12	Overview of the system for measuring the π -hole	111
4.13	nc-AFM of FCl-An and An as a function of the tip-sample distance	112
4.14	LCPD mapping of an area containing a unit cell of FCl-An and An.l	112

4.15 Simulated and experimental charge distributions of An and FCl-An.	113
4.16 Charge transfer and -hole effect on the adsorption height	114

List of abbreviations

AFM Atomic force microscopy

CO Carbon monoxide

CPD Contact potential difference

DFT Density functional theory

DFT Density Functional Theory

FWHM Full width at half-maximum

HOMO Highest occupied molecularorbital

KPFM Kelvin Probe Force microscopy

LCPD Local contact potential difference

LDOS Local density of states

LHe Liquid helium

LN2 Liquid nitrogen

LUMO Lowest unoccupied molecularorbital

nc-AFM Non-contact atomic forcemicroscopy

OSS On-surface synthesis

PLL Phase locked-loop

PP Probe Particle

STM Scanning tunneling microscopy

STS Scanning tunnelling spectroscopy

UHV Ultra-high vacuum

1D One-dimensional

3D Three-dimensional

Chemical and physical properties
of molecular nanostructures on
surfaces investigated by means of
scanning probe microscopy.

a Ph.D. thesis by

Benjamin Jose Mallada Faes



Department of Physical Chemistry | Faculty of
Science

Palacký University

Olomouc
2023

Study programme: Nanomaterial Chemistry (NMCHA)

Field of study: Physical Chemistry

Form of study: Full-time

Author's first name and surname:

Benjamin Jose Mallada Faes

Supervisor: doc. Ing. Pavel Jelínek, Ph.D.

Opponents:

doc. Mgr. Martin Setvín, Ph.D.

Prof. Dimas G. de Oteyza, Ph.D.

Place and date of defence:

List of publications

- [1] A. Jimenez-Martin, F. Villalobos, **B. Mallada**, S. Edalatmanesh, A. Matěj, J. M. Cuerva, P. Jelinek, A. G. Campaña, and B. de la Torre, “On-surface synthesis of non-benzenoid conjugated polymers by selective atomic rearrangement of ethynylarenes”, *Chemical Science* 14, 1403–1412 (2023).
- [2] **B. Mallada**, Q. Chen, T. Chutora, A. Sanchez-Grande, B. Cirera, J. Santos, N. Martin, D. Ecija, P. Jelinek, and B. de la Torre, “Resolving atomic-scale defects in conjugated polymers on-surfaces”, *Chemistry–A European Journal* 28, e202200944 (2022).
- [3] J. I. Mendieta-Moreno, **B. Mallada**, B. de la Torre, T. Cadart, M. Kotora, and P. Jelínek, “Unusual scaffold rearrangement in polyaromatic hydrocarbons driven by concerted action of single gold atoms on a gold surface”, *Angewandte Chemie International Edition* 61, e202208010 (2022).
- [4] K. Biswas, J. I. Urgel, K. Xu, J. Ma, A. Sanchez-Grande, P. Mutombo, A. Gallardo, K. Lauwaet, **B. Mallada**, B. de la Torre, et al., “On-surface synthesis of a dicationic diazahexabenzocoronene derivative on the au (111) surface”, *Angewandte Chemie International Edition* 60, 25551–25556 (2021).
- [5] **B. Mallada**, P. Blonski, R. Langer, P. Jelinek, M. Otyepka, and B. de la Torre, “On-surface synthesis of one-dimensional coordination polymers with tailored magnetic anisotropy”, *ACS Applied Materials & Interfaces* 13, 32393–32401 (2021).
- [6] **B. Mallada** *, A. Gallardo*, M. Lamanec*, B. De La Torre, V. Spirko, P. Hobza, and P. Jelinek, “Real-space imaging of anisotropic charge of σ -hole by means of kelvin probe force microscopy”, *Science* 374, 863–867 (2021).

[7] **B. Mallada** *, B. de la Torre*, J. I. Mendieta-Moreno, D. Nachtigallova, A. Matěj, M. Matoušek, P. Mutombo, J. Brabec, L. Veis, T. Cadart, et al., “On-surface strain-driven synthesis of nonalternant non-benzenoid aromatic compounds containing four-to eightmembered rings”, *Journal of the American Chemical Society* 143, 14694–14702 (2021).

[8] B. Cirera, A. Sanchez-Grande, B. de la Torre, J. Santos, S. Edalatmanesh, E. RodríguezSanchez, K. Lauwaet, **B. Mallada**, R. Zbořil, R. Miranda, et al., “Tailoring topological order and π -conjugation to engineer quasi-metallic polymers”, *Nature nanotechnology* 15, 437–443 (2020).

[9] **B. Mallada**, S. Edalatmanesh, P. Lazar, J. Redondo, A. Gallardo, R. Zbořil, P. Jelínek, M. Švec, and B. de la Torre, “Atomic-scale charge distribution mapping of single substitutional p-and n-type dopants in graphene”, *ACS Sustainable Chemistry & Engineering* 8, 3437– 3444 (2020).

[10] B. de la Torre, A. Matěj, A. Sanchez-Grande, B. Cirera, **B. Mallada**, E. RodríguezSanchez, J. Santos, J. I. Mendieta-Moreno, S. Edalatmanesh, K. Lauwaet, et al., “Tailoring π -conjugation and vibrational modes to steer on-surface synthesis of pentalene-bridged ladder polymers”, *Nature Communications* 11, 4567 (2020).

[11] J. Redondo, P. Lazar, P. Prochazka, S. Průša, **B. Mallada**, A. Cahlík, J. Lachnitt, J. Berger, B. Šmíd, L. Kormoš, et al., “Identification of two-dimensional feo2 termination of bulk hematite α -fe2o3 (0001) surface”, *The Journal of Physical Chemistry C* 123, 14312–14318 (2019).

Contents

1	Introduction and aim of the thesis	6
2	Experimental techniques	7
2.1	Scanning Tunneling Microscopy	7
2.2	Atomic Force Microscopy	10
2.3	Kelvin Probe Force Microscopy	13
3	On-surface synthesis of molecular nanostructures	14
3.1	Strain-driven synthesis of non-benzenoid compounds from helical precursors	15
3.2	Magnetic anisotropy of one-dimensional porphyrin co- ordination polymers	18
3.3	Characterization of defects in 1D-anthracene conjugated polyme	21
4	Charge distribution visualization with KPFM	24
4.1	Charge Distribution of single boron and nitrogen dopants in graphene	26
4.2	Direct imaging of σ -hole	29
4.3	Direct imaging of π -hole	33
5	Conclusions and outlook	36
	Bibliography	39

1 Introduction and aim of the thesis

Basic science drives breakthroughs and accumulates knowledge for future applications. Scanning probe microscopy techniques, such as Kelvin Probe Force Microscopy (KPFM), enable precise imaging and manipulation of atoms and molecules. This thesis explores atomic-scale systems using scanning probe microscopy, presenting results in on-surface synthesis and charge distribution imaging within single atoms and molecules. In the on-surface synthesis section, it is studied in Section 3.1 how strain-driven chemical reactions in an helical compound can produce multiple non-benzenoid regions with 4 to 9 membered rings. In Section 3.2, it is studied the effect of planarization in iron porphyrin-based polymers on the magnetic anisotropy of the central iron of the monomers. Finally, in the last section Section 3.3, the defect incorporation within anthracen-based polymers provides insight on the possibility of carbon magnetism in organic polymers. In the charge distribution section, KPFM is used to visualize charge distributions in single molecules and atoms, including boron and nitrogen in graphene, a σ -hole in a brominated tetraphenyl molecule, and a π -hole in halogenated polyaromatic hydrocarbons. In Section 4 is discussed the visualization of charge distributions in single molecules and atoms by means of Kelvin probe force microscopy. In the Section 4.1, it is introduced the real space imaging of the extension of charges of a single boron and nitrogen atoms in substitu-

tional positions in graphene. In the Section 4.2 the addressed topic is the visualization of the charge distribution of a σ -hole in a brominated tetraphenyl molecule. This phenomenon, predicted to appear in some systems containing halogen atoms, is experimentally characterized with subatomic resolution using KPFM with different tip functionalizations and complemented with a theoretical framework that provides the simulation of experimental images. Finally, in Section 4.3 is introduced the measurement of the spatial charge distribution of a π -hole, a positive anisotropic charge distribution within an halogenated polyaromatic hydrocarbon.

2 Experimental techniques

2.1 Scanning Tunneling Microscopy

Scanning Tunneling Microscopy (STM) was first discovered in the early 1980s by Gerd Binnig and Heinrich Rohrer (Nobel Prize,1986) at IBM Zurich Research Laboratory in Switzerland[1]. The physical principle behind STM is the quantum tunnelling of electrons, which is a quantum mechanical effect that occurs when electrons have a non-zero probability of passing through a potential barrier that could not pass through. For the STM, the potential barrier is the vacuum between the metallic tip and the sample surface. The experimental realization of this principle is done by applying a bias voltage V to

the sample and bringing the tip close to the surface. In this regime, electrons can tunnel through the vacuum and generate a detectable current in the order of the $I \approx 1 \text{ nA}$ (10^{-9} A) from the sample to the tip.

The tunnelling current exhibits an exponential behaviour as a function of tip-sample distance, with the current rapidly decreasing as the tip is moved further away from the surface. This exponential behaviour is due to the exponential decay of the wavefunction Ψ of the tunnelling electrons, which determines the probability of finding the electrons on the other side of the potential barrier. The solution of the Schrodinger equation inside of the region defined by the barrier (see Fig. 1) yields a solution of the form:

$$\Psi(z) = \Psi(0)e^{-kz} \tag{1}$$

Where $\Psi(0)$ is a constant depending on the boundary conditions and the decay constant k depending on the effective work function Φ inside the barrier:

$$k = \sqrt{\frac{2m\Phi}{\hbar^2}} \tag{2}$$

The atomic resolution is achieved thanks to this exponential character of the wavefunction Ψ of the electrons inside the barrier, as the majority of the current will flow just through the closest atoms of the tip and sample and decay fast elsewhere. This provides STM with a

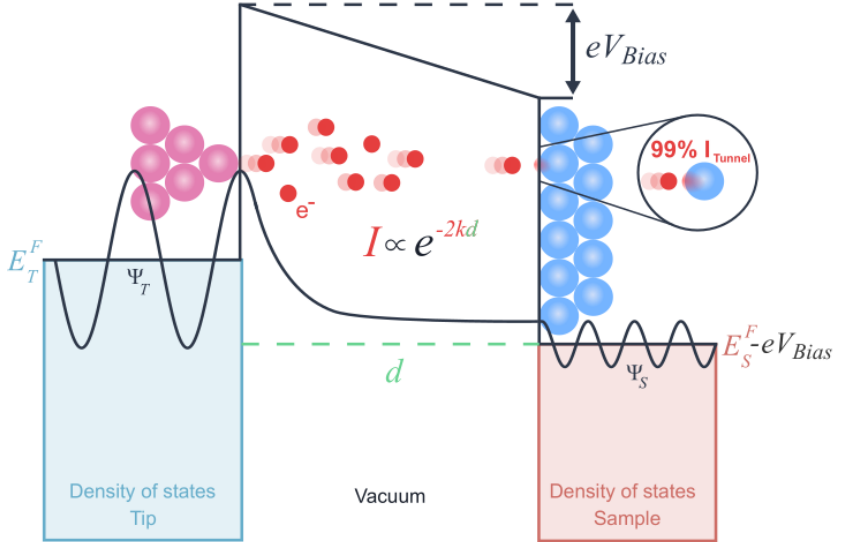


Figure 1: Energy level diagram of the tip-sample system. In the experimental setup used in this work, a bias voltage V_{Bias} is applied to the sample, while the tip is grounded. The following sign convention is used: $V_{\text{Bias}} > 0$ explores the empty states of the sample, with electrons flowing from the tip to the sample, while $V_{\text{Bias}} < 0$ probes the occupied states of the sample, where electrons tunnel from the sample to the tip.

great lateral and vertical resolution, as objects changing in height by 100 pm will change the tunnelling current by an order of magnitude.

The Scanning Tunneling Microscope (STM) employs a piezoelectric scanner element for precise positioning of the tip relative to the sample. The scanner, typically a piezoelectric tube, has electrodes controlling movement in the $\pm X$ and $\pm Y$ directions, while another electrode regulates the extension and retraction of the tip along the Z

axis. A voltage applied to the electrodes enables controlled positioning of the tip.

STM operates in two modes: constant current and constant height. In the constant current mode, a feedback loop compares the measured tunneling current at the tip with a setpoint. The difference between the two, called the error signal, is used in a Digital Signal Processor (DSP) to control the movement of the tip. A Proportional-Integral controller in the DSP processes the error signal, generating an output signal Δz , which represents the desired topography. The Δz signal is then amplified to drive the piezoelectric tube. This mode allows the STM to track variations in the position of the tip in the Z direction while scanning the XY plane.

Constant height mode, on the other hand, operates without a feedback loop. The measured signal is the tunneling current as the tip scans the XY plane. The resulting image captures topographic information, with variations in the tunneling current indicating smaller or larger surface features. In this mode, higher scanning speeds are achievable as the current signal bandwidth is determined by preamplifiers, rather than the signal processing stages.

2.2 Atomic Force Microscopy

Non-contact atomic force microscopy (AFM) is an imaging technique that overcomes the limitations of the scanning tunneling microscope

(STM) by allowing imaging of insulating materials and reducing tip-sample interactions. In AFM, a cantilever with a tip attached is used to measure the interactions between the tip and the sample[2]. The cantilever acts as a simple harmonic oscillator with a resonance frequency, stiffness, and quality factor. The tip is brought close to the surface without making contact, and the short-range and long-range interactions between the tip and the sample are detected by monitoring changes in the cantilever's amplitude and frequency.

Two modes of operation are commonly used in AFM: amplitude modulation (AM) and frequency modulation (FM). In the AM-AFM mode, the tip is vibrated with a fixed amplitude and frequency, and changes in the resonant frequency of the cantilever caused by attractive or repulsive interactions with the sample are recorded. However, this mode has limitations at the atomic scale and can be slow in ultrahigh vacuum (UHV) environments.

To overcome these limitations, FM-AFM was introduced. In FM-AFM, the cantilever is driven at its resonance frequency while keeping the amplitude constant[3]. Changes in the frequency, known as the frequency shift, indicate the presence of forces between the tip and the sample. This mode offers increased sensitivity and reduced noise compared to AM-AFM, especially in UHV conditions. The frequency shift and other parameters such as amplitude, phase, and dissipation contain valuable information about the tip-sample interaction.

FM-AFM utilizes two feedback loops: one for frequency and another for amplitude control. The feedback system drives the cantilever at its resonance frequency using an actuator, and the deflection of the cantilever is converted into an AC voltage signal. This signal is processed through a phase-locked loop (PLL), where the phase and amplitude information is extracted and compared to setpoints. The output of the PLL controls the drive signal to maintain the desired frequency and amplitude, allowing precise measurement of the tip-sample interaction.

2.3 Kelvin Probe Force Microscopy

Kelvin Probe Force Microscopy (KPFM) is a technique that is more sensitive to the electrostatic properties of molecules and surfaces compared to traditional atomic force microscopy (AFM). It utilizes the principle of a capacitor to measure the contact potential difference (CPD) between a conducting tip and a sample[4].

$$\Delta f = \frac{1}{2} \frac{\partial C(z)}{\partial z} (V - V_{CPD})^2 \quad (3)$$

By applying an external electric field and measuring the frequency shift of the AFM cantilever, the CPD can be determined. KPFM provides a global picture of the electrostatics of the system in the far distance regime, but in the close distance regime, it can also capture local variations known as local contact potential differences (LCPD). The KPFM signal is composed of a large-range component that produces a parabolic behavior and a short-range component that follows Coulomb's law. The interaction between these components results in a lineal shift of the KPFM parabola, which allows resolution between positive and negative regions of the sample. The experimental images obtained using KPFM represent a combination of the charges from the tip and the sample, and the polarizability of the tip can influence the contribution of the sample charges in the image.

3 On-surface synthesis of molecular nanostructures

On-surface synthesis (OSS) is a promising method for creating atomically precise molecular nanostructures by performing chemical reactions on solid surfaces[5]. It offers advantages over traditional solution-based methods, leveraging the unique chemical environment and molecule-surface interactions. Geometrical boundaries and surface confinement frequently lead to ordered and regular structures, modifying reaction pathways and enabling control at the atomic level. OSS has achieved precise control over material composition, including the synthesis of conjugated organic polymers and graphene nanoribbons. Various reaction mechanisms, such as Ullmann coupling and cyclohydrogenations, play a crucial role in OSS. However, other mechanisms such as internal rearrangements within molecules and polymers contribute to the specific and efficient reactions on the surface. In this section are presented three selected results that demonstrate the formation of well-defined structures such as synthesis of products with non-benzenoid regions and 4 to 8 membered rings, tailored magnetic properties in coordinated iron porphyrin-based polymers, and the effects of the incorporation of defects behavior in anthracene polymers joined by ethynylene bridges.

3.1 Strain-driven synthesis of non-benzenoid compounds from helical precursors

The stability of chemical compounds is influenced by the spatial arrangement of functional groups on the molecule. Steric hindrance can arise from different hybridizations or chemical species, leading to strain in the molecular scaffold. Geometrical constraints and surface effects can modulate this strain by inducing molecular rearrangements upon adsorption. This rearrangement can have significant consequences, such as locking the chirality of a molecule or determining its conversion into other products. Non-benzenoid regions in molecules, which can be achieved through strain, have unique electronic properties and can alter optical properties, symmetry, charges, and aromaticity. However, wet chemistry synthesis of compounds with non-benzenoid regions faces challenges due to reactivity and solvent effects, necessitating alternative approaches.

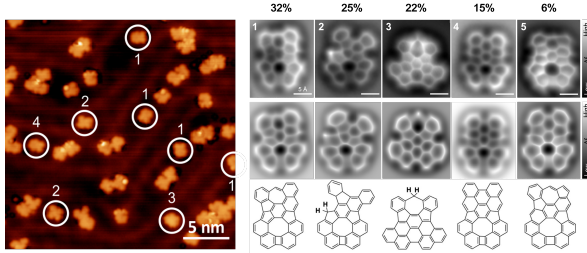


Figure 2: The collection of planar objects on the Au(111) surface. In the left panel, an STM topography image ($V_{Bias} = 100$ mV, 10 pA). In the right panel, the experimental constant height nc-AFM with CO-tip (top row), simulated PP nc-AFM (middle row) and structural models (bottom row).

This study[6] focuses on a helical, strained molecule called the precursor, which undergoes a skeletal rearrangement on an Au(111) surface in ultrahigh vacuum (UHV), resulting in the production of planar products with non-benzenoid regions. The precursor is sublimated in UHV and deposited on the Au(111) surface. Scanning tunneling microscopy (STM) and non-contact atomic force microscopy (nc-AFM) at low temperatures are used to characterize the adsorbed molecules. The precursor is thermally activated by heating the sample, promoting the production of planar products. High-resolution nc-AFM identifies all products on the surface, including non-planar or ill-defined molecules.

The planar structures, distinguished by the absence of bright spots in STM images, are further analyzed. The planar products are categorized into five molecules (P1 to P5), with P1 (All-in) being par-

ticularly relevant due to its non-benzenoid 4-5-6-7-8 membered rings. The distribution of products on the surface is not consistent with thermodynamic stability since the more stable P4 is found in lower proportions compared to All-in. This suggests that the reaction is kinetically driven. Molecular dynamics simulations are employed to understand the chemical pathway from the precursor to All-in. The simulations track relevant spatial coordinates and reveal that the minimization of free energy plays a role in the higher yield of All-in. The planarization of a methyl group into a hexagonal ring increases dispersive forces, leading to subsequent steps in the reaction pathway.

The All-in product is extensively characterized experimentally and theoretically. Scanning tunneling spectroscopy (STS) measurements and maps show a molecular band-gap and electron localization in the azulene moiety. The global aromaticity of All-in is determined through a combination of theoretical techniques and experimental bond length analysis. The results demonstrate a strong main aromatic current involving all the π -electrons, contributing to the global aromaticity while avoiding antiaromatic regions.

3.2 Magnetic anisotropy of one-dimensional porphyrin coordination polymers

One-dimensional organic magnets with regularly spaced magnetic centers have gained attention for their potential use in spintronic devices due to their extended spin coherence length, mechanical flexibility, and advantageous array-like geometry for industrial applications. However, the synthesis of 1D polymeric molecular spintronics remains challenging. One approach to address this challenge is through the use of well-defined, straight, conjugated polymers such as porphyrin molecules with coordinated transition metal atoms. Porphyrins exhibit high thermal stability and tend to form well-ordered assemblies on solid surfaces, making them ideal for on-surface synthesis of 1D organometallic polymers. The interaction between ligands and a metal ion surrounding them creates a region of negative charge that interacts with the positively charged metal ion, leading to the splitting of the d-orbitals into two energy levels. The magnetic anisotropy of the central metal atom is determined by the coordination of the ligand field, offering the potential to control it by modifying either the coordinated metal atom or the ligand. By tailoring the coupling between the molecular ligand field and the magnetic anisotropy of the metal atom, new opportunities for spintronic applications in arrays of organometallic systems containing magnetic atoms can be created.

In this study[7] it is introduced the synthesis of 1D polymeric

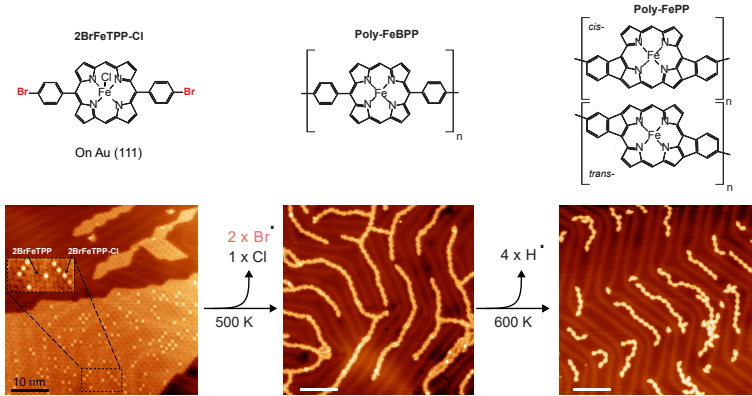


Figure 3: The reaction proceeds in three stages: first, the material is deposited at room temperature; next, the temperature is raised to 500 K to induce the formation of non-planar polymers; and finally, the temperature is further increased to 600 K to promote the formation of planar polymers.

porphyrin-based wires with iron coordinated atoms. First, the precursor compound Iron(III) 5,15-(di-4-bromophenyl)porphyrin chloride (2BrFeDPP-Cl) is deposited on the surface, forming ordered, closely packed islands with both Cl-containing and Cl-free molecules in a random distribution. Subsequent annealing at 500 K induces debromination and aryl-aryl coupling between monomers, resulting in the formation of covalently bonded molecular wires known as Poly-FeDPP. However, steric hindrance causes the aryl-aryl linkers to be twisted and obscure the visualization of the lower porphyrin core. Further annealing at 600 K leads to intramolecular rearrangements of the aryl groups and cyclization of the aryl and pyrrolic groups of the porphyrins, resulting in the planarization of the polymer, now called Poly-FePP. The pla-

nar polymers are connected by covalent bonds, and the cis and trans FePP units are formed in roughly equal amounts.

During the reaction steps, the magnetic anisotropy of the coordinated Fe is affected by the local chemical and geometrical environment. The precursor compound 2BrFeDPP-Cl has a net spin of $S=3/2$, while the dechlorinated 2BrFeDPP has a lower oxidation state of the iron, leading to a total spin of $S=1$. The measurement of magnetic anisotropy is performed using inelastic spin excitation in dI/dV curves of the Fe atoms. The experimental magnetic anisotropy in single 2BrFeDPP and linked monomers of FeDPP is minimally affected by the polymerization process, indicating a triple with $S=1$. However, planarization of FePP does reduce the magnetic anisotropy, attributed to the breaking of square-planar symmetry and subsequent charge redistribution during the planarization process. In conclusion, the modulation of the magnetic anisotropy by different states of the polymerization reaction provides insight in the potential application of on-surface synthesis protocols to create polymers with well defined magnetic anisotropies depending on the manipulation of the geometry of the monomers.

3.3 Characterization of defects in 1D-anthracene conjugated polyme

The emergence of on-surface synthesis as a new method for designing nanomaterials with precise atomic structures and customized electronic properties has opened up new possibilities in the field. This approach allows for the production of large conjugated polymers with atomic precision under ultra-high vacuum (UHV) conditions, which are not attainable through solution chemistry. One such example is the synthesis of ethynylene-bridged polymers derived from anthracene, pentacene, and bisanthene. These one-dimensional polymers exhibit two resonance forms: fully aromatic acenes with ethynylene bridges or quinoid acenes with cumulene bridges. The ground state of these polymers is a combination of both forms, and the dominant resonance structure is determined by the interplay between repulsive electron-electron interaction and electron-phonon coupling.

Introducing atomic-scale defects in these polymers allows for the manipulation of their electronic properties. In the case of anthracene wires, defects [8] can disrupt electronic conjugation, resulting in reduced electron mobility, changes in the intrinsic band structure, or the formation of open-shell configurations with nontrivial pi-magnetism. Defect engineering provides valuable insights into the synthetic limitations of pi-conjugated polymers.

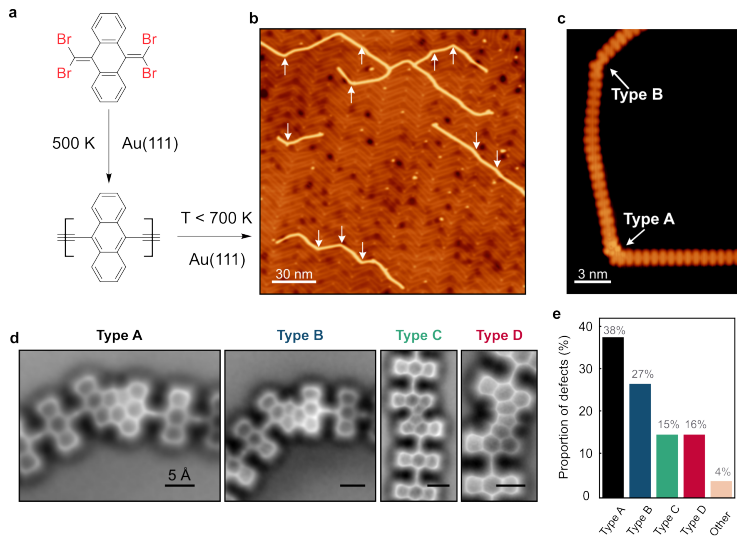


Figure 4: a, Scheme of the reaction sequence of 4BrAn wires and the incorporation of defects. b, STM topography ($V_{Bias} = 200$ mV, $I_{set} = 5$ pA) showing the defects as kinks in the wires. c) Detail ($V_{Bias} = 5$ mV, $I_{set} = 10$ pA) of two kinks incorporating the most common defects type A and B. d) Constant height nc-AFM with CO-tip (Laplacian filtered) images of the most common defects. e) Histogram of relative abundance of the most common defects.

In this project, the authors focused on studying the consequences of introducing defects in anthracene ethynylene-bridged polymers through thermal annealing. The process began with the deposition of the molecular precursor 11,11,12,12-tetrabromoanthra-p-quinodimethane (4BrAn) onto a clean Au(111) surface using organic molecular beam epitaxy. The sample was then annealed at 500 K for 30 minutes in UHV to promote the synthesis of ethynylene-bridged anthracene polymers. Heating the surface at this temperature resulted in distorted

molecular wires with a significantly higher density of structural defects. Further annealing up to 700 K introduced intermolecular defects into the anthracene wires, typically in the form of laterally fused chains.

The defects observed in the molecular wires were classified as type A and B. Type A defects involved in-plane joints or kinks between pristine ethynylene-bridged anthracene segments, while type B defects constituted six- and five-membered rings at the junctions. Statistical analysis revealed that type A defects were the most common, while type B defects were less prevalent. The presence of these defects had varying degrees of impact on the electronic structure. Type A defects disrupted the band structure locally and exhibited a characteristic Kondo resonance resulting from the screening of a magnetic moment. On the other hand, type B defects showed featureless characteristics, suggesting a closed-shell structure with cumulene-like bridges.

The formation of these defects could potentially be controlled by introducing external sources of atomic carbon atoms during the polymerization reaction. Although a detailed understanding of the defect formation mechanism requires complex quantum molecular mechanics calculations, this study provided valuable insights into the role of these defects in the conjugation of anthracene-ethynylene polymers on Au(111).

4 Charge distribution visualization with KPFM

The role of charge and its spatial distribution at the atomic and molecular scale is crucial in understanding the behavior of various physical and chemical systems. Electrostatic interactions between charged regions of molecules are particularly important in biological processes such as protein folding, where they influence the stability and function of protein structures. The influence of charge distribution in surfaces and molecular systems has wide-ranging consequences, from protein studies to experimental realization of theoretical predictions in non-covalent interactions.

Atomic force microscopy (AFM), but more specifically Kelvin probe force microscopy (KPFM), a member of the AFM techniques, has emerged as a valuable tool for visualizing electrical charge distributions on surfaces at the atomic scale. KPFM has been successfully used to achieve submolecular resolution in imaging the charge distribution of individual molecules, measuring dipole moments, characterizing charge states of atoms, and discerning elements in epitaxial systems.

This study investigates the significance of charge distribution in various atomic and molecular systems and its visualization using KPFM. The charge distribution of single substitutional dopants (boron and

nitrogen) in graphene is investigated, demonstrating their divergent chemical activity and providing insights into the atomic-level functionalization of graphene derivatives. Additionally, subatomic resolution of anisotropic charge distributions within single halogen atoms is examined, revealing the existence of σ -holes and enabling the quantification of non-covalent interactions. Finally, the existence of π -holes in organic molecular systems and their impact on electrostatic interactions with metallic surfaces are experimentally confirmed using an halogenated PAH based on anthracene.

4.1 Charge Distribution of single boron and nitrogen dopants in graphene

Graphene, the first isolated 2D material, possesses unique mechanical and electronic properties but lacks control over its chemical and electronic behavior. In this project, the focus is on incorporating boron and nitrogen atoms into graphene to explore their effects on its properties. Monolayer graphene is grown on a SiC(0001) substrate, and boron and nitrogen dopants are introduced through a two-step process. The dopants are characterized using scanning tunneling microscopy (STM), atomic force microscopy (AFM), and Kelvin probe force microscopy (KPFM)[9].

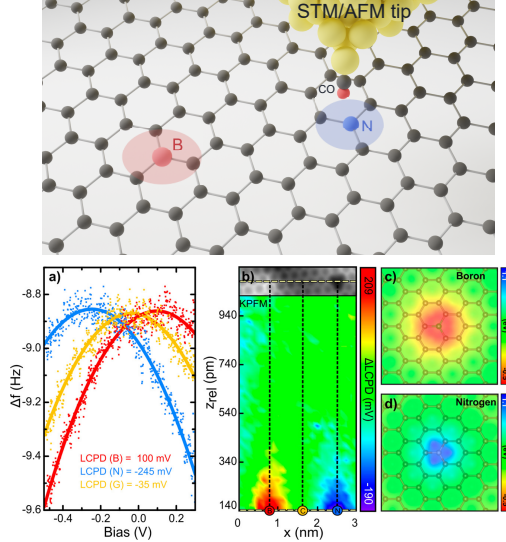


Figure 5: Schematic of the BN-G system. The CO-tip, with the STM feedback open, acquires single KPFM spectroscopies (a) on B (red), N (blue), and C (yellow). (b) LCPD map in the XY plane. Red represents a positive LCPD (negative charge) and blue a negative shift (positive charge). The DFT calculated Hartree potentials for both dopants (d) confirms the experimental results where B/N behave as negative/positive point-like charges confined to the surroundings of the dopants.

STM imaging reveals the presence of dopants as bright objects with three-fold symmetry. However, high-resolution AFM with a CO-tip allows for direct atomic identification. The honeycomb structure of carbon atoms is resolved, and boron and nitrogen atoms appear brighter and darker, respectively. The surrounding carbon atoms exhibit bond length distortions due to localized electrostatic charges induced by the dopants. KPFM is used to characterize the charge

distribution surrounding the dopants.

The KPFM results show that the dopants induce a shift in the local contact potential difference (LCPD), reflecting changes in the surface dipole and local work function. Nitrogen dopants result in a positive LCPD shift, indicating an increase in local work function, while boron dopants cause a negative LCPD shift, indicating a decrease in local work function. This difference in LCPD sign reveals the localization of positive and negative net charges on nitrogen and boron sites, respectively. The magnitude of the LCPD difference indicates a comparable level of opposite charge doping by boron and nitrogen. The net charge on the dopants arises from electron acceptance/donation to the graphene's π -band and subsequent electronic redistribution.

DFT calculations support the experimental findings, showing negative/positive net charges on boron/nitrogen dopants in the Hartree potential images. The chemical properties of the dopants are assessed by measuring the interaction between the CO tip and the dopants, confirming that the interaction is primarily driven by weak electrostatic forces.

4.2 Direct imaging of σ -hole

Noncovalent interactions (NCIs), such as hydrogen bonding, electrostatic interactions, van der Waals forces, and halogen bonding, play a fundamental role in various chemical systems. Halogen bonding, a subset of NCIs, involves the interaction of halogen atoms (e.g., F, Cl, Br) with Lewis bases. It has gained attention due to its unique properties in terms of directionality and strength of interaction. Halogen bonding has been utilized in the design of drug molecules to increase their binding affinity to specific receptors.

The halogen bond arises from the formation of an electron-depleted region on the halogen atom, which is covalently bonded to another element, typically carbon. This electron-depleted region, known as the σ -hole, acts as an electrophilic site that can interact with negatively charged Lewis bases. The σ -hole emerges due to the anisotropy of the electron distribution around the halogen atom, resulting in a region of positive electrostatic potential along the covalent bond axis.

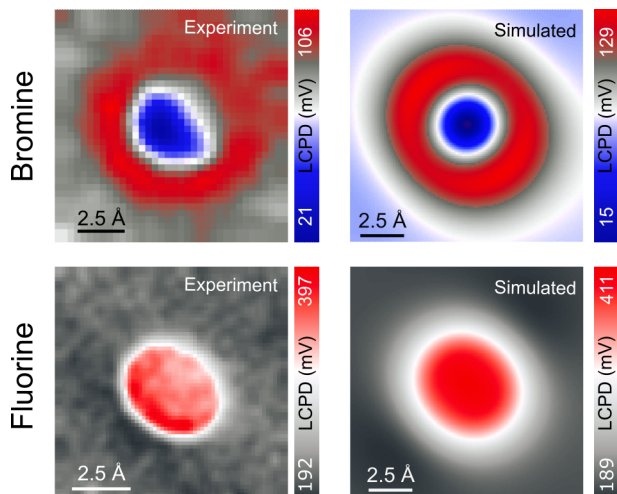


Figure 6: Experimental and PP-simulated LCPD maps of the σ -hole in Br (top row) and its absence in F (bottom row).

This section [10] is aimed to visualize the anisotropic charge distribution known as the σ -hole in single bromine atoms using real-space visualization techniques. A comparison was made between two molecular systems: one with a fluorine atom (without a σ -hole) and one with a bromine atom displaying the σ -hole. This not only provided visualization of the σ -hole but also contributed to the development of a more comprehensive theory of Kelvin probe force microscopy (KPFM). This section examines the capabilities and limitation of noncontact atomic force microscopy (nc-AFM) in imaging systems with complex electrostatic behavior. It also discusses the potential applications of KPFM in determining anisotropic charge distributions in single atoms or molecules, the impact of tip functionalization, and the importance

of a solid theoretical understanding of KPFM signal origins.

The experimental setup involved using scanning tunneling microscopy (STM), nc-AFM, and KPFM to visualize the σ -hole in a tetragonal molecule with phenyl groups, where each phenyl contains one halogen (bromine or fluorine) joined by a single bond to the phenyl group. The molecules were individually deposited on an Ag(111) surface using thermal sublimation. The Ag(111) surface was chosen to avoid interference from surface corrugation. The coverage of each molecule type was adjusted to approximately 20-30% of the surface, leading to the formation of rectangular islands primarily driven by electrostatic interactions.

The nc-AFM characterization using CO-tips did not reveal any subatomic features associated with the presence of a σ -hole in either the brominated or fluorinated molecules. The AFM contrast observed was predominantly governed by attractive dispersion forces and Pauli interactions, which exhibited a spherical nature. The electrostatic interaction responsible for the anisotropic charge distribution of the σ -hole was significantly weaker compared to dispersion and Pauli interactions.

To enhance the electrostatic interaction, KPFM was employed. Initially, using CO-tips resulted in donut-shaped charge distributions in the local contact potential difference (LCPD) maps for both bromine and fluorine. The ambiguity in the contrast of both atom types origi-

nated from the robust quadrupolar charge distribution of the CO-tip. To address this issue, the CO-tip was replaced with a Xe-tip, which facilitated a direct depiction of the σ -hole charge distribution in the brominated version of the molecule through KPFM. This study revealed the presence of the σ -hole as a region of negative LCPD with a width of approximately 200 pm at different heights. This electron-depleted region was surrounded by a crown of a more electron-rich region. The LCPD maps depended on the tip-sample distance and provided information about the electrostatic interaction between the tip and the molecule. In contrast, the fluorinated molecule exhibited a positive shift in LCPD and a homogeneous charge distribution. Finally non-covalent interaction between the CO and Xe tips and the halogenated atoms was measured to be below 1 kcal/mol, confirming the dominance of dispersion and electrostatic interactions.

4.3 Direct imaging of π -hole

This section presents one of the most recent results in the field of anisotropic charge visualization in halogenated systems [11]. The submolecular charge distribution in single atoms or molecules plays a crucial role in determining their physical-chemical properties and intermolecular interactions. One interesting manifestation of an anisotropic charge distribution is the presence of a π -hole, which refers to a π -electron-deficient region found in certain halogen-substituted polycyclic aromatic hydrocarbon compounds.

The electron distribution within these molecules is strongly influenced by the electronegativity of peripheral halogen substituents, such as fluorine or chlorine, resulting in an electron withdrawal from carbon atoms towards the halogens. This change in the occupied orbitals leads to a depletion of electron density in the central π -system on the carbon atoms. This electron-deficient area, located in the same plane as the π electrons of the hydrocarbon compound, can influence the stabilization of intermolecular π stacking interactions.

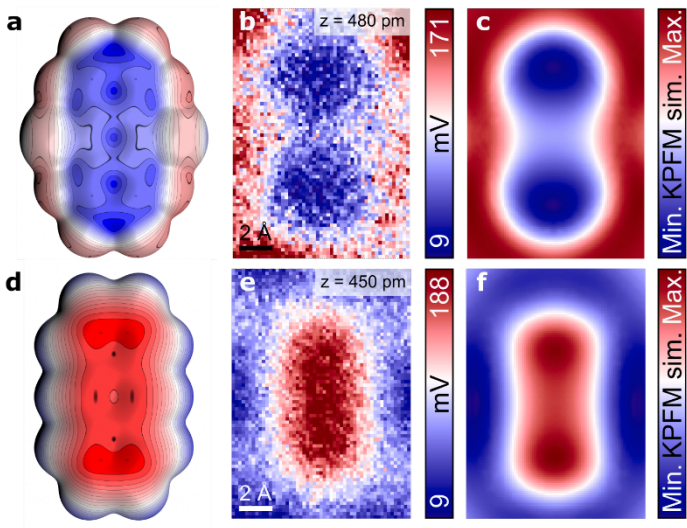


Figure 7: (a, d), Electrostatic potential maps of free-standing FCl-An and An molecules. (b, e), Experimental LCPD maps of An and FCl-An acquired with the same CO-tip in constant height mode. (c, f), Probe Particle simulated LCPD maps of FCl-An and An.

While the existence of π -holes has been theoretically established, direct experimental observation has remained elusive. This study aims to visualize the π -hole in a molecule of Dichlorooctafluoroanthracene (FCl-An) and compare it with a molecule of anthracene (An) that does not develop a π -hole. The experimental setup involves depositing the molecules on a gold (111) substrate under ultrahigh vacuum conditions and characterizing the resulting self-assembled structure using scanning tunneling microscopy (STM) and non-contact atomic force microscopy (nc-AFM) with a carbon monoxide (CO) tip.

To visualize the charge distribution within each molecule, Kelvin

probe force microscopy (KPFM) is employed, which allows the visualization of the purely electrostatic phenomenon of the π -hole. Big-scale local contact potential difference (LCPD) maps reveal a distinct difference in contrast between FCl-An and An, with FCl-An exhibiting a bow-tie shape of negative LCPD and An showing a uniform, more positive LCPD associated with a negative charge distribution.

High-resolution LCPD images of single molecules further confirm the distinct charge distribution patterns. Anthracene molecules exhibit fully delocalized π -electrons and a uniformly distributed electron density, while FCl-An molecules display an anisotropic charge distribution due to electron migration towards the halogenated atoms. The addition of chlorine in specific positions results in the formation of a σ -hole, contributing to an uneven depletion in the middle section of the molecule and creating the bow-tie shape.

The presence of the π -hole also affects the adsorption of molecules on a metallic substrate. AFM images indicate submolecular contrast on FCl-An molecules, indicating different adsorption heights compared to An. Force-distance spectroscopy reveals a 30 pm difference in the curves, reflecting the variation in adsorption height. Density functional theory (DFT) calculations show that the presence of the π -hole in FCl-An suppresses the charge density induction at the molecule/metal interface, resulting in a higher adsorption distance compared to An.

5 Conclusions and outlook

This thesis presents a range of results obtained since 2017 using scanning probe microscopy (SPM) techniques in the field of on-surface synthesis (OSS) and the visualization of charge distributions in single atoms/molecules using Kelvin probe force microscopy (KPFM). Within the OSS field, my research primarily focused on investigating the impact of intramolecular and intermolecular rearrangements on the production of diverse objects, including polymers and individual molecules.

One aspect of my research explored temperature-dependent intramolecular rearrangements in iron porphyrin polymers, which play a crucial role in magnetic properties. Non-planar regions or entirely planar polymers influence properties such as magnetic anisotropy, which is fundamentally influenced by molecular geometry and its impact on the crystal field.

In the synthesis of π -conjugated polymers derived from acene precursors, I investigated the incorporation of defects into quasi-metallic anthracene ethynylene-bridged polymers. Internal rearrangements between monomers were found to significantly disrupt or modify electronic and magnetic properties by affecting π -electron conjugation. Additionally, I participated in the synthesis of other polymers by precisely engineering the size of acene monomers, enabling the tailoring of topological order and π -conjugation to create quasi-metallic poly-

mers. Furthermore, I explored other approaches for tailoring polymer properties, such as using monomers with vibronic modes compatible with specific chemical paths or hydrogenating polymers through the SPM head.

In addition to polymers, I dedicated time to studying single polyaromatic hydrocarbons with non-benzenoid regions, particularly examining the role of strain in helical molecules for possible on-surface reactions. The molecule "All-in," which encompasses cyclic groups ranging from four to eight-membered rings, demonstrated the role of strain, especially in helical compounds, in synthesizing non-benzenoid regions with potential optoelectronic properties.

A significant portion of my research focused on visualizing charge distributions in single atoms, such as boron and nitrogen dopants in graphene, as well as the presence of the σ -hole in bromine atoms. The study of the σ -hole spanned three years and involved exploring a range of molecules containing different halogen atoms in various molecular scaffolds. By employing KPFM and switching from a CO-tip to a Xe-tip, we achieved direct observation of the anisotropic charge distribution associated with the σ -hole. The observed properties matched with theoretical predictions, and the development of the Probe Particle model enhanced the understanding of KPFM signals. Lastly, as a recent result, we have achieved the the measurement of the spatial charge distribution of a π -hole within halogenated polyaromatic hy-

drocarbons. By examining a single molecule of Dichlorooctafluoroanthracene and comparing it with the hydrogenated anthracene, the presence of a positive anisotropic charge distribution is confirmed.

References

- ¹G. Binnig, H. Rohrer, C. Gerber, and E. Weibel, “Tunneling through a controllable vacuum gap”, *Applied Physics Letters* **40**, 178–180 (1982).
- ²G. Binnig, C. F. Quate, and C. Gerber, “Atomic force microscope”, *Physical Review Letters* **56**, 930–933 (1986).
- ³T. R. Albrecht, P. Grütter, D. Horne, and D. Rugar, “Frequency modulation detection using highq cantilevers for enhanced force microscope sensitivity”, *Journal of Applied Physics* **69**, 668–673 (1991).
- ⁴M. Nonnenmacher, M. P. O’Boyle, and H. K. Wickramasinghe, “Kelvin probe force microscopy”, *Applied Physics Letters* **58**, 2921–2923 (1991).
- ⁵L. Grill and S. Hecht, “Covalent on-surface polymerization”, *Nature Chemistry* **12**, 115–130 (2020).
- ⁶B. Mallada, B. de la Torre, J. I. Mendieta-Moreno, D. Nachtigallová, A. Matj, M. Matouek, P. Mutombo, J. Brabec, L. Veis, T. Cadart, M. Kotora, and P. Jelínek, “On-surface strain-driven synthesis of nonalternant non-benzenoid aromatic compounds containing four- to eight-membered rings”, *Journal of the American Chemical Society* **143**, 14694–14702 (2021).

- ⁷B. Mallada, P. Boski, R. Langer, P. Jelínek, M. Otyepka, and B. de la Torre, “On-surface synthesis of one-dimensional coordination polymers with tailored magnetic anisotropy”, *ACS Applied Materials & Interfaces* **13**, 32393–32401 (2021).
- ⁸B. Mallada, Q. Chen, T. Chutora, A. Sanchez-Grande, B. Cirera, J. Santos, N. Martin, D. Ecija, P. Jelinek, and B. de la Torre, “Resolving atomic-scale defects in conjugated polymers on-surfaces”, *Chemistry – A European Journal*, 10.1002/CHEM.202200944 (2022).
- ⁹B. Mallada, S. Edalatmanesh, P. Lazar, J. Redondo, A. Gallardo, R. Zboil, P. Jelínek, M. vec, and B. de la Torre, “Atomic-scale charge distribution mapping of single substitutional p- and n-type dopants in graphene”, *ACS Sustainable Chemistry & Engineering* **8**, 3437–3444 (2020).
- ¹⁰B. Mallada, A. Gallardo, M. Lamanec, B. de la Torre, V. pirko, P. Hobza, and P. Jelinek, “Real-space imaging of anisotropic charge of π -hole by means of kelvin probe force microscopy”, *Science* **374**, 863–867 (2021).
- ¹¹B. Mallada, M. Ondracek, M. Lamanec, A. Gallardo, A. Jimenez-Martin, B. de la Torre, P. Hobza, and P. Jelinek, “Visualization of π -hole in molecules by means of kelvin probe force microscopy”, Preprint, 10.26434/chemrxiv-2023-gw0xn (2023).